A Contribution to the Study of the Near-Field Contrail by Using a High-Fidelity Computational Method Combined to an Advanced Microphysical Model

by

Parisa AFKARI

MANUSCRIPT-BASED THESIS PRESENTED TO ÉCOLE DE TECHNOLOGIE SUPÉRIEURE IN PARTIAL FULFILLEMENT FOR THE DEGREE OF DOCTOR OF PHILOSOPHY
Ph.D.

MONTREAL, JANUARY 21, 2026

ÉCOLE DE TECHNOLOGIE SUPÉRIEURE
UNIVERSITÉ DU QUÉBEC

BOARD OF EXAMINERS

THIS THESIS HAS BEEN EVALUATED

BY THE FOLLOWING BOARD OF EXAMINERS

Mr. François Garnier, Thesis Supervisor
Department of Aerospace Engineering at École de technologie supérieure

Ms. Claudiane Ouellet-Plamondon, President of the Board of Examiners
Department of Construction Engineering at École de technologie supérieure

Mr. Louis Dufresne, Member of the Jury
Department of Mechanical Engineering at École de technologie supérieure

Mr. Leonid Nichman, External Evaluator
Aerospace Research Center at the National Research Council of Canada

THIS THESIS WAS PRENSENTED AND DEFENDED

IN THE PRESENCE OF A BOARD OF EXAMINERS AND PUBLIC

ON DECEMBER 15, 2025

AT ÉCOLE DE TECHNOLOGIE SUPÉRIEURE

ACKNOWLEDGMENT

I would like to express my deepest gratitude to Prof. François Garnier, my supervisor, whose unwavering support, insightful guidance, and expertise were invaluable throughout my PhD. He has been a role model to me as a professor, and his patience, constructive feedback, and constant encouragement shaped my research and academic growth.

I also wish to thank Dr. Mohamed Chouak, a research assistant in our group, for his significant contributions and technical support across multiple phases of my work. I am especially grateful to Dr. Sébastien Cantin, my desk neighbor, for his thoughtful advice and for collaborating with me on two journal papers. I am grateful to my colleagues and friends at the Safran Chair (AeroPropulsion Laboratory, ÉTS) for their collaboration, insightful discussions, and encouragement, which created a stimulating research environment. I also thank the students from other laboratories I had the opportunity to meet during these years.

Special thanks go to our industrial partner, Safran, for supporting this project. I also extend my sincere gratitude to the Digital Research Alliance of Canada for providing high performance computing resources that made my simulations feasible.

Finally, I thank my loved ones, beginning with my husband, Dr. Sajad Mirzaei. From the day we met as master's students to completing our PhDs together, his unwavering support, patience, and strength have been invaluable. His understanding has carried me through every challenge and has made this work possible. I also thank my family, including my brother and sister, and especially my parents. Being far from them was difficult, yet their belief in my progress never wavered. My parents' sacrifices and encouragement carried me to this milestone. I dedicate this achievement to them with love and respect; whatever I am, I owe to them.

Contribution À L'Étude Des Traînées De Condensation En Champ Proche En Utilisant Une Méthode Numérique Haute-Fidélité Combinée Avec Un Modèle De Microphysique Avancé

Parisa AFKARI

RÉSUMÉ

L'importance accordée à la protection de l'environnement, la croissance attendue du trafic aérien et l'accumulation de preuves sur le forçage radiatif non-CO_2 de l'aviation ont fait des traînées de condensation un sujet central dans l'évaluation des impacts climatiques de l'aviation. L'influence climatique des cirrus formés à partir des traînées de condensation d'aéronefs demeure l'un des volets les plus incertains du forçage radiatif anthropique. Des observations et des modèles sont mobilisés pour préciser la façon dont les cristaux de glace se forment dans le sillage proche de l'avion et pour estimer les distributions globales de leurs propriétés microphysiques et optiques. L'effet radiatif des traînées dépend de la taille des cristaux et de la concentration numérique, mais ces deux grandeurs sont difficiles à quantifier en raison des hypothèses sur la dynamique du sillage et des traitements simplifiés de la microphysique de phase glace aux tout premiers stades.

L'objectif de cette thèse est de développer et de valider un cadre de modélisation qui simule l'écoulement du jet d'éjection derrière un turboréacteur à double flux réaliste et son entraînement précoce dans le champ de vortex de sillage, tout en intégrant des processus microphysiques couplés en ligne afin de déterminer les propriétés initiales des particules de glace. Les simulations dynamiques sont réalisées avec un code CFD interne (FludiLES) en simulation des grandes échelles (LES), avec une précision spatiale d'ordre 6 et temporelle d'ordre 3. Un jet libre à pression atmosphérique et à nombre de Reynolds réaliste ($Re \approx 10^6$) est calculé et validé par confrontation à des résultats expérimentaux. Pour la microphysique, les particules de suie et les aérosols ambiants sont suivis par une méthode lagrangienne. Un couplage bidirectionnel est appliqué au transfert de masse de vapeur et à l'énergie, tandis que la quantité de mouvement est traitée en sens unique (fluide → particules); la rétroaction particules → fluide sur la quantité de mouvement est négligeable et la rétroaction énergétique est faible.

Un jet bi-flux (cœur et flux secondaire) est simulé pour quantifier l'effet du taux de dilution (bypass ratio) en considérant trois moteurs—CFM56-5B3/3, LEAP-1A/33 et une configuration à très haut taux de dilution (UHBR)—à des températures ambiantes de 215, 220 et 225 K. Une comparaison initiale entre un turboréacteur à double flux et un turbojet équivalent a montré que le flux secondaire accélère le mélange et le refroidissement en champ proche du panache cœur, augmentant le rayon moyen des particules jusqu'à 30 %. Sur l'ensemble des moteurs, des taux de dilution plus élevés intensifient davantage le mélange, favorisent l'activation des suies puis leur congélation, et conduisent à des propriétés initiales de traînées moins sensibles à la température ambiante.

Le modèle microphysique a ensuite été étendu pour inclure les effets de soluté via le paramètre d'hygroscopicité (κ) et évalué en configurations couplée en ligne et « boîte » hors ligne. Dans des conditions réalistes de croisière pour un LEAP-1A, trois groupes de scénarios sont examinés: (i) κ = 0.0005, 0.005, 0.0142, correspondant à des teneurs équivalentes en soufre du carburant (FSC) de 50, 410 et 1270 ppm; (ii) des indices d'émission en nombre de suie de 10^{13} à 10^{15} #/kg de carburant; et (iii) des rayons de noyau de suie de 10 à 30 nm. La diminution de κ de 0.0142 à 0.0005 réduit légèrement le rayon des particules mais accroît la fraction activée d'environ 20 % en raison d'une plus grande disponibilité de vapeur. Abaisser l'indice initial en nombre de suie de 10^{15} à 10^{13} particules par kilogramme de carburant augmente le rayon moyen d'environ 0.3 μm à 2.4 μm à 1 s et élève la fraction activée d'environ 66 %. Des noyaux de suie plus gros renforcent l'activation d'environ 20 %, avec des différences de rayon moyen atteignant ~80 % vers 0.4 s puis se resserrant à ~10 % à 1 s. Les LES 3D avec microphysique couplée en ligne s'avèrent indispensables pour l'analyse de sensibilité en champ proche; un modèle 0D en boîte hors ligne surestime l'activation et représente mal la sensibilité à κ.

Les simulations sont ensuite prolongées dans la phase de vortex afin de comparer les formulations LES temporelle et spatiale et de quantifier l'influence de la méthodologie numérique sur la microphysique pour des scénarios « suie seule » et « suie + ambiant ». Pour évaluer les effets de l'initialisation, le vortex de sillage est initialisé à partir de la modélisation de la phase jet à t_j= 0.12 s et t_j= 0.5 s. Dans des conditions de croisière représentatives d'un Airbus A320neo motorisé par LEAP-1A, la formulation temporelle présente un mélange plus vigoureux au début et une dissipation scalaire plus rapide dans la phase jet que la formulation spatiale, produisant ~60 % de cristaux de glace activés en plus pour le cas « suie seule » et ~70 % de plus lorsque les aérosols ambiants sont inclus. Pour une initialisation précoce du vortex, les cas initialisés temporellement maintiennent légèrement plus de glace activée, tandis que l'initialisation spatiale engendre des rayons moyens plus grands à temps tardif; ces écarts s'atténuent, en particulier en présence d'aérosols ambiants. Pour une initialisation tardive du vortex, la tendance s'inverse: l'initialisation spatiale donne davantage de glace activée, alors que l'initialisation temporelle conserve le rayon moyen le plus élevé. Dans tous les cas, l'aérosol ambiant augmente le nombre de cristaux de glace tout en limitant la croissance par cristal via la compétition pour la vapeur, ce qui modère la sensibilité à l'initialisation du jet. Globalement, l'entraînement en phase de vortex est relativement insensible au choix de modélisation de la phase jet; en revanche, l'instant de démarrage du vortex demeure déterminant, et les valeurs microphysiques absolues conservent une mémoire mesurable du mélange en champ proche du jet.

Mots-clés: Traînée de condensation, Aéronef, Climat, Écoulement de jet, Vortex de sillage, Turbulence, Simulation CFD, Simulation des grandes échelles (LES), Microphysique, Particule de suie, Condition ambiante, Turboréacteur à double flux

A Contribution to the Study of the Near-Field Contrail by Using a High-Fidelity Computational Method Combined to an Advanced Microphysical Model

Parisa AFKARI

ABSTRACT

Global emphasis on environmental protection, expected growth in air traffic, and accumulating evidence on aviation's non-CO_2 radiative forcing have made contrails an important component in assessments of aviation climate impacts. The climate influence of cirrus formed from aircraft condensation trails remains one of the most uncertain components of anthropogenic radiative forcing. Observations and models are used to clarify how ice crystals form in the near-field aircraft wake and to estimate global distributions of their microphysical and optical properties. The radiative effect of contrails depends on ice crystal size and number concentration, yet both are difficult to quantify because of assumptions about wake dynamics and simplified treatments of early ice-phase microphysics.

The objective of this thesis is to develop and validate a modeling framework that simulates exhaust jet flow behind a realistic turbofan and its early entrainment into the wake-vortex field, while integrating online-coupled microphysical processes to determine the initial properties of ice particles. Dynamic simulations are performed with an in-house CFD code (FludiLES) using large-eddy simulation (LES) with sixth-order spatial and third-order temporal accuracy. A free jet at atmospheric pressure and a realistic Reynolds number ($Re \approx 10^6$) is computed and validated against experimental results. For the microphysics, soot and ambient aerosol particles are tracked with a Lagrangian method. Two-way coupling is applied to vapor mass transfer and energy, whereas momentum is one-way (fluid → particles); particle-to-fluid momentum feedback is negligible, and energy feedback is small.

A dual-stream jet (core and bypass) is simulated to quantify bypass ratio effects using three engines—CFM56-5B3/3, Leading Edge Aviation Propulsion (LEAP)-1A/33, and an ultra-high-bypass-ratio (UHBR) configuration—at ambient temperatures of 215, 220, and 225 K. An initial comparison of a turbofan with an equivalent turbojet showed that the bypass stream accelerated near-field mixing and cooling of the core plume, increasing the mean particle radius by up to 30%. Across the engine set, larger bypass ratios further intensified mixing, promoted soot activation and subsequent freezing, and yielded initial contrail properties that were less sensitive to ambient temperature.

Subsequently, the microphysical model was extended to include solute effects through the hygroscopicity parameter (κ) and was evaluated in both online-coupled and offline box model configurations. Under realistic LEAP-1A cruise conditions, three scenario groups are examined: (i) $\kappa = 0.0005$, 0.005, 0.0142, corresponding to equivalent fuel sulfur contents (FSC) of 50, 410, and 1270 ppm; (ii) soot number emission indices of 10^{13} to 10^{15} #/kg-fuel; and (iii) soot core radii of 10–30 nm. Reducing κ from 0.0142 to 0.0005 slightly decreases particle

radius but increases the activation fraction by about 20% due to greater vapor availability. Lowering the initial soot number from 10^{15} to 10^{13} particles per kilogram of fuel increases the mean particle radius from roughly 0.3 μm to 2.4 μm at 1 s and raises the activated fraction by about 66%. Larger soot cores enhance activation by about 20%, with mean-radius differences reaching approximately 80% near 0.4 s and narrowing to about 10% by 1 s. Three-dimensional LES with online-coupled microphysics is shown to be essential for near-field sensitivity analysis; a zero-dimensional offline box model overpredicts activation and misrepresents κ sensitivity.

Simulations are then extended into the vortex phase to compare temporal and spatial LES formulations and to quantify how numerical methodology influences microphysics for soot-only and soot+ambient scenarios. To assess the effects of initialization, the wake-vortex was initialized from jet phase modeling at t_j= 0.12s and t_j= 0.5s. Under cruise conditions representative of a LEAP-1A powered Airbus A320neo, the temporal modeling shows stronger early-stage mixing and faster scalar dissipation in the jet phase than the spatial modeling, yielding approximately 60% more activated ice crystals in the soot-only case and approximately 70% more when ambient aerosols are included. At early vortex initialization, temporally initialized cases sustained slightly higher activated ice numbers, whereas spatial initialization produced larger late-time mean radii; these disparities diminished, particularly when ambient aerosols were present. At late vortex initialization, the trend reversed: spatial initialization yielded higher activated ice numbers, while temporal initialization retained the larger mean radius. In all cases, ambient aerosol increases ice number yet limits per-crystal growth through vapor competition, which moderates sensitivity to jet initialization. Overall, vortex phase entrainment is relatively insensitive to the jet phase modeling choice; however, the vortex start time remains consequential, and absolute microphysical values retain a measurable memory of near-field jet mixing.

Keywords: Contrail, Aircraft, Climate, Jet flow, Wake-vortex, Turbulence, CFD simulation, Large eddy simulation, Microphysics, Soot particle, Ambient condition, Turbofan

TABLE OF CONTENTS

Page

LIST OF TABLES

Page

LIST OF FIGURES

Page

LIST OF ABREVIATIONS

3D	Three-Dimensional
2D	Two-Dimensional
1D	One-Dimensional
0D	Zero-Dimensional
AFR	Air to Fuel Ratio
AIC	Aircraft Induced Clouds
AITA	International Air Transport Association
APEX	Aircraft Particle Emissions Experiment
bpr	Bypass Ratio
CARMA	Community Aerosol and Radiation Model for Atmospheres
CFD	Computational Fluid Dynamics
CFL	Courant–Friedrichs–Lewy Number
CIC	Cloud-In-Cell
CoCiP	Contrail Cirrus Prediction Tool
DLR	German Aerospace Center (Deutsches Zentrum für Luft- und Raumfahrt)
DNS	Direct Numerical Simulation
ECLIF	Emission and Climate Impact of Alternative Fuels
EI	Emission Index
ERF	Effective Radiative Forcing
FSC	Fuel Sulfur Content
GCI	Grid Convergence Index
ICAO	International Civil Aviation Organization
ISABE	International Society for Air Breathing Engines
LCM	Lagrangian Cloud Module
LES	Large Eddy Simulation
LTO	Landing Take-Off
MOMIE	Microphysical Model of Effluents
NASA	National Aeronautics and Space Administration
NGP	Nearest-Grid-Point

ONERA	French Aerospace Lab. (Office National d'Études et de Recherche Aérospatiales)
PDF	Probability Distribution Function
PM	Particulate Matter
RANS	Reynolds-Averaged Navier–Stokes Equations
RF	Radiative Forcing
RMSE	Root Mean Squared Error
SAF	Sustainable Aviation Fuel
SGS	Sub-grid scale
SST	Menter Shear Stress Transport Turbulence Model
TKE	Turbulent Kinetic Energy
VOLCAN	Alternative Fuels for New Aircraft (VOL avec Carburants Alternatifs Nouveaux)

LIST OF SYMBOLS

Latin symbols

A	Kelvin parameter
a_1, a_2	Empirical constants
a, b, c, d	Constants related to engine exhaust parameters and core/bypass radii
B	Wing span (m)
c_p	Specific heat at constant pressure $(J/K\ kg)$
c_v	Specific heat at constant volume $(J/K\ kg)$
C_T, C_ρ	Factors controlling water vapor temperature and air density above the particle surface
D_v	Thermal diffusivity of water vapor (m^2/s)
F	Engine thrust (N)
F_M, F_H	Terms related to mass and heat diffusion, respectively
$\tilde{f}$	Favre average
g	Gravitational acceleration (m/s^2)
h	Enthalpy (J/kg)
k	Thermal conductivity $(W/m\ K)$
L	Computational domain dimension (m)
L_0	Reference length
m	Mas (kg)
$\dot{m}$	Mass flow rate (kg/s)
N	Number of particles
n_{trans}	Number of physical particles represented by one numerical particle
n_p	Total number of particles
Pr	Prandtl number
P_v	Partial vapor pressure (Pa)
P_{sat}	Saturated vapor pressure (Pa)
R	Radius of the jet shear layer (m)

R	Universal gas constant ($J/K\ mol$)
Re	Reynolds number
r_d	Radius of the dry core (μm)
r_p	Radius of the particle (μm)
r_k	Kelvin radius
r_{act}	Critical activation radius of aerosol particles
r, θ, z	Cylindrical coordinates
S_w	Saturation ratio with respect to water
S_i	Saturation ratio with respect to ice
T	Temperature (K)
$\dot{T}$	Plume cooling rate
t	Time variable (s)
U	Velocity (m/s)
U_0	Aircraft speed (m/s)
$\tilde{u}$	Non-dimensional velocity component
V	Volume (m^3)
$V_{aircraft}$	Velocity of plane (m/s)
Y	Mass fraction
$\tilde{Y}_v$	Water vapor mass ratio
X	Molar fraction
x_p	Particle position (m)
x, y, z	Cartesian spatial directions
Z	Passive scalar
Greek symbols	
α, β	Sponge zone parameters
a_w	Water activity
β_m, β_t	Transitional correction factors
γ	Ratio of specific heat
Γ	Circulation of velocities

Δ	Filter cutoff length
Θ	Boundary-layer momentum thickness (m)
κ	Hygroscopicity parameter
$\bar{\mu}$	Non-dimensional dynamic viscosity
ξ	Smagorinsky subgrid-scale vapor flux (non-dimensional)
$\bar{\rho}$	Non-dimensional density
σ	Particle surface tension (J/m^2)
τ	Characteristic time (s)
$\bar{\psi}$	Source term representing the rate of condensed water vapor (non-dimensional)
$\bar{\omega}$	Vorticity magnitude (non-dimensional)

Subscripts

amb/a	Ambient
b	Bypass jet
c	Core jet
g	Gas phase
Ice/i	Ice particle
i, j, k	Indices of the Cartesian directions
frz	Freezing
liq	Liquid
p	Particle
s	Single jet (without bypass)
soot	Soot particle
sat	Saturation
υ	Water vapor
ω	Water droplet
∞	Freestream conditions

INTRODUCTION

This introduction starts by presenting the general problematic related to the environmental impact of aviation and the general objective of this thesis. It then outlines the research problematic and challenges to which this thesis responds, and specifies the research hypotheses, the main research objective, and the sub-objectives. Next, it summarizes the methodology used and the main contributions and finishes with an overview of the structure of the thesis.

0.1 General Problematic and Objective: Environmental Impact of Aviation

The contribution of aviation to global warming is well established, although significant scientific uncertainties remain. The Intergovernmental Panel on Climate Change (IPCC) released its first detailed report of aviation's climate effects in 1999 (Penner, Lister, Griggs, Dokken, & McFarland, 1999). It delivered a benchmark assessment quantifying aviation's environmental impact, projecting substantial growth by 2050, and evaluating its contribution to climate change to guide research and policy. Since then, the industry has continued to expand, with commercial air traffic projected to grow by 5–7% per year from 2005 to 2025 (Wilkerson et al., 2010). Aviation contributes to anthropogenic climate change through complex interconnected physical and chemical processes (Lee et al., 2021). Most of these processes are triggered by aircraft exhaust emissions and the ambient conditions they encounter. As a result, the environmental and climatic effects of aircraft emissions are drawing growing attention from researchers and policymakers (Lee et al., 2021; Lee et al., 2009).

Radiative forcing, and more specifically, effective radiative forcing (ERF), is the standard metric used to quantify aviation's climate impact, expressed in watts per square meter (W/m^2) (Fuglestvedt et al., 2003). ERF represents the change in atmospheric energy flux caused by anthropogenic or natural factors (Stocker, 2014). Figure 0.1 shows the component-wise effective radiative forcing for global aviation, decomposed into CO_2 and non-CO_2 contributions (net NO_x effects, contrail cirrus, stratospheric H_2O, and aerosol terms) with

associated uncertainty ranges. CO_2-related forcing is comparatively well constrained, with low uncertainty and high confidence, whereas several non-CO_2 effects, particularly contrail cirrus, remain subject to substantial uncertainties and incomplete process understanding, requiring further investigation (Lee et al., 2021). The IPCC's 6th assessment report in 2022 (Jaramillo, 2022) estimated that aviation's non-CO_2 short-lived climate forcers (SLCFs) account for ~66% of the sector's present ERF; using standard emission metrics, the net (overall) aviation impact is ≈4.0× the CO_2-only value over a 20-year horizon and ≈1.7× over a 100-year horizon.

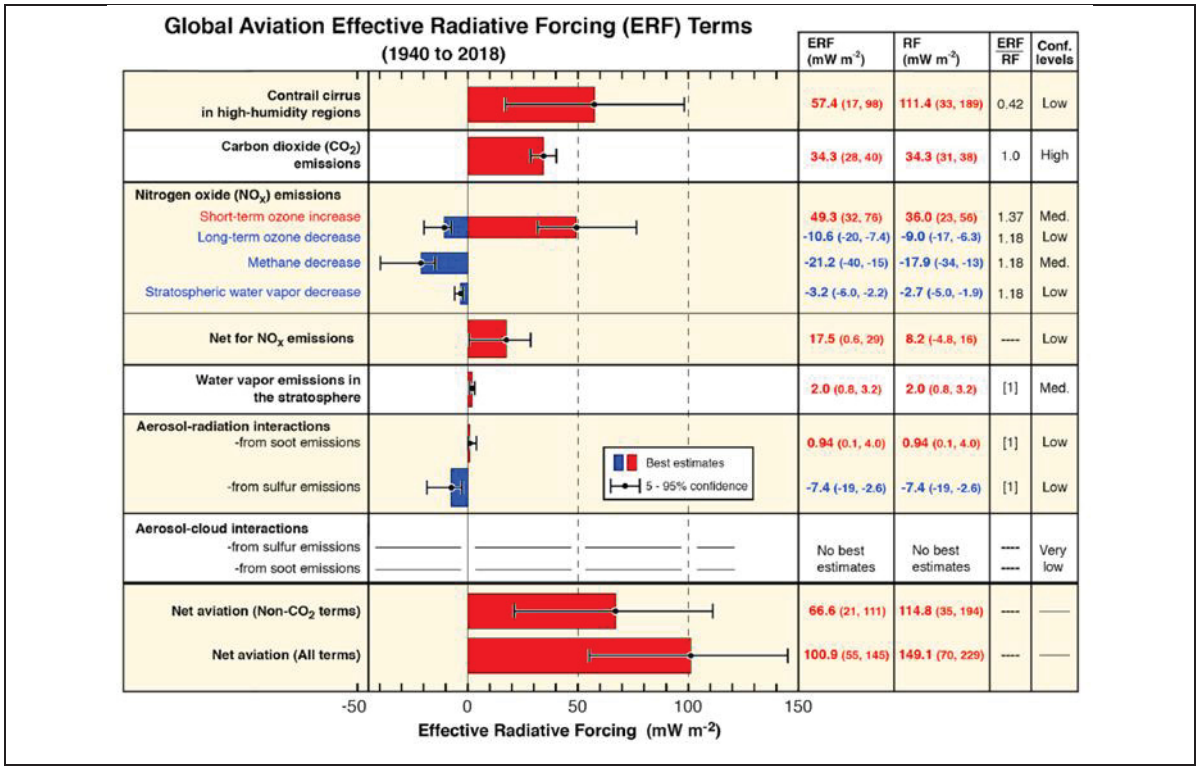

Figure 0.1 Component-wise ERF for global aviation, showing CO_2 and non-CO_2 contributions with associated uncertainty ranges
Taken from Lee et al. (2021, p. 6)

Most long-haul flight emissions occur in the upper troposphere–lower stratosphere (UTLS, ~9–12 km) (Penner et al., 1999), where residence times are long and background concentrations are low, aircraft exhaust perturbs atmospheric composition. It alters the Earth's radiation budget and uniquely modifies cloud cover by generating persistent contrails and

aviation-induced cirrus (Riese et al., 2012). Differentiating between natural cirrus clouds and contrail-induced cirrus remains difficult, complicating global assessment (Burkhardt & Kärcher, 2011; Petzold et al., 2025). This uncertainty at small scales propagates into large-scale climate models (B Kärcher, 2018).

Reducing these uncertainties requires targeted experiments, detailed process-level modeling, and robust attribution methods to quantify non-CO_2 effects, including contrail formation. The general objective of this thesis is to strengthen the scientific understanding of contrail formation and evolution by developing a modeling framework that generates evidence that can guide mitigation strategies for the climate impact of aviation-induced clouds. The framework is conceived as a reliable decision-making tool designed for integration into models operating at larger spatial and temporal scales and, eventually, into global climate models. Ultimately, the intent is to provide robust evidence to support near-term operational decisions and, over time, technological development.

0.2 Research Problematic

Both experimental and numerical studies have examined contrail formation processes. Large ground-based and airborne campaigns have characterized key contrail properties and identified the parameters that influence their formation and dispersion. However, experiments are costly, and numerical modeling has become increasingly important with advances in computing power.

Contrail modeling remains a multiscale challenge: particle sizes at the nanometer scale, plume lengths of hundreds of meters, and timescales ranging from tenths of a second for ice particle formation to roughly ten hours for the contrail lifetime (Roberto Paoli & Shariff, 2016). Early microphysical processes strongly determine subsequent contrail properties; consequently, modeling this stage is essential for predicting the number and characteristics of persisting ice particles. In jet exhaust, soot remains the dominant non-volatile exhaust aerosol that contributes to the seeding of initial ice crystals (Kärcher & Yu, 2009; Fangqun Yu, Karcher,

& Anderson, 2024). Accordingly, the model's sensitivity to near-field soot microphysical evolution under varying ambient conditions must be explicitly addressed to design effective reduction strategies. Three main challenges emerge for numerical modeling:

1. **Dynamics and mixing:** Correct representation of plume dilution as engine exhaust mixes with the aircraft wake and ambient air is fundamental. The hot core jet interacts with the colder bypass stream and entrains ambient air to form a single jet, later ingested into the wake-vortex system. Ice crystals form predominantly near jet shear layers and during early entrainment. This requires realistic exhaust modeling and fully 3D resolution of boundary- and shear-layer development. Achieving high-fidelity predictions of early jet flow development and mixing remains difficult. Spatial Large Eddy Simulations (LES) are recognized today as powerful Computational Fluid Dynamics (CFD) tools for the analysis of turbulent mixing phenomena but are computationally expensive, so a lower-cost alternative is temporal LES with some hypotheses applied i.e., "frozen turbulence" to tracks a plume segment in the ambient frame with axial periodic boundaries.
2. **Microphysical representation:** Microphysics relevant to contrail onset includes activation of soot particles, homogeneous and heterogeneous nucleation, freezing of supercooled droplets, and vapor-driven growth/sublimation. Detailed schemes are often indispensable to capture these processes but can be computationally demanding, especially when coupled to realistic jet/wake dynamics.
3. **Coupling strategy:** Even with appropriate dynamics and microphysics, their interaction governing supersaturation, nucleation, and growth, remains a central challenge. Two approaches are commonly distinguished: online coupling, in which the flow and particle fields are advanced simultaneously at each time step, often with simplified microphysics for tractability; and offline coupling, where detailed microphysics is applied along trajectories extracted from a prior flow solution or an analytical approximation. Each approach involves trade-offs among fidelity, transparency, and computational cost.

0.3 Research Questions and Hypotheses

This thesis is guided by the following research questions:

1. How can realistic turbofan exhaust profiles be modeled to capture jet development and mixing with ambient air during the initial stages of contrail formation?
2. How can soot and ice microphysics be coupled with high-fidelity CFD dynamics to capture dominant processes under various scenarios?
3. Which dynamical simulation approach is most suitable for the contrail-formation stage, particularly with respect to accuracy at a reasonable computational cost?

From these questions, six research hypotheses are proposed:

1. Realistic turbofan exhaust profile, including core and bypass streams across different bypass ratios, alters near-field jet development and plume dilution, which in turn modifies initial ice properties and the radiative impact of persistent contrails.
2. Detailed microphysical model that includes soot activation, nucleation, freezing, and vapor deposition or sublimation improves the prediction of near-field ice formation.
3. Temporal LES can reproduce key jet-regime statistics (e.g., dilution rate, turbulent kinetic energy) and contrail-initiation metrics (e.g., onset timing, activation fraction) at substantially lower computational cost; however, a systematic comparison with spatial LES is needed to quantify its fidelity limits.
4. Coupling between microphysics and dynamics is essential in contrail modeling: mixing sets supersaturation and thus microphysical evolution of particles. In online mode, only mass and energy are two-way coupled. Offline treatment neglects these couplings, altering microphysical properties.
5. Entrainment of ambient aerosols into the plume can substantially alter contrail initiation and early microphysical evolution; accounting for ambient particles is therefore necessary for realistic predictions.
6. The vortex phase largely determines the fate of young contrails: entrainment of the jet into the vortex and the ensuing jet/vortex interaction govern early microphysical development, thereby setting subsequent evolution.

0.4 Research Objective

The main objective of this thesis is to develop a modeling framework that simulates exhaust jet flow behind a realistic turbofan configuration and its early entrainment into the wake-vortex field, while integrating microphysical processes to characterize the initial properties of ice particles. Sub-objectives are defined as follows:

1. Assessing how the engine bypass ratio affects near-field contrail microphysical characteristics for soot-dominated emissions, using high-fidelity LES coupled with an advanced microphysical model.
2. Developing and validating an improved microphysical model that incorporates solute effects via a hygroscopicity parameter, including soot-particle activation and condensation, and testing online vs. offline coupling methodology.
3. Comparing temporal and spatial jet phase LES, quantify their effects on early contrail microphysics under soot-only and soot+ambient aerosol scenarios, and derive modeling guidance for initializing the vortex phase from each jet formulation.

0.5 Methodology and Summary of the Main Contributions of this Doctorate

To address sub-objective 1, fluid dynamics was modeled using the high-order (sixth-order in space, third-order in time) compressible CFD code FludiLES. First, a 3D LES was carried out for a realistic CFM56-5B3/3 configuration, extending the downstream domain to cover the plume ages of interest. Microphysics used a Lagrangian soot formulation coupled to a legacy condensation scheme: activation occurred once supersaturation exceeded unity ($S > 1$), after which ice particles grew by kinetic condensation according to the Fukuta–Walter model (Fukuta & Walter, 1970). The results of this initial effort were presented in:

- P. Afkari, M. Chouak, F. Garnier, “Spatial Large Eddy Simulation of Contrail Formation in a Near Field of an Aircraft Engine: Comparative Study of Different Ambient Humidity,” CSME & CFD Canada International Congress, Sherbrooke, Québec, May 28–31, 2023. https://doi.org/10.17118/11143/20979

In this work, the spatial simulation approach indicated that assessing bypass effects with full-domain LES is computationally too demanding for parametric studies. Therefore, based on the temporal LES, three realistic turbofan configurations were compared: CFM56-5B3/3, LEAP-1A/33, and an UHBR concept with different bypass ratios. Furthermore, LEAP-1A/33 was compared with an equivalent turbojet obtained by removing the bypass stream. These engines were also examined under different ambient temperatures. In this step, the microphysics was refined to use a solubility-based activation for soot, with subsequent water vapor deposition and heterogeneous nucleation and ice growth computed with the same model (Fukuta & Walter, 1970) but using particle-specific freezing criteria. The main contributions for this first sub-objective are reported in:

- P. Afkari, M. Chouak, F. Garnier, "Contrail Formation Modeling in the Near Field of an Aircraft Engine: Effects of the Bypass Flow", 26th International Society for Air Breathing Engines (ISABE) Conference, September 22-27, 2024, Toulouse, France

- P. Afkari, M. Chouak, S. Cantin, F. Garnier, “Evaluating Bypass Effects of Advanced Turbofan Engines on Contrail Microphysical Properties Using Large-Eddy Simulations,” Journal of Aircraft, 1–14, 2025. https://doi.org/10.2514/1.C038376

Work under sub-objective 2 advanced the solubility threshold criterion with a κ-Köhler activation framework and updated the particle-growth model to account for activation consistently. Using this enhanced microphysics, a parametric study was conducted for a LEAP-1A engine under realistic cruise conditions, examining three cases: (i) variations in the hygroscopicity parameter (κ) as a proxy for fuel sulfur content, (ii) variations in soot number emission indices, and (iii) variations in initial soot dry-core radius. The study employed a temporal LES configuration. In addition, a mean dilution history was extracted from FludiLES along a representative trajectory, and the same microphysics was run in an offline 0D box model to compare with the 3D online-coupled LES, thereby isolating the role of dynamical coupling in soot activation within jet phase contrails. The contributions arising from sub-objective 2 are documented in the submitted article listed below:

- P. Afkari, M. Chouak, S. Cantin, F. Garnier, “Role of Soot Particle Properties and Activation in Contrail Formation Using LES with Online-Coupled Microphysics,” Journal of Aerosol Science (submitted; under final review).

Sub-objective 3 extended the analysis from the jet regime to the vortex regime, employing two LES approaches: temporal and spatial. Following validation, wake-vortex simulations were initialized from jet phase fields generated by each LES approach at two start times: early (≈0.12 s) and mature (≈0.5 s). Simulations were performed under realistic cruise conditions for the LEAP-1A/33 plume representative of an Airbus A320neo. For microphysics, the scheme developed under sub-objective 2 was retained and augmented with a second ambient-aerosol population, enabling evaluation of soot-only and soot+ambient scenarios via an online-coupled Lagrangian approach. A parametric study quantified dynamical and microphysical differences between temporal and spatial jet modeling and assessed the impact of the corresponding initializations on the vortex field. These results are presented in a submitted article:

- P. Afkari, M. Chouak, S. Cantin, F. Garnier, “Large Eddy Simulations of Aircraft Contrail Formation: Effect of Vortex Initialization from Temporal vs. Spatial Jet Phase Modeling on Ice Microphysical Properties” (submitted).

0.6 Structure of the Thesis

This thesis, presented as a collection of articles, is organized into five chapters. CHAPTER 1 reviews contrail formation and evolution, covering thermodynamic, chemical, and microphysical processes and dynamics, and surveys numerical models for contrail formation and evolution, including both dynamical and microphysical studies.

CHAPTER 2 details the modeling of dynamical and microphysical processes and the integration of the microphysics into the FludiLES code used for the simulations.

CHAPTER 3 to CHAPTER 5 contain the core results as three scientific articles, respectively: (i) assessment of bypass effects of advanced turbofan engines on contrail formation using LES;

(ii) role of soot particle properties and activation in contrail formation using LES with online-coupled microphysics; and (iii) LES of aircraft contrails: vortex initialization from temporal vs. spatial jet phase modeling and microphysical sensitivity.

Finally, Figure 0.2 summarizes the thesis's main objective and sub-objectives and links them to the corresponding chapters.

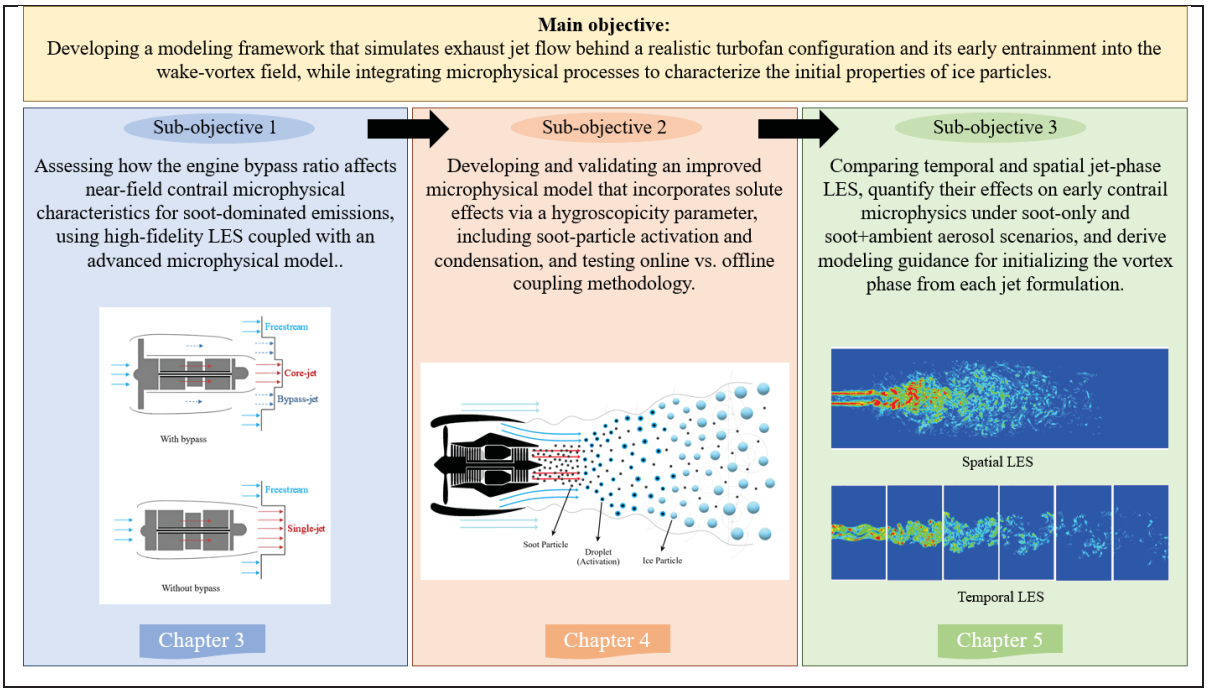

Figure 0.2 Summary of the thesis main objective and sub-objectives

CHAPTER 1

LITERATURE REVIEW AND PROBLEM DEFINITION

Current knowledge on aircraft engine emissions, with an emphasis on the formation and evolution of contrails, is reviewed in this chapter, together with the modeling approaches used to study these processes. The chapter is organized into two parts. In Section 1.1, the physics of contrail formation and evolution is synthesized across four interacting processes: thermodynamic, chemical, dynamical, and microphysical. In Section 1.2, numerical models of contrail formation and evolution are surveyed. Dynamical modeling is considered first, followed by microphysical modeling. Through this review, the present work is positioned within the literature, and a foundation is provided for the developments presented in the following chapters.

1.1 Contrail Formation and Evolution

Contrails (condensation trails) are line-shaped clouds formed from ice particles (Ulrich Schumann, 2005) when jet exhaust containing combustion products mixes with cold ambient air in the upper troposphere and lower stratosphere, typically at about 8-13 km (Penner et al., 1999). They can be short-lived or long-lived depending mainly on ambient temperature and relative humidity over ice, with greater persistence in cold, ice-supersaturated air (Iwabuchi, Yang, Liou, & Minnis, 2012). Systematic contrail observation records from airborne, satellite, and ground-based measurements began around 1952 (Havens, 1952), although the earliest documented sightings of aircraft exhaust contrails date to 1915 (Ettenreich, 1919).

Figure 1.1 provides an overview of contrail formation and evolution: nearly isobaric mixing produces droplets that subsequently freeze by homogeneous or heterogeneous pathways (immersion, deposition, or pore condensation and freezing). The mixed plume either sublimates rapidly or, if ice supersaturation persists, develops into a long-lived contrail that can spread into contrail cirrus under ambient shear. Interactions between aerosols and clouds, especially soot acting as cloud-condensation nuclei (CCN) and ice-nucleating particles (INPs),

mediate these transitions. Overall, contrail formation can be understood in terms of four coupled processes: thermodynamic, chemical, microphysical, and dynamical (Roberto Paoli & Shariff, 2016). Accurate prediction of initial contrail properties requires a coherent treatment of all four (Bernd Kärcher, 2018). The following subsection provides a successive presentation of each of them.

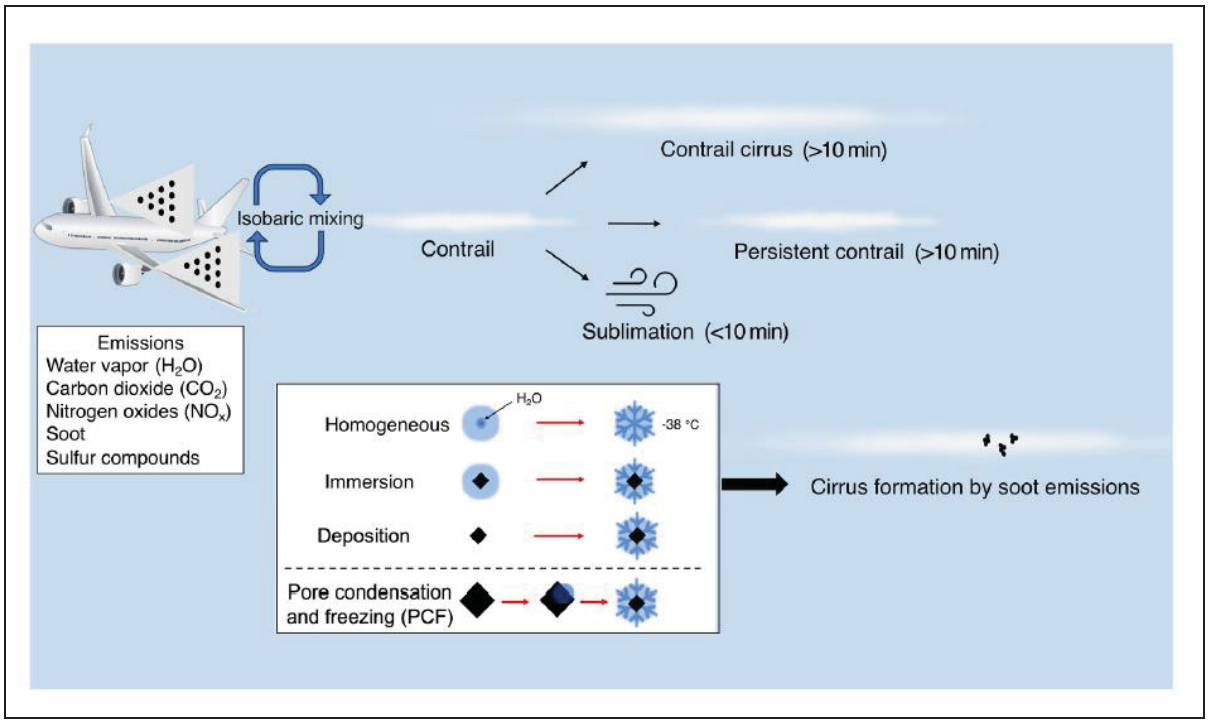

Figure 1.1 Overview of contrail formation and evolution and their contribution to cirrus clouds
Taken from Alsante and Cheng (2024, p. 4)

1.1.1 Contrail Thermodynamics

The foundational theoretical treatments of contrail formation were developed by Schmidt (1941) and Appleman (1953), who described formation in terms of plume–ambient thermodynamics. In this framework, contrails alter temperature and water vapor partial pressure along a mixing line in thermodynamic space (Appleman, 1953). According to the Schmidt-Appleman criterion, a threshold ambient temperature can be defined such that, for a

given pressure and humidity, the plume–ambient mixing line is tangent to the water saturation curve at the onset of visible condensation (Figure 1.2). If the water saturation curve is crossed by the mixing line, as shown in Figure 1.2(b), droplets form and, under typical cruise conditions, rapidly freeze into ice; if it is not crossed (Figure 1.2(a)), no contrail forms (Ulrich Schumann, 1996). Persistence then depends on the terminal mixing state: contrails persist when the ambient air is supersaturated with respect to ice and dissipate when the ambient air is subsaturated, in which case the ice particles sublimate (Appleman, 1953; Schmidt, 1941).

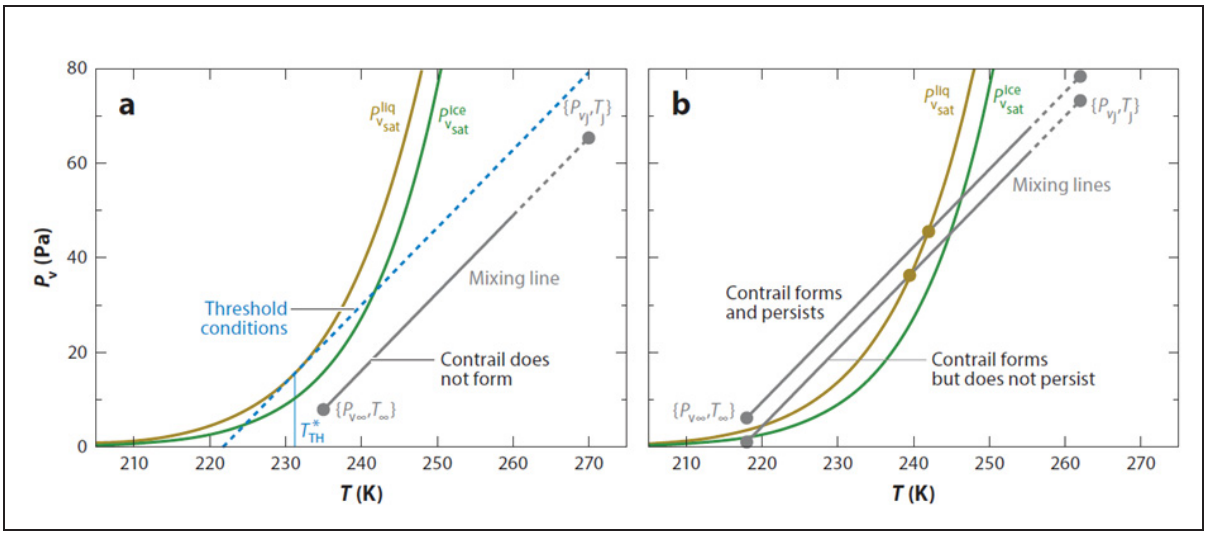

Figure 1.2 Schmidt-Appleman criterion for contrail formation. (a) Mixing path stays below liquid-water saturation; droplets do not form and no contrail forms and, (b) Mixing path crosses liquid-water saturation; droplets form, and the contrail persists only if the mixed state is supersaturated with respect to ice, otherwise it dissipates
Taken from Roberto Paoli and Shariff (2016, p. 6)

Ulrich Schumann (1996) refined the criterion by expressing how propulsion and atmospheric parameters set the slope G of the mixing line and, therefore, the onset temperature. With:

$$\eta = \frac{FU_\infty}{\dot{m}_f Q} \tag{1.1}$$

the overall propulsion efficiency, the mixing-line slope can be written:

$$G = \frac{c_p P_{amb} EI_{H_2O}}{\varepsilon_v Q(1-\eta)} \tag{1.2}$$

where F is the thrust, $\dot{m}_f$ fuel mass flow rate, U_∞ the free-stream airspeed, c_p is the specific heat of air, P_{amb} the ambient pressure, EI_{H_2O} the water-vapour emission index, Q the fuel lower heating value, and ε_v the molar-mass ratio (water vapour to air). A higher η (typical of modern engines) increases G and makes the line intersect saturation at warmer ambient temperatures, broadening the altitude/temperature range for contrail formation (Ulrich Schumann, Busen, & Plohr, 2000). Furthermore, this thermodynamic approach has been used to parameterize contrail occurrence in large-scale models (Ponater, Marquart, & Sausen, 2002).

Let $RH_v = P_v / P_{v_{sat}}^{liq}(T)$ and $RH_i = P_v / P_{v_{sat}}^{ice}(T)$. Denote by T_{th} the temperature at which the mixing line is tangent to the liquid-water saturation curve (maximum potential supersaturation in the plume). The warmest ambient temperature that still permits onset for a given ambient humidity, T_{LC}, satisfies the implicit Schumann relation (Ulrich Schumann, 1996):

$$T_{LC} = T_{th} - \frac{P_{v_{sat}}^{liq}(T_{th}) - RH_v P_{v_{sat}}^{liq}(T_{LC})}{G} \tag{1.3}$$

which reduces to a G-only condition when $RH_v = 1$. In practice T_{LC} is obtained by a simple iteration using standard saturation formulae. Persistence further requires the terminal mixed state to satisfy $RH_i \geq 1$.

This thermodynamic criterion is widely used in large-scale models to parameterize contrail occurrence (Ponater et al., 2002) and to diagnose persistence in ice-supersaturated regions (Burkhardt, Kärcher, Ponater, Gierens, & Gettelman, 2008). The thermodynamic-equilibrium framing assumes near-adiabatic, near-isobaric mixing of hot, moist exhaust with colder ambient air at (approximately) fixed total water. In this picture, onset occurs when the maximum saturation along the mixing line reaches liquid-water saturation (i.e., $RH_v \geq 1$), and

persistence requires that the final mixed state be supersaturated with respect to ice (i.e., $RH_i \geq 1$). After water saturation is reached, droplets freeze rapidly—by homogeneous freezing once temperatures are sufficiently low (typical thresholds ≈231–235 K in young contrails; Kärcher, Burkhardt, Bier, Bock, and Ford (2015)) or via heterogeneous/immersion pathways at somewhat warmer temperatures depending on the availability and efficacy of ice-nucleating particles (Kärcher, DeMott, Jensen, & Harrington, 2022). This Schmidt–Appleman based approach predicts the onset temperature of contrails well (Busen & Schumann, 1995; Ulrich Schumann, 2000), but it does not represent the microphysical mechanisms that set the initial ice number and size distribution. In reality, contrails form in the jet regime as hot, moist exhaust mixes with cold ambient air; exhaust aerosols act as condensation/ice nuclei (Kärcher, Peter, Biermann, & Schumann, 1996), and their emitted number, size, and hygroscopicity exert first-order control. To capture these effects, physically based microphysical models couple the mixing history to aerosol activation, condensational growth, freezing, and subsequent depositional growth or sublimation (Brown, Miake-Lye, Anderson, Kolb, & Resch, 1996; Kärcher, Yu, Schröder, & Turco, 1998; H-W Wong & Miake-Lye, 2010; F. Yu & Turco, 1998), consistently showing strong sensitivity to soot number and size and, where relevant, to entrained ambient aerosols.

1.1.2 Contrail Chemistry

The chemistry of aviation-generated particles plays a role in the formation of aerosols and ice crystals. As shown in Figure 1.3, aircraft exhaust gases contain reactive and condensable species that drive particle formation and growth in the near-field plume (Roberto Paoli & Shariff, 2016). Many commercial aircraft jet engines still burn kerosene-type fuel (Jet A/Jet A-1). Their exhaust is mostly CO_2 and H_2O, with smaller amounts of NO_x, SO_x, organics, soot, and lubricating-oil vapors.

In aviation emissions, non-volatile particulate matter (nvPM) refers to refractory soot particles with trace metals from engine wear that do not volatilize under the ~350°C thermal conditioning used at the exhaust plane (H.-W. Wong, Jun, Peck, Waitz, & Miake-Lye, 2014;

Hsi-Wu Wong, Jun, Peck, Waitz, & Miake-Lye, 2015), whereas volatile particulate matter (vPM) consists of condensable material (primarily H_2SO_4–H_2O and organics) that forms by gas-to-particle conversion and can evaporate upon heating (Lobo et al., 2020).

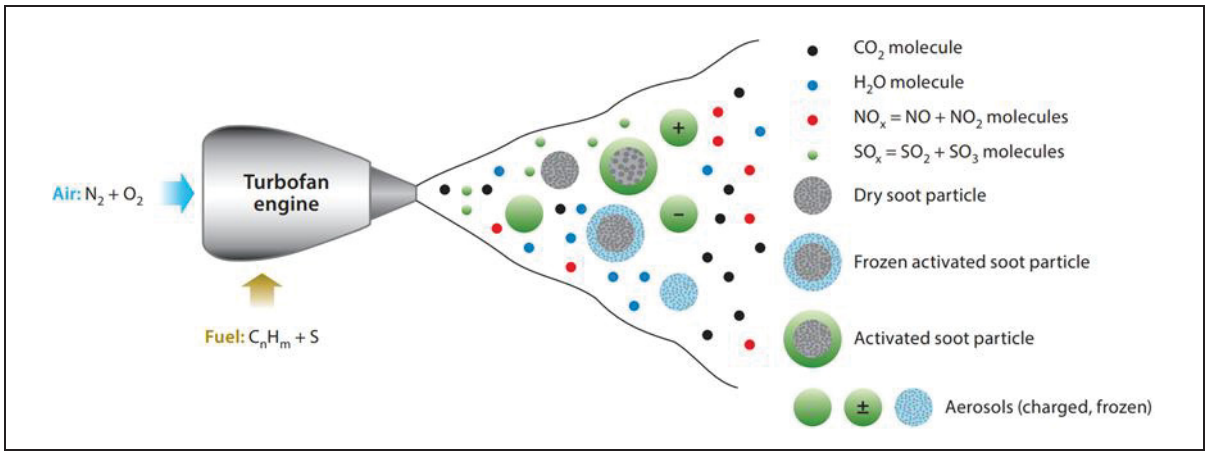

Figure 1.3 Schematic of commercial aircraft engine emissions
Taken from Roberto Paoli and Shariff (2016, p. 2)

Most fuel sulfur leaves the combustor as SO_2; a few percent is present as SO_3 at the engine exit, limited by kinetics (Kärcher et al., 2000). SO_3 is rapidly converted to H_2SO_4 (Kolb et al., 1994), which has very low vapor pressure, nucleates new particles, and condenses on soot in the near-field exhaust plume (H.-W. Wong et al., 2014). Soot surfaces are rendered hygroscopic by uptake of sulfuric acid and water, often followed by partial neutralization with ammonia to form ammonium bisulfate or sulfate (Henning et al., 2012; Sorokin, Katragkou, Arnold, Busen, & Schumann, 2004). Nitric acid and low-volatility organics can also be taken up, further increasing surface acidity and hygroscopicity (Abegglen et al., 2016; Longfellow, Ravishankara, & Hanson, 2000). Moreover, chemi-ionization in the combustor generates ions that seed electrically charged H_2SO_4–H_2O clusters, accelerating new-particle formation and enhancing growth via electrostatically aided condensation and coagulation in the young plume (Fangqun Yu & Turco, 1997).

Complementing the ion pathway, organic species from the exhaust readily condense onto ions/charged particles and are taken up by liquid H_2SO_4 droplets, providing condensation sites

and boosting early ultrafine particle mass; at very low fuel-sulfur levels they can dominate the volatile particle burden, and even at moderate to high sulfur they remain a significant fraction of exhaust aerosol (Fangqun Yu, Turco, & Kärcher, 1999). Recent work, such as Ungeheuer et al. (2022), also shows that emissions from the aircraft lubrication system contribute to particulate matter by forming nucleated particles from oil in the exhaust. Furthermore, in the near field, NO_x does not control particle nucleation or growth; its primary impacts are chemical, altering ozone and methane on regional to global scales over longer time horizons (Lee et al., 2021). These chemical pathways help set whether cold UTLS mixing meets the Schmidt–Appleman threshold and how contrails evolve (Ulrich Schumann, 2005).

1.1.3 Contrail Microphysics

Building on the Schmidt–Appleman thermodynamic criterion, in which microphysical processes are omitted, a microphysical approach is introduced to explicitly represent particle nucleation, growth, and loss, thereby capturing the conversion of aircraft exhaust into ice crystals and their subsequent evolution (Kärcher et al., 2015). Microphysical processes may include chemical reactions, but they can also proceed without them (Kärcher, 1999). In the young plume, rapid cooling and mixing set the ice supersaturation (S_i); a subset of soot and newly formed volatile particles activates to liquid droplets, which then freeze within fractions of a second at low temperatures (Ponsonby, Teoh, Kärcher, & Stettler, 2025). Subsequent evolution involves depositional growth or sublimation, while coagulation, aggregation, and sedimentation shape particle number, size, and lifetime (Heymsfield et al., 2010; X. P. Vancassel, Garnier, & Mirabel, 2010). Figure 1.4 summarizes the transformation pathways from gaseous and particulate combustion products. Sulfuric-acid water coating layers produced by near-field chemistry, together with condensing organics, increase the hygroscopicity of soot particles. Hygroscopicity here denotes the ability of a particle to take up water vapor and grow at a given relative humidity. These changes enable activation, followed by water condensation and freezing, while newly formed volatile particles can also take up water and subsequently freeze (Roberto Paoli & Shariff, 2016; H.-W. Wong et al., 2014). Activation of entrained ambient aerosols occurs when plume water supersaturation

exceeds their Köhler critical supersaturation; once activated, the droplets freeze at upper-tropospheric temperatures (Bier et al., 2024).

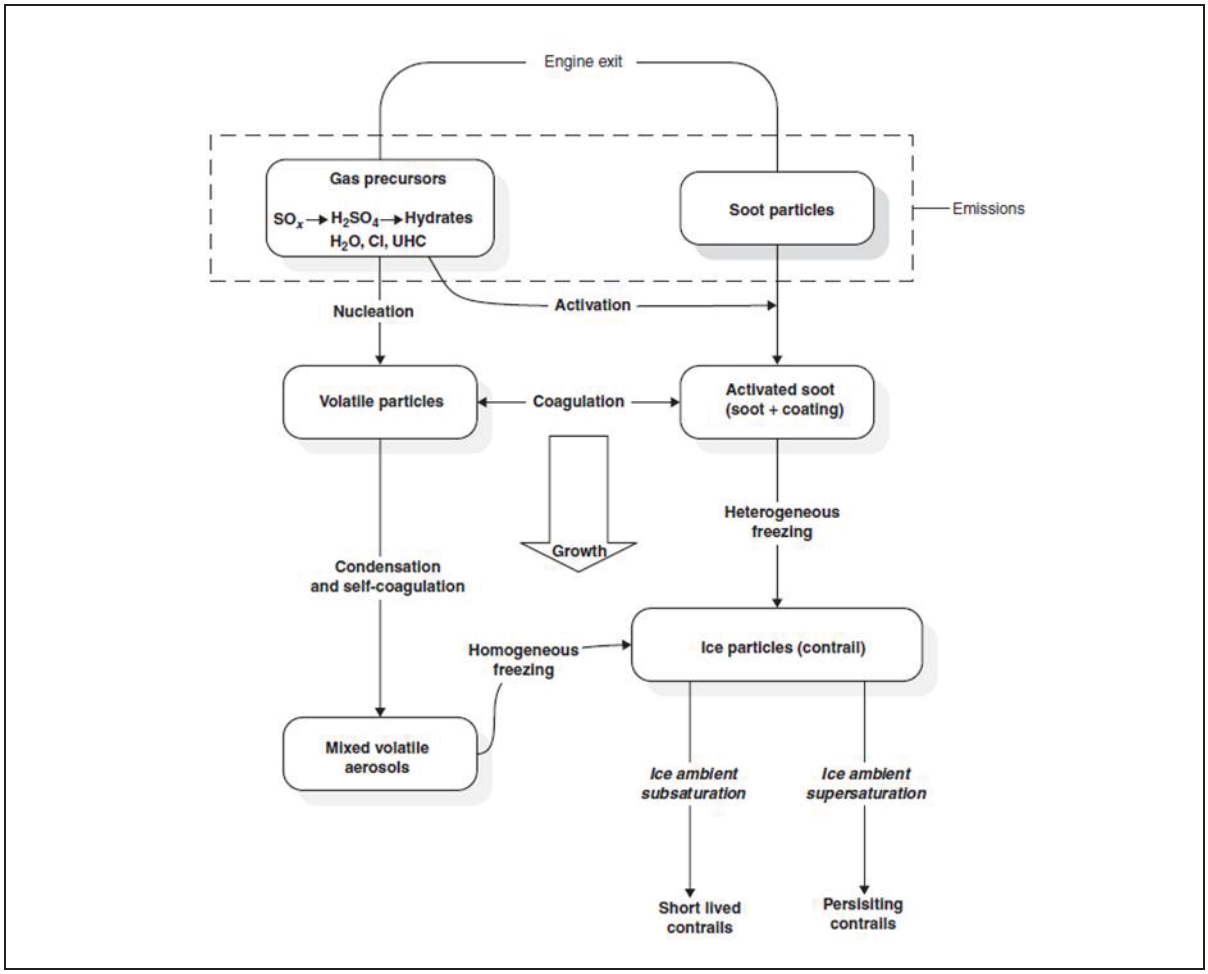

Figure 1.4 Diagram of the microphysical processes governing the transformation of gaseous and particulate combustion products
Taken from X. P. Vancassel et al. (2010, p. 10)

In the absence of effective ice-nucleating particles (INPs), solution droplets—formed first by activation of cloud condensation nuclei (CCN)—freeze homogeneously; when suitable INPs are present, ice forms heterogeneously on preexisting particles, typically via immersion freezing after activation (K. Gierens, 2003; Kärcher et al., 2022). By contrast, forming pure-water droplets without any aerosol surface is not expected in the troposphere, because it would require unrealistically high supersaturation with respect to water (RH_w well above typical

cloud values—often >110% and potentially several hundred percent, depending on embryo size) (Curtius, 2009). Deposition nucleation occurs when the plume is supersaturated with respect to ice but subsaturated with respect to liquid water (RH_i> 1, RH_w< 1), whereas condensation freezing occurs near water saturation during initial condensation on an ice-nucleating particle and is often operationally indistinguishable from immersion freezing (Boose et al., 2019; Kanji et al., 2017; Paramonov et al., 2020). The relative roles of soot versus volatile or ambient particles depend on the emission regime, with soot-poor plumes ($EI_{soot} \lesssim 10^{13}$) producing fewer initial ice crystals from soot particles (B Kärcher, 2018; Ponsonby et al., 2025). As ice forms, water vapor is depleted and the plume relaxes toward or below ice saturation; these activation-relaxation and freezing-relaxation cycles set the initial ice number and size distribution (Kärcher et al., 2015).

After freezing, ice crystals grow by vapor deposition when S_i is positive; growth rates are controlled by diffusion and thermal resistances and by ventilation. Growth slows as S_i decreases and reverses (sublimates) in subsaturated air (K. M. Gierens, Monier, & Gayet, 2003; Pruppacher & Klett, 1979). In ice-subsaturated conditions, the contrail decays by sublimation on timescales of seconds to minutes, whereas contrail persistence requires ambient ice supersaturation (Kärcher, Kleine, Sauer, & Voigt, 2018). Number concentrations decrease through coagulation and, later, aggregation as ice crystals grow and spread; sedimentation becomes important only for larger and older contrail cirrus (Marcolli, Mahrt, & Kärcher, 2021; Ulrich Schumann & Heymsfield, 2017; Testa, Durdina, Edebeli, Spirig, & Kanji, 2024). Shear and entrainment during the vortex and diffusion phases modify S_i and ice crystals number, controlling the transition from line-shaped contrails to contrail cirrus with broader lifetimes and optical depths (Unterstrasser, 2014; Unterstrasser & Gierens, 2010b).

1.1.4 Contrail Dynamics

Dynamic processes govern how the young exhaust plume mixes, spreads, and transitions from line-shaped contrails to contrail cirrus (Roberto Paoli & Shariff, 2016). By controlling dilution, cooling, and entrainment from the jet phase, through the vortex, and into the diffusion phase,

plume dynamics set the thermodynamic supersaturation and the pace of chemical processing. They also govern the microphysical processes of activation, freezing, growth, and decay that determine contrail properties (D. Lewellen & Lewellen, 2001). Contrail evolution is typically described by four aircraft-wake regimes (Figure 1.5): the jet regime, the vortex regime, the dissipation (vortex-dissipation) regime, and the diffusion regime (Roberto Paoli & Shariff, 2016). H. Hoshizaki and J. W. Meyer (1972) were among the first to characterize these regimes and to provide a comprehensive study of wake dynamics.

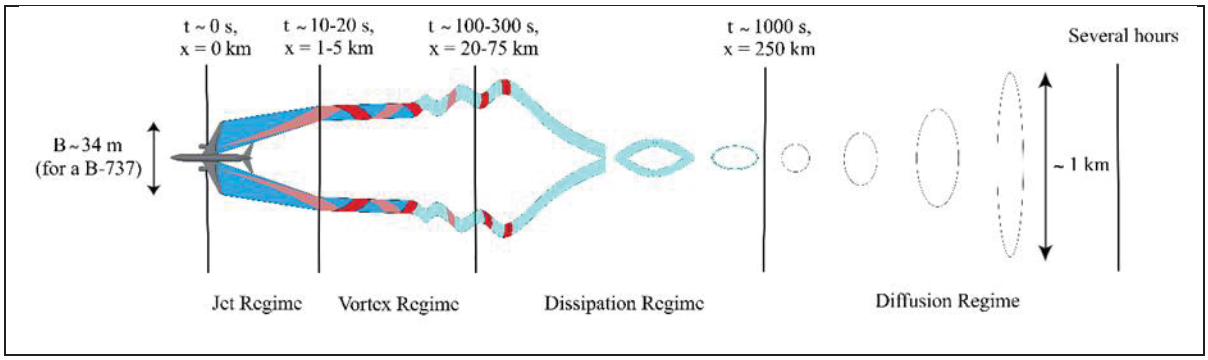

Figure 1.5 Classification of the evolution of an aircraft wake into four regimes, illustrated by a passive tracer from the engine exit (t = 0 s), where the distance behind the aircraft is given by $x = U_a \times t$, with U_a the aircraft speed
Adapted from Saulgeot (2023, p. 10)

In the jet regime, turbulent jet expansion into quiescent air controls the initial dilution and cooling rate (D. Lewellen & Lewellen, 2001). The jet breaks down from a potential core into shear layers through Kelvin–Helmholtz instability, and the centerline velocity decays while entrainment grows with axial distance (Hanasz & Sol, 1996). These dynamics determine the early plume volume, temperature drop, and mixing timescale, which precondition everything that follows in the wake (D. Lewellen & Lewellen, 2001). Key jet-dynamic parameters include the exit momentum flux, exit temperature, the jet-to-ambient density ratio at the nozzle exit (ρ_j/ρ_a), Mach and Reynolds numbers, and exhaust nozzle geometry (Christophe Bogey & Marsden, 2014; Roberto Paoli, Helie, & Poinsot, 2004). Jet dynamics is further affected by ambient wind shear and static stability (Roberto Paoli et al., 2004).

In the vortex regime, wing-tip shear layers roll up into a counter-rotating vortex pair that descends under its own circulation until arrested by ambient stratification (Roberto Paoli & Garnier, 2005); the descent and lifetime scale with the initial circulation and the Brunt–Väisälä frequency (Schooley, 1969). Most exhaust is captured in the primary cores, where strong swirl and subsidence impose adiabatic warming and water vapor depletion (Sussmann & Gierens, 1999; Unterstrasser & Sölch, 2010); a secondary wake remains above and outside the sinking cores and mixes more gently with ambient air (Sussmann & Gierens, 1999). The vortex pair becomes unstable to Crow-type perturbations (Crow, 1970) and breaks up under background turbulence and shear, releasing the trapped exhaust and ice crystals for further spreading (S Brunet, Garnier, & Sagaut, 1999). Key controls here are circulation strength, lateral vortex spacing, ambient stability, and the turbulence dissipation rate (Körner & Holzäpfel, 2016; Phillips, Alley, & Goodrich, 2004; Widnall, Bliss, & Tsai, 1974). In the late vortex regime, Crow-instability breakup of the descending vortex pair produces a quasi-periodic chain of 'puffs,' marking the transition to the diffusion regime (Thomas Gerz & Holzapfel, 1999).

During the dissipation (vortex-dissipation) regime, after breakup, enhanced small-scale turbulence and ambient shear drive rapid three-dimensional (3D) spreading (Misaka et al., 2012). The wake transitions from organized coherent motion to turbulence-dominated diffusion, with entrainment rates set by the local shear and stratification (Hennemann & Holzapfel, 2007). This regime sets the initial depth and width of the post-vortex contrail sheet and the survival fraction of wake-borne material that proceeds to larger scales (Proctor, Ahmad, Switzer, & Limon Duparcmeur, 2010).

Finally, in the diffusion regime, large-scale winds, vertical shear, and stratification control the continued horizontal and vertical dispersion (Roberto Paoli & Shariff, 2016). The wake loses memory of aircraft-specific structures and becomes an advected, sheared, slowly deepening layer that sets the planform and optical footprint of contrail cirrus (Jensen, Ackerman, Stevens, Toon, & Minnis, 1998; Picot, Paoli, Thouron, & Cariolle, 2015). At this stage, dynamical control is exerted by the ambient flow: shear governs lateral growth, stability caps vertical

extent, and mesoscale variability modulates lifetime and spatial inhomogeneity (Jensen, Ackerman, et al., 1998; Unterstrasser & Gierens, 2010a).

1.2 Numerical Models of Contrail Formation and Evolution

Contrail formation and evolution are multi-physics and multi-scale phenomena. Despite significant progress, key lifecycle properties and their climate impacts remain uncertain, which underscores the need for continued investigation (Bernd Kärcher, 2018). Direct evidence is invaluable but hard-won. In situ measurement programs and coordinated flight campaigns (e.g., NASA's ACCESS (Moore et al., 2015) and DLR's ECLIF (Kleine et al., 2018)) require multiple aircraft flying in formation at cruise altitude with extensive instrumentation and logistics; they are expensive, time-consuming, and necessarily limited in coverage (National Academies of Sciences, 2025). Even when such campaigns are flown, interpretation remains challenging; examples include particle-ice interactions and rapidly evolving plumes (Afchine et al., 2018; Kleine et al., 2018). These realities motivate numerical modeling as a complementary path, coupling dynamics with microphysical modeling to predict contrail formation and evolution. In this first subsection, dynamic models, including analytical entrainment laws, CFD-resolved jet and wake mixing, and prescribed dilution/entrainment trajectories extracted from CFD are presented. In the second subsection, microphysical models, implemented either online (coupled to CFD) or offline (box- or trajectory-driven), are reviewed for predicting contrail properties.

1.2.1 Dynamic Modeling

1.2.1.1 Analytical Flow Models

Analytical flow models represent turbulent jet and plume mixing using integral balances with simple similarity closures rather than solving the full flow numerically. These representations are predominantly 0D/1D for entrainment and mixing histories, but 2D fields are also used for the primary wake to represent or initialize the vortex phase (Kärcher et al., 2015). Closure is

provided by an entrainment hypothesis, which relates lateral mass inflow at the plume edge to a characteristic mean velocity through an entrainment coefficient (Enjalbert, Galley, & Pierrot, 2009; Ricou & Spalding, 1961). Given source fluxes and the ambient state, the resulting coupled ordinary differential equations (ODEs) yield tractable laws for centerline decay, plume-radius growth, rise height, and dilution history (Garvey & Fowler, 2023). In practice, these models produce time- or distance-based parameterizations for variables that drive contrail microphysics, such as dilution or mixing fraction, temperature, pressure, and water vapor mixing ratio (Matulka, López, Redondo, & Tarquis, 2014). Analytical models are used both for near-field jet–plume mixing (Kärcher et al., 2015) and for the far-field of the contrail life-cycle, which is difficult to represent comprehensively in global climate and chemistry transport models because of coarse resolution, and in high-fidelity CFD or LES because of computational cost (Rosenow, Hospodka, Lán, & Fricke, 2023; Ulrich Schumann, 2012).

Foundational entrainment theory for turbulent jets and plumes was formalized by Morton, Taylor, and Turner (1956). They developed an integral, Boussinesq framework for turbulent convection from maintained sources (plumes) and instantaneous releases (clouds) in uniform and stably stratified environments. The model assumed self-similar mean profiles and used an entrainment hypothesis that links lateral mass influx at the plume edge to a characteristic mean velocity via an entrainment coefficient. Conservation of volume, momentum, and buoyancy leads to coupled ODEs solved in non-dimensional form using the source buoyancy flux and the ambient stratification (e.g., buoyancy frequency). The theory predicted centerline decay, plume-radius growth, and rise height, introduced the virtual origin, and, through potential temperature, extended to the compressible atmosphere, giving practical rise-height and dilution laws widely used in aircraft-plume integral models (Roberto Paoli & Shariff, 2016). As another foundational contribution, Turner (1979) systematized integral (entrainment) theory for turbulent jets, plumes, and forced plumes based on self-similar profiles and the entrainment hypothesis.

In one of the earliest analytical/parametric plume treatments of contrail onset, Ulrich Schumann (1996) modeled the young exhaust plume as near-isobaric mixing between hot,

moist exhaust and cold ambient air along a one-parameter mixing line (exhaust mass fraction, i.e., dilution).

With specified source terms (water vapor emission index, exhaust temperature) and ambient state (pressure, temperature, relative humidity over ice), the formulation yielded closed-form relations for water vapor partial pressure or mixing ratio. The formation criterion was that the peak saturation ratio with respect to ice along this mixing path satisfied $S_{i,max} \geq 1$ (equivalently, $RH_{i,max} \geq 1$), which yielded a critical ambient temperature (with explicit humidity dependence) for contrail formation without solving the flow field. Extending the near-field analytical approach, Kärcher et al. (2015) represented the young exhaust as an isobaric, self-similar jet and parameterized centerline mixing with an entrainment-type law. The authors introduced a short mixing timescale for the primary shear layer and a dilution exponent so that dilution followed a power law in plume age. From this formulation, they obtained closed-form trajectories for the plume temperature and dilution factor, as well as an explicit cooling rate proportional to the temperature excess over time. The analysis remained within the jet regime prior to wingtip-vortex capture and was designed to feed microphysics calculations. Furthermore, the plume dynamics were prescribed analytically by Fangqun Yu, Karcher, et al. (2024). The young exhaust was treated as a near-isobaric, self-similar jet, and time-dependent dilution and cooling histories were specified via an entrainment-type parameterization.

As a complement to the analytical onset framework, Ulrich Schumann et al. (1998) assembled more than 70 in-situ plume encounters spanning milliseconds to ~95 minutes, thereby linking near-field onset to far-field dispersion. They introduced a bulk dilution ratio (mass of ambient air mixed per unit fuel burned) and, using conservative tracers, temperature excess, and observed contrail geometry, inferred time-dependent dilution and plume cross-section. The authors summarized mixing behavior across the jet, wake-vortex, vortex-breakup, and atmospheric dispersion regimes. Near the plume center, their dataset collapsed to an empirical interpolation $N = 7000(t/t_0)^{0.8}$, with $t_0 = 1\ s$. Subsequent studies used this interpolation to validate simulated plume dilution, including those very near-field by T Gerz and Ehret (1997)

and by F Garnier, Baudoin, Woods, and Louisnard (1997) for CFM56 and RB211 engines, and adopted it as a parameterized dilution law in plume and contrail models (Fangqun Yu, Anderson, et al., 2024). Its robustness, supported by multiple in-flight measurements, suggested a near-universality of early-plume mixing that was largely independent of aircraft and atmospheric scales (Ulrich Schumann et al., 1998), while individual cases still showed substantial scatter of roughly a factor of three to five.

Following onset into the far-field regime, the Contrail Cirrus Prediction Tool (CoCiP) was used to represent contrail–plume dynamics with a Lagrangian Gaussian plume whose cross-section was evolved analytically (Ulrich Schumann, 2012). The wake-vortex phase was not explicitly simulated; instead, downwash and initial plume geometry were prescribed from a parametric wake model and calibrated so that early-time dilution matched an empirical bulk-dilution law derived from in-situ encounters. As another far-field study for cirrus parameterization, Kärcher (2022) treated ice-supersaturation tendencies as driven by a prescribed vertical-wind-induced cooling rate and derived closed-form expressions that avoided numerical integration of the supersaturation equation. In practice, the host model supplied parameterized vertical-wind speeds (or their statistics), which defined an effective cooling timescale; this forcing then fed compact formulas for the maximum supersaturation and the partitioning between heterogeneous activation and homogeneous freezing. The dynamics remained at the level of analytical cooling forcing coupled to microphysics, enabling efficient use in large-scale models without resolving a flow field. At the lifecycle scale, Rosenow et al. (2023) employed an analytical framework based on a sheared two-dimensional Gaussian plume with wake-vortex initialization. Initial geometry after the wake phase was prescribed from a parametric wake-vortex model, then dilution and spread followed closed-form updates of the variance matrix, with diffusivities linked to eddy-dissipation rate and typical flight-level values. Temperature after the first seconds was treated in equilibrium with the ambient, and lifetimes from the analytical model were validated against photographic observations, achieving ~10% mean error.

1.2.1.2 CFD Simulations

Compared with analytical models, the CFD method resolves the unsteady flow and scalar transport under realistic boundary conditions, yielding predictions closer to operational reality. In this context, CFD denotes time-resolved solutions of the Navier–Stokes equations with advective–diffusive transport of temperature and water vapor, predicting how engine exhaust mixes, dilutes, and entrains ambient air from the near-jet region into the evolving wake (Roberto Paoli & Shariff, 2016). The governing partial differential equations—statements of mass, momentum, energy, and species conservation—describe the plume's evolution in 2D (axisymmetric) or 3D domains. Turbulence modelling is central to credible predictions. For contrail dynamics, three CFD approaches are commonly used: Reynolds averaged Navier Stokes (RANS)/URANS, large eddy simulation (LES), and rarely direct numerical simulation (DNS) (Poroseva, Colmenares F, & Murman, 2016; Whitman, Xu, & Som, 2025).

Within a RANS framework, Guignery, Montreuil, Thual, and Vancassel (2012) simulated the near-wake flow over a simplified wing–injector to resolve jet roll-up, vortex capture, and scalar dilution from the nozzle exit to ~8 wingspans. Using the multi-physics solver CEDRE, enriched with a microphysical model, the authors investigated the growth of ice particles from the nozzle exit to eight wingspans downstream. Using 3D RANS simulations, J.-C. Khou, Ghedhaifi, Vancassel, and Garnier (2015) resolved the near-field flow of a realistic commercial aircraft, including core and bypass jets, under cruise conditions. The CFD setup captured bulk mixing in the jet plume with an Eulerian microphysics module to model particle growth. Flow predictions showed good agreement with the literature on near-wake dilution and entrainment, validating RANS for this regime. The same 3D RANS jet–vortex framework was also adopted by J. Khou, Ghedhaïfi, Vancassel, Montreuil, and Garnier (2017), who applied it to a Boeing 737 geometry with Eulerian microphysics and sulfur chemistry to assess fuel sulfur content effects on contrail formation. Montreuil et al. (2018) also used a 3D RANS approach applied to the NASA-CRM wing/body/engine configuration with adaptive meshing to analyze near-field dilution and contrail onset.

As a URANS example, Cantin, Chouak, Morency, and Garnier (2022) simulated a realistic turbofan nozzle (core plus bypass), solving the gas phase in an Eulerian framework while tracking soot and ice with a Lagrangian approach, and showed that nozzle-exit geometry governs dilution, activation, and early ice growth. In the most recent work, Annunziata, Bonne, and Garnier (2025) applied 3D RANS with adaptive meshing and an Eulerian microphysics model to a B777-like full-aircraft configuration, demonstrating that engine position reshaped dilution and wake structure, which in turn controlled plume microphysical characteristics. Together, these studies extended RANS/URANS contrail modeling from nozzle-exit dynamics to aircraft-scale installation effects.

Starting with LES modeling of contrail formation and establishing LES of the jet–vortex interaction as a credible dynamic backbone for onset, R Paoli, Hélie, Poinsot, and Ghosal (2002) and Roberto Paoli et al. (2004) used LES at flight-relevant Reynolds numbers to resolve an engine jet interacting with a wing-tip trailing vortex. The simulations identified where and when localized supersaturation formed within the rolled-up wake, linking turbulent mixing and vortex dynamics to the earliest ice formation. Furthermore, Ferreira, Alonso, and Gorlé (2025) employed particle-laden, compressible LES to simulate the jet decay and the early jet–vortex-interaction phase. An idealized jet and a rolled-up Lamb–Oseen vortex pair were initialized, followed by expanded refinement across the vortex pair to capture entrainment and shear-layer growth without prohibitive cost. This setup directly resolved near-field turbulent mixing and the onset of vortex capture, with ice activation and subsequent freezing computed inline during the LES time-stepping. D. C. Lewellen (2020) performed LES of the exhaust jet to simulate ice nucleation and early growth and to quantify the effective ice-number emission index; plume mixing was resolved with size-resolved (binned) microphysics, and the jet segment was then stitched into the wake by embedding the jet-LES output into velocity fields from two-dimensional RANS wake runs.

Further downstream in the vortex phase and into early dissipation, LES has been used to resolve wake-driven controls on contrail evolution. Picot et al. (2015) performed fully 3D LES coupled to Lagrangian particle tracking, initializing the wake from a prior jet LES and

imposing stably stratified background turbulence via stochastic forcing. They found that stronger ambient turbulence accelerated the onset of wake instability, shortened contrail descent, and enhanced interior mixing; after vortex breakup, self-induced turbulence governed the mixing. Similarly, Unterstrasser (2014) applied LES with Lagrangian ice microphysics for a large transport aircraft and showed that adiabatic heating in the sinking vortex cores controlled ice crystal loss with a marked dependence on relative humidity and temperature; contrail depth reached about 450 m across the explored cases. Sensitivity tests indicated that initial ice crystal size and number influenced losses, fuel-flow variations had the smallest effect, and the vortex phase evolution preconditioned the subsequent contrail-to-cirrus transition.

For the contrail-to-cirrus transition over tens of minutes to hours, Unterstrasser and Gierens (2010a) conducted multi-hour LES sensitivity experiments and showed that relative humidity with respect to ice dominated the evolution, with substantial lateral spreading only under high supersaturation, while vertical wind shear had a secondary influence on optical properties. They also found that vapor removal by sedimenting ice far exceeded the instantaneous ice mass within the layer. In addition, D. Lewellen (2014) applied LES from several-seconds plume age through the vortex and dissipation phases to demise, analyzing lifetime, width, ice mass, and the time-integrated ice surface area; jet phase nucleation was not simulated and was instead prescribed via an effective ice-number emission index.

At DNS resolution, which is used only rarely in contrail-dynamics simulations, wake dynamics have been examined in simplified settings. In the very near field, F Garnier, Brunet, and Jacquin (1997) coupled an integral jet model to a two-dimensional DNS of passive-scalar convection–diffusion in an imposed Lamb–Oseen vortex pair to quantify dilution and entrainment during jet–wake interaction. The DNS showed that wing-tip vortices rapidly accelerate mixing and trap the exhaust plume (with outboard engines trapped fastest), that buoyancy becomes important mainly after trapping begins, and that, relative to an isolated jet, counter-rotating vortices reduce centerline dilution by several-fold over tens of wingspans downstream. Likewise, Saulgeot, Brion, Bonne, Dormy, and Jacquin (2023) performed 2D

DNS (Boussinesq) of the vortex phase, starting after jet diffusion/roll-up and initial ice formation, with analytic initialization of the jet, a Lamb–Oseen vortex pair, and the ice plume. They highlighted the roles of stratification and engine position on the wing. The dynamics were governed by primary two-dimensional wake mechanisms, and their parameter maps indicate that, for modern twin-engine aircraft, the ice plume is often no longer present in the vortices by the end of the vortex phase. For a more comprehensive DNS case, C Ferreira Gago, Brunet, and Garnier (2002) performed a 3D DNS of the compressible Navier–Stokes equations in two stages: a jet-only computation to the end of the jet regime, then coupling to a Lamb–Oseen trailing vortex to study near-wake jet–vortex interaction and scalar dilution, with validation against wind-tunnel velocity and temperature fields. The DNS showed that the vortex core stays essentially laminar while jet-induced turbulence generates large-scale vortical structures outside the core; the passive scalar concentrates in those structures and does not enter the core, and the turbulent kinetic energy exhibits a complete evolution.

1.2.1.3 Prescribed CFD-Derived Trajectories

In the prescribed dilution/entrainment trajectory approach, the jet–wake flow is first resolved with CFD (typically 3D LES); Lagrangian parcel histories of temperature, humidity, and mixture fraction are then extracted and used to drive microphysics. This retains 3D mixing fidelity via 1D parcel time histories, while avoiding the cost of fully coupled simulations.

To quantify how resolved mixing affects near-field activation, Roberto Paoli, Vancassel, Garnier, and Mirabel (2008) computed activation along LES-derived trajectories. The authors first ran a two-phase LES of a turbulent jet interacting with a vortex sheet to resolve the 3D, time-dependent mixing field, then fed many Lagrangian fluid-parcel trajectories extracted from that LES into a detailed microphysics solver. They showed that using LES-resolved mixing changes early particle properties and size distributions relative to single-trajectory or mean-mixing treatments. Within the jet-to-early-vortex regime, X. Vancassel, Mirabel, and Garnier (2014) modeled the first ~10 s of an A340 wake by resolving jet–wake dilution with 3D LES and then computing microphysics along LES-derived Lagrangian fluid trajectories. The

trajectory set supplied realistic time histories of temperature, humidity, and mixture fraction through the evolving jet/vortex field, enabling prediction of soot activation, vapor deposition on soot, heterogeneous and homogeneous freezing, and charge effects. They found that the mean ice-particle radius evolution matched a simpler inline scheme, while size distributions varied strongly by trajectory, showing charging-induced bimodality and confirming that trajectory-driven mixing controls near-field microphysics.

Continuing with near-field studies, Bier, Unterstrasser, and Vancassel (2022) and Bier et al. (2024) employed CFD-driven, trajectory-based dynamics. In Bier et al. (2022), ~25,000 Lagrangian parcel trajectories were extracted from a 3D LES (FludiLES) of an A340 plume for about 10 s; temperature histories along each trajectory were used to diagnose dilution, and microphysics was computed per trajectory, revealing a strong radial dependence of cooling/activation and attributing inter-study differences chiefly to the plume-mixing representation. In the hydrogen study (Bier et al., 2024), the LES trajectory database was curated and reused to prescribe thermodynamic histories, and ensemble trajectory simulations were performed without resolving dynamics in the box model, including a reduction to about 1,000 merged trajectories to retain heterogeneity while limiting artificial mixing across paths.

For far-field contrails, prescribed CFD-derived parcel trajectories are not used because they would necessitate prior 3D CFD of the wake; instead, the literature models far-field evolution with simplified frameworks or with inline LES.

1.2.2 Microphysical Modeling

1.2.2.1 Inline Analytical–Microphysics Coupling

In inline analytical–microphysics coupling, reduced jet–plume dynamical equations (0D/1D ODEs for entrainment, dilution, temperature, and pressure) and particle microphysics are solved on the same time grid, so feedbacks between mixing and phase change are preserved. The term inline is used because dynamics and microphysics are integrated within the same

reduced ODE system rather than inside a time-advancing 3D CFD solver; the term online is reserved for microphysics coupled directly within RANS/LES flow solvers. Box models are included here as the limiting case in which thermodynamic and dilution histories are prescribed from external sources, so microphysics is advanced without feedback to the entraining plume equations. Within this family of models for cruise conditions, researchers have successively examined the following particle processes contributing in contrail formation:

- **Volatile particles:** sulfuric acid, nucleation and growth of volatile aerosols, and their contribution to soot particle activation.
- **Soot particles:** how soot emissions (number, size, hygroscopicity, mixing state) set the initial ice-crystal number. Additionally, how background particles mixed into the plume compete with soot for activation.
- **Ion effects:** how combustion ions affect cluster formation and volatile particle growth.
- **Organics:** how organic compounds in the plume affect nucleation pathways and the activation of soot particles.

Within the exhaust plume, phase changes control both new-particle formation and subsequent aerosol growth. Volatile H_2SO_4–H_2O hydrated clusters nucleate new aerosol particles that grow to ultrafine particles (<10 nm) in young plumes and coats soot, enhancing hygroscopicity and lowering the supersaturation needed for activation (Ulrich Schumann et al., 2002). Including volatile-particle effects, Kärcher (1998) implemented an analytical plume model in which entrainment-driven cooling and dilution were cast as reduced ODEs and solved on the same time grid as the aerosol microphysics, preserving feedbacks between mixing and phase change. The microphysical module tracks gas-to-particle conversion of sulfur species to sulfuric acid, binary and ternary nucleation of volatile particles, condensational growth on soot and new particles, coagulation, and scavenging, with particle number and size updated prognostically across discrete size classes. This inline coupling provides self-consistent thermodynamic and compositional histories in the first seconds of the jet regime and predicts volatile particle number emission indices and early size spectra as functions of fuel sulfur, ambient conditions, and dilution rate. Building on this framework, Kärcher et al. (2000) consolidated the plume dynamics and aerosol physicochemistry into a unified calculation and

expanded the pathways considered, quantifying number emission indices and size distributions for volatile particles and processed soot across ranges of fuel-sulfur content, ambient thermodynamics, and dilution rate. As a recent refinement on soot sensitivity, Fangqun Yu, Karcher, et al. (2024) analyzed cruise-phase contrail onset with a size-resolved trajectory box model in which dilution, temperature, and humidity are prescribed versus plume age. The microphysics tracked heterogeneous ice activation on emitted soot, depositional growth/sublimation of ice, and the formation/evolution of volatile H_2SO_4–H_2O hydrated cluster. They concluded that ice activation is governed by the primary soot particle size (not aggregate effective size): smaller primary soot delays onset and raises peak plume supersaturation, which in turn widens the conditions under which small volatile particles can contribute to the total ice number. Implications are that assessments should consider both the emission index of non-volatile soot and primary soot sizes, especially for lean-burn/SAF trends.

Soot particles are the dominant exhaust aerosol from engines burning conventional fuels (Kärcher & Yu, 2009). Initially hydrophobic, they rapidly become hydrophilic as sulfuric acid and water vapor adsorb to their surfaces (H-W Wong & Miake-Lye, 2010). The resulting coated soot provides ice-nucleating surfaces, promotes vapor uptake and particle growth, and enables heterogeneous ice-crystal formation in the young plume. Activation cast as a soot-controlled threshold, Kärcher and Yu (2009) developed a compact analytical framework showing how soot number emissions govern contrail onset. They defined a critical soot number emission index for given ambient temperature, pressure, and relative humidity; linked initial ice number to soot abundance, size, hygroscopicity, and mixing state via an activation probability; and demonstrated threshold behavior in which contrails can be suppressed below that critical soot abundance even when the Schmidt–Appleman condition is met. They also showed that surface processing/coatings (e.g., sulfuric acid) increase soot hygroscopicity and activation efficiency. Focusing on onset physics, Kärcher et al. (2015) solved jet-plume entrainment, cooling, and dilution ODEs together with activation and freezing microphysics to predict initial ice number and size. Soot was treated as the primary water-activating nucleus, with soluble ambient aerosol also considered. The entrainment rate set centerline cooling and

dilution, defining the brief interval between water saturation and homogeneous freezing, while plume relative humidity was tracked along the mixing line. The framework yielded physically based onset relationships for the jet regime prior to vortex capture. Thus, the role of soot particles in ice activation appears both complex and highly conditional.

The work of Fangqun Yu and Turco (1997) marks a significant advance by highlighting the role of ions in the growth of volatile particles, notably through coagulation. The plume thermodynamics were represented with a reduced (parcel/box) framework, and ion-mediated nucleation and growth were integrated on the same time grid within that reduced system. Positive/negative combustion ions, ion–(H_2SO_4–H_2O) hydrated clusters, and neutral H_2SO_4–H_2O embryos evolving into ultrafine volatile particles were considered. The model established that ion chemistry can generate very high nucleation-mode number emission indices in cruise conditions and thereby precondition near-field microphysics, especially in soot-poor regimes where volatile particles can dominate later activation. Testing volatile–soot–ion interplay, H-W Wong and Miake-Lye (2010) modeled jet-regime contrail formation with a microphysical parcel model to about 1000 m (~4s) downstream in soot-rich plumes. Dilution was prescribed using a Schumann-type profile (Ulrich Schumann et al., 1998), with sensitivity tests against the Davidson–Wang jet law and a hybrid profile that follows the faster Davidson–Wang (Davidson & Wang, 2002) dilution over the first ~500 m but approaches the Schumann final dilution at 1000 m. Results showed that ice formed predominantly by water condensation on soot cores; chemi-ions strengthened volatile nucleation but did not increase ice; fuel-sulfur effects were small over typical ranges; and initial soot number and size dominated outcomes, with a very high number and very small cores suppressing ice growth.

Estimates by Brown et al. (1996) suggested the likely presence of other compounds contributing to the formation of condensation nuclei, such as organic compounds (Bernd Kärcher et al., 1998; Fangqun Yu & Turco, 1997; Fangqun Yu et al., 1999), which are inevitably present in the plume in addition to combustion by-products. The work of Fangqun Yu et al. (1999) highlighted that organic compounds contribute to the growth of nanoparticles (5–10 nm in diameter), particularly when the sulfur content in the fuel is low (0.02 g/kg-fuel).

Indeed, these compounds have the capacity to condense and contribute to the growth of volatile particles, as shown by Wang et al. (2010). The initialization of these organic species from their emission index remains difficult due to the complexity of their speciation (Beyersdorf et al., 2012). Working on organics through inline analytical-microphysical coupling, Rojo, Vancassel, Mirabel, Ponche, and Garnier (2015) analyzed how alternative jet fuels modify near-field aerosols and contrail propensity using a trajectory box model with parameterized, isobaric dilution. The microphysics tracked 11 particle categories, including chemi-ions, neutral/charged sulfate and organic clusters, dry and activated soot, mixed (neutral/positive/negative) aerosol, and ice formed heterogeneously and homogeneously. The authors concluded that with alternative fuels, lower soot and sulfur shift freezing toward the homogeneous pathway; entrained ambient particles become a significant contributor in the near field; and mixed-soot coatings become more organic with blending, indicating fuel-dependent changes in activation behavior.

1.2.2.2 Online CFD–Microphysics Coupling

Online CFD–microphysics coupling advances the microphysics inside the 3D CFD loop, updating particle/ice tendencies at each flow time step from the instantaneous fields. In near-field CFD, the microphysical modules are typically simplified relative to detailed 1D models because of the high computational cost of simulations (Grabowski et al., 2019; Roberto Paoli & Shariff, 2016). A common treatment assumes depositional growth of ice at a rate proportional to the difference between ambient vapor pressure and the vapor pressure just above the ice crystal surface—taken as saturation over ice with a Kelvin curvature correction (Petters & Kreidenweis, 2007). Water vapor is supplied first by the hot, moist exhaust jet and then by entrainment of supersaturated ambient air. For the particle representation, the online update can be done per-particle using Lagrangian tracking (Sölch & Kärcher, 2010), or as a mean-field using Eulerian sections (binned microphysics) or bulk equivalents (method of moments) (Grabowski et al., 2019). Within online CFD–microphysics coupling, studies advance microphysics inside the CFD time step; three main representations are used to track ice particles with the flow:

- **Eulerian—moments (bulk):** Solve advection–diffusion for a few low-order moments of the size distribution (e.g., mass, number), closing with an assumed spectral shape (lognormal/gamma) so microphysical tendencies update the moments (D. Lewellen & Lewellen, 2001; Paugam, Paoli, & Cariolle, 2010).
- **Eulerian—sections (binned):** Discretize particle size into bins and solve the transport equation in physical–size space for each bin, with microphysical processes (e.g., condensation, coagulation, nucleation) transferring mass/number between bins (D. Lewellen, Meza, & Huebsch, 2014; D. C. Lewellen, 2020).
- **Lagrangian (parcels):** Represent particles by numerical particles that move with the flow; each carries multiplicity and microphysical state updated from local fields each time step (F Garnier, Gago, Brasseur, Paoli, & Cuenot, 2003; Roberto Paoli & Garnier, 2005; Roberto Paoli et al., 2004; R Paoli et al., 2002).

In the Eulerian approach with the method of moments (bulk), ice crystal growth is modeled using a condensation/sublimation equation driven by water vapor diffusion, integrating an ice microphysics parameterization and accounting for the full particle size distribution. With a 3D LES model in the incompressible regime, D. Lewellen and Lewellen (2001) implemented an online-coupled LES of the counter-rotating wake in a stably stratified environments, with a bulk ice–vapor microphysics step applied each time step. Ice crystal number was prescribed (no aerosol activation); diffusional deposition/sublimation adjusted vapor and ice with latent-heat feedback to temperature (total-water conserving), while sedimentation was neglected. This tight coupling showed that wake-driven dilution and thermodynamics set the supersaturation field, thereby governing ice crystal growth and early-wake persistence. Paugam et al. (2010) advanced this framework with an online-coupled LES using an Eulerian bulk (two-moment) microphysics scheme, assuming locally monodisperse crystals and conserving total water with latent-heat feedback each time step. Ice crystal number was fixed after activation, growth and sublimation responded to the supersaturation field produced by wake mixing, and radiation heating/cooling (longwave/shortwave) and sedimentation were negligible over the first half hour. The authors highlighted two advantages of this design: resolving turbulence–microphysics interactions that are missing from common

parameterizations, and generating high-fidelity datasets that can inform contrail parameterizations in larger-scale models and support longer-age extensions.

In the Eulerian sectional (bin) framework, the particle size distribution is prognosed directly by solving transport and microphysical tendency equations on a discretized mass/size grid, so no assumed spectral shape is required. Each bin carries number or mass density and is advected and mixed with the flow, while size-dependent processes—diffusional growth and sublimation, nucleation/activation, coagulation/collisions, and optional sedimentation—redistribute material between bins using flux-conservative operators (Morrison et al., 2020). Online coupling to a 3D LES lets wake-driven dilution and supersaturation set bin-wise growth rates, yielding spectra that can evolve from narrow to multimodal as the plume transitions from vortex to early dispersion (D. Lewellen et al., 2014). Compared with bulk moments, sectional schemes are computationally costlier (tens to hundreds of bins and stiff tendencies often need sub-stepping), but they provide higher fidelity for size-dependent diagnostics such as surface area, effective radius, extinction/optical depth, and scavenging efficiencies. Grabowski et al. (2019) concluded that bulk schemes predict low-order moments and assume a spectral shape, whereas bin schemes prognose the full-size spectrum (and, if needed, added attributes), at substantially higher computational cost but with greater size-dependent fidelity. Implementations used in contrail studies commonly adapt CARMA-derived size-resolved routines for diffusional growth/sublimation within an incompressible LES, while habit and detailed radiative effects are typically handled by simplified parameterizations or post-processing (D. Lewellen, 2014; D. C. Lewellen, 2020). Key considerations include bin-grid design and limiting numerical diffusion in size space, which control accuracy–cost trade-offs.

The Lagrangian approach, on the other hand follows computational “parcels,” each representing many real particles, that are advected by the resolved flow while carrying multiplicity and microphysical state (e.g., phase, radius, hygroscopicity). This particle-centric view is well suited to represent processes that act on individual nuclei without prescribing a spectral shape (Unterstrasser & Sölch, 2010). When online-coupled to a dynamic (CFD) solver, parcels exchange water mass and latent heat with the Eulerian vapor/temperature fields every

time step, so wake-driven dilution and thermodynamics directly control particle growth and survival (Roberto Paoli et al., 2004). Early implementations applied simplified contrail microphysics in 0D/1D plume models to treat soot activation and ice growth (Kärcher et al., 1996), later extended to 3D LES for young-wake evolution and sensitivity studies.

Additionally, Roberto Paoli et al. (2004) conducted one of the first LES studies using an online Eulerian–Lagrangian two-phase formulation: an Eulerian LES for the jet/wake flow coupled each time step to Lagrangian parcels representing soot-ice clusters. The microphysics followed a simplified diffusion-limited growth law of Kärcher type (Kärcher et al., 1996). Building on this, Roberto Paoli and Garnier (2005) applied the same online-coupled framework to the jet–vortex interaction, coupling LES dynamics with Lagrangian microphysics to resolve near-field mixing and early contrail growth. Furthermore, Naiman, Lele, and Jacobson (2011) employed a 3D incompressible LES with online Lagrangian, size-resolved ice microphysics: computational particles follow the resolved flow, grow or sublimate by diffusion, and feed back to the Eulerian fields through water vapor and latent-heat source terms each time step. Advantages noted include capturing wake–microphysics interactions at realistic resolution and producing optical-property diagnostics (width, optical depth) consistent with limited observations, though the authors flag limits from Lagrangian sampling, neglected settling, and sub-grid dispersion.

In a recent work, Lottermoser and Unterstraßer (2025) simulated early hydrogen contrails with a 3D anelastic large-eddy flow solver (EULAG) online-coupled to a Lagrangian Cloud Model, in which ice is represented by simulation particles that exchange water mass and latent heat with the Eulerian temperature and vapor fields each time step. The microphysics focused on deposition growth and sublimation (aggregation and radiation disabled) to isolate young-wake processes. The key finding was that vortex phase dynamics compress a four orders of magnitude spread in initial ice number to about two orders of magnitude, with losses increasing at warmer temperatures and lower humidity; the study also extended an existing parameterization of vortex phase ice loss to hydrogen scenarios. In the Lagrangian category, online Eulerian–Lagrangian couplings span work based on FludiLES (a 3D LES jet/wake

solver with online contrail microphysics) from the one-way inline condensation scheme of X. Vancassel et al. (2014) to the fully 3D LES with Lagrangian ice tracking of Picot et al. (2015), with François Garnier, Maglaras, Morency, and Vancassel (2014) documenting the solver that underpinned these implementations.

1.2.2.3 Offline Trajectory–Microphysics Coupling (CFD-Derived)

In this approach, a prior CFD simulation provides the velocity and thermodynamic fields that drive a separate, high-fidelity microphysics solver. Thermodynamic and dilution histories (temperature, pressure, water vapor, scalars) are sampled from the simulation along prescribed paths, and the microphysics predicts particle activation, growth/sublimation, and size spectra without feedback to the flow (Roberto Paoli et al., 2008). This coupling enables computationally demanding schemes (e.g., sectional/bin microphysics, detailed chemistry) and long integrations at modest cost while retaining realistic mixing histories along the sampled paths (X. Vancassel et al., 2014). The trade-off is that latent-heat and mass-loading effects on dynamics are omitted, and results depend on trajectory definition, interpolation, and any sub-grid dispersion treatment. Practically, CFD-derived trajectory forcing is specified in two configurations:

- **Ensemble of trajectories:** multiple paths sampled across plume radii and times; retains variability in dilution and supersaturation and yields distributions as well as means. Considerations include higher computational cost and sensitivity to the trajectory-sampling strategy and any dispersion model.
- **Single mean trajectory:** one representative path derived from the CFD fields; useful for mechanism testing and rapid sensitivity scans. A limitation is that sub-plume variability is smoothed, so onset timing and ice crystal number predictions can be biased and depend on how the averaging is defined.

In the ensemble-trajectory configuration, tens of thousands of paths are sampled to capture thermodynamic variability; Roberto Paoli et al. (2008) used on the order of 25,000 LES-derived trajectories. The offline microphysics includes kinetic H_2SO_4-H_2O nucleation,

condensation/evaporation, Brownian coagulation, activation and coating of soot, and heterogeneous freezing to form contrail ice, implemented with a sectional size representation for both volatile aerosol and soot. This LES-derived-trajectory strategy provides physically consistent, CFD-informed forcing to the microphysics while keeping the chemistry–microphysics model flexible and computationally tractable for sensitivity studies to fuel sulfur content and mixing efficiency. Having presented the online coupling before, X. Vancassel et al. (2014) then implemented an offline, trajectory-driven configuration: a time-resolved FludiLES LES supplied an ensemble of fluid-parcel trajectories from the nozzle to ~10 s, and the Microphysical Model of Effluents (MoMiE) microphysics model was integrated separately along each path using the local temperature, pressure, and dilution histories, with no feedback to the flow. This offline setup employed more detailed sectional microphysics than the online case, resolving neutral/charged volatile particles, dry and activated soot, and ice from homogeneous/heterogeneous freezing. It reproduced characteristic wake structure—a ring of supersaturation around the vortex core with ice diameters of ~0.6–1.2 μm, while the core remained subsaturated with small ice crystals (<100 nm) due to weak mixing—and sampled ~25,000 parcel positions to capture spatial variability; the evolution of mean ice radius remained consistent.

Furthermore, Bier et al. (2022) and Bier et al. (2024) applied a particle-based Lagrangian Cloud Module (LCM) box model along LES-derived trajectory ensembles from FludiLES to study contrail formation offline. The 2022 study ran LCM on 25,000 plume trajectories (and a single "average-trajectory" variant), showing strong radial variability, earlier/later onset differences tied to the prescribed dilution history, and that conclusions hinge more on mixing representations than on microphysics choice. The H_2 study reused the FludiLES set but merged it to ~1,000 trajectories for efficiency, documented preprocessing of the temperature-based dilution histories, and extended LCM to contrail formation on ambient particles (soot-free). It found an H_2 Schmidt–Appleman threshold ≈10 K higher, stronger early supersaturation, and 80–90% lower ice number than kerosene cases, with pronounced sensitivity to ambient aerosol number, size, and hygroscopicity. Finally, both papers cautioned that ensemble runs without

inter-trajectory mixing can overestimate ice numbers relative to single-path setups, underscoring the role of plume-mixing variability.

As a counterpoint to the ensemble analysis presented earlier, Roberto Paoli et al. (2008) also evaluated the microphysics along a single "average" trajectory constructed by averaging the LES temperature and dilution over ~25,000 paths. This smoothing of mixing fluctuations weakened early formation signals—at 1 s the mean-path run lacked the small-size nucleation mode that appeared with the full ensemble—and it produced lower particle abundances than the ensemble case. The paper attributes these differences chiefly to the different vapor histories, noting that the ensemble run had roughly twice the water vapor pressure of the mean-path run. Bier and Burkhardt (2022) also employed a single-trajectory ("average-traj") variant, in which the LES-derived temperature histories from 25,000 paths were averaged and converted to a mean dilution curve that then drove one box model run. Relative to the ensemble framework, the average-traj run showed a sharper, pulse-like activation signal (the ensemble increased more smoothly) and typically lower final freezing fractions under the same conditions. Importantly, they argued that offline ensembles without inter-trajectory mixing can overestimate ice numbers, so an ensemble is not inherently more reliable than the single-trajectory setup; the main differences were traced to how mixing is represented, not to microphysics per se.

1.3 Chapter Conclusion

This chapter delivered a literature review that complements the three articles forming this thesis. It opened by introducing contrail formation as the central focus and summarized contrail evolution and underlying processes across thermodynamics, chemistry, microphysics, and flow dynamics, with brief introductions to each and their key studies.

To introduce the structured toolkit on which this thesis builds, this chapter organized numerical models of contrail formation and evolution into two parts: dynamic modeling and microphysical modeling. The dynamic modeling section presented three ways to obtain plume

mixing, temperature, and scalar fields: (i) analytical flow models (including mathematical formulations and interpolated equations), (ii) CFD simulations as the primary approach used here covering RANS, LES, and DNS, and (iii) prescribed CFD-derived trajectories, extracted from CFD and used to represent near-field dilution histories at far lower cost than fully coupled simulations, while noting their limited suitability for far-field evolution.

The microphysical modeling section began with inline analytical–microphysics coupling, in which 0D/1D analytical plume models are integrated on the same time grid with more detailed microphysics. It then outlined the species and processes commonly considered—volatile particles, soot particles, ion effects, and organic compounds—and proceeded to online CFD–microphysics coupling, where 2D/3D flow fields are coupled with microphysical solvers in Eulerian–moments (bulk), Eulerian–sections (binned), or Lagrangian (parcels) form. Finally, the chapter described offline trajectory–microphysics coupling (CFD-derived), in which trajectories extracted from CFD drive microphysics outside the flow solver, using either a single averaged ("mean") trajectory or an ensemble to represent spatial variability.

The existing literature has often treated jet/wake dynamics and microphysics in partially decoupled ways, with entrainment and dilution histories prescribed rather than prognosed, so feedbacks that set near-field supersaturation have been simplified. Realistic engine architecture has been underrepresented, and the influence of bypass ratio on early ice properties has not been isolated under controlled flow and chemistry. Solute effects have typically been implicit, activation of entrained ambient aerosols has been examined only in narrow regimes, and comparisons of online versus offline coupling under matched conditions have been limited. Guidance for initializing the vortex phase from temporal versus spatial jet formulations has been inconsistent and rarely tested across jet maturity. Accordingly, the thesis is structured so that the limitations identified above are examined, the remaining knowledge gaps are made explicit, and their resolution is advanced.

The remainder of this thesis is organized as follows. CHAPTER 2 details the governing equations and numerical framework used throughout the thesis. CHAPTER 3 evaluates the

bypass effects of advanced turbofan engines on contrail formation using LES, comparing CFM56-5B3/3, LEAP-1A/33, and a UHBR configuration in terms of their microphysical signatures. CHAPTER 4 investigates the role of soot particle properties and activation using LES with online-coupled microphysics, building on activation developments implemented in the FludiLES code. Finally, CHAPTER 5 incorporates ambient particles and extends the analysis into the vortex phase, comparing spatial and temporal modeling approaches across the jet and vortex initialization regimes for two aerosol scenarios, soot-only and soot+ambient.

CHAPTER 2

METHODOLOGY

In this chapter, the methodology used to achieve the research objectives is discussed. We present the mathematical formulation and numerical techniques employed to simulate the aircraft-engine jet and its initial entrainment into the vortex phase under cruise conditions. The framework combines high-order compressible CFD with an online Lagrangian microphysics module to resolve soot and ambient-aerosol activation and early ice growth. Both spatial and temporal LES formulations are used; key modeling assumptions, discretization choices, boundary treatments, and validation steps are documented to ensure reproducibility.

To this end, this Chapter is organized into four main sections. Section 2.1 presents the governing equations, separating the gas phase conservation laws from the solid phase Lagrangian particle equations. Section 2.2 details the numerical method—the LES formulation and sub-grid scale (SGS) modeling; discretization and time-integration schemes; the particle microphysics algorithm; the gas–particle coupling term; and the computational framework and setup, which covers the FludiLES architecture and modules, domain and mesh, initialization procedures, boundary conditions, and validation. Section 2.3 describes the post-processing workflow and performance metrics used to analyze the simulations. Finally, Section 2.4 concludes the chapter by summarizing the principal methodological choices and their implications for the results presented in the subsequent chapters.

2.1 Governing Equations

2.1.1 Gas Phase Equations

The compressible Navier–Stokes equations for a Newtonian fluid are written in conservative form for the variables $(\rho, \rho u_i, \rho E, \rho Y)$, where Y is the water vapor mass fraction. The equations are non-dimensionalized using the reference scales $L_0, U_0, \rho_0, T_0, \mu_0$, and Z_0, representing a

characteristic length, velocity, density, temperature, dynamic viscosity, and mass fraction corresponding to the jet exit conditions, respectively. These are defined as:

$$u = \frac{u^*}{U_0}, T = \frac{T^*}{T_0}, \rho = \frac{\rho^*}{\rho_0}, P = \frac{P^*}{\rho_0 U_0^2}, E = \frac{E^*}{\rho_0 U_0^2}, \mu = \frac{\mu^*}{\mu_0}, Z = \frac{Y - Y_a}{Y_j - Y_a} \tag{2.1}$$

where dimensional variables are marked with the symbol (*). Therefore, the system formed by continuity, momentum, total energy, and water vapor mass fraction transport is written as follows:

$$\frac{\partial \rho}{\partial t} + \frac{\partial (\rho u_j)}{\partial x_j} = 0 \tag{2.2}$$

$$\frac{\partial (\rho u_i)}{\partial t} + \frac{\partial (\rho u_i u_j)}{\partial x_j} + \frac{\partial P}{\partial x_i} = \frac{\partial \sigma_{ij}}{\partial x_j} \tag{2.3}$$

$$\frac{\partial E}{\partial t} + \frac{\partial (E + P) u_j}{\partial x_j} = \frac{\partial \sigma_{ij} u_i}{\partial x_j} - \frac{\partial q_j}{\partial x_j} + \dot{q}_\ell \tag{2.4}$$

$$\frac{\partial \rho Z}{\partial t} + \frac{\partial \rho Z u_j}{\partial x_j} = \frac{1}{Re\ Pr} \frac{\partial}{\partial x_j} \left(\frac{\partial Z}{\partial x_j} \right) + \dot{\omega}_v \tag{2.5}$$

Here t and x_j are independent variables representing time and Cartesian spatial coordinates, respectively. The three velocity components are denoted u_i (i=1, 2, 3). Einstein summation over repeated indices is used.

The viscous stress tensor is defined through the temperature-dependent viscosity $\mu(T)$ and the strain rate tensor S_{ij}:

$$\sigma_{ij} = \frac{\mu(T)}{Re} S_{ij} \tag{2.6}$$

$$S_{ij} = \frac{\partial u_i}{\partial x_j} + \frac{\partial u_j}{\partial x_i} - \frac{2}{3} \delta_{ij} \frac{\partial u_k}{\partial x_k} \tag{2.7}$$

δ_{ij} denotes the Kronecker delta.

The specific total energy E is defined as:

$$E = \frac{P}{(\gamma - 1)\rho} + \frac{1}{2} u_i u_i \tag{2.8}$$

The heat flux vector follows Fourier's law:

$$q_j = \frac{-\mu(T)}{(\gamma - 1) Re\ Pr M^2} \frac{\partial T}{\partial x_j} \tag{2.9}$$

The $\mu(T)$ follows Sutherland's law with reference (T_0, μ_0). The pressure P, temperature T, and density ρ are related by the ideal gas equation of state:

$$P = \frac{\rho T}{\gamma M^2} \tag{2.10}$$

The water vapor mass fraction is non-dimensionalized by normalizing with its jet exit and ambient values Y_j and Y_a; this defines the scalar Z:

$$Z = \frac{Y - Y_a}{Y_j - Y_a} \tag{2.11}$$

Furthermore, the terms $\dot{q}_\ell$ and $\dot{\omega}_v$ provide two-way coupling in mass and energy. Their construction from the solid phase is given in Section 2.1.2 and their discrete implementation in Section 2.2.4.

The dimensionless numbers are:

- The reference Reynolds number, comparing inertial and viscous effects:

$$Re = \frac{\rho_0 U_0 L_0}{\mu_0} \tag{2.12}$$

- The heat capacity ratio $\gamma = C_{p0}/C_{v0}$; to avoid additional nonlinearity, γ is held constant at 1.4, the commonly accepted value for dry air:

$$\gamma = C_{p0}/C_{v0} \tag{2.13}$$

- The reference Prandtl number, comparing momentum and heat diffusion; here it is taken constant and set to 0.7, representative of air:

$$Pr = \frac{\mu_0 C_p}{k} \tag{2.14}$$

- The reference Mach number *M* is defined as:

$$M = \frac{U_0}{a_0} \tag{2.15}$$

where the reference speed of sound C_0 is:

$$a_0 = \sqrt{\gamma R_s T_0} \tag{2.16}$$

R_s denotes the ratio:

$$R_s = \frac{R_u}{M_\omega} \tag{2.17}$$

where R_u is the universal gas constant and M_ω is the molar mass (kg/mol). For dry air, $R_s = 287\ J/(kg.K)$.

2.1.2 Solid Phase Equations

A Lagrangian approach is employed to track the particles. Particles are assumed spherical and monodisperse at injection. The solid phase is taken in thermal equilibrium with the carrier gas; thus, the particle temperature T_p equals the gas temperature T. The particle position is obtained by integrating:

$$\frac{dx_p}{dt} = u(x_p, t) \tag{2.18}$$

Here u is the fluid velocity evaluated at the particle location x_p.

The Stokes number $St_v = \tau_v / t_0$ compares the particle relaxation time τ_v to the characteristic flow time t_0. For submicron particles, τ_v is extremely small (typically $10^{-6} - 10^{-4}$ s), while the flow timescale remains of the order of 10^{-2} s. Consequently, $St_v \ll 1$, indicating that particles rapidly adjust to local velocity fluctuations and closely follow the carrier phase. So, the particle velocity is assumed equal to the local fluid velocity ($u_p = u$).

Maxwell's continuum description assumes vapor and temperature fields remain continuous up to the particle surface and yields the classical diffusive/conductive limits at $r = r_p$. For small particles, however, this assumption fails when the near-surface length scale becomes comparable to the mean free path λ. Experiments by Langmuir (1915) and the analysis of Schäfer (1932) and Fuchs (2013) showed that diffusion equations apply only outside a thin, near-surface Knudsen layer, within which transport is molecular (ballistic). Following the transition formulation of Fukuta and Walter (1970), we therefore correct the continuum flux by a factor ($f_{3\beta}$) that accounts for molecular transport and the mass accommodation coefficient. The expression used here is given next in Equation (2.19)–(2.20); it recovers the continuum limit $f_{3\beta} \to 1$ for $r_p \gg \lambda$ and smoothly bridges toward the free molecular behavior as r_p decreases (Radiative transfer is neglected.)

Particle growth occurs when turbulent mixing with ambient air cools the jet and produces supersaturation, leading to heterogeneous nucleation and condensation of water vapor onto the particles. Under these saturation conditions, gravitational settling is neglected because of the small particle size (order of 1–2 μm). The ice crystal size, assumed spherical, evolves with the local temperature and relative humidity. The particle mass evolution is computed following the condensation/evaporation formulations of François Garnier et al. (2014):

$$\frac{dm_p}{dt} = \frac{4\pi r_p D_v M_v}{RT_P} f_{3\beta}(P_w - P_{sat}) \tag{2.19}$$

$$f_{3\beta} = \frac{r_p}{r_p + D_v\sqrt{\frac{2\pi M_v}{RT_P}}} \tag{2.20}$$

Here m_p is the particle mass; D_v the molecular diffusivity of water vapor in air; M_v the molar mass of water; $f_{3\beta}$ a correction factor accounting for the gas–liquid density contrast; P_w the partial pressure of water vapor; and P_{sat} the saturation vapor pressure of water. D_v is related to the Schmidt number by $Sc_v = \mu/(\rho D_v)$.The preceding equation can be rearranged to express the rate of change of particle radius as:

$$\frac{dr_P}{dt} = \frac{D_v\, M_v}{r_P R T_P \rho_P} f_{3\beta}(P_w - P_{sat}) \tag{2.21}$$

Accordingly, the particle radius evolves following the Fukuta and Walter (1970) growth law, with the numerator modified in this thesis to account for water activity via κ-Köhler theory:

$$r_P \frac{dr_P}{dt} = \frac{S_w - S_k}{C_t S_k + C_P} \tag{2.22}$$

with:

$$S_w = \frac{P_{H_2O,actual}}{P_{sat}(T_P)} \tag{2.23}$$

$$S_k = \alpha_w . \exp\left(\frac{Ke}{r_p}\right) = \frac{{r_p}^3 - {r_d}^3}{{r_p}^3 - {r_d}^3(1-\kappa)} \exp\left(\frac{Ke}{r_p}\right) \tag{2.24}$$

$$C_t = \bar{r}^2 L_0 U_0 \left(\frac{L^2 M_v \rho_P}{k_g R\, T_P^2 f_{3\alpha}}\right) \tag{2.25}$$

$$C_p = \bar{r}^2 L_0 U_0 \left(\frac{R\, T_P \rho_P}{P_{sat} D_v\, M_v f_{3\beta}}\right) \tag{2.26}$$

$$f_{3\alpha} = \frac{r_p}{r_p + \frac{k_g \sqrt{2\pi M_a R T_P}}{P(C_{P,a} - R/2)}} \tag{2.27}$$

Here, S_w, is the actual saturation ratio of water vapor determined based on the local available water vapor content in the environment, which varies due to the mixing between the jet plume and the ambient atmosphere. S_k is the equilibrium saturation ratio which depends on the local properties of each particle and α_w is the water activity in the droplet solution. C_t and C_p are the coefficients governing growth and evaporation. $f_{3\alpha}$ is the non-continuum heat transfer correction; thermal accommodation α is taken as unity (no explicit coefficient). Moreover, κ (kappa) is a dimensionless hygroscopicity parameter in κ-Köhler theory that collapses particle composition into one number describing how readily a particle takes up water (Petters & Kreidenweis, 2007).

The sink/source of water vapor in an Eulerian control volume V is obtained from the parcel mass change $\dot{m}_p$. Using $\dot{m}_p = \rho_p 4\pi r_p^2 \frac{dr_p}{dt}$, the volumetric source in the vapor transport equation is:

$$\omega_v(x) = \frac{r_s^3}{Y_w} . \frac{1}{V(x)} n_P \sum_{k=1}^{n_P} \rho_P 4\pi r_P^2 \frac{dr_P}{dt} \tag{2.28}$$

where Y_w is the water mass fraction, r_s a dimensionless number depending on the initial radius of the soot particles and n_P is the number of particles with a density of ρ_P contained in a volume $V(x)$.

The heat released/absorbed by phase change follows the particle-scale energy balance, where latent heat exactly balances conductive heat away from the interface. Aggregating to the Eulerian cell gives the latent-heat source:

$$\dot{q}_\ell = \frac{n_P}{V(x)} \sum_{k=1}^{n_P} L_p(T_{p,s}) \frac{dm_P}{dt} \tag{2.29}$$

where $L_p(T_{p,s})$ is the latent heat of sublimation evaluated at the particle surface temperature, $T_{p,s}$. With $\frac{dm_P}{dt} > 0$ (condensation/icing, particle mass increases), $\dot{q}_\ell > 0$ — heat is released to the gas; if $\frac{dm_P}{dt} < 0$ (evaporation/sublimation), $\dot{q}_\ell < 0$. In the jet phase, $\dot{q}_\ell$ is usually negligible compared with advective–diffusive energy terms because ice mass remains small and the supersaturation is short-lived; accordingly, energy two-way coupling is often omitted while the vapor mass source is retained.

2.2 Numerical Method

2.2.1 LES Formulation & SGS

At the high Reynolds numbers considered, turbulence spans a broad range of scales. Energy-containing eddies at the integral scale l transfer kinetic energy downscale through a Kolmogorov cascade to dissipative scales l_k, where viscosity removes it. The scale separation follows $l_k/l = Re_l^{-3/4}$, so the number of dynamically relevant scales—and thus the grid demand—grows as $O(Re_l^{-3/4})$ per spatial direction, making DNS infeasible. Consequently, we adopt LES: large structures are resolved, while unresolved motions are represented by a sub-grid scale (SGS) closure derived from the spatially filtered Navier–Stokes equations. Only

the fundamental definitions are recalled. The idealized case of homogeneous, isotropic turbulence is considered, following E. Garnier, Adams, and Sagaut (2009). The filter is assumed translation- and rotation-invariant, and a uniform cut-off length Δ, identical in all directions, is adopted.

For any flow variable f, the decomposition is:

$$f = \bar{f} + f' \tag{2.30}$$

Scale separation is achieved by applying a low-pass spatial filter (i.e., removing high-wavenumber content) to the exact field. $\bar{f}$ denotes the low frequency, large scale component of f, and f' its complementary high-frequency part. The filtering operation is represented in physical space as a convolution. Thus, the resolved part $\bar{f}$ is formally defined by:

$$\bar{f} = \int_{\Omega} G_{\Delta}(x - \xi) f(\xi)\, d\xi \tag{2.31}$$

This relation is written symbolically as $\bar{f} = G_{\Delta} f$, so that:

$$f' = (1 - G_{\Delta}) f \tag{2.32}$$

The convolution kernel G_{Δ} characterizes the filter; it depends on the cut-off length Δ and satisfies the following normalization relation:

$$\int_{\Omega} G_{\Delta}(x - \xi) d\xi = 1 \tag{2.33}$$

Filters commonly used in LES include the box (top-hat), Gaussian, and spectral cut-off filters. To permit manipulation of the Navier–Stokes equations after filtering, the filter must preserve constants, be linear, and commute with spatial differentiation. In other words:

$$\bar{a} = a \; if \; a = cste \tag{2.34}$$

$$\overline{\Phi + \Psi} = \bar{\Phi} + \bar{\Psi} \tag{2.35}$$

$$\frac{\overline{\partial \Phi}}{\partial s} = \frac{\partial \bar{\Phi}}{\partial s}, \qquad s = x_i, t \quad i = 1,2,3 \tag{2.36}$$

Filters that satisfy the three properties stated above are, in general, not Reynolds operators; hence the idempotence property does not hold:

$$\bar{\bar{\Phi}} = {G_\Delta}^2 \Phi \neq \bar{\Phi} = G_\Delta \Phi \tag{2.37}$$

$$\bar{\Phi}' = G_\Delta (1 - G_\Delta) \Phi \neq 0 \tag{2.38}$$

In this case the filter operator is, in principle, invertible: the null space (kernel) of G_Δ is trivial, $\ker(G_\Delta) = \{0\}$, so a single filtering does not irretrievably remove information. By contrast, a Reynolds operator is idempotent and acts as a projection; its null space contains the sub-grid component, and information is therefore lost by filtering.

The filter cut-off length is most commonly defined following Deardorff as ($\Delta = \Delta_{iso}$):

$$\Delta_{iso} = (\Delta_x \Delta_y \Delta_z)^{\frac{1}{3}} \tag{2.39}$$

where Δ_x, Δ_y, and Δ_z are the grid spacings in the x, y, and z directions. For an isotropic grid (Δ_x=Δ_y=Δ_z), Δ_{iso} reduces to the common spacing.

In compressible-flow LES, density-weighted filtering (Favre averaging) is employed ((Cécile Ferreira Gago, 2002; E. Garnier et al., 2009)). It is defined by:

$$\overline{\rho f} = \bar{\rho} \tilde{f} \tag{2.40}$$

Hence, any scalar or vector field is decomposed as:

$$f = \tilde{f} + f'' \tag{2.41}$$

where ($\tilde{.}$) denotes the Favre-filtered quantity and ($.''$) the Favre fluctuation. The tilde operator is linear but, in general, does not commute with temporal or spatial differentiation:

$$\widetilde{\frac{\partial f}{\partial s}} \neq \frac{\partial \tilde{f}}{\partial s}, \qquad s = x_i, t \ , t = 1,2,3 \tag{2.42}$$

Here, the Navier–Stokes equations used in LES are obtained by applying the spatial filter. The nonlinear products generate sub-grid terms, which are gathered on the right-hand side; the left-hand side is kept in terms of resolved quantities only.

Here, the Navier–Stokes equations used in LES are obtained by applying the spatial filter. The nonlinear products generate sub-grid terms, which are gathered on the right-hand side; the left-hand side is kept in terms of resolved quantities only.

Continuity equation

Applying the spatial filter to the mass conservation Equation (2.2) gives:

$$\frac{\partial \bar{\rho}}{\partial t} + \frac{\partial \left(\overline{\rho u_j}\right)}{\partial x_j} = 0 \tag{2.43}$$

By adopting Favre filtering, a form free of sub-grid terms is obtained, which is the main motivation for the change of variables, this yields:

$$\frac{\partial \bar{\rho}}{\partial t} + \frac{\partial \left(\bar{\rho}\widetilde{u_j}\right)}{\partial x_j} = 0 \tag{2.44}$$

Momentum equation

Filtering the momentum equation leads to:

$$\frac{\partial(\bar{\rho}\widetilde{u_i})}{\partial t}+\frac{\partial(\bar{\rho}\tilde{u}_i\tilde{u}_j)}{\partial x_j}+\frac{\partial \bar{P}}{\partial x_i}-\frac{\partial\widehat{\sigma_{ij}}}{\partial x_j}=-\frac{\partial}{\partial x_j}\left(\tau_{ij}\right)+\frac{\partial}{\partial x_j}(\overline{\sigma_{ij}}-\widehat{\sigma_{ij}}) \tag{2.45}$$

where the additional right-hand-side term is the sub-grid scale (SGS) stress divergence. The SGS stress tensor is defined by:

$$A_1=\tau_{ij}=\bar{\rho}(\widehat{u_i u_j}-\widetilde{u_i}\widetilde{u_j}) \tag{2.46}$$

The viscous stress is evaluated from resolved fields (for constant μ the term is closed; with $\mu(T)$ it is computed using the resolved temperature).

A_2 is defined as the difference between the filtered viscous stress and the viscous stress built from Favre-filtered fields, and $\tilde{S}_{ij}$ is the Favre strain rate tensor:

$$A_2=\left(\overline{\sigma_{ij}}-\widehat{\sigma_{ij}}\right)=\frac{\overline{\mu(T)S_{ij}}}{Re}-\frac{\mu(\tilde{T})\tilde{S}_{ij}}{Re} \tag{2.47}$$

$$\tilde{S}_{ij}=\frac{\partial\tilde{u}_i}{\partial x_j}+\frac{\partial\tilde{u}_j}{\partial x_i}-\frac{2}{3}\delta_{ij}\frac{\partial\tilde{u}_k}{\partial x_k} \tag{2.48}$$

The two sub-grid contributions, A_1 and A_2, arise respectively from the non-linear convective term (SGS stress divergence) and from the viscous term with temperature-dependent viscosity in Equation (2.3). Closure requires that they be expressed in terms of the resolved variables, here $\tilde{\rho}\tilde{u}_i$.

Energy conservation equation

Filtering Equation (2.4) yields:

$$\frac{\partial \hat{E}}{\partial t} + \frac{\partial}{\partial x_j}\{(\hat{E} + \bar{P})\tilde{u}_j\} - \frac{\partial}{\partial x_j}(\widehat{\sigma_{ij}}\tilde{u}_i) + \frac{\partial \widehat{q_j}}{\partial x_j} = -B_1 - B_2 - B_3 - B_4 - B_5 - B_6 - B_7 \tag{2.49}$$

with:

$$\hat{E} = \frac{\bar{P}}{\gamma - 1} + \frac{1}{2}\bar{\rho}\tilde{u}_i\tilde{u}_i \tag{2.50}$$

$$\widehat{q_j} = \frac{-\mu(\tilde{T})}{(\gamma - 1)Re\ PrM^2}\frac{\partial \tilde{T}}{\partial x_j} \tag{2.51}$$

The *B* terms collect the sub-grid contributions generated by filtering (turbulent transport, pressure–velocity correlations, viscous work, and heat flux) and must be modeled by an SGS closure:

$$B_1 = \frac{1}{\gamma - 1}\frac{\partial}{\partial x_j}\left(\overline{Pu_j} - \bar{P}\tilde{u}_j\right) \tag{2.52}$$

$$B_2 = \overline{P\frac{\partial u_k}{\partial x_k}} - \bar{P}\frac{\partial \tilde{u}_k}{\partial x_k} \tag{2.53}$$

$$B_3 = \frac{\partial}{\partial x_j}\left(\tau_{kj}\tilde{u}_k\right) \tag{2.54}$$

$$B_4 = \tau_{kj}\frac{\partial}{\partial x_j}\tilde{u}_k \tag{2.55}$$

$$B_5 = \overline{\sigma_{kj}\frac{\partial}{\partial x_j}u_k} - \overline{\sigma_{kj}}\frac{\partial}{\partial x_j}\tilde{u}_k \tag{2.56}$$

$$B_6 = \frac{\partial}{\partial x_j}(\overline{\sigma_{ij}}\tilde{u}_i - \widehat{\sigma_{ij}}\tilde{u}_i) \tag{2.57}$$

$$B_7 = \frac{\partial}{\partial x_j}(\overline{q_j} - \widehat{q_j}) \tag{2.58}$$

The pressure–velocity correlation term B_1 represents the action of sub-grid turbulence on the scale-resolved pressure forces. The pressure dilatation term B_2 accounts for purely compressible effects and vanishes in the incompressible limit. The pair $(B_3 - B_4)$ corresponds to the transport of kinetic energy from resolved to sub-grid scales. The sub-grid dissipation B_5 measures the conversion of kinetic energy into internal energy by viscous action. The last two contributions, B_6 and B_7, arise from the non-linearities of the viscous work and heat-flux terms.

Vapor Conservation Equation

Filtering the vapor transport equation yields the following equation, in which the sub-grid scalar flux appears; its definition is given in:

$$\frac{\partial \bar{\rho} Z}{\partial t} + \frac{\partial \rho Z \tilde{u}_j}{\partial x_j} - \frac{1}{Re\ Pr} \frac{\partial}{\partial x_j} \left(\mu(T) \frac{\partial Z}{\partial x_j} \right) + \bar{S}_N = -\frac{\partial C_1}{\partial x_j} + C_2 \tag{2.59}$$

$$C_1 = \bar{\rho}(\widetilde{Z u_j} - \tilde{Z} \tilde{u}_j) \tag{2.60}$$

$$C_2 = \frac{1}{Re\ Pr} \frac{\partial}{\partial x_j} (\overline{\mu \frac{\partial Z}{\partial x_j}} - \mu \tilde{T} \frac{\partial \tilde{Z}}{\partial x_j}) \tag{2.61}$$

Filtering of the coupling term introduces the notion of a numerical particle (Leboissetier, Okong'o, & Bellan, 2004). The number of particles used in the numerical resolution is therefore reduced, while maintaining the same physical density:

$$\bar{S}_N = \frac{10^3 \bar{r}^3}{Z_0} \frac{1}{V_{cell}} n_{trans} \sum_{k=1}^{n_p} \dot{m}_k^* \tag{2.62}$$

where Z_0 is the reference vapor mass fraction, V_{cell} is the control volume, n_{trans} is the number of physical particles represented by one numerical particle, and $\dot{m}_k^*$ denotes the mass transfer rate associated with each particle.

SGS Model

Building on the filtered forms derived above, attention is now turned to the closure of the SGS contributions. In the filtered momentum Equation (2.45) two SGS terms appear: A_1, written through the SGS stress tensor τ_{ij} and originating from the nonlinear convection, and A_2, associated with the viscous term when the viscosity depends on temperature. Consistent with common LES practice—and with Vreman's assessment in shear layers—the effect of A_2 is neglected. The modeling therefore focuses on τ_{ij}, for which a hybrid Smagorinsky formulation (functional eddy viscosity + structural scale similarity) is adopted following Cécile Ferreira Gago (2002).

A functional (eddy-viscosity) approach is adopted, consistent with the direct cascade of energy. The transfer from resolved to sub-grid scales is represented analogously to molecular diffusion: the anisotropic (deviatoric) part of the SGS stress is taken proportional to the resolved strain-rate tensor through an eddy viscosity ν_{sm}. With the usual decomposition:

$$\tau_{ij} = \tau_{ij}^{I} + \tau_{ij}^{D} \tag{2.63}$$

$$\tau_{ij}^{I} = \frac{1}{3}\tau_{kk}\delta_{ij} \tag{2.64}$$

the deviatoric part is modeled as:

$$\tau_{ij} - \frac{1}{3}\tau_{kk}\delta_{ij} = \tau_{ij}^{D} = -2\bar{\rho}\nu_{sm}S_{ij}(\tilde{u}) \tag{2.65}$$

In compressible flows the trace of τ_{ij} is dominated by thermodynamic effects and is therefore absorbed into the filtered pressure rather than modeled explicitly. Historically, the Smagorinsky model was the first SGS closure proposed; the eddy viscosity depends on the filter width Δ and on the instantaneous energy flux across the cut-off, which may be written abstractly as:

$$\nu_{sm} = V_{sm}(\Delta, \dot{\varepsilon}) \tag{2.66}$$

A dimensional analysis in the inertial range, under the hypothesis of local spectral equilibrium ($\varepsilon_k = \varepsilon$), leads to:

$$\nu_{sm} \propto \varepsilon^{1/3}\Delta^{4/3} \tag{2.67}$$

Moreover, in the case of isotropic homogeneous turbulence, the rate of kinetic energy dissipation is evaluated as:

$$\varepsilon \propto \Delta^2|S(\tilde{u})|^3 \tag{2.68}$$

Assuming that the flow is in a situation of constant spectral equilibrium ($\varepsilon_1 = \tilde{\varepsilon} = \varepsilon$), and substituting Equation (2.68) into Equation (2.67) gives:

$$\nu_{sm} = (C_s\Delta)^2|S(\tilde{u})| \tag{2.69}$$

$$|S(\tilde{u})|^2 = 2S_{ij}(\tilde{u})S_{ij}(\tilde{u}) \tag{2.70}$$

The deviatoric SGS stress is then modeled by:

$$\tau_{ij} = -2\bar{\rho}(C_s\Delta)^2|S(\tilde{u})|S_{ij}(\tilde{u}) \tag{2.71}$$

The constant C_s is often adjusted to improve results; values around $C_s \cong 0.2$ are commonly reported in the literature (Bardina, Ferziger, & Reynolds, 1980; Pope, 2000).

The principal shortcoming of the constant coefficient Smagorinsky model is its excessive dissipation. Because the eddy viscosity depends solely on the resolved strain rate, regions with strong shear (large $|S|$) produce very large ν_{sm}, which can drain energy too rapidly, impede laminar–turbulent transition, and overdamp near-wall motions. Moreover, the model does not account for anisotropy of the sub-grid stresses, nor for possible backscatter (energy transfer

from sub-grid to resolved scales). These limitations motivate the use of dynamic, or hybrid formulations presented next.

The Smagorinsky component relies on a proportionality hypothesis between the SGS stress to be modeled and the resolved strain-rate tensor; it therefore represents mainly the dissipative effect of the unresolved scales on the resolved field, without attempting to reproduce the small-scale structure. In contrast, a structural approach seeks to model the SGS stress directly. Unlike the Smagorinsky model, it requires information about inter-filter interactions so that the organization of the small scales can be represented and the SGS tensor τ_{ij} can be approximated more faithfully.

The structural model adopted here follows the scale-similarity hypothesis of Liu–Meneveau–Katz (LMK). In this approach, the SGS tensor at the grid scale Δ is approximated by the stress built from the resolved field observed at two nearby filter levels. Let $\bar{(\cdot)}$ denote grid filtering at Δ and $\widehat{(\cdot)}$ a test filter of larger width $\widehat{\Delta} > \Delta$ (implemented with a compact 1–2–1 top-hat stencil in each Cartesian direction). For compressible LES, Favre filtering is employed, $\tilde{\phi} = \overline{\rho\phi}/\bar{\rho}$, and the isotropic trace of τ_{ij} is absorbed into the filtered pressure. Under these conventions, the deviatoric LMK approximation is written as:

$$\tau_{ij}^{LMK,D} = \left[(\widehat{\bar{\rho}\tilde{u}_i\tilde{u}_j}) - \frac{(\widehat{\overline{\rho u_i}})(\widehat{\overline{\rho u_j}})}{(\widehat{\bar{\rho}})} \right]_D \tag{2.72}$$

This term transfers structure from the test-filtered resolved field to the modeled SGS tensor and permits limited backscatter. The similarity idea traces to Bardina et al. (1980), with LMK providing experimental support and a multiband interpretation. The discrete (1–2–1) test filter and use of two levels of filtering follow standard dynamic LES practice. In compressible LES, density-weighted (Favre) filtering and the handling of the SGS trace via a modified pressure are standard; these conventions are used here.

To combine the correct dissipation level of eddy viscosity closures with the improved structural fidelity of similarity models, a mixed form is employed:

$$\tau_{ij}^{D} = \alpha\tau_{ij}^{LMK,D} - 2(1-\alpha)\bar{\rho}(C_s\Delta)^2|S(\tilde{u})|S_{ij}(\tilde{u}) \tag{2.73}$$

with:

$$S_{ij}(\tilde{u}) = \frac{1}{2}(\partial_i\tilde{u}_j + \partial_j\tilde{u}_i) \tag{2.74}$$

$$\lfloor S \rfloor = \sqrt{2S_{mn}S_{mn}} \tag{2.75}$$

$$\Delta = (\Delta x\Delta y\Delta z)^{1/3} \tag{2.76}$$

This "mixed" construction—similarity plus a dissipative Smagorinsky term—has been widely used; compressible generalizations formulate the similarity and eddy viscosity parts in Favre variables as written above (Winckelmans, Wray, & Vasilyev, 1998).

Typical constants used in practice are $C_s \approx 0.17 - 0.2$, and (unless otherwise stated) $\alpha = 0.5$ is adopted for equal weighting of structural and dissipative effects. Constant-coefficient Smagorinsky closures are known to be overly dissipative—particularly in strong-shear or near-wall regions—which motivates the mixed strategy used here (Lévêque, Toschi, Shao, & Bertoglio, 2007).

A compact 1–2–1 top-hat test filter is applied direction-wise (yielding $\hat{f}_i = \frac{1}{4}f_{i-1} + \frac{1}{2}f_i + \frac{1}{4}f_{i+1}$); the ratio $\hat{\Delta}/\Delta$ is chosen per the discrete filter's effective width and is larger than one (commonly around two in practice). Results are known to be only weakly sensitive to moderate changes of this ratio in dynamic-type formulations (Sagaut & Grohens, 1999).

2.2.2 Discretization & Numerical Scheme

This section presents the numerical methods used to solve the filtered Navier-Stokes equations (LES). The velocity, pressure, temperature and density variables are discretized on a Cartesian mesh of *m* nodes with:

$$\begin{gathered} m = m_1 \times m_2 \times m_3 \\ [x, y, z] = [x, y, z]\,(i, j, k) \\ i = 1, m_1 \\ j = 1, m_2 \\ k = 1, m_3 \end{gathered} \tag{2.77}$$

Spatial Discretization

Discretization of the Convective Terms: A compact scheme of order 6 is used for the discretization of the convective terms present in the equations of continuity, momentum, energy and water vapor. In order to facilitate reading, the direction *x* will be taken as a reference, the expressions of the derivatives remaining the same whatever the direction considered. For node i, the approximation of the first derivative, ϕ_i' , is written in the form:

$$\alpha\phi'_{i-1} + \phi'_i + \alpha\phi'_{i+1} = b\frac{\phi_{i+2} - \phi_{i-2}}{4h} + a\frac{\phi_{i+1} - \phi_{i-1}}{2h} \tag{2.78}$$

where h denotes the spatial step defined by:

$$h = x_{i+1} - x_{i-1} \tag{2.79}$$

The coefficients a, α and b are obtained by equalizing the coefficients of the truncated Taylor expansions of successive orders.

- **First case:** $3 \leq i \leq m_1 - 2 :\ \alpha = 1/3\,, a = 14/9\,, and\ b = 1/9$. The scheme is of order six and the truncation error is $4/7\,! \times h^6 \times \phi_i$.

- **Second case:** $i = 2\ and\ i = m_1 - 1$: $\alpha = 1/4\,, a = 3/2\,, and\ b = 0$. The scheme is of order four and the truncation error is $1/5\,! \times h^4 \times \phi_i$.
- **Third and fourth case:** $i = 1\ and\ i = m_1$:
  The processing of boundaries by a compact scheme can be done to order four, three or two. Among these three possibilities, we opted for the scheme of order three. Indeed, for the even-order schemes the truncation error is of dispersive type while, for the third-order scheme, it is dissipative. It should also be noted that the dissipative part of the error associated with the compact scheme of order three is concentrated at large wavenumbers.

  The approximation of the first derivative at node $i = 1$ is written:

$$\phi_1' + 2\phi_2' = 1/h\,[2\phi_2 + 0.5\phi_3 - 2.5\phi_1] \tag{2.80}$$

  The scheme is of order three and the truncation error is $1/12 \times h^3 \times u_1$. The approximation of the first derivative at node $i = m_1$ is written:

$$\phi_{m_1}' + 2\phi_{m_1-1}' = 1/h\,[2.5\phi_{m_1} - 2\phi_{m_1-1} - 0.5\phi_{m_1-2}] \tag{2.81}$$

  The scheme is of order three and the truncation error is $1/12 \times h^3 \times \phi_{m_1}$.

To minimize aliasing error (energy pile-up at high wavenumbers that can produce oscillations and degrade the solution), a semi-conservative formulation of the convective terms is used (Blaisdell, Spyropoulos, & Qin, 1996):

$$\frac{\partial(\rho_g^* q u^*)}{\partial x^*} = \frac{1}{2}\left[\frac{\partial(\rho_g^* q u^*)}{\partial x^*} + \rho_g^* q \frac{\partial u^*}{\partial x^*} + u^* \frac{\partial(\rho_g^* q)}{\partial x^*}\right] \tag{2.82}$$

where q denotes a scalar. Note that these schemes can also be used on non-uniform grids; Gamet, Ducros, Nicoud, and Poinsot (1999) describe a fourth-order compact scheme for such meshes.

Discretization of Water Vapor Transport (Convection–Diffusion): Normalizing the water vapor mass fraction defines the passive scalar Z bounded between 0 and 1. Treating the convection of a scalar is delicate because this quantity must remain bounded in [0,1]. In the presence of strong gradients, the use of a high-order scheme—such as a compact scheme—can produce non-physical oscillatory behavior (aliasing) (Tamamidis & Assanis, 1993).

As evidence, Stéphane Brunet (1999) performed a calculation using a compact scheme for scalar convection in a vortical velocity field. In this test, the tracer concentration profile was initialized as a Gaussian bounded between 0 and 1. Brunet observed that, during the simulation, the passive-scalar field showed negative values of order −0.1. Nevertheless, front-resolution problems can be remedied by using a flux limiter. In this context, Brunet carried out a comparative study and showed that the MSOU Superbee limiter (Monotonic Second-Order Upwind) (Sweby, 1984) offered the most suitable behaviour for the convection of a Gaussian and a square profile of a passive scalar in a vortical flow. For this reason, that limiter is employed here for the convective terms associated with the passive-scalar field. A very brief description of the principle of this limiter is recalled below. Comprehensive discussions of the Superbee limiter are provided in Hirsch (1990), Sweby (1984), and Tamamidis and Assanis (1993).

To simplify the explanation, a one-dimensional (1D) case is considered in the x direction. The convective term then takes the form:

$$\frac{\partial(\rho_g^* Z u^*)}{\partial x^*} \tag{2.83}$$

Using the finite-volume method, this expression can be approximated by:

$$\frac{(\rho_g^* Z u^*)_{i+1/2} - (\rho_g^* Z u^*)_{i-1/2}}{h} = \frac{F_{i+1/2} - F_{i-1/2}}{h} \tag{2.84}$$

Using the MSOU Superbee limiter, we obtain:

$$\begin{aligned} F_{i+1/2} = {} & \frac{(u_{i+1/2}^* + |u_{i+1/2}^*|)}{2}\left[(\rho_g^* Z)_i + \frac{1}{2}\left[(\rho_g^* Z)_i - (\rho_g^* Z u^*)_{i-1}\right]\varphi_{RC}(r_i^-)\right] \\ & + \frac{(u_{i+1/2}^* + |u_{i+1/2}^*|)}{2}\left[(\rho_g^* Z)_{i+1}\right. \\ & \left. - \frac{1}{2}\left[(\rho_g^* Z)_{i+2} - (\rho_g^* Z u^*)_{i+1}\right]\varphi_{RC}(r_i^+)\right] \end{aligned} \tag{2.85}$$

with:

$$u_{i+1/2}^* = \frac{1}{12}[-u_{i+2}^* + 7(u_{i+1}^* + u_i^*) - u_{i-1}^*] \tag{2.86}$$

$$r_i^- = \frac{(\rho_g^* Z)_{i+1} - (\rho_g^* Z)_i}{(\rho_g^* Z)_i - (\rho_g^* Z)_{i-1}} \tag{2.87}$$

$$r_i^+ = \frac{(\rho_g^* Z)_{i+1} - (\rho_g^* Z)_i}{(\rho_g^* Z)_{i+2} - (\rho_g^* Z)_{i+1}} \tag{2.88}$$

$$\varphi_{RC}(r) = \max(0, \min(2r, 1), \min(r, 2)) \tag{2.89}$$

Discretization of the Viscous Terms: The diffusive terms are discretized by a centered scheme of order two, and the first derivative is approximated as follows:

$$\frac{\partial \phi}{\partial x}(x_i) = \frac{\Delta_{i-1}/\Delta_i(\phi_{i+1} - \phi_i) + \Delta_{i-1}/\Delta_i(\phi_i - \phi_{i-1})}{\Delta_{i-1} + \Delta_i} \tag{2.90}$$

$$\Delta_{i-1} = x_i - x_{i-1} \tag{2.91}$$

These definitions make it possible to discretize the cross terms present in the diffusive part of the Navier-stokes equation such as $\frac{\partial}{\partial x_i}\mu\frac{\partial \phi}{\partial x_j}$ with $i \neq j$. However, for the case $i = j$, strong oscillations appear. Therefore, the following definitions are used:

If the mesh is constant:

$$\frac{\partial}{\partial x}\mu\frac{\partial \phi}{\partial x}(x_i) = \frac{1}{2\Delta_i^2}[(\mu_i + \mu_{i+1})\phi_{i+1} - 2\left(\mu_i + \frac{\mu_{i-1} - \mu_{i+1}}{2}\right)\phi_i + (\mu_{i-1} - \mu_i)\phi_{i-1}] \tag{2.92}$$

otherwise:

$$\frac{\partial}{\partial x}\mu\frac{\partial \phi}{\partial x}(x_i) = \frac{1}{\Delta_{i-1} + \Delta_i}[(\mu_{i+1} + \mu_i)\frac{\phi_{i+1} - \phi_i}{\Delta_i} - (\mu_{i-1} + \mu_i)\frac{\phi_i - \phi_{i-1}}{\Delta_{i-1}}] \tag{2.93}$$

The Equations (2.92) and (2.93) are second order as long as the stretching of the mesh remains weak between two consecutive meshes when one uses the expression (2.93).

Temporal Discretization

Temporal integration is done using a Runge-Kutta scheme of order three and requires only two storage arrays per variable. This scheme is easy to implement and it offers a good compromise between accuracy, stability, storage cost and computation time.

For the sake of readability, the equations are written in the symbolic form:

$$\frac{\partial \phi}{\partial t} = H(\phi) = -C(\phi) + D(\phi) - P(\phi) \tag{2.94}$$

where ϕ represents the conservative variables $[\rho, \rho u_i, E]^T$ and the operators C, D and P represent the convection, diffusion and pressure terms respectively. Taking n as the time increment, the Runge-Kutta scheme is written as follows:

$$\begin{aligned} \phi_0 &= \phi^n \\ \phi_1 &= \phi_0 + \gamma_1 \Delta t H_0 \qquad H_0 = H(\phi_0) \\ \phi_2 &= \phi_1 + \gamma_2 \Delta t H_1 \qquad H_1 = H(\phi_1) + \varepsilon_1 H_0 \\ \phi_3 &= \phi_2 + \gamma_3 \Delta t H_2 \qquad H_2 = H(\phi_2) + \varepsilon_2 H_1 \\ \phi^{n+1} &= \phi_3 \end{aligned} \tag{2.95}$$

To have an order three, the coefficients γ_k and ϵ_k must satisfy the following system:

$$\begin{aligned} \gamma_1 + \gamma_2(1+\varepsilon_1) + \gamma_3[1+\varepsilon_2(1+\varepsilon_1)] &= 1 \\ \gamma_1\gamma_2 + \gamma_3[\gamma_1 + (1+\varepsilon_2) + \gamma_2(1+\varepsilon_1)] &= 1/2 \\ \gamma_1^2\gamma_2 + \gamma_3[\gamma_1 + \gamma_2(1+\varepsilon_1)^2] + \gamma_1\gamma_3\varepsilon_2 &= 1/3 \\ \gamma_1\gamma_2\gamma_3 &= 1/6 \end{aligned} \tag{2.96}$$

The values recommended by Maglaras (2007) (low memory footprint method) are:

$$\begin{aligned} \gamma_1 &= \frac{1}{2} \\ \gamma_2 &= 0.9106836025229591 \\ \gamma_3 &= 0.3660254037844387 \\ \varepsilon_1 &= -0.6830127018922193 \\ \varepsilon_2 &= -4/3 \end{aligned} \tag{2.97}$$

The Courant number or the Courant-Fredrichs-Levy (CFL) condition is used to establish the stability of a numerical scheme. In the case of the study, the stability is given by the following condition:

$$\Delta t \leq \left(\frac{|u_1|}{\Delta x} + \frac{|u_2|}{\Delta y} + \frac{|u_3|}{\Delta z} + \frac{1}{M}\sqrt{\frac{1}{\Delta_x^2} + \frac{1}{\Delta_y^2} + \frac{1}{\Delta_z^2}}\right)^{-1} \tag{2.98}$$

2.2.3 Particle Microphysics Algorithm

Before introducing the microphysical formulations, several simplifying hypotheses are adopted to reduce the computational complexity while preserving the essential physics of the problem:

1. Gravitational effects are neglected in both the gas and particle phases, since buoyancy and sedimentation forces are insignificant compared with inertial and aerodynamic forces in the high Reynolds number jet flow.
2. Chemical reactions were not included in the microphysical model. The scheme accounts only for water-phase mass and heat transfer (condensation/evaporation and deposition/sublimation) around inert particles, without gas-phase chemistry or heterogeneous reactions.
3. Particle–particle interactions and hydrodynamic coupling are ignored because the suspension is highly dilute; the low number concentration ensures that collisions, coagulation/aggregation, and mutual flow disturbances between particles are negligible. Each particle therefore evolves independently within the carrier-phase fields.
4. Condensation and evaporation kinetics are treated under the quasi-steady assumption. The rate of mass transfer at the particle surface is small compared with the characteristic flow timescale, allowing the droplet growth (or sublimation) to be modeled as a steady diffusion process around each particle.
5. In our contrail microphysics, soot nuclei and entrained ambient aerosol are represented as spherical particles, so that surface area and growth depend only on particle radius, following common practice in near-field contrail modeling.

Calculation of the Position of the Particles

It should be remembered that the particles are followed by a Lagrangian approach, which assumes that their position does not necessarily correspond to one of the points of the mesh. However, the velocity, the temperature, the pressure and the quantity of vapor are calculated at the nodes of the mesh. The first part consists in seeking the mesh in which the particle is located then an interpolation of the known parameters at the nodes of the mesh is made. As a reminder, Equation (2.18) is to be solved, and the particle velocity is now known. To solve this equation, the Adams-Bashforth multipoint method of sixth-order is used. For ease of reading, the 1D formula of the equation is used:

$$\frac{dx}{dt} = u \tag{2.99}$$

It should be noted that the position *x* at a given time t_n, $x(t_n)$, is written x^n in index format. The position of the particle at time *n+1* is calculated by:

$$x^{n+1} = x^n + \frac{\Delta t}{1440}(4277u^{n-1} - 7923u^{n-2} + 9982u^{n-3} - 7298u^{n-4} + 2877u^{n-5} - 475\,u^{n-6}) \tag{2.100}$$

At the time of the first moments of computation, the scheme order is reduced because there are no prior existing values to populate all stages.

The update is applied component-wise to $X_p = (x_p, y_p, z_p)$, with u_p the particle velocity obtained in the previous step (equal to the carrier velocity in the passive-tracer limit). At each time level, the host cell is located, and the required Eulerian fields are interpolated at X_p (trilinear on the containing hexahedron; bilinear in 2D). The sixth-order Adams–Bashforth scheme is used with a constant time step Δt; during start-up the order is degraded (Euler → AB2 → AB3 → AB4 → AB5) until a full history of velocities is available. To avoid particles skipping cells, Δt is chosen so that $\|u_p\|\Delta t \leq \min(\Delta x, \Delta y, \Delta z)$; otherwise, sub-stepping is applied. Boundary handling follows the Eulerian setup: directions treated as periodic cause

wrap-around, whereas open/non-reflecting boundaries allow particles to exit and be removed from the active list. The velocity history is updated after each advance and reinitialized for injected or reseeded particles.

Thermodynamic Parameters: Computational Strategy

Given the local gas state, particle type, and properties, the main steps for calculating the thermodynamic properties are as follows:

- **Vapor state:** The vapor partial pressure was obtained as $P_v = X_v P$. Saturation vapor pressures over ice and liquid were then evaluated from standard correlations (Murphy & Koop, 2005) and the ratios:

$$S_{ice} = \frac{P_v}{P_{sat}^{ice}(T)}, \qquad S_{liq} = \frac{P_v}{P_{sat}^{liq}(T)} \tag{2.101}$$

  were formed. These ratios denote the local saturation with respect to ice and liquid water, respectively; they were computed irrespective of the particle's current phase, and the appropriate reference was selected after the phase diagnosis.
- **Phase selection:** The condensed phase (ice or liquid) was determined from a freezing criterion based on the instantaneous cooling rate and droplet volume ($T < T^*(\dot{T}, V)$); properties for the diagnosed phase were used thereafter. Equilibrium supersaturation (κ–Köhler) For the selected phase, the equilibrium supersaturation at wet radius was computed as:

$$S_{eq}(r_p) = \frac{{r_p}^3 - {r_d}^3}{{r_p}^3 - {r_d}^3(1-\kappa)} \exp\left(\frac{2\sigma(T)\, M_v}{\rho(T)\, R\, T\, r_p}\right) \tag{2.102}$$

  with r_d the dry-core radius and κ the hygroscopicity assigned by nucleus type.
  Consistent with the κ –Köhler equilibrium, the sign of the growth rate is governed by the departure of the local supersaturation from its equilibrium value; rewriting Equation (2.21) gives:

$$\frac{dr_p}{dt} = \frac{D_v\, M_v}{r_P R T_P \rho_P} f_{3\beta} P_{sat}^{phase}(T)\left[S - S_{eq}(T)\right] \tag{2.103}$$

Hence, growth/condensation occurs for $S > S_{eq}$, evaporation/sublimation for $S < S_{eq}$, and the radius is steady for $S = S_{eq}$ (with "evaporation" or "sublimation" determined by the diagnosed phase).

- **Thermophysical properties:** Phase-consistent temperature-dependent fits were used to obtain the latent heat $H_v(T)$ (vaporization or sublimation), condensed-phase density $\rho(T)$, surface tension $\sigma(T)$, vapor diffusivity $D_v(T, P)$, and gas (and, for ice, solid) thermal conductivity $k_g(T)[k_i(T)]$.

The outputs $\{P_{sat}, S, S_{eq}, H_v, \rho, \sigma, D_v, k_g(, k_i)\}$ are used for the growth step evaluating consistently with the diagnosed phase and nucleus type.

Solving the Particle Growth Model

To solve the particle growth equation (Equation (2.103)), the Runge-Kutta fourth-order method is used. With H_Φ denoting the right-hand side of Equation (2.103), the scheme is:

$$\begin{aligned} \Phi_0 &= \Phi^n \\ \Phi_1 &= \Phi_0 + \gamma_1 \Delta t_P H_0 \\ \Phi_2 &= \Phi_1 + \gamma_2 \Delta t_P H_1 \\ \Phi_3 &= \Phi_2 + \gamma_3 \Delta t_P H_2 \\ \Phi_4 &= \Phi_3 + \gamma_4 \Delta t_P H_3 \\ \Phi^{n+1} &= \Phi_4 \end{aligned} \tag{2.104}$$

With:

$$\begin{aligned} \gamma_1 &= 1/6 \\ \gamma_2 &= 1/3 \end{aligned} \tag{2.105}$$

$$\gamma_3 = 1/3$$
$$\gamma_4 = 1/6$$

It should be noted that the time step stability (CFL) used for the Navier–Stokes equations need not be satisfied for the particle update. For this, the stability limit of the resolution of the Fukuta-Walter equation is given by:

$$\Delta t \leq \bar{r}^2 r_P^2 L_0 U_0 \left(\frac{S_{eq}\frac{L^2 M_v \rho_P}{k_g R T_P^2 f_{3\alpha}} + \frac{R T_P \rho_P}{P_{sat} D_v M_v f_{3\beta}}}{\left|S - S_{eq}\right|}\right) \tag{2.106}$$

In the case where the time step to calculate the fluid part does not respect this last condition, a time step relative to the particles is introduced such that:

$$n.\Delta t_p = \Delta t \tag{2.107}$$

and a displacement constraint that prevents particles from skipping cells:

$$\Delta t_{p,adv} = C_{disp}\frac{\min\left(\Delta x, \Delta y, \Delta z\right)}{\left\|u_p\right\|} \tag{2.108}$$

with $C_{disp} \leq 1$ and u_p the particle velocity (equal to gas velocity in the tracer limit). Here n is an integer and corresponds to the number of particle sub-iterations performed per fluid step. Within each fluid step, the gas fields are frozen; thermodynamic properties are recomputed at every particle sub-step.

Coupling Strategies: 3D Online vs 0D Offline

Two complementary approaches were employed to couple plume dynamics with particle microphysics that share the same κ-Köhler activation, condensational growth/sublimation, and freezing scheme.

- **3D Online:** In FludiLES, Lagrangian particle parcels exchange mass and heat with the gas each LES time step. The parcel growth law gives a per-parcel mass rate dm_p/dt; the corresponding cell-wise vapor sink/source $\omega_v(x,t)$ is added to the water vapor transport equation and the latent heat term $\dot{q}_\ell = L_s(T_{p,s})\, dm_p/dt$ to the energy equation. This will be explained in detail in Section 2.2.4. This resolves spatial heterogeneity, inter-parcel competition for vapor, and feedback (vapor-sink and latent-heat) that can suppress later activation or even deactivate droplets—processes that depend on local mixing and cannot be represented by a single plume-mean trajectory.
- **0D Offline:** A companion temporal LES without microphysics is run to diagnose plume-mean drivers: temperature $\bar{T}_p(t)$ and dilution/entrainment rate $\mathcal{D}(t)$ (via a passive exhaust tracer). These histories are stored on the LES time grid and subsequently drive a time-dependent 0D box model that integrates the same microphysics as online. Gas-phase tendencies follow:

$$\frac{dY_v}{dt} = \frac{\omega_v}{\rho_g} \tag{2.109}$$

$$\frac{dT}{dt} = \frac{\dot{q}_\ell}{(\rho_g c_p)} \tag{2.110}$$

with ω_v and $\dot{q}_\ell$ assembled from the parcel growth law; no spatial transport or feedback to the flow is applied. The box model thus isolates microphysics at plume-mean conditions and enables fast parametric sweeps, but it omits sub-grid variability, inter-parcel mixing, and vapor-sink feedback.

2.2.4 Coupling Term

In the present work, the gas phase (air water vapor mixture) is advanced on an Eulerian grid, while particles are followed in a Lagrangian framework. The interphase interaction is introduced exclusively through right-hand-side source terms in the gas conservation laws, built from per-particle microphysical rates evaluated along trajectories inside a control volume V

containing N particles. Particles are assumed in dynamic and thermal equilibrium with the filtered gas fields, so that their velocity and temperature equal the local gas values; this justifies omitting momentum coupling in the present work.

Water vapor (mass transfer)

Accounting for phase change at particles, the water vapor conservation reads:

$$\frac{\partial \rho_v}{\partial t} + \nabla.(\rho_v u) + \nabla.J_v = -n\dot{m} \tag{2.111}$$

with $\rho_v = \rho_g Y$ the vapor density, J_v the vapor diffusive flux, n the local number density of particles, and $\dot{m}$ the single-particle mass variation rate due to condensation/evaporation. The diffusive flux is modeled as:

$$J_v = -\rho_g D_v \nabla Y_v \tag{2.112}$$

where D_v is the water vapor diffusivity in the gas.

The sign of $\dot{m}$ is consistent with the total-mass and vapor equations: condensation increases particle mass ($\dot{m} > 0$) and removes mass from the gas phase ($-n\dot{m}$).

Energy (latent & sensible exchange)

The total-energy balance of the gas includes interphase heat exchange and the enthalpy carried by the mass flux at the particle surface. In compact form:

$$\frac{\partial E_g}{\partial t} + \nabla.\left(E_g u + q_g\right) - \nabla.(\sigma u) = -VF_{tr} - n\dot{Q} - n\,\dot{m}\,h_{v,S} \tag{2.113}$$

where:

$$q_g = -k_g \nabla T_g + (h_v - h_a)\, J_v \tag{2.114}$$

$$J_v = -\rho_g D_v \nabla Y_v \tag{2.115}$$

q_g is the heat flux, $h_{v,S}$ denotes the vapor enthalpy at the particle surface, and $\dot{Q}$ characterizes sensible heat exchange between a particle and the gas (often expressed via a Nusselt correlation). In our regime, the momentum-exchange work term VF_{tr} is not retained (dynamic equilibrium), while the latent and sensible energy terms are kept but remain moderate because (i) the vapor mass fraction is small, $Y_v < 0.02$, so $r_g \cong r_a$ and $C_{p,g} \cong C_{p,a}$, and (ii) thermal Stokes numbers are small, driving $T_p \cong T_g$.

Discrete (cell-based) assembly of coupling source terms

Each numerical particle represents n_{trans} physical particles (parcel multiplicity). Denote by $\mathcal{P}_i$ the set of parcels whose support deposits into cell i of volume V_i. Over one time step, the volumetric source terms injected into the Eulerian scalars are formed as:

$$\Omega_{Y_v}^{(i)} = -\frac{1}{V_i} \sum_{p \in \mathcal{P}_i} n_{trans,p}\, \dot{m}_p\, W(x_i - x_p) \tag{2.116}$$

$$\Omega_E^{(i)} = -\frac{1}{V_i} \sum_{p \in \mathcal{P}_i} n_{trans,p}\, (\dot{Q}_p + \dot{m}_p h_{v,S,p})\, W(x_i - x_p) \tag{2.117}$$

where W is a partition-of-unity deposition kernel (e.g. NGP or trilinear CIC on the Cartesian mesh). These formulas are the discrete counterparts of the control-volume balances where the coupling terms appear on the right-hand side. The per-parcel $\dot{m}_p$ comes from the microphysical growth law. The $\dot{Q}_p$ is per-particle sensible heat exchange rate. These depositions guarantee global conservation of vapor mass and of energy (latent+sensible) provided the same n_{trans} and the same kernel W are used consistently for every parcel, and the gas equations are advanced with the assembled Ω-terms.

Time integration and operator split

At each gas time step $t^n \rightarrow t^{n+1}$, coupling is advanced by the following operator-split sequence (all steps in passive form):

1. Sampling: Gas fields required by microphysics (e.g. T_g, Y_v, ρ_g) are evaluated at particle positions by grid interpolation. Dynamic/thermal equilibrium implies $v_p = u_g$ and $T_p = T_g$.
2. Microphysics update (Lagrangian): Each parcel's growth law is integrated to obtain $\dot{m}_p$ (and, where used, $\dot{Q}_p$) over $[t^n, t^{n+1}]$.
3. Deposition (Eulerian): Mass and energy sources $\Omega_{Y_v}^{(i)}$ and $\Omega_E^{(i)}$ are assembled using the parcel multiplicity n_{trans}.
4. Scalar updates: The vapor and energy equations are advanced with the sources and with diffusive/convective fluxes, using the existing solver and time integrator. The flux definitions of Equation (2.113) and below that are retained.

2.2.5 Computational Framework & Setup

2.2.5.1 FludiLES Architecture & Modules

FludiLES is a high-order (sixth order in space; third order in time) compressible CFD code for solving the Navier–Stokes equations, supporting both DNS and LES, and was developed from the PEGASE code (Stéphane Brunet, 1999; Cécile Ferreira Gago, 2002). FludiLES was developed for contrail studies, resolving the high-Reynolds-number jet and the ensuing jet–vortex interaction, with wake roll-up represented via a Lamb–Oseen initialization. Contrail ice-particle microphysics is incorporated into FludiLES through an online Lagrangian module. Originally implemented for soot particles, the module has been progressively refined and, in the present study, extended to include ambient aerosol as a second particle class. Gas–microphysics coupling is performed primarily within the LES framework, as coupling to DNS would be computationally prohibitive. The variables in FludiLES are non-dimensionalized; the

gas follows the ideal-gas law, and dynamic viscosity depends on temperature via a power law (Sutherland-type).

The solver workflow is outlined next, proceeding from core discretization to user-level controls and outputs:

Numerical methods & stability

Users select the order for diffusive-term discretization (second-order or a higher-order compact option). Time stepping must respect a CFL stability guideline (typically 0.6), with an example expression linking the time step to the smallest grid spacing and the Mach number.

Run configuration (high-level switches)

A single input file controls: DNS vs LES, diffusive-scheme order, activation of a selection function for sub-grid modeling, optional hybridization (for momentum, temperature, or passive scalar), choice of sub-grid model (Smagorinsky or Mixed-Scale), anisotropic cutoff correction, and an optional Bardina term. A consistency rule applies: when the Bardina option is enabled, hybridization flags must be off.

Initialization, restart & checkpointing

Runs may start fresh or resume from prior states. A configurable write interval produces 3D binary snapshots (“fort.101”, “fort.102”, …) plus a rolling latest snapshot, enabling long integrations with periodic data extraction and safe restarts.

Physical & control parameters

Key non-dimensional inputs include Reynolds, Mach, Prandtl, and Richardson numbers; users also set the total number of time steps, and the time step itself (bounded by the chosen CFL ceiling).

LES framework (filtering & cutoff length)

For compressible LES, variables use Favre (density-weighted) filtering. The filter length can be defined isotropically from grid spacings or by an anisotropic expression suited to stretched meshes; both definitions are available in the implementation.

Sub-grid scale (SGS) modeling

Two SGS options are provided:

- Smagorinsky: an eddy-viscosity model based on the magnitude of the resolved strain-rate tensor and the filter length.
- Mixed-Scale: combines energy- and structure-based measures (e.g., velocity-fluctuation energy and resolved gradients) to form the eddy viscosity.

In-run statistics & diagnostics

Users can compute running means/RMS after flow stabilization (with a one-step initialization followed by accumulation) and optionally streamwise "Vreman-type" averages. These are toggled independently in the input.

Spectral probes

A Fast Fourier Transform (FFT)-based probe performs spectral analysis along the periodic streamwise (*y*) direction. The number of retained modes (*npfilt*) must be a power of two and should be chosen as close as possible to—ideally equal to—the grid-point count in that direction.

Output & post-processing

During a run, 1D/2D field files and 3D snapshots are produced; a separate post-processor reads these binaries and exports Tecplot or CGNS files. It can also extract fixed planes or full 3D fields by specifying a "subzone" (I/J/K) or "none" for full volumes.

Figure 2.1 presents a high-level schematic of the FludiLES architecture and workflow described above.

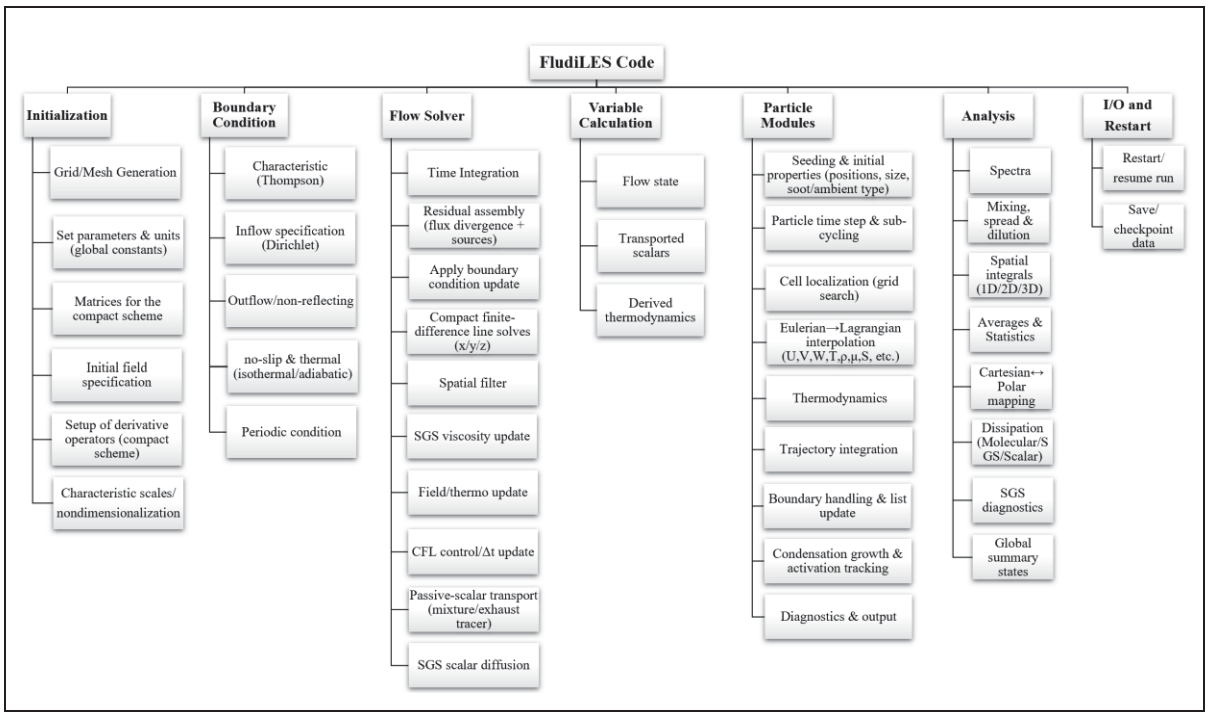

Figure 2.1 A schematic of the FludiLES code architecture and workflow

2.2.5.2 Domain & Mesh

A Cartesian, structured mesh is employed with the jet aligned to the y-direction and the cross-stream plane (x, y). All lengths are non-dimensionalized by the jet radius r_j. The computational domain spans (L_x, L_y, L_z) in units of r_j. A uniform-resolution core of width L_{reg} is discretized with $\Delta = \Delta_x = \Delta_y = \Delta_z$ (here, $\Delta = 0.15 r_j$); outside this region, optional mesh stretching can be used to limit the overall size, however in all cases of this thesis, the regular mesh without stretching used. Figure 2.2 presents a representative regular mesh; the example shown illustrates the spatial and temporal configurations.

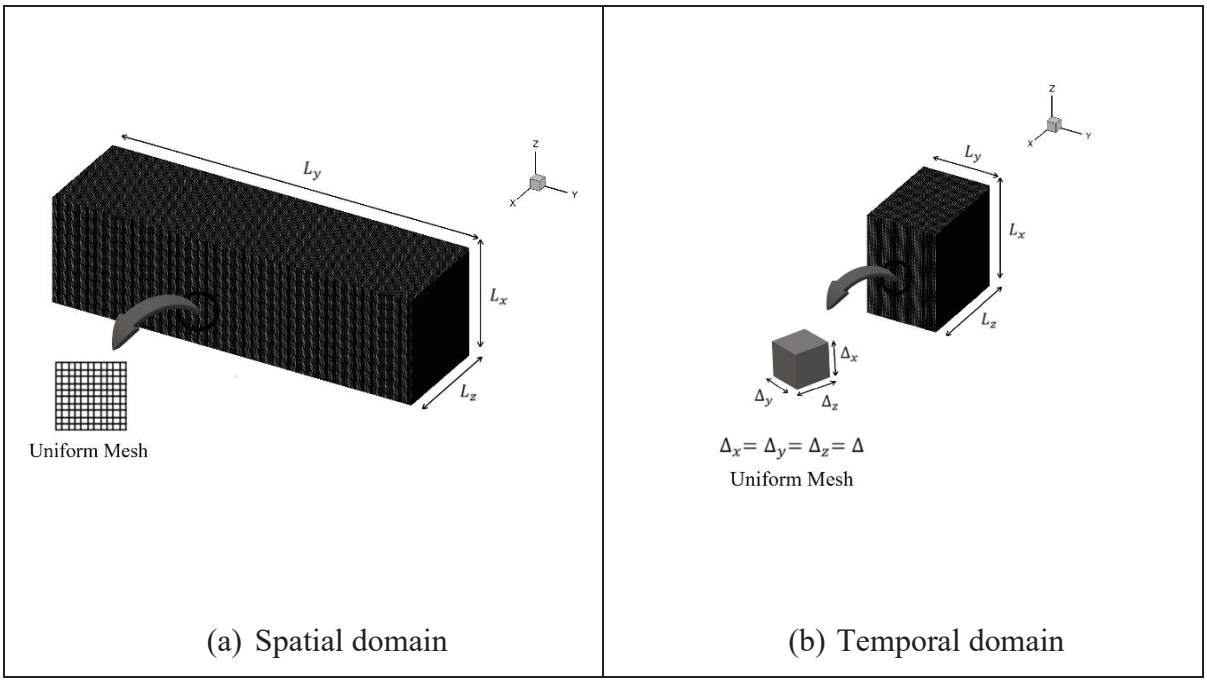

(a) Spatial domain (b) Temporal domain

Figure 2.2 The computational domains for both modeling strategies. Both are discretized with a uniform Cartesian mesh of cubic cells

With uniform spacing Δ, the node counts (m_1, m_2, m_3) were chosen to satisfy $m_i \approx L_i/\Delta + 1$ based on the domain extents, and grid independence was verified. For the mesh-refinement study, the streamwise resolution m_2 was increased in some cases until the solution met the convergence criteria.

In the temporal formulation, the streamwise domain is truncated; consequently, L_y and m_2 are set to roughly one-twelfth of the values used in the spatial formulation, where L_y (and thus m_2) is determined by the downstream extent to be modeled, from the inflow to the farthest measurement plane.

Mesh adequacy was appraised from the kinetic-energy spectrum E(k) for all cases; as an example, Figure 2.3 presents the spectra for the CFM56, LEAP, and UHBR engines. In LES, acceptable resolution is indicated when an inertial subrange follows Kolmogorov's law, $E(k) = C_k \varepsilon^{2/3} k^{-5/3}$ (with $C_k \approx 1.5$; ε mean dissipation rate; k wavenumber magnitude)

(Pope, 2000), and when the spectra steepen at high k, consistent with the expected grid cut-off $k_{max} \approx \pi/\Delta$ (with Δ the effective grid/filter scale). In Figure 2.3 the curves display a segment quasi-parallel to the $-5/3$ reference and a pronounced high-k decay, indicating sufficient inertial-range coverage for inter-engine comparison. Furthermore, differences in level are attributed to turbulence intensity rather than mesh bias.

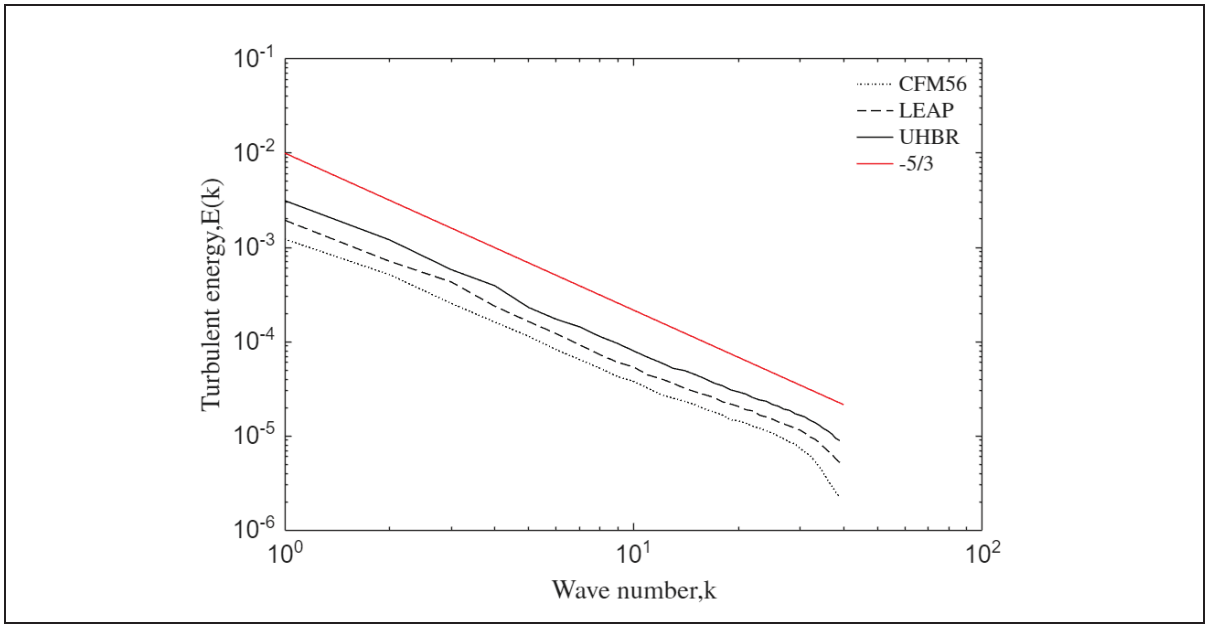

Figure 2.3 Turbulent kinetic energy spectra for the CFM56, LEAP and UHBR engine configurations

To sample the temporal jet into the temporal domain that contains both the jet and the vortex, the global domain extents (L_x, L_y, L_z) are chosen to be identical to the larger wake box. The size of this extended domain was defined as a rectangular box of $42r_c \times 6r_c \times 42r_c$ (as shown in Figure 2.4) where r_c is the Lamb–Oseen vortex core radius (distance from the vortex center to the peak azimuthal velocity).

A jet subdomain is then defined for the hand-off. In practice, the subdomain spans the full cross-stream extents as below while the streamwise extent is truncated to the sampling window:

$$L_{xj}^{min} = -\frac{L_x}{2}, \quad L_{xj}^{max} = +\frac{L_x}{2}$$
$$L_{zj}^{min} = -\frac{L_z}{2}, \quad L_{zj}^{max} = +\frac{L_z}{2} \tag{2.118}$$
$$L_{yj}^{min} = 0, \quad L_{yj}^{max} = +L_y$$

The jet axis is positioned at $(x_{jet}, z_{jet}) \neq 0$ to reflect the seeding/location choice, whereas the Lamb–Oseen vortex pair is centered at the origin of the large box. As illustrated in Figure 2.4, the jet subdomain (dashed inner box) spans the full cross-stream extents of the larger wake/interaction domain, with the streamwise window truncated for sampling; the Lamb–Oseen vortex pair is centered at the box origin, while the jet axis is offset by (x_{jet}, z_{jet}).

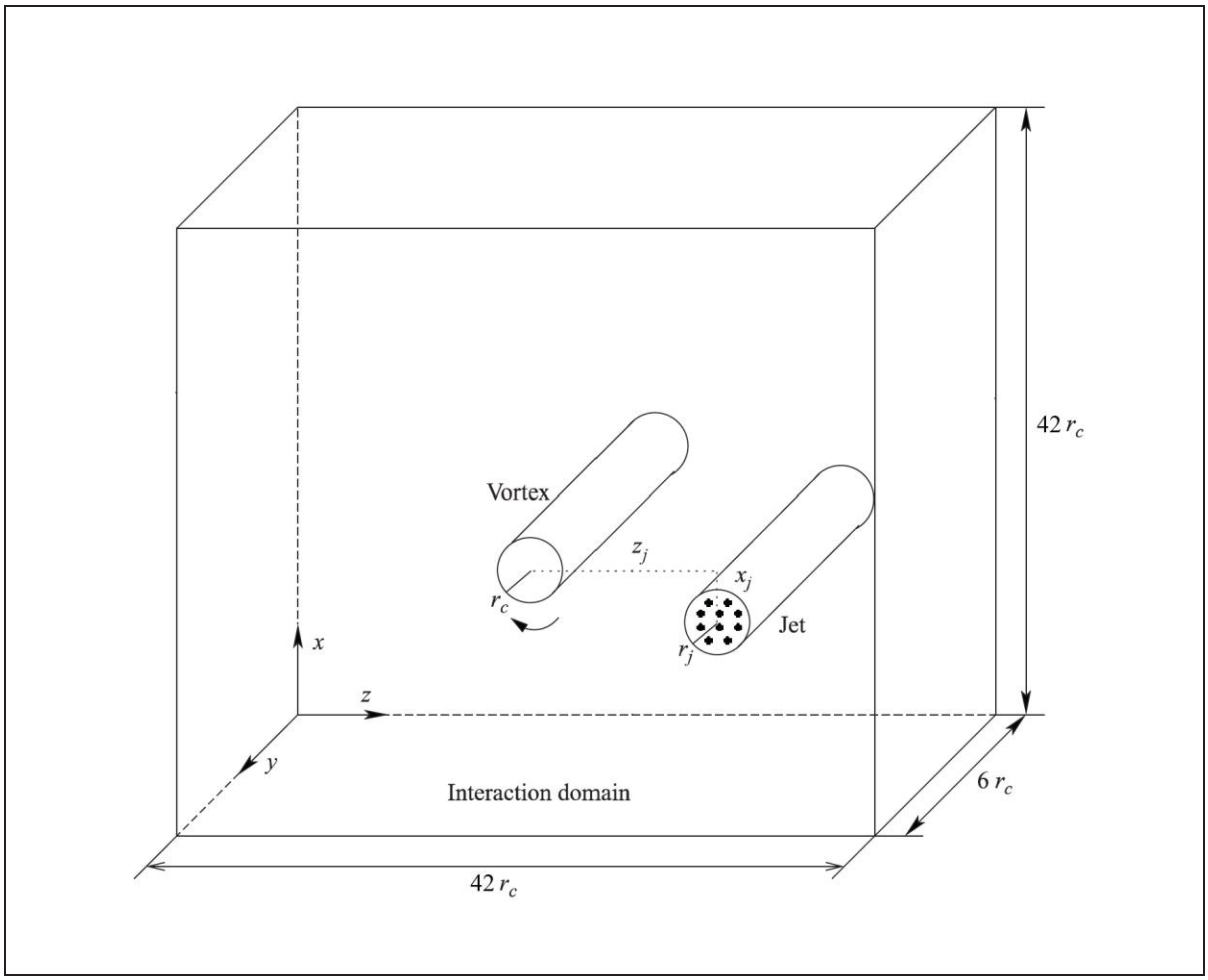

Figure 2.4 Sketch of the computational domains for the jet and the interaction phases

Adapted from Roberto Paoli et al. (2004, p. 6)

To use a spatial jet as the initial condition for a temporal jet–vortex calculation, a full spatial simulation is first advanced to a (quasi) self-similar state. A streamwise sampling window—matched to the temporal wake domain length—is then extracted by selecting a segment of $m_{2,sp}$ points from the spatial solution and centering it within the temporal grid of m_2 points:

$$j_{start,sp} = \frac{m_2 - m_{2,sp}}{2} + 1, \quad j_{end,sp} = j_{start,sp} + m_{2,sp} - 1 \tag{2.119}$$

so that the embedded spatial segment aligns with the periodic y-grid. At the sampling time t_s, the selected spatial-jet segment is inserted into the temporal wake box (same as Figure 2.4), a Lamb–Oseen vortex pair is superposed to initialize the vortex phase, and the subsequent evolution proceeds with periodicity in y.

2.2.5.3 Initialization

Flow field initialization

Dynamic initialization of the flow field is performed on a computational domain oriented with the streamwise axis along y and the cross-stream plane (x, z). All primitive and conserved variables are initialized in non-dimensional form using the reference scales $(U_0, T_{0,ref}, \rho_0, P_0, C_{p,0})$ defined in the solver parameters. In all cases, the reference length is the radius R, defined as the position at the middle of the jet shear layer such that $U(R) = (U(0) + U_\infty)/2$, where $U(0)$ is the jet centerline velocity. The reference temperature is the initial jet temperature $T_{0,ref} = T_{0,j}$. The Reynolds and Mach numbers are based on these reference quantities.

For parameters required to initialize the flow field in each case, the jet/ambient static temperatures $(T_{0,j}, T_{amb})$, reference temperature $T_{0,ref}$, jet and ambient speeds $(U_{0,j}, U_\infty)$, swirl magnitude U_θ, non-dimensional core radius r_c, specific heat ratio γ, Mach number *M*, and Prandtl number are user inputs. The shear-layer location (half-velocity radius) and thickness enter through the internal non-dimensional radial coordinate $\xi(r)$, which is used consistently for both velocity and temperature transitions.

The ideal-gas relation and a tabulated/functional enthalpy $h(T)$ are used to ensure thermodynamic consistency at $t = 0$. The time variable can be either the physical time (in seconds) or the dimensionless time t/t_0, depending on the need. In each case, the reference time is calculated using the reference length and velocity, defined as:

$$t_0 = \frac{R}{\sqrt{M/\gamma}\, RT_j} \tag{2.120}$$

where γ can be defined as c_P/c_v. A uniform ambient state is first prescribed. The static temperature is set to the ambient value T_{amb} (normalized by $T_{0,ref}$), and the static pressure is initialized uniformly consistent with the chosen reference M and γ (uniform $P = 1/(\gamma M^2)$ in non-dimensional form).

We consider a jet issuing from a nozzle of radius r_j with axial velocity u_j into a surrounding fluid whose axial velocity is u_a. The region near the nozzle is commonly called the potential-core region. In this region, the jet core coincides with a nucleus of fluid whose axial velocity remains equal to u_j. The flow therefore resembles an axisymmetric mixing layer between two streams of respective velocities u_j and u_a. A unidirectional flow, whose velocity profile corresponds to the region of the potential core, is considered. This velocity profile is of the "top-hat" type, which closely follows a hyperbolic tangent law, commonly used for stability calculations. The temperature profile is initialized using the Crocco–Busemann law (Schlichting & Gersten, 2017):

$$u_y(r) = U_{amb} + \frac{1}{2}(U_{0,j} - U_{amb})[1 - \tanh \xi(r)] \tag{2.121}$$

$$T(r) = T_{amb} + \frac{1}{2}(T_{0,j} - T_{amb})[1 - \tanh \xi(r)] \tag{2.122}$$

Here $\xi(r)$ is a non-dimensionalized radial coordinate that centers the transition around the half-velocity radius and controls the shear-layer thickness (the same control is used internally for the temperature transition). For cases configured with a bypass-like profile, Gaussian envelopes are used for optional auxiliary radial distributions (e.g., for a passive scalar marker). The cross-stream velocities are initialized with a small 3D perturbation scaled by the local axial profile and if swirl is enabled, an azimuthal field $u_x = zc_2(r)$, $u_z = -xc_2(r)$ is superposed; the streamwise component remains $u_y(r) = U_j(r)$ (with perturbations).

An azimuthal component is superimposed to represent a weak initial swirl of magnitude u_θ. In cylindrical coordinates the tangential speed is prescribed as a regularized solid-body core that decays smoothly outside a non-dimensional core radius r_c:

$$u_\theta(r) \propto \frac{r_c}{r}(1 - exp[-\beta(r/r_c)^2] \tag{2.123}$$

with $\beta > 1$ a decay constant. This field is mapped to Cartesian components as $u_x = u_\theta \sin\phi$ and as $u_z = -u_\theta \cos\phi$; so it can be said that the $c_2(r) = u_\theta(r)/r$.

Building on this baseline, two spatial jet–initialization strategies were employed to introduce the jet smoothly along the streamwise direction y. In both cases, the radial transition is controlled by the non-dimensional coordinate $\xi(r)$ (implemented as $qsi \propto (\frac{r}{R} - \frac{R}{r})$), which shapes the hyperbolic-tangent velocity and temperature profiles in (x, z) at every y. A streamwise blending function:

$$F(y) = \frac{1}{2}[1 - \tanh(a(y_{tr} - y))] \tag{2.124}$$

is used wherever a gradual ramp from ambient toward the target jet state is required. The Crocco–Busemann relation is applied for temperature (with optional core/bypass blending), and density is set consistently via the ideal gas closure. Small 3D perturbations are added with compact radial envelopes, as described earlier.

In the first spatial initialization strategy, the jet develops spatially from near-ambient conditions: the axial velocity and temperature are blended from ambient to their cylindrical target profiles using $F(y)$. Concretely, the code forms the Crocco–Busemann temperature for the core/bypass and then applies the streamwise ramp:

$$T(x,y,z) \leftarrow F(y)T_{CB}(r) + [1 - F(y)]T_{\infty} \tag{2.125}$$

and the axial velocity receives the same $F(y)$ blending (with superposed small fluctuations). The passive scalar (jet marker) is initialized with a smooth radial *tanh* profile to aid diagnostics of dilution and nominal radius; it does not introduce discontinuities and can be treated as optional for the dynamics.

In the second spatial initialization strategy, the axial velocity is ramped exactly as in the first strategy using the same $F(y)$, while the thermodynamic and marker fields are imposed cylindrically at $t = 0$ across the domain: $T(x,z,0) = T_{CB}(r)$ and $Z(x,z,0) = Z_j(r)$ everywhere. The initial mismatch between momentum and thermodynamics relaxes naturally as the velocity field grows, and the solution converges to a self-consistent jet/wake state without streamwise transients.

To trigger shear-layer transition without introducing spurious transients, low-amplitude pseudo-random perturbations are superposed on the initialized mean field. Let $r = \sqrt{(x - x_{jet})^2 + (z - z_{jet})^2}$ be the radial distance from the jet axis, and θ a thickness parameter. Independent pseudo-random deviates are generated at each grid point and for each velocity component as:

$$f_i(x) = 2 \times randome_{number} - 1 \in [-1,1], \qquad i \in \{x,y,z\} \tag{2.126}$$

this yields one turbulence realization of the fluctuation field. Two Gaussian-type envelopes weight the perturbations and confine them to the shear layer:

$$G_{\perp}(r) = \left[\exp\left(-\frac{1}{4\theta}\left(\frac{r}{R} - \frac{R}{r}\right)^2\right)\right]^{1/2} \tag{2.127}$$

$$G_{\parallel}(r) = \left[0.95\exp\left(-\frac{1}{4\theta}\left(\frac{r}{R} - R\right)^2\right) + 0.05(1 - U(r))\right]^{1/2} \tag{2.128}$$

where $U(r)$ is the non-dimensional mean axial profile (unity in the jet core and approaching zero in the ambient). With a chosen amplitude A (fraction of a reference speed U_{ref}), the component-wise perturbations are:

$$u_x' = AU_{ref} f_x G_\perp(r), \qquad u_z' = AU_{ref} f_z G_\perp(r), \qquad u_y' = AU_{ref} f_y G_\parallel(r) \tag{2.129}$$

and the initialized field is updated as $u_i + u_i' \to u_i$. The envelopes peak near $r \approx R$ and decay toward both the jet axis and the far field, ensuring negligible perturbations outside the shear layer. Independent f_x, f_y, f_z yield zero-mean, uncorrelated disturbances, so that no net momentum bias is introduced at $t = 0$.

Thus, in this setup the exit turbulence intensity is measured as $TI(r) = u_{rms}'(r)/U_{ref}$ and scales approximately as:

$$TI(r) \approx A\, \sigma_f\, G_n(r) \tag{2.130}$$

where:

$$\sigma_f = RMS\{filtered\ f_i\} \tag{2.131}$$

Consequently, $TI(r)$ varies with radius, scales approximately with the imposed amplitude A and depends on the chosen turbulence realization to shape the random field for a specific velocity profile. Because the exit *TI* is controlled by the scaling of the synthetic fluctuations, in this study, the perturbation amplitude A was changed to match prescribed *TI* levels and to test sensitivity. This is standard in digital-filter/synthetic-inflow methods, where the fluctuation field is normalized so its RMS (and thus *TI*) follows the chosen scaling (Klein, Sadiki, & Janicka, 2003; Xie & Castro, 2008). For jets specifically, nozzle-exit turbulence level strongly affects development, so scanning A (i.e., *TI*) is recommended (Christophe Bogey & Bailly, 2010).

To assess sensitivity, three turbulence amplitudes were tested: $A = \{0.01, 0.05, 0.10\}$ (i.e., 1%, 5%, and 10%). Figure 2.5 reports the azimuthally averaged self-similar axial-velocity profiles for the spatial (Figure 2.5(a)) and temporal (Figure 2.5(b)) LES approaches. In both formulations, 1% under-trips the shear layer and deviates from the experiment near the core–shear-layer shoulder. By contrast, 5% and 10% are nearly indistinguishable over the entire shear layer and both closely follow the measurements; residual differences between 5% and 10% are small relative to experimental/numerical uncertainty. We therefore adopt 5% as the baseline exit fluctuation amplitude: it reproduces the data while avoiding unnecessary over-energization of the near field.

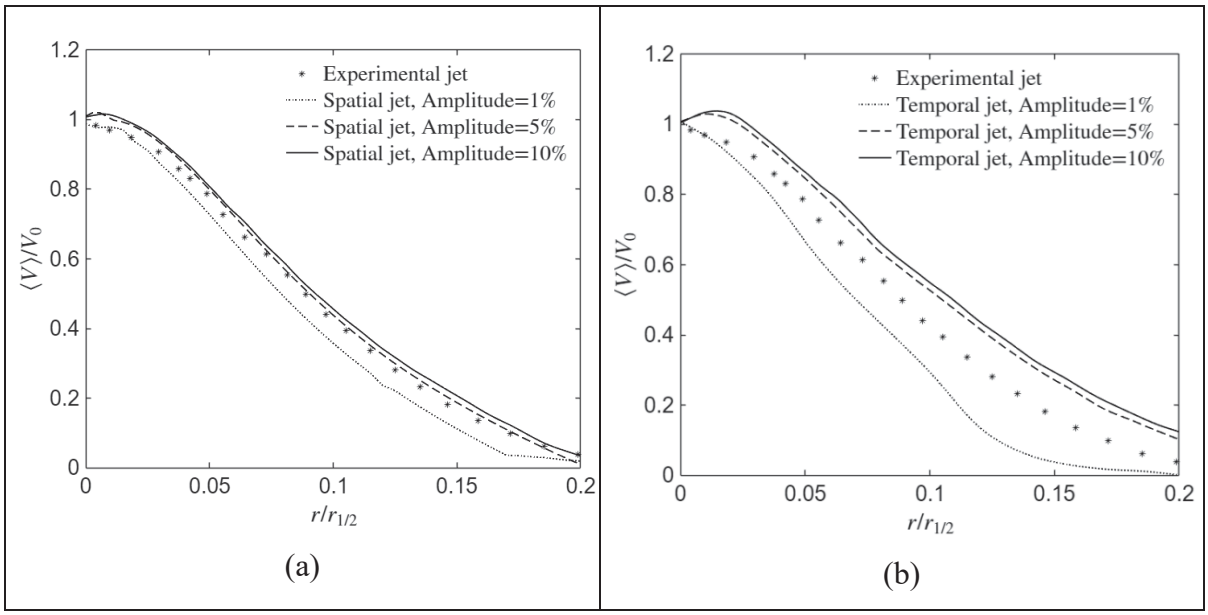

Figure 2.5 Self-similar mean axial velocity profiles versus radial with three nozzle exit fluctuation amplitudes *A*=1%, 5%, 10% for a) Spatial and, (b) Temporal jet

After the velocity, temperature, and pressure fields are set, density is recomputed using the ideal-gas relation. The inverse density $r_1 = 1/\rho$ is stored for efficiency. The conservative variables are formed as $\rho u_x, \rho u_y, \rho u_z$ and $\rho e_{tot} = \rho h(T)$. When a bypass flow is specified, the appropriate Dirichlet condition is imposed on the inflow plane in the streamwise direction so that the initial field and boundary treatment are consistent. Furthermore, a passive scalar Z (stored in ρr_{dilu}) is initialized to identify jet fluid. It is set to unity (or a specified core value)

near the axis and decays smoothly to zero in the ambient, typically via a Gaussian in r. This marker is used later to quantify dilution and entrainment without introducing sharp initial gradients.

When a far-wake or vortex initialization is requested, a Lamb–Oseen–type vortex pair is first generated on the (x, z) cross-section to provide a realistic wake background. The pressure field associated with the vortex is computed to satisfy the radial momentum balance, and (ρ, P) are made thermodynamically consistent with the velocity field. The jet subdomain defined above, is then embedded into this background by adding the jet–ambient differences (scaled to the global non-dimensional references and, where applicable, to the jet's Mach number) so that no discontinuities arise at the patch edges. This yields a composite initial condition that already contains the large-scale wake structure around the issuing jet.

Particle initialization

The particulate matter is represented with Lagrangian simulation particles, split into soot and ambient aerosol populations, in this study. The total number of particles is $N_{part} = N_{part,soot} + N_{part,amb}$. Internally, each particle is tagged by a species flag $type \in \{1(soot), 2(ambient)\}$ and carries its (non-dimensional) initial radius $r_{part,init} = r_d$ and current radius r_{part} along with position and velocity. At $t = 0$, each particle is assigned a dry radius: soot uses its chosen effective dry size, and ambient NH_4NO_3 uses $r_d = 30\,nm$. For convenience, soot particles are flagged as "already in the jet", while ambient particles start as "not yet entrained"; a Boolean flag is toggled when ambient particles cross into the jet core.

The emission index (*EI*) refers to the number of particles emitted per unit mass of fuel at the nozzle exit and depends on fuel composition, engine architecture, and operating condition. To obtain the initial number concentration at the nozzle plane, $[\#/m^3]$, we convert the number-based *EI* [#/kg−fuel] by mass–volume consistency. Burning 1 kg of fuel produces approximately (AFR+1) kg of exhaust (entrained air plus combustion products). For a jet/exhaust density ρ_j, the corresponding exhaust volume per kilogram of fuel is:

$$V_{exh} = \frac{(AFR + 1)}{\rho_j} \tag{2.132}$$

Hence (X. Vancassel, 2003):

$$n_0 = \frac{EI\ \rho_j}{AFR + 1} \qquad [\#/m^3] \tag{2.133}$$

In FludiLES, the particle field is represented as a number concentration ($\#/m^3$), obtained by multiplying the number of numerical parcels (*nb_part*) by the physical particles (*n_trans*) per parcel. The *nb_part* count was held constant at 250,000 in all cases, and particle number concentration was varied solely by adjusting the *n_trans*.

For temporal simulations, the field is initialized once at $t = 0$ throughout the domain with $n = n_0$ (or with a prescribed profile) and then evolves due to transport and microphysics. For spatial simulations, the inflow boundary condition prescribes $n = n_0$ (tanh profile), so particles are introduced continuously each time step via the inlet.

In this study, the ambient aerosol entrained into the exhaust is represented by ammonium nitrate (NH_4NO_3) with dry radius $r_d = 30\,nm$ (Aitken mode) and number concentration $n_{amb} = 100\ \#/cm^3$. A 30 *nm* particle lies squarely in the Aitken mode size range, which is widely used as background CCN in upper-tropospheric studies (Griffin, 2013). The adopted 100 cm^{-3} baseline is within observed UT ranges from aircraft campaigns (typically $10^2 - 10^3$ ($\#/cm^3$) depending on hemisphere, latitude, and air-traffic influence) (Beer et al., 2020; Hermann et al., 2003; Voigt et al., 2022).

In the temporal LES, the domain is initialized at $t = 0$ with an ambient field outside the exhaust core. The turbulent mixing and dilution then draw these ambient particles into the plume exactly as background air is entrained. This follows the standard temporal-box representation of ambient aerosol as an environmental number density that mixes into the jet. In the spatial LES, ambient particles are added continuously via entrainment of background air across the

jet shear layer; operationally, the cumulative number entrained is advanced using the plume dilution factor $\mathcal{D}$(t), so that the source of ambient particles scales with the fresh ambient air mixed in at each time step.

The placement of particles supports three seeding modes as follows:

- **Random cloud (inside/outside jet core):**
  The parcels are drawn uniformly at random. Soot is seeded inside the initial jet core of radius r_{core}; ambient parcels are seeded outside that core in the remainder of the domain (rejection sampling excludes $r \leq r_{core}$). This mode naturally represents a temporal setup: at $t = 0$ the plume core contains soot, while the surrounding fluid already contains ambient aerosol that is subsequently entrained. In the spatial formulation, soot is injected at the inlet with a radial hyperbolic-tangent profile centered on the jet radius, whereas ambient particles are treated as a uniform background ($100\ \#/cm^3$) across the domain and are continuously replenished by entrainment.
- **Unit square around the axis (diagnostic):**
  For this, exactly one parcel is placed in each cell of a 1×1 (non-dimensional) square centered on the jet axis in every $x - z$ plane. This is a diagnostic/verification seeding (e.g., to visualize advection and deformation near the axis) rather than a production configuration.
- **One-per-cell inside the initial jet (dense jet seeding):**
  Here, exactly one parcel is placed in every cell inside the initial jet region ($r \leq r_{core}$); ambient parcels are not initialized in this mode. It is convenient for creating a dense, uniform soot sampling of the nascent jet (commonly used in spatial inflow–outflow runs where ambient aerosol is added later via entrainment).

In all modes, positions are shifted by the specified jet center (x_{jet}, z_{jet}), and parcels start co-moving with the gas (zero initial slip).

2.2.5.4 Boundary Conditions

Longitudinal Boundary

A spatial simulation resolves the flow field as a function of position. However, when investigating phenomena that extend over hundreds of meters, the number of grid points required can become extremely large, leading to high computational cost. In the spatial formulation, the plume evolves downstream in physical space: the computational domain is bounded by an inflow plane at $y = 0$ and an outflow plane at $y = L_y$.

A temporal simulation overcomes this limitation by invoking Taylor's hypothesis (LeBoeuf & Mehta, 1995; Taylor, 1935), according to which the time variable t and the streamwise spatial coordinate can be considered equivalent. The two are related by:

$$t = \frac{y}{V_0} \tag{2.134}$$

where V_0 is the free-stream velocity (for example, the aircraft's velocity). In other words, the computation is performed in a fixed reference frame (the Earth's frame), while the aircraft moves at velocity V_0; in this frame, the flow is assumed to be periodic in the y-direction (C Ferreira Gago et al., 2002; Poinsot, amp, & Lelef, 1992). This approach therefore allows, in principle, the representation of an infinite domain in space (Coppens, 1998).

Given the large extent of the phenomena related to contrail formation (spanning several wingspans behind the aircraft), periodic conditions are thus applied to the longitudinal boundaries of the computational domain in the temporal approach. This corresponds to a simple two-point periodic formulation.

The computational domain extends along the flow direction, with point indices from 1 to m_2 (mesh points) and φ represents any instantaneous variable in the computation. The boundary conditions are expressed as:

$$\begin{cases} \varphi(1) = \varphi(m_2 - 1) \\ \varphi(m_2) = \varphi(2) \end{cases} \quad (2.135)$$

It is important to note that the validity domain of the temporal simulation lies under Taylor's-hypothesis assumptions: longitudinal gradients must remain negligible compared to transverse gradients.

Transverse Boundaries

Transverse boundaries are applied to both temporal and spatial simulations. The x and z boundaries are treated with characteristic non-reflecting conditions plus a sponge layer to emulate an unconfined free jet and avoid artificial reflections. The definition of the boundary conditions on the transverse boundaries of the computation domain is tricky, because here it is necessary to simulate an unconfined jet, and the latter must in no case modify the physics of the jet. The formulation of the boundary conditions retained was that of the conditions of non-reflecting and whose objective is to recreate with artificial boundaries the behavior of an unconfined free flow. The latter presents better results compared to those obtained with periodicity and symmetry conditions (Christophe Bogey & Bailly, 2002; Givoli, 1991).

The principle of this method is to linearize at each time step the Navier-Stokes equation (i.e. equation of conservation of mass, momentum, energy and water vapor). Then, the method consists in studying the 1D characteristic variables normal to the border considered. The Navier-Stokes equation can be rewritten as follows:

$$\frac{\partial \overline{U}}{\partial t} + \bar{\bar{A}}\frac{\partial \overline{U}}{\partial x} + \bar{\bar{B}}\frac{\partial \overline{U}}{\partial y} + \bar{\bar{C}}\frac{\partial \overline{U}}{\partial z} = S \quad (2.136)$$

With:

$$\overline{U} = [\rho \quad \rho u \quad \rho v \quad \rho w \quad P \quad Y]^T \quad (2.137)$$

$$\bar{\bar{A}} = \begin{bmatrix} 0 & 1 & 0 & 0 & 0 \\ -u^2 & 2u & 0 & 0 & 1 \\ -uv & v & u & 0 & 0 \\ -uw & w & 0 & u & 0 \\ -c^2u & c^2 & 0 & 0 & u \end{bmatrix}$$

$$\bar{\bar{B}} = \begin{bmatrix} 0 & 0 & 1 & 0 & 0 \\ -uv & v & u & 0 & 0 \\ -v^2 & 0 & 2v & 0 & 1 \\ -vw & 0 & w & v & 0 \\ -c^2v & 0 & c^2 & 0 & v \end{bmatrix}$$

$$\bar{\bar{C}} = \begin{bmatrix} 0 & 0 & 0 & 1 & 0 \\ -uw & w & 0 & u & 0 \\ -vw & 0 & w & v & 0 \\ -w^2 & 0 & 0 & 2w & 1 \\ -c^2w & 0 & 0 & c^2 & w \end{bmatrix}$$

Here c stands for the speed of sound.

$\bar{\bar{A}}$, $\bar{\bar{B}}$ and $\bar{\bar{C}}$ are diagonalizable matrices. S contains the coupling terms, the viscous terms and the sub-grid terms. The propagation of information in a direction x_i gives the equation of the type:

$$\frac{\partial \bar{U}}{\partial t} + \bar{\bar{M}} \frac{\partial \bar{U}}{\partial x_i} = \bar{\bar{D}} \tag{2.138}$$

where $\bar{\bar{M}}$ indicates the matrix $\bar{\bar{A}}$, $\bar{\bar{B}}$ and $\bar{\bar{C}}$ according to the direction x_i considered. $\bar{\bar{D}}$ contains the derivatives with respect to the other variables, the viscous and coupling terms.

By diagonalizing the matrix $\bar{\bar{M}}$, the eigenvalues λ_i and vectors ψ_i appear. The multiplication of Equation (2.136) by ψ_i gives a new function W_i which is defined such that for all *i* we have:

$$dW_i = \psi_i \overline{dU} \tag{2.139}$$

Equation (2.136) then becomes:

$$\frac{\partial W_i}{\partial t} + \lambda_i \frac{\partial W_i}{\partial x_i} = \psi_i D \tag{2.140}$$

W_i are defined as characteristic variables and are written as follows on the boundaries:

$$\begin{gathered} dW_1 = dp - c^2 d\rho \\ dW_2 = dU.n_1 \\ dW_3 = dU.n_2 \\ dW_4 = dp + \tilde{\rho} c dU.n \\ dW_5 = dp - \tilde{\rho} c dU \\ dW_4 = dY \end{gathered} \tag{2.141}$$

The eigenvalues λ_i satisfy:

$$\begin{gathered} \lambda_1 = \lambda_2 = \lambda_3 = \lambda_4 = U.n \\ \lambda_4 = U.n + c \\ \lambda_5 = U.n - c \end{gathered} \tag{2.142}$$

where n_1 and n_2 are orthonormal tangential unit vectors on the boundary, $dU = (du, dv, dw)$, c speed of sound and $\tilde{\rho}$ is the density evaluated at the previous time step ("~" remark). It can be said:

$$U.n = un_x + vn_y + wn_z \tag{2.143}$$

The boundary conditions are calculated in three steps and in all directions x_i. The first step consists in imposing boundary conditions of the Von Neumann type (zero slope) then computing the temporal variations of dW_i for each characteristic variable at the boundaries. The second step consists of a correction of the boundary conditions. The latter consists in canceling the temporal variations such as:

$$\forall \lambda_i < 0, \qquad dW_i = 0 \tag{2.144}$$

Finally, the third step consists in solving the system Equation (2.136) for solutions of the types:

$$dP = P^{n+1} - P^n, \qquad dU = U^{n+1} - U^n, \qquad d\rho = \rho^{n+1} - \rho^n \tag{2.145}$$

and to look for all the variables at time step *n+1* on the borders. In addition, a sponge zone is added to the non-reflecting boundary conditions to ensure the damping of turbulent fluctuations. The latter adds a source term to the Navier-Stokes equations in a predefined area. This source term is defined as $\sigma(U - U_{ref})$. U_{ref} designates the desired state for the outlet flow. In the context of our study, this is the initial state. Moreover, $\sigma(x)$ is defined such that:

$$\sigma(x) = \alpha \left(\frac{x - x_e}{x_f - x_e}\right)^{\beta} \tag{2.146}$$

where the coefficient α and the exponent β denote integers fixed at each calculation configuration, x_e the abscissa of the beginning of the sponge zone and x_f the abscissa of the end of the domain. The sponge zone extends over 9 cells, with $\alpha = 5$ and $\beta = 3$.

All radial blends (tanh and Gaussian) are used to avoid discontinuities and Gibbs-type artifacts at $t = 0$. If the sponge/diagnostic option is enabled, the initialized conservative fields are written to an auxiliary file to facilitate verification runs or sponge-layer spin-up.

2.2.5.5 Validation

The previously described numerical configuration is used to simulate the turbulent air jet using two LES approaches and the results are compared with experimental results by Hussein, Capp, and George (1994) and Amielh, Djeridane, Anselmet, and Fulachier (1996) as well as numerical data from D. Li, Fan, Luo, and Cen (2011). The discrepancy between numerical values from the LES simulation and experimental results was also observed by Lodato,

Vervisch, and Domingo (2009) and attributed to the sub-grid models used, thus indicating that the sub-grid model does not account for the transfer of energy from small scales to large ones.

Mean Jet Flow Properties

The decrease in the average axial velocity along the jet axis is shown in Figure 2.6. The velocity profile of the simulated air jet from the temporal and spatial approaches shows good agreement with the experimental results of Amielh et al. (1996). Since the results of the temporal modeling are presented in different time zones, the plume was reconstructed to ensure compatibility for comparison in the spatial domain on a physical length scale with the axial results.

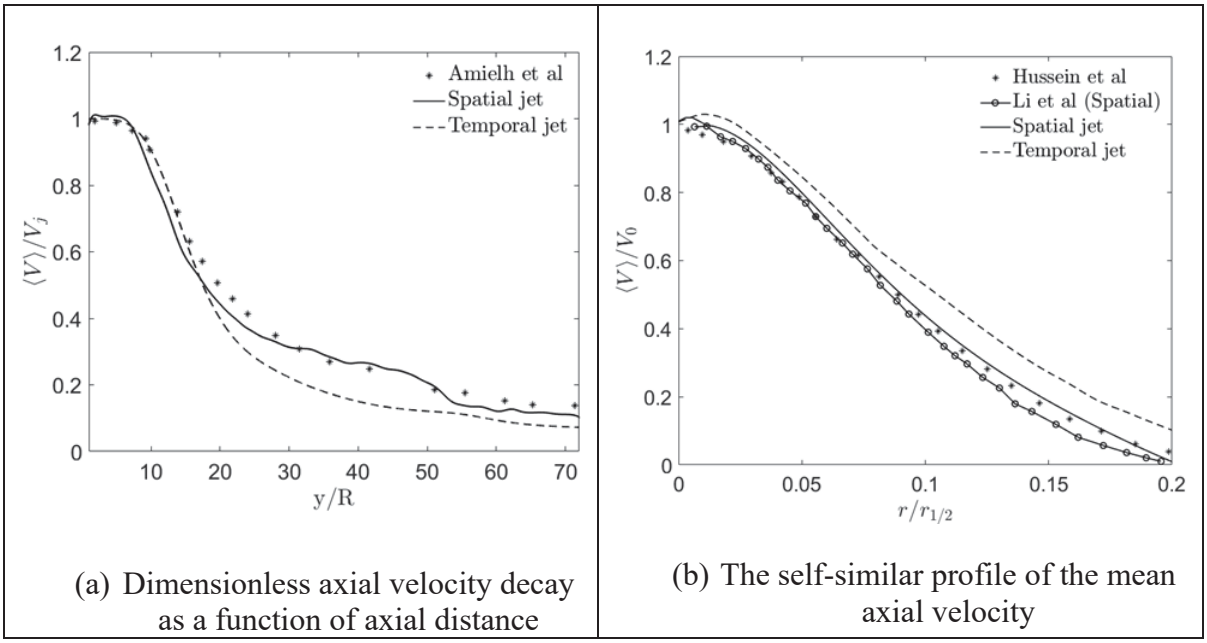

(a) Dimensionless axial velocity decay as a function of axial distance

(b) The self-similar profile of the mean axial velocity

Figure 2.6 Comparison of Spatial and temporal turbulence modeling results and experimental data from Amielh et al. (1996) and Hussein et al. (1994) as well as numerical data from D. Li et al. (2011)

The spatial simulation aligns more closely with the measurements of Amielh et al. (1996) across most of the range. Both approaches exhibit a potential core of ~10 R, within which the velocity remains near the exhaust jet velocity, V_j. Downstream of the potential core, the temporal case underpredicts the centerline velocity relative to both the spatial case and the

data, likely due to strong axial gradients that weaken the time-to-space reconstruction assumption in the near-field. The rapid drop after the potential core followed by gradual decay downstream is consistent with canonical round-jet behavior (Ball, Fellouah, & Pollard, 2012).

The centerline velocity scaled by mean axial velocity profile as a self-similar profile, V/V_0, is plotted as a function of the scaled radial coordinate at a distance beyond the developing region (y>20R), in Figure 2.6(b). This axial distance was to place the jet in the self-similar region. The mean velocity profile in the self-similar round jet are obtained as (Pope, 2000):

$$< V(y,r,0) >= V_0(y)\bar{f}(\zeta) \tag{2.147}$$

$$\zeta = r/r_{1/2}(y) \tag{2.148}$$

where $V_0(y)$ is the centerline velocity as a function of axial distance ($V_0(y) = V(y,0,0)$) and $\bar{f}(\zeta)$ is the similarity profile. As expected, the axial velocity decreases with radial distance. The results obtained from the numerical simulation of the spatial domain are found to be nearly superimposed on the findings of Hussein et al. (1994) and D. Li et al. (2011). However, in the temporal modeling, the curve initially exhibits good agreement, but the deviation gradually increases at larger radial distances.

2nd Order Statistics of Turbulence

To deepen the validation of the chosen numerical simulations, the second-order Reynolds tensors of the velocity field are presented in Figure 2.7 and compared with the experimental results of Hussein et al. (1994) and numerical data from D. Li et al. (2011). The profiles are presented in the similarity zone as explained in the previous section. Turbulent intensities begin to develop in the mixing layer between the jet and the surrounding medium, then the flow becomes fully turbulent. The results obtained on the turbulent fluctuations follow the trends shown in the literature (C Ferreira Gago et al., 2002; White & Majdalani, 2006). Indeed, the dimensionless axial turbulence intensity, here $\langle v'v' \rangle$, is greater than the transverse turbulence intensity $\langle u'u' \rangle$. This is due to the fact that large flow structures have a preferential direction, that of the flow, and because the turbulence field cannot be assumed to be isotropic in this

region. It should be noted that $\langle u'u' \rangle$ and $\langle w'w' \rangle$ are almost similar for the flow. Additionally, the temporal approach appears to overpredict, whereas the spatial approach aligns more closely with the experimental Reynolds stress tensor values reported by Hussein et al. (1994).

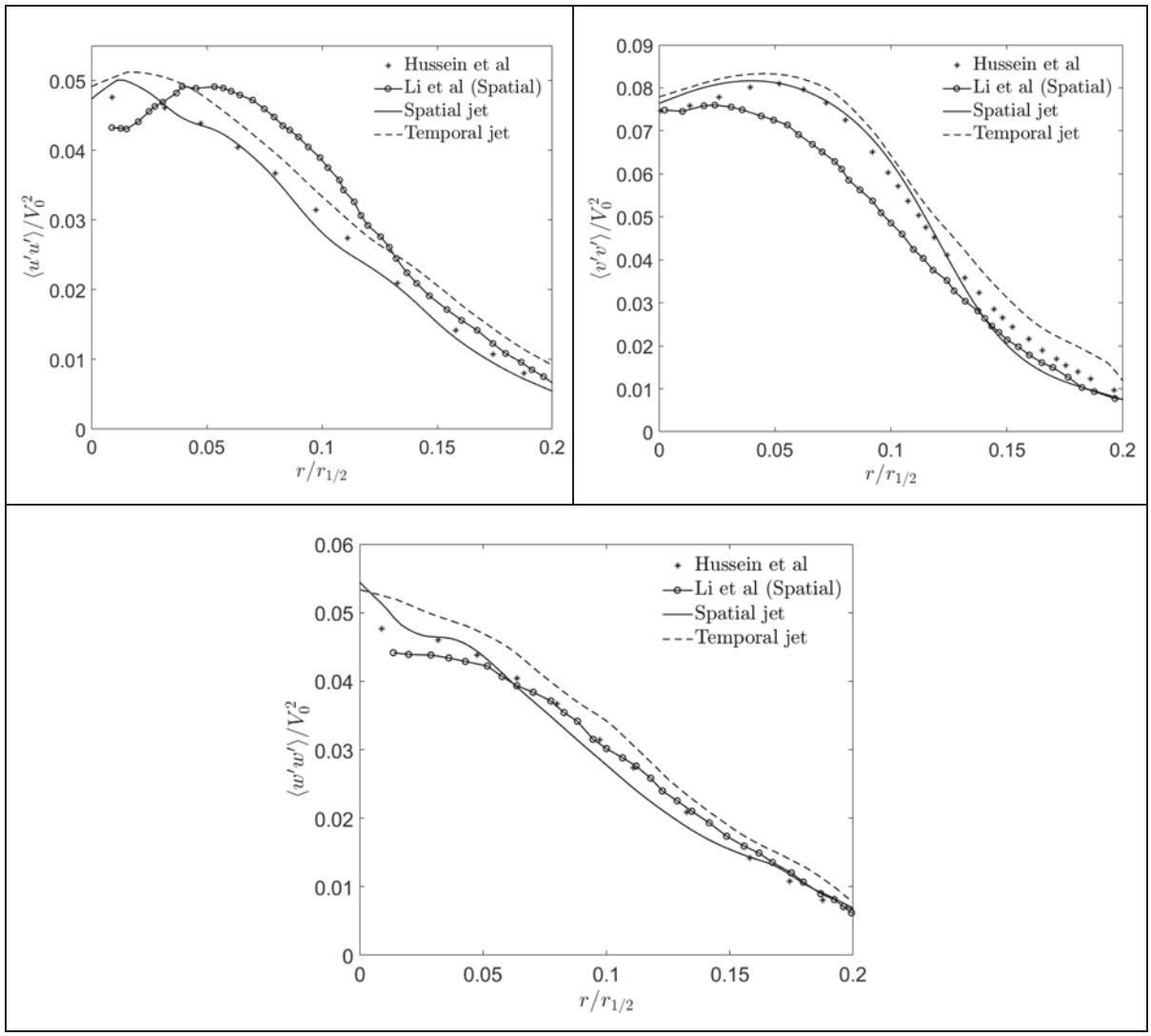

Figure 2.7 Presenting second order Reynolds tensors in the self-similar zone. Comparison of Spatial and temporal modeling results as well as experimental and associated numerical results from literature (Hussein et al. (1994) and D. Li et al. (2011))

2.3 Post-Processing & Metrics

In-Code Analysis

The workflow begins by ingesting simulation snapshots from unformatted binaries into consistently typed, analysis-ready arrays. Alongside the primary fields (density, velocity components, temperature, pressure, transport variables) the reader also loads coordinates, grid sizes, and run metadata (e.g., non-dimensional groups, time step, CFL). All arrays use a unified numeric convention—32-bit indices and 64-bit reals—to ensure stable I/O and reproducibility across compilers.

Next, the code prepares differential operators and computes spatial derivatives. First derivatives are evaluated with centered finite differences in the interior and second-order one-sided stencils at the domain faces; metric factors from the nonuniform grid are applied afterward. These operators feed the construction of derived kinematic fields, including the velocity magnitude, the vorticity vector and its Euclidean norm, and the azimuthal vorticity defined in the cross-stream cylindrical frame.

Thermodynamic diagnostics are then assembled using a mixture-fraction framework for water vapor: end-member compositions (jet and ambient) are mixed linearly in mass fraction, converted to mole fraction, and combined with the reference pressure to form the vapor partial pressure. Supersaturation is obtained by normalizing with the saturation pressure given by standard formulae over liquid water or ice, depending on temperature. This approach can also form a domain-wide probability density of vapor mole fraction to verify the mixing envelope.

To support comparisons and visualization, the pipeline provides plane-averaged projections and cross-stream radial profiles. Plane averages are computed by trapezoidal integration along the orthogonal coordinate and normalization by the domain span, yielding mean maps on the $xy, xz,$ and yz planes for any scalar field. Radial profiles extract quantities such as $r\overline{u_\theta}(r)$ for circulation metrics and $S(r)$ for thermodynamics, using the same sampling and saturation

model as the 3D diagnostics. Optional cut planes at prescribed indices can be generated in the same pass.

Particle post-processing operates in two modes. For Eulerian, cell-centered statistics, the code aggregates per-cell activation into cross-sectional tallies and bins them into concentric annuli, producing radial distributions of activated versus non-activated particles. For Lagrangian lists, the reader exposes particle positions and attributes (radius, local thermodynamic state), from which PDFs/CDFs and joint distributions can be computed, as needed.

At each time step, the code forms snapshot-level statistics. Field variables are volume-averaged over the plume sub-volume defined by the analysis mask, yielding $\langle\phi\rangle V(t)$. Microphysical quantities are ensemble-averaged over all particles present at that step, yielding $\langle . \rangle_p(t)$ (e.g., mean radius, saturation fraction). For each microphysical process, the pipeline writes a dedicated, column-oriented time-series file at every step that records the timestamp and the corresponding plume-volume and/or particle-ensemble averages (optionally with min/max and standard deviation). These files provide clean inputs for downstream plotting, trend analysis, and ensemble aggregation.

Finally, the assembled fields, diagnostics, and profiles are exported to self-describing formats suitable for analysis and archiving. Ordered, nodal datasets are written either as Tecplot binary files (BLOCK packing with variable/coordinate names and AUXDATA) or as CGNS files (structured zones with double-precision fields, vertex-based solution nodes, and proper base/zone metadata). The exporter follows an initialize → append → finalize pattern so that time-accurate sequences, planes, and profiles are appended consistently within the same artifact. Throughout, the pipeline prints range checks and maintains coherent naming of variables and coordinates so figures, tables, and metrics in the thesis can be generated directly from these outputs.

Post-Export Analysis

After the in-code post-processing writes column-oriented time-series files and CGNS snapshots, the external analysis reconstructs physical units, aggregates ensemble statistics, and generates publication-quality figures. Two complementary tools are used: MATLAB for statistical time-series and distribution plots, and Tecplot for spatial fields stored in CGNS.

- **Inputs and unit reconstruction:** All exported time-series are non-dimensional. Before plotting, time is mapped to seconds using the nozzle-exit acoustic scale:

$$t_0 = \frac{r_j}{M_j c_j} \tag{2.149}$$

$$c_j = \sqrt{\gamma R_d T_j} \tag{2.150}$$

  where r_j is the jet radius, M_j the exit Mach number, γ the ratio of specific heats, $R_d = 287\ J/kg\ K$ for dry air, and T_j the exit temperature. Each engine/ambient configuration (UHBR, LEAP, CFM56; =215,220,225 K) has its own t_0 and is applied consistently in the MATLAB parameter block. Particle radius is reported in micrometres using a fixed particle scale $r_{ref} = 20\ nm = 0.02\ \mu m$ (implemented as *rapp_long*). Other variables plotted (e.g., the mean ice saturation ratio) are dimensionless as exported.

- **Particle statistics and distributions:** For selected physical times, spatial samples of particle radius are imported from the *xyz* files. Unique support points are constructed, and kernel density estimation (*ksdensity*) is applied to obtain smooth PDFs. A common bandwidth policy is maintained within each figure so that cross-case differences reflect physics rather than smoothing. Axes are unit-correct (radius in μm; PDF in μ/m).

  For each snapshot file *rayon_moy*, the analysis reads non-dimensional time τ, mean particle radius $\bar{r}_p$, mean particle temperature $\bar{T}_p$, mean vapor pressure $\bar{P}_v$, and mean ice saturation ratio $\bar{S}_{ice}$. Time is dimensionalized ($t = \tau t_0$); radius is scaled by r_{ref}.

Files *nb_de_sat* provide the number of saturated (activated/frozen) particles $n_{sat}(t)$. Counts are normalized using the numerical-parcel representation: the total particle concentration ($\#/m^3$) equals the number of numerical parcels times the physical particles carried by each parcel. Because a constant parcel weight is used here, normalization reduces to dividing by the total number of parcels (250,000).

- **3D fields and profiles:** The external visualization uses the CGNS snapshots written by the solver, which group three zone types per time step:
  (i) 3D ordered volumes (I×J×K) for full fields;
  (ii) 2D ordered planes (I×J, I×K, or J×K) for extracted cut-planes or plane-averaged maps; and
  (iii) 1D ordered lines (I) for radial or centerline profiles. All variables are stored nodally in double precision, and each zone carries solution-time metadata so Tecplot can treat them as a linked time sequence.

  CGNS files are opened directly; Tecplot recognizes each zone's dimensionality and coordinates. A small set of layout equations defines dimensionalization constants once (per engine/ambient case) and applies them to all zones regardless of dimension.

Zone *StrandID*/solution time are used to synchronize animations and to ensure that 1D/2D/3D views at a given timestamp are directly comparable. Layout templates enforce common colormaps, tick marks, and legends; Tecplot equations guarantee that the same unit conversions are applied to every zone type in the file. Final figures (PNG/EPS) are exported from these templates so typography and scales match the MATLAB plots used for PDFs, mean-radius, and activation-fraction time series.

2.4 Chapter Conclusion

This second chapter establishes the methodological foundation for simulating near-field contrail formation from aircraft exhaust, integrating high-order compressible CFD with online microphysics in the FludiLES framework. The solver advances the Favre-filtered Navier–

Stokes equations with sixth-order spatial accuracy and third-order Runge–Kutta time integration; it is purpose-built to resolve the exhaust jet and its transition into the wake regime, where a Lamb–Oseen vortex pair represents the rolled-up wake. Microphysics are treated in an online-coupled Lagrangian module (originally soot; extended here to include ambient aerosol as a second class), with coupling performed within the LES setting for tractability. Two-way coupling is applied to the vapor (mass transfer) and energy equations; momentum coupling is neglected, and even in energy the effect is small in the jet phase.

Within LES, density-weighted (Favre) filtering and an explicit specification of the cut-off length are adopted, and hybrid (mixed) Smagorinsky/scale-similarity closures are available to accommodate different grid resolutions and shear-layer dynamics. Time stepping follows a conservative CFL guideline (~0.6) to maintain stability at relevant Mach numbers. Together these choices balance accuracy, stability, and computational efficiency for the present problem class.

Two complementary domain strategies are employed. Spatial simulations resolve the full downstream development from a smooth nozzle-exit profile; temporal simulations truncate the streamwise extent and impose periodicity to follow the coupled jet/vortex evolution at reduced cost. Uniform Cartesian meshes and node counts are chosen from the required extents, and mesh-resolution studies verify grid convergence. Transverse boundaries use characteristic non-reflecting conditions with thin sponge layers; the implementation follows a characteristic decomposition with a three-stage update (zero-slope prediction, correction to cancel spurious temporal variations, final characteristic solution) to ensure physically transparent outflow.

Inflow perturbations consist of low-amplitude, shear-layer-confined synthetic fluctuations with amplitude A that sets the nozzle-exit turbulence intensity TI. A brief sensitivity scan (A = 1%, 5%, 10%) shows that 1% under-trips the shear layer relative to measurements, while 5% and 10% yield nearly indistinguishable mean profiles in both spatial and temporal formulations; hence 5% is adopted as the baseline to match data without over-energizing the

near field. This choice sets inflow coherence and accelerates transition in a controlled manner for the subsequent physics analysis.

Particles are represented by numerical parcels with constant multiplicity (physical particles per parcel). All particle-based tallies (e.g., activation counts) are normalized accordingly. A fixed parcel count of 250,000 is used across cases so that concentration changes reflect only the physical multiplicity. Post-processing reconstructs dimensional units, assembles time series of microphysical and thermodynamic statistics, and harmonizes spatial visualizations via CGNS/Tecplot export templates, ensuring consistent axes, conversions, and layout across 1D/2D/3D output.

The next chapters present results obtained with this framework, with the ultimate goal of simulating the exhaust jet and ensuing wake-vortex of an aircraft engine under cruise conditions using advanced microphysical modeling that accounts for gas–particle interactions involving soot and ambient aerosol.

CHAPTER 3

EVALUATING BYPASS EFFECTS OF ADVANCED TURBOFAN ENGINES ON CONTRAIL FORMATION USING LARGE EDDY SIMULATIONS

Parisa Afkari [a], Mohamed Chouak [a], Sébastien Cantin [a], François Garnier [a]

[a] Département de Génie Mécanique, École de Technologie Supérieure,
1100 Notre-Dame West, Montreal, Quebec, Canada H3C 1K3

Paper published in *Journal of Aircraft*, June 2025

Abstract

Condensation trails formed behind cruising aircraft engines contribute to climate change through radiative forcing. While most contrail studies consider parameterized single-jet profiles, this CFD study investigates dual-stream jets to characterize turbofan bypass effects on contrail microphysics. High-resolution large eddy simulations (LES) refined early plume dynamics for a dual-stream jet, consisting of a bypass jet and a core jet of air and water vapor (Eulerian phase) laden with soot particles (Lagrangian phase). Microphysical modeling employs a solubility model for soot activation, while the subsequent water vapor condensation processes on activated soot particles and ice growth on freezing particles are computed using a deposition model. The first comparison of a turbofan with its equivalent turbojet showed that the bypass jet enhances the mixing and cooling of the core jet, with a mean particle radius increase of up to 30%. Thereafter, three realistic turbofans—CFM56-5B3/3, LEAP-1A/33, and UHBR—classified respectively as medium, high, and ultra-high bypass ratio engines, were compared at ambient temperatures of 215 K, 220 K, and 225 K. The analysis showed that higher bypass ratios enhance jet mixing in the near field, increasing soot activation and droplet freezing processes, and resulting in initial contrail properties that are less sensitive to ambient temperatures.

3.1 Introduction

According to the International Civil Aviation Organization (ICAO) (ICAO, 2022), one of the major impacts of aviation on the climate is attributable to non-CO_2 emissions; specifically, Aircraft-Induced Clouds (AIC), which contribute to global warming. Depending on ambient conditions, contrails can form as soot particles, and water vapor emissions from cruising aircraft engines initiate the heterogeneous nucleation of water droplets (Kärcher et al., 2015). These droplets, after a limited growth, undergo homogeneous freezing to form ice particles, which continue to grow by accreting additional condensable matter. Persistent contrails in an ice-supersaturated area can trigger the formation of large cirrus clouds covering a wide horizontal area up to 50,000 km^2, for tens of hours (Haywood et al., 2009). By reflecting incoming and outgoing radiations, AIC produce a positive radiative forcing (warming) effect (Lee et al., 2010). Global assessments by Intergovernmental Panel on Climate Change (IPCC) estimated that the AIC impacts are three times greater than the aviation CO_2 impact alone (IPCC, 2023). The most recent calculations of radiative forcing from global aviation covering the 2000 to 2018 period (Lee et al., 2021) showed that the impact of non-CO_2 emissions constitutes about two-thirds of the net radiative forcing. Moreover, AIC, including persistent contrails and contrail cirrus, accounts for approximately 90% of aviation's non-CO_2 radiative forcing (Bernd Kärcher, 2018). As non-CO_2 terms contribute about eight times more than CO_2 to the uncertainty in net RF, the climate impact of AIC remains a major source of uncertainty (Lee et al., 2021). These non-CO_2 effects, primarily resulting from contrail cirrus, contribute significantly to the overall climate impact of aviation.

Despite extensive research, contrail formation remains very complex, with substantial knowledge gaps and uncertainties arising from the interaction of various aircraft and environmental factors, highlighting the need for further investigations (Voigt et al., 2010). Regarding the impact of ambient conditions, Jensen, Toon, et al. (1998) emphasized their role in contrail formation, noting that contrails only form and persist when there is substantial supersaturation with respect to ice. Flight campaigns, such as those reported by Jensen, Toon, et al. (1998) (SUCCESS campaign) and Voigt et al. (2021) (ECLIF1 and ECLIF2/ND-MAX

campaigns), have also highlighted the critical role of ambient temperature and humidity in contrail formation and persistence. Likewise, Jeßberger et al. (2013), Haglind (2008) and F Garnier and Laverdant (1999) highlighted the influence of aircraft type, design, and engine differences on contrail formation thresholds, on the long-term dependency of contrail properties on their lifetime, and on the mixing effects of the exhaust plume, demonstrating the combined effects of environmental and aircraft/engine factors.

Regarding the impact of engine properties, the effect of the overall propulsion efficiency of the engine on contrail formation—called the η-effect—was investigated by Ulrich Schumann (2000). As an example of this effect, observations of contrail formations with a low (bpr=1.4–2) and a medium bypass-ratio (bpr= 6.8) engine confirmed the theoretical conclusions from the revised Schmidt–Appleman criterion (Ulrich Schumann, 1996). These conclusions indicated that contrails form at lower altitudes (i.e., a higher ambient temperature) with higher bypass ratios, or with a more efficient engine. While the current trend in civil aviation engine developments is towards ultra-high bypass ratio engines (Barbosa, 2022), the impact of engine bypass in dual-stream jets on contrail formation remains unclear. Many studies, such as Dahm, Frieler, and Tryggvason (1992), Villermaux and Rehab (2000) and Van Hoot, Murugan, Mitra, and Cukurel (2021), have investigated the dynamic characteristics of the bypass flow, including the mixing effects in dual-stream round jets. However, most existing contrail models in the literature do not distinguish between core and bypass jets, but rather, consider a highly parametrized simple mixed jet. For example, Unterstrasser and Görsch (2014) used Gaussian-like jet-plume profiles to characterize the impact of aircraft on contrail evolution. Such simplified representations of the exhaust jet do not provide a better understanding of the bypass jet effect in modern turbofan engines, as also highlighted by Detwiler and Jackson (2002). The bypass effect (Ferreira, Alonso, & Gorlé, 2024), as well as the engine size (D. C. Lewellen, 2020), might have a significant impact on jet mixing, and hence, on the formation of ice crystals. This highlights the need to characterize the bypass effect on the microphysical properties of contrails.

Many studies highlighted the importance of investigating near field contrail properties (Kärcher, 2016; Kärcher et al., 2015). For instance, Ulrich Schumann et al. (2017) stated that the number of ice crystals nucleated in the near field is directly influenced by the engine exhaust conditions, and remains relatively constant throughout the contrail lifetime, as the subsequent evolution into contrail cirrus involves a series of successive dynamic and microphysical processes that are difficult to control or alter. Indeed, the impact of contrails on climate is a function of the optical properties of ice particles, including their size and number (P. Yang et al., 2015). As such, a better characterization of near field contrail properties in the jet regime is crucial for designing aircraft engines with a reduced contrail impact.

Given the high costs of in-flight experiments, there is growing interest in numerical investigations to characterize the exhaust-related factors influencing contrail formation. Such investigations—involving a coupling of fluid dynamics (e.g., mixing effects, aircraft wake interactions), thermodynamics (e.g., condensation and evaporation processes), microphysics (e.g., nucleation, particle growth and depletion), and chemistry (e.g., atmospheric reactions and post-ejection chemical transformations)—have been widely studied over the last few decades (Ferreira et al., 2024; J. Khou et al., 2017; D. C. Lewellen, 2020). As a dominant feature in this equation, the microphysical modeling can be accomplished either with trajectory-box models (Bier et al., 2022; X. Vancassel et al., 2014) or with 3D CFD models (Cantin et al., 2022; Ferreira et al., 2024; J. Khou et al., 2017; Ramsay, Tristanto, Shahpar, & John, 2024). While trajectory box models can provide valuable insights at larger scales, limitations may be encountered in accurately predicting contrail formation behind commercial aircraft, particularly due to the simplified representation of spatial variability in jet plumes (Bier et al., 2022; X. Vancassel et al., 2014). As such, X. Vancassel et al. (2014) compared different jet dilution calculations and coupling strategies: a multiple-trajectory box model (offline coupling with detailed microphysics) versus a 3D LES model (online coupling with ice-only microphysics). Even though plume-averaged characteristics results were in good agreement overall, a spatial non-homogeneity of the near field particle properties pointed to local discrepancies in the ice crystal size. Therefore, such, a coupled online microphysics-dynamics approach is required to accurately account for jet-mixing inhomogeneities,

variations in local dilution rates, and temperature gradients (Cantin et al., 2022; Roberto Paoli et al., 2004).

The main objective of this work is thus to characterize the engine bypass effect on near field contrail properties. To the authors' knowledge, no previous study has investigated the impact of bypass flow using different turbofan exhaust conditions on the microphysical properties of ice particles. For the characterization herein, a high-resolution LES approach for turbulence was adopted to refine the representation of early plume dynamics, especially the mixing within jet shear layers. The paper is structured as follows. Section 3.2 provides an overview of the governing equations for both flow dynamics and ice particle microphysics. Section 3.3 presents the numerical setup as well as the initial and boundary conditions. Section 3.4 provides the results from three comparative studies, along with a detailed analysis of both bypass flow and bypass rate effects on near field contrail properties.

3.2 Governing Equations

The modeling approach incorporates an exhaust jet from an aircraft engine, composed of a gaseous mixture of air and water vapor (gas phase) laden with soot particles (solid phase) from the core flow and ambient air from the bypass flow. Ice particles can form later in the jet plume. First, the mathematical equations for the gas phase are presented in this section. Finally, the solid phase modeling for soot particles and ice crystals is presented, followed by a description of the microphysical model for contrail formation.

3.2.1 Gas Phase Equations

The bulk flow motion was simulated using a Eulerian-based Large Eddy Simulation (LES) approach. This method directly resolves the large energy-carrying scales of turbulence, while the behavior of the smaller, more isotropic, scales is accounted for using the hybrid Smagorinsky Subgrid-Scale (SGS) model (C Ferreira Gago, Garnier, & Utheza, 2003). This model is a linear combination of the Smagorinsky model (Smagorinsky, 1963) of the eddy

viscosity type, and the similarity model (Liu, Meneveau, & Katz, 1994), which better represents the energy backscatter (C Ferreira Gago et al., 2003). Furthermore, a spatial filter was used to extract the large scales from the flow field. Applying the former filtering operation to the nondimensional form of the 3D compressible Navier-Stokes equations yields the LES equations of the compressible gas-flow mixture, including the continuity equation, the momentum equation, and the total energy equation, presented in François Garnier et al. (2014). In this study, the water vapor transport equation, which includes the coupling term, is presented to emphasize the method of coupling between the gas and solid phases in the FludiLES code:

$$\frac{\partial\left(\overline{\rho}_g\tilde{Y}_v\right)}{\partial t}+\frac{\partial\left(\overline{\rho}_g\tilde{Y}_v\tilde{u}_j\right)}{\partial x_j}-\frac{\partial}{\partial x_j}\left(\frac{\bar{\mu}_g}{\mathrm{Re\ Pr}}\frac{\partial\tilde{Y}_v}{\partial x_j}\right)+\overline{\psi}=\frac{\partial\xi_j}{\partial x_j} \tag{3.1}$$

Where the Favre average defined as $\tilde{f}=\overline{\rho_g f}/\overline{\rho_g}$, was used to account for the compressibility effects, $\overline{\rho_g}$ denotes the gas phase density, $\tilde{u}_j$ the velocity component along the j-direction, ξ is the SGS vapor flux, and $\tilde{Y}_v$ the water vapor mass ratio. The Reynolds number (Re) is based on the nozzle diameter and the exhaust jet velocity at the nozzle exit. The Prandtl number Pr and the ratio of specific heat γ are set equal to 0.7 and 1.4, respectively, i.e., the assumed values for air (Lenormand, 1999).

In Equation (3.1), the source term $\overline{\psi}$ represents the rate of condensed water vapor, which is computed using both droplet and ice particle growth models.

3.2.2 Solid Phase Equations and Microphysical Model

Solid particles were tracked within the Lagrangian framework in which each particle is followed individually. Due to the relatively high number density of soot particles that initially form in an engine combustor (for example, in the order of 10^{13}–10^{14} #/kg-fuel for the type of engines used in this study at sea level and cruise-level operation, according to the ICAO emissions databank (ICAO, 2024)), the simulation cost was alleviated by considering

numerical particles instead of physical particles. Each numerical particle, treated as a sphere of radius r_p, represents the motion of N_p physical particles. Due to their relatively small size and mass, both particle drag and gravity forces are neglected. Hence, the particles are considered as passive tracers having the same velocity as the carrier phase. The starting point was the microphysical model described in François Garnier et al. (2014). In the LES approach, the filtered velocity field $\tilde{u}$ was used in the particle-movement equation expressed as:

$$\frac{dx_p}{dt} = \tilde{u}(x_p) \tag{3.2}$$

Where x_p is the particle position vector.

Hydrophobic soot particles at the nozzle exit need to be activated in order to become water droplets (Kärcher et al., 1996). To model the activation of exhaust particles into water droplets, a solubility model that relies on the activation radius associated with the plume's saturation ratio (Kärcher et al., 2015) was employed. Soot particles—acting as condensation nuclei due to their shape and surface properties—become activated when the saturation ratio exceeds a critical threshold. As a result, they rapidly grow by taking up condensable matter (i.e., water vapor). Lastly, the cooling of the exhaust jet by mixing with the ambient atmosphere leads to water vapor condensation on soot particles, and hence, to contrail formation. The ice particle growth is dominated by heterogeneous nucleation in exhaust jets (K. Gierens, 2003). The physical parameter known as the saturation ratio, S, defined by Equation (3.3) as the local ratio between the partial vapor pressure P_v and the saturated vapor pressure P_{sat} with respect to liquid water (for water droplets) or ice (for ice particles), plays a crucial role in determining the formation and growth of these particles. This ratio is expressed as:

$$S = \frac{P_v(\tilde{T}_p)}{P_{sat}(\tilde{T}_p)} \tag{3.3}$$

where $\tilde{T}_p$ is the local temperature at the particle interface.

As demonstrated by Kärcher et al. (2015), the likelihood of aerosol particles becoming activated into water droplets is significantly higher with increasing supersaturation levels of the plume above water bodies. Within this framework, the critical radius of dry aerosol particles (r_{act}) depends on the saturation ratio (S), indicative of the transition point to activation under supersaturated conditions (Petters & Kreidenweis, 2007):

$$ln(S) = \sqrt{\frac{(r_k/r_{act})^3}{54\kappa}} \tag{3.4}$$

Where r_k is the Kelvin radius set at 1 nm, κ is the solubility parameter influenced by the solutes' chemical nature, with values of 0.5 and 0.005, for fully soluble atmospheric aerosol and coated aircraft soot particles, respectively (Kreidenweis, Petters, & Chuang, 2009).

In analyzing the droplet growth during contrail formation, the mass change equation for spherical droplets proposed by Bier et al. (2022) is computed, with modifications such as updating the formulas for saturation pressure based on Murphy and Koop (2005) to suit the specific conditions of this study:

$$\dot{m}_w = \frac{dm_w}{dt} = \frac{4\pi r_w (P_v(\tilde{T}_p) - P_{sat}(\tilde{T}_p))}{F_M \beta_m^{-1} + F_H \beta_t^{-1}} \tag{3.5}$$

In this equation, m_w is the droplet mass, r_w is the droplet radius, constants and terms such as F_M, F_H, β_m, and β_t have specific physical interpretations related to mass and heat diffusion terms, respectively.

In alignment with the slow growth regime defined by Kärcher et al. (2015) for homogeneous freezing, it is possible to deduce the freezing temperature, T_*, represented by the following equation:

$$T_* \cong \frac{1}{a_1}[\ln\left(\frac{a_1\dot{T}}{V_w}\right) - a_2] \tag{3.6}$$

where $a_1 = -3.5714\ (K^{-1})$ and $a_2 = 858.719$ are empirical constants (Riechers, Wittbracht, Hütten, & Koop, 2013), $\dot{T}$ is the plume cooling rate and V_w is the droplet volume. Once the droplets reach the freezing temperature, the size of the ice crystals that form becomes a function of the local temperature and relative humidity. The net mass change of ice per particle is computed using the Fukuta and Walter (1970) model as follows:

$$\dot{m}_{ice} = \frac{dm_{ice}}{dt} = \frac{4\pi\rho_{ice}r_{ice}\ (S - A)}{C_T A + C_\rho} \tag{3.7}$$

Where m_{ice} is the ice particle mass, ρ_{ice} is the particle density, and A the Kelvin effect, defined as the ratio between the vapor pressure at the water droplet surface before freezing and the saturated vapor pressure over a flat surface at the droplet temperature. The two factors C_T and C_ρ control the water vapor temperature and air density above the particle surface. Their formulations can be found in the original paper (Fukuta & Walter, 1970). The model accounts for the reduction of water vapor through processes of condensation and vaporization onto existing particles, which effectively function as sink terms by reducing the water vapor content of gas phase.

3.2.3 Numerical Setup and Testing

A high order (six orders in space; three orders in time), compressible CFD code, FludiLES, was used in this study. This research code, based on the finite difference scheme with spectral-like resolution (Lele, 1992), has been extensively used and validated for engine jet and aircraft-wake applications (Bier et al., 2022; François Garnier et al., 2014; Labbe, Maglaras, & Garnier, 2007; X. Vancassel et al., 2014). The code effectively captures key flow instabilities, such as the Kelvin-Helmholtz instability, a primary convective instability in jets, which can be modeled using a temporal approach, as demonstrated by Brancher (1996). Furthermore, the

temporal representation (temporal turbulence) can accurately reproduce the jet dynamics with fewer mesh points as compared to a spatial simulation (spatial turbulence) (D. C. Lewellen, 2020). As such, the temporal evolution of turbulent hot jets from kerosene-fueled turbofan engines with different bypass ratios was examined. The temporal representation is based on the Taylor hypothesis (Taylor, 1935) also known as the frozen-turbulence approximation, according to which the time variable t and the axis position y are linked by the relation $t = y/U_0$, where U_0 denotes the aircraft speed.

Two jet configurations from typical aircraft engines were considered, as shown in Figure 3.1, in which the coordinate system was associated with the cruising engine at speed U_∞. The exhaust jet profile in Figure 3.1(a) represents a turbofan configuration, referred to hereafter as "with bypass," in which a portion of the inlet air is bypassed around the core jet. The latter drives the gaseous mixture of kerosene combustion products, while the bypass jet drives the ambient moist air, which is only slightly accelerated. Both exhaust jets are mixed with the freestream moist air downstream. The bypass ratio, or bypass rate, of a turbofan is defined as the ratio of the mass of air passing through the fan (bypass jet) $\dot{m}_b$ to that crossing the core (core jet) $\dot{m}_c$, as described by Equation (3.8):

$$bpr = \frac{\dot{m}_b}{\dot{m}_c} \tag{3.8}$$

The simple turbojet configuration without a bypass stream was also considered for comparison purposes, as shown in Figure 3.1(b), and is known below as "without bypass." The equivalence between the two configurations (Figure 3.1(a) and (b)) was ensured by preserving the same momentum budget, as expressed by Equations (3.9) to (3.11), where F denotes the engine thrust. Equation (3.11) yields the exhaust velocity of the turbojet configuration.

$$F_{turbofan} = (\dot{m}_c + \dot{m}_b)\left(\frac{U_c + bpr\, U_b}{1 + bpr} - U_\infty\right) \tag{3.9}$$

$$F_{turbojet} = \dot{m}_s(U_s - U_\infty) \tag{3.10}$$

$$U_s = \frac{U_c + bpr\, U_b}{1 + bpr} \tag{3.11}$$

For the jet-regime simulation, the plume jet was solved within the rectangular box of dimensions $L_x = 20R$, $L_y = 12R$, and $L_z = 20R$ in the spanwise, streamwise, and vertical directions, respectively. The radius R defines the middle of the jet shear layer such that $U(R) = (U(0) + U_\infty)/2$, where $U(0)$ is the jet centerline velocity. Regarding boundary conditions, periodic boundaries were applied in the streamwise direction, while a nonreflective condition (Thompson, 1987) was applied to the remaining planes. The velocity field in the computational domain was initialized with the velocity profile of the exhaust jet.

For the without bypass configuration (Figure 3.1(b)), the velocity field was initialized with the typical jet (hyperbolic tangent) profile expressed in cylindrical coordinates (r, θ, z) as follows:

$$U(r) = \frac{1}{2}(U_s + U_\infty) - \frac{1}{2}(U_s - U_\infty)\tanh\left(\frac{1}{4}\frac{R}{\theta}\left(\frac{r}{R} - \frac{R}{r}\right)\right) \tag{3.12}$$

The parameter θ denotes the momentum boundary layer thickness of the jet shear layer computed, as follows:

$$\theta = \int_0^\infty \left(\frac{U - U_\infty}{U_s - U_\infty}\right)\left(1 - \frac{U - U_\infty}{U_s - U_\infty}\right) dr \tag{3.13}$$

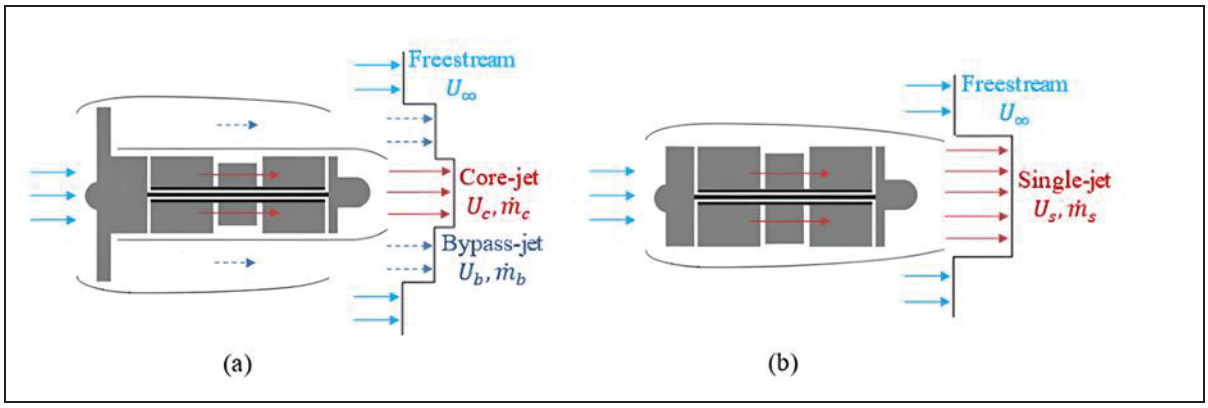

Figure 3.1 Schematic representation of the exhaust flow from typical jet engines: (a) with bypass (turbofan configuration); (b) without bypass (simple turbojet configuration)

The jet parameter R/θ characterizes the jet velocity profile along the streamwise direction. A value of R/θ=10 was used, corresponding to the case of an unstable jet (Michalke & Hermann, 1982). Random Gaussian-shaped perturbations were superimposed on the component of the initial velocity field.

For the with bypass configuration (Figure 3.1(b)), the velocity field was initialized by the sum of two hyperbolic tangent profiles as follows:

$$U(r) = aU_1(r) + bU_2(r) \tag{3.14}$$

$$U_1(r) = \frac{1}{2}(U_c + U_\infty) - \frac{1}{2}(U_c - U_\infty)\tanh\left(\frac{1}{4}\frac{R}{\theta}\left(c\frac{r}{R} - \frac{1}{c}\frac{R}{r}\right)\right) \tag{3.15}$$

$$U_2(r) = \frac{1}{2}(U_b + U_\infty) - \frac{1}{2}(U_b - U_\infty)\tanh\left(\frac{1}{4}\frac{R}{\theta}\left(d\frac{r}{R} - \frac{1}{d}\frac{R}{r}\right)\right) \tag{3.16}$$

Where the constants a, b, c, and d depend on the engine exhaust parameters and are related to the core and bypass radii. For the with bypass configuration of the LEAP-1A/33 engine, a was taken equal to 0.63 and b set to 0.37, c set to 1.2, and d set to 0.5. The inlet velocity profiles for both the with bypass and the equivalent without bypass configurations for the LEAP-1A/33 engine are plotted in Figure 3.2. The temperature field was initialized using the Crocco–

Busemann relation (Schlichting & Gersten, 2017). As for the initial number of soot particles, the method implemented by Ahrens, Méry, Guénard, and Miake-Lye (2023) was used to determine the emission indices of soot particles at cruise altitude for all three engines, based on the ICAO Aircraft Engine Emissions Databank (ICAO, 2024). To ensure a fair comparison focused on the effect of bypass ratio, an average soot emission index of 4×10^{13} #/kg-fuel was adopted for all three engines, along with an initial mean soot particle radius of 20 nm. Additionally, Figure 3.14 presents a direct comparison between the LEAP-1A/33 and CFM56-5B3/3 engines, highlighting the differences in their respective emission indices under cruise conditions. Further, Table 3.1 summarizes the primary input parameters for the three turbofan engines at varying ambient conditions, with ice relative humidity ranging from 100% to 140%, corresponding to the highest to lowest ambient temperatures, respectively.

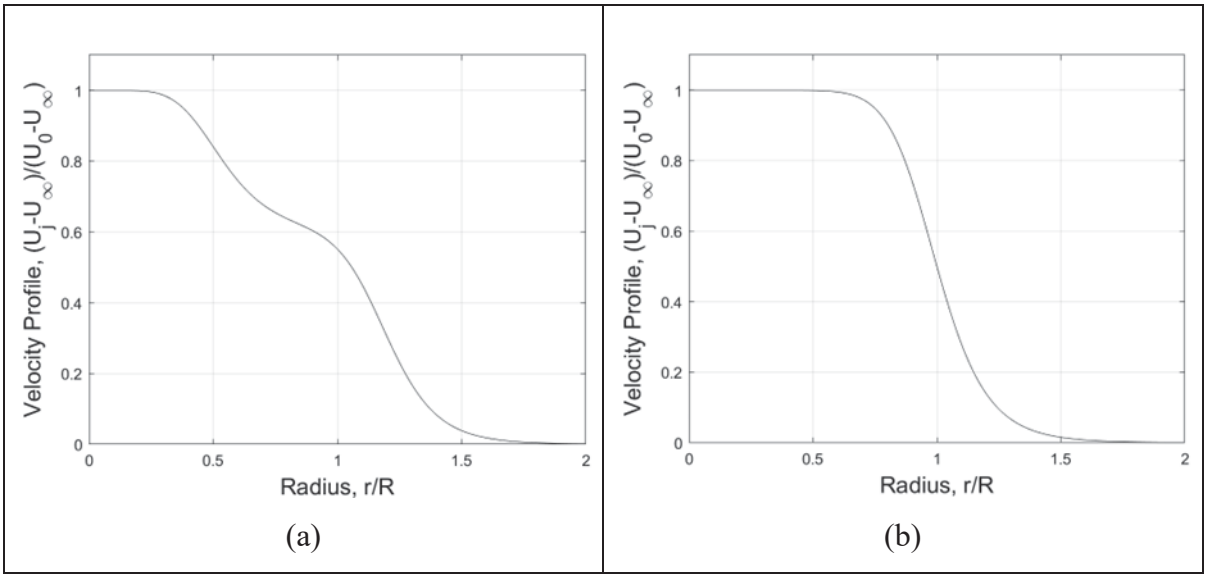

Figure 3.2 Initial jet-velocity profile for the LEAP-1A/33 engine: (a) with bypass configuration (realistic profile); (b) without bypass configuration (equivalent profile)

LES simulations were carried out for 2 s of plume age, i.e., after nozzle emission, using high-order schemes with a dimensionless time step $\Delta t_j = 0.02$ for jet phase, i.e., CFL is less than 0.6, where R and $U(R)$ are the length and velocity scale used. Specifically, a sixth-order compact scheme (Lele, 1992) and a third-order Runge-Kutta scheme were respectively used in

space and time to solve the Eulerian phase equations. The particle position was computed from Equation (3.2) using a fourth-order Adams-Bashforth scheme, while a fourth-order Runge-Kutta scheme was used to compute the particle radius. The cells have a constant grid size, $\Delta x = \Delta y = \Delta z = 0.15R$ and consists of 141×141×82 grid points. This mesh configuration was quantitatively assessed by checking the energy spectra in the jet plume as suggested by Georgiadis, Rizzetta, and Fureby (2010).

Table 3.1 Input parameters for jet contrail simulations for three turbofan engines at cruise condition: CFM56-5B3/3 (medium), LEAP-1A/33 (high), and UHBR (ultra-high bypass-ratio)

Engine type	CFM56-5B3/3			LEAP-1A A33			UHBR		
Ambient Conditions (35000 ft)	215 K	220 K	225 k	215 K	220 K	225 k	215 K	220 K	225 k
Bypass ratio, bpr (-)	5.4			10.5			15		
Core velocity, U_c (m.s-1)	548	552	554	409	415	420	377	382	387
Bypass velocity, U_b (m.s-1)	309	312	316	304	307	311	298	301	305
Bypass static temperature, T_b (K)	237	242	248	229	234	240	220	226	231
Core static temperature, T_c (K)	607	613	622	568	582	597	601	616	631

Figure 3.3 presents the energy spectra of with bypass and without bypass simulations at 0.5 s. The range of turbulent scales covers the inertial zone where the energy transfer from large to small scales, i.e., small to large wavenumbers, follows the universal power-law rate, with a slope of -5/3. The results confirmed that the grid size used provided a well-resolved LES configuration in which the energy contained in small scales was three orders of magnitude below that of the large ones.

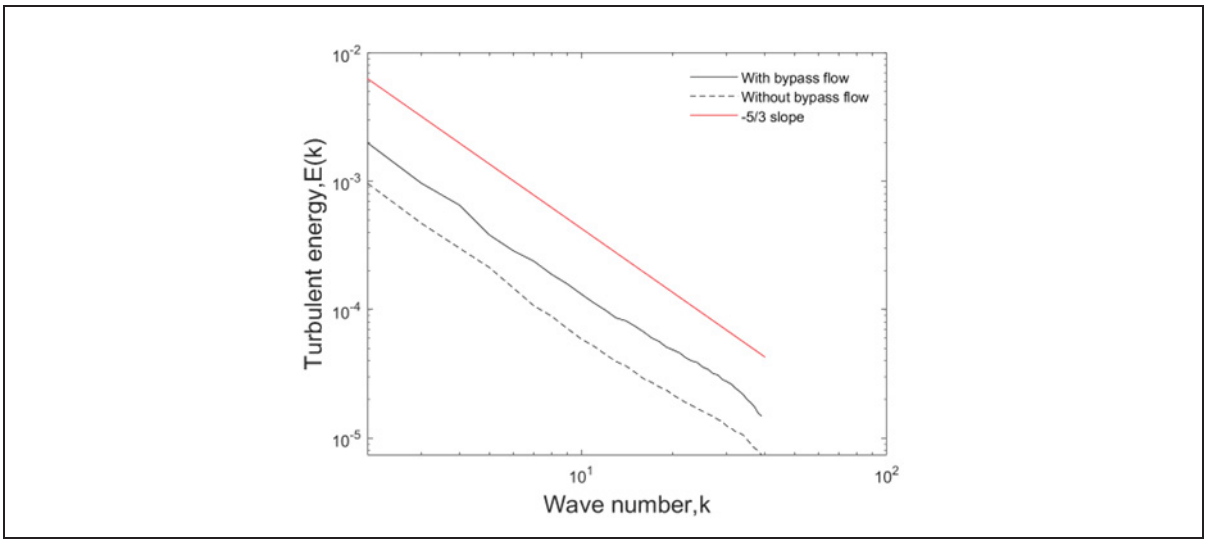

Figure 3.3 Turbulent kinetic energy spectra for the with bypass and without bypass configurations at 0.5 s under baseline ambient conditions (T_a= 220 K)

Numerical simulations of contrail formation in the literature mainly employ a temporal approach due to the high computational costs associated with the spatial modeling approach. In this approach, the length of computational domain is significantly reduced, allowing for a finer grid resolution in the cross-section, thereby enhancing the accuracy of turbulent mixing calculations between the hot exhaust and cold ambient air. The predictive capability of the proposed microphysical model, coupled with a temporal jet simulation, was demonstrated herein by evaluating the CFM56-3 engine under the baseline conditions described by D. C. Lewellen (2020). The simulation was conducted at an ambient temperature of T_a=218.8 K, with a monodisperse distribution of soot particles and an initial emission index of soot $EI_{soot} = 10^{16}$ (#/kg-fuel). Unlike the modeling approach of Lewellen (D. C. Lewellen, 2020), which initialized the temporal LES fields 1 m downstream using RANS and employed a binned microphysics model, the initialization employed in present study was different, as explained in Section 3.2, and an online detailed Lagrangian microphysical approach was utilized as detailed in Section 3.3. Differences in the initialization, in microphysical modeling, and in averaging may contribute to variations in results. Nevertheless, the results (Figure 3.4) showed a consistent trend with the findings from one of Lewellen's turbulence realizations (D. C.

Lewellen, 2020), suggesting that both studies capture similar primary effects of mixing and subsequent moisture competition to reach the same ice emission index at around 0.23 s.

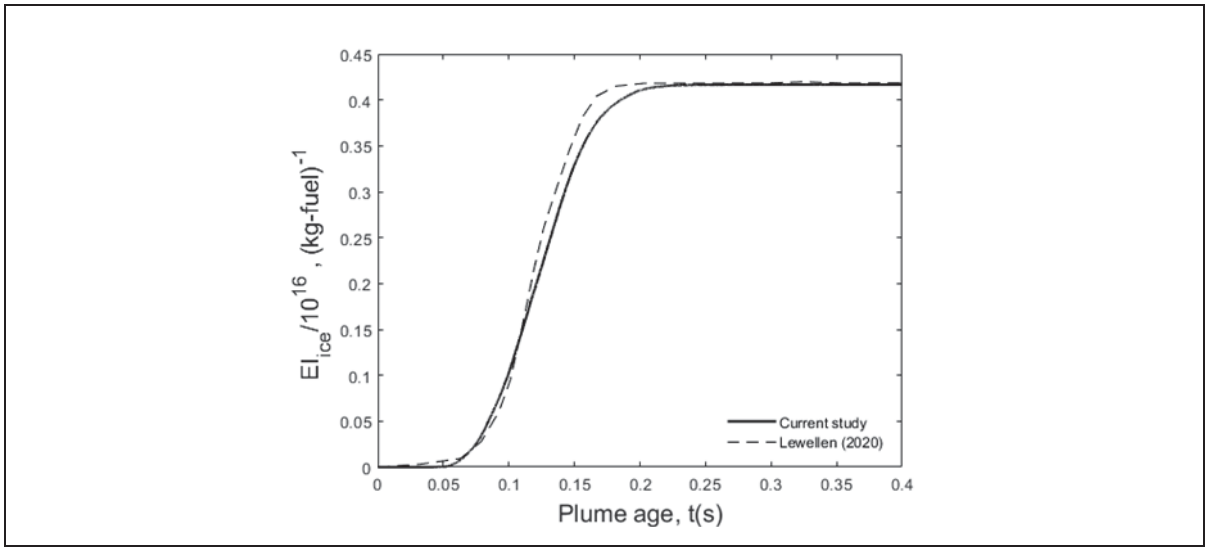

Figure 3.4 Temporal evolution of the apparent ice number emission index under the baseline conditions of Lewellen (D. C. Lewellen, 2020)

3.3 Results and Discussion

3.3.1 Bypass Flow Effect: Comparison between Turbofan and Turbojet

The near field contrail from the LEAP-1A/33 engine (bpr = 10.5) was compared to its equivalent turbojet configuration with the same specific thrust, as presented in Figure 3.1. Figure 3.5 presents the evolution of mean water vapor pressure (Figure 3.5(a)) and mean ice saturation ratio (Figure 3.5(b)), calculated by averaging over all particles in 3D domain at each time step along the exhaust jet, as functions of particle temperature, for both the with bypass and without bypass configurations. The results correspond to the time interval from approximately 0.23 to 2 s, starting from the onset of plume saturation. These figures illustrate differences in the vapor pressure and saturation behavior, particularly when the early plume condenses and becomes supersaturated. Based on Ulrich Schumann (2000), the bypass engine demonstrates greater overall propulsion efficiency by generating thrust more effectively by

moving a larger volume of air at a lower velocity. As a result, the mixing line slope is anticipated to be steeper, as shown in Figure 3.5(a).

A further analysis of mixing lines as a function of temperature, depicted in Figure 3.5(b), reveals that the average mixing lines, with and without bypass flow, cool down and become ice-saturated at around 252-255 K. The formation threshold temperature for a water-saturated atmosphere falls within the freezing range defined in the figures of Kärcher et al. (2015). The results in Figure 3.5(a) and Figure 3.5(b) indicate that the bypass flow promotes higher mean water vapor pressure and mean ice saturation ratios. This highlights the role of engine bypass flow in the near field, as it influences the thermodynamic properties and potentially affects contrail formation.

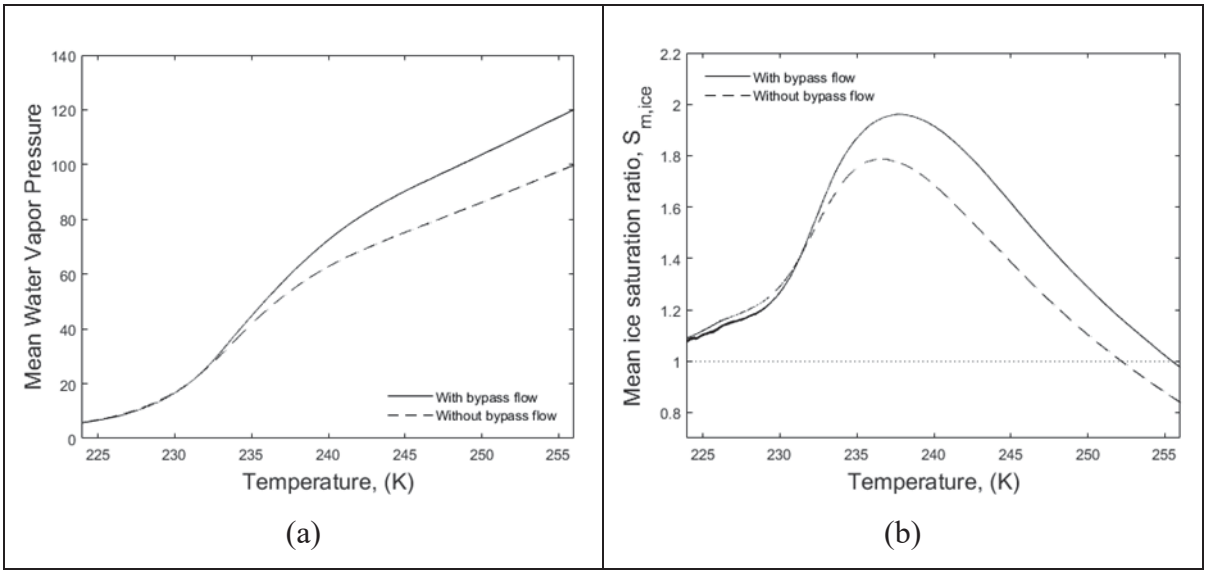

Figure 3.5 a) Mean saturation vapor pressure and b) mean ice saturation ratio as functions of temperature for with bypass and without bypass configurations at T_a=220 K

Following the temperature-dependent results, Figure 3.6 illustrates the time evolution of the mean ice saturation, calculated over all particles, from plume release up to 2 s, comparing with bypass and without bypass configurations. After plume release, the ice saturation ratio rapidly increases, reaching a peak around 0.4–0.5 s, with the with bypass case peaking slightly earlier. The with bypass configuration exhibits a higher maximum value (~1.96) compared to the

without bypass case, reflecting enhanced moisture availability due to bypass flow entrainment. After the peak, both curves gradually decline and stabilize at values slightly above 1, indicating persistent supersaturation conditions that are conducive to ice crystal growth.

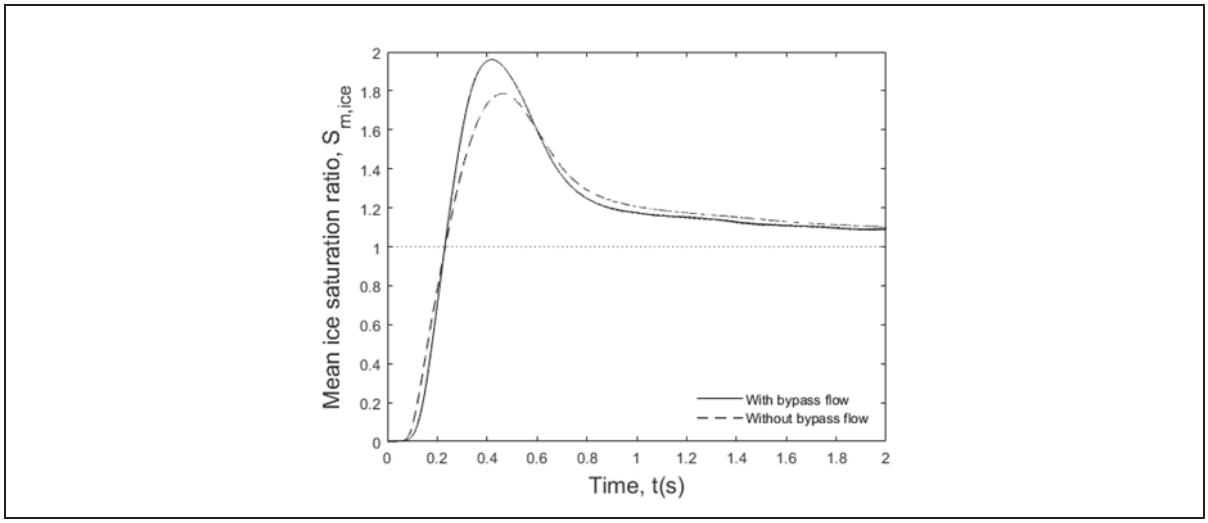

Figure 3.6 Temporal evolution the mean ice saturation ratio along the exhaust jet for with bypass and without bypass configurations at T_a=220 K

The bypass flow affects the mean saturation and particle activation, influencing the ice particle size in the engine near field. Similar to the behavior observed in coaxial jets, where the introduction of a secondary flow enhances the mixing efficiency (Van Hoot et al., 2021), the bypass configuration, as shown in Figure 3.7(a), results in a larger mean particle radius as compared to the engine without bypass. Figure 3.7(b) reveals that at up to 0.2 s, the bypass effect is minimal, reflecting the elongation of the potential core (as also illustrated in Figure 3.6), which initially slows down the mixing process. However, after 0.2 s, the bypass flow accelerates the activation process due to enhanced mixing (Villermaux & Rehab, 2000), leading to a higher fraction of activated/freezing particles over a shorter time period.

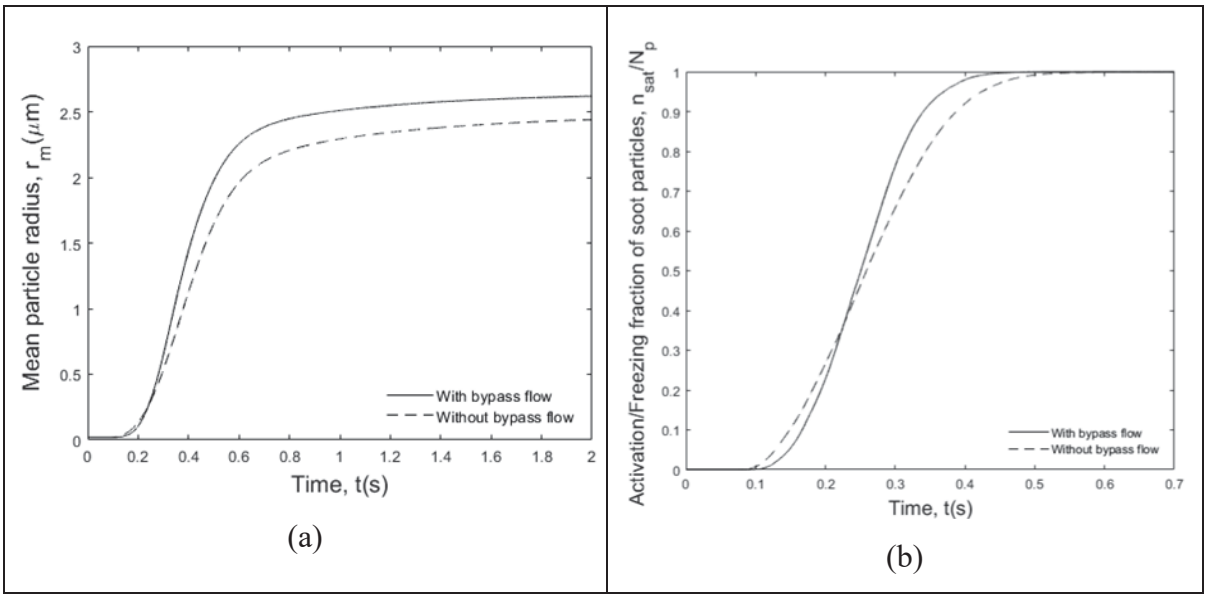

Figure 3.7 Temporal evolution of a) mean particle radius and b) fraction of activated soot particles for with bypass and without bypass configurations at T_a=220 K

From the comparison of the with and without bypass flow configurations, the key factors influencing these setups were identified as relating to mixing, which ties directly to the dynamics of the flow. Figure 3.8 presents the iso-surfaces of dimensionless vorticity magnitude at different time intervals during the temporal modeling of the with and without bypass configurations. It illustrates the temporal evolution of vorticity structures from 0.05 s to 0.075 s. These instantaneous turbulent structures are generated by Kelvin-Helmholtz instabilities in the jet mixing layer, becoming less organized and persistent due to the complex dynamics at hand. As shown in Figure 3.3, the with bypass case exhibited a higher turbulent energy as compared to the without bypass case. For the same iso-surface values at different time steps, the higher turbulent energy associated with larger eddies resulted in a greater dimensionless vorticity magnitude for the with bypass configuration, as demonstrated in the comparison between Figure 3.8(a) and Figure 3.8(b). The vortex structures in the with bypass case are more dispersed and less concentrated, as observed from 0.3 s onward. This dispersion is due to the increased velocity ratio between the secondary and primary flows in the with bypass case (see Table 3.1 for the velocity values of core and bypass flows), which enhances mixing and promotes a greater radial development of turbulence (Villermaux & Rehab, 2000). As the

simulation progresses, the jet flow transitions to a fully turbulent state, characterized by the breakdown of large turbulent structures, into smaller, more chaotic ones.

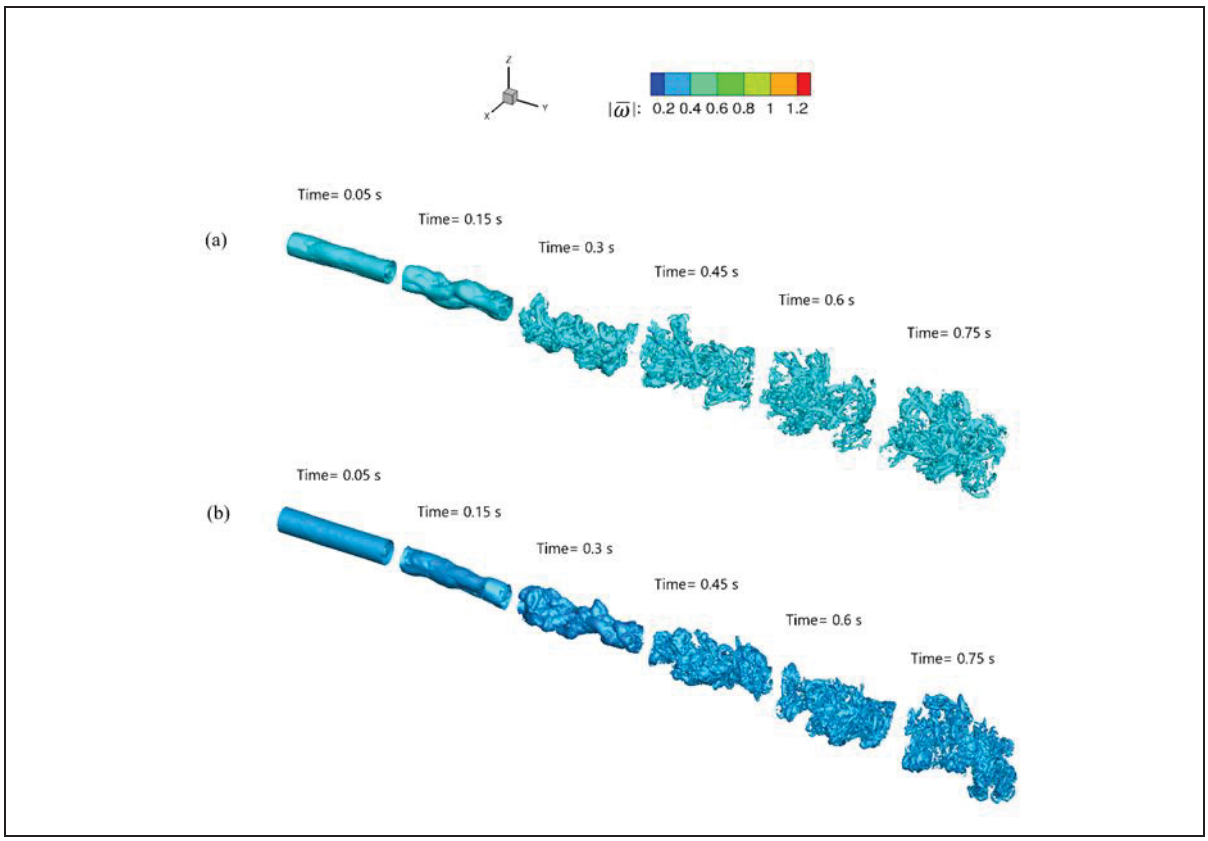

Figure 3.8 Iso-surfaces of coherent structures from dimensionless vorticity for the LEAP-1A/33 at T_a=220 K, from 0.05 s to 0.75 for a) with and b) without bypass configurations

3.3.2 Bypass ratio Effect: Comparison between Realistic Engine configurations

The near field contrails from three realistic turbofan engines having different bypass ratios were compared: CFM56-5B3/3 (medium bpr=5.4), LEAP-1A/33 (high bpr=10.5), and UHBR (ultra-high bpr=15).

To visually elucidate the contrail formation within the jet regime, Figure 3.9 shows the temporal evolution of temperature contours for the UHBR and CFM56-5B3/3 engines, under base ambient condition (T_a= 220 K). Figure 3.9 illustrates the formation of activated/freezing

particles (white spheres) from soot (black spheres) within the jet mixing zone as it interacts with the surrounding (cooler) ambient air. The activation and freezing processes for particles initiate at the jet periphery, where molecular and turbulent diffusion mechanisms blend with the cold atmosphere, causing a drop in temperature. Conversely, in the central region of the jet, the temperature remains relatively higher, inhibiting the immediate formation of ice. Subsequently, as the plume progresses in the atmosphere, activation of soot particles and freezing of ice crystals occur within the core jet. This phenomenon is accelerated by turbulent mixing in the UHBR engine, as is evident from the contours (Figure 3.9(a)); no soot particles remain inactivated in the plume at 0.45 s, in contrast to the CFM56-5B3/3 engine.

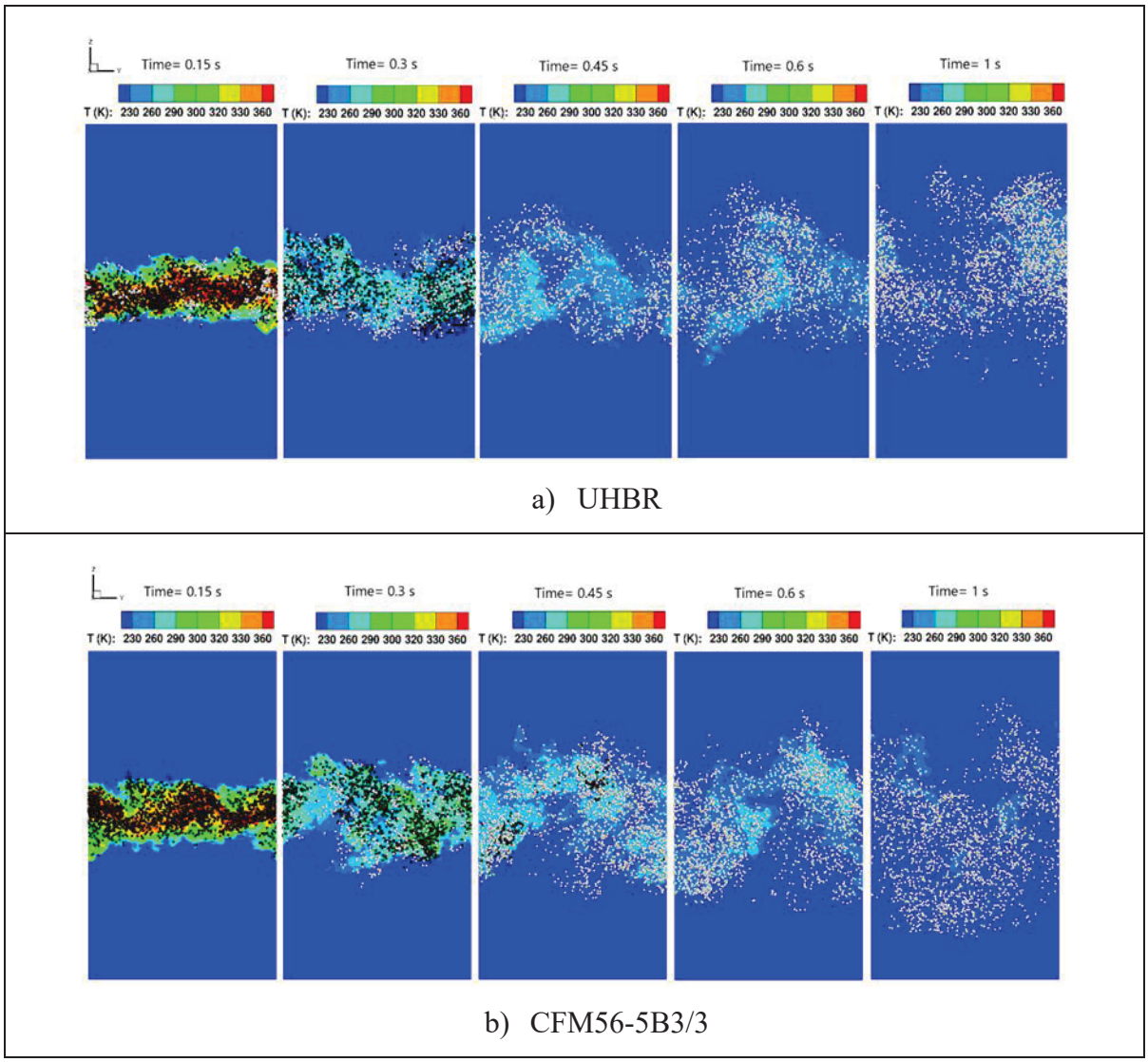

Figure 3.9 Temporal evolution of temperature with particle distribution for (a) UHBR and (b) CFM56-5B3/3 at T_a=220K. Black particles represent soot, while white particles denote activating/freezing particles

Figure 3.10(a) illustrates the temporal evolution of the mean particle radius along the jet plume for three different engines: UHBR, LEAP-1A/33, and CFM56-5B3/3 under base ambient conditions (T_a=220 K). The mean particle radius for all three engines increases over time, demonstrating the particle growth process from activation to droplet formation, freezing, and subsequent ice particle growth, as the exhaust gases cool and mix with the ambient air. The growth curves of the mean particle radius begin to plateau around 0.6-0.8 s, indicating that a

balance has been achieved between the particle growth and the jet dispersion or dilution. Initially, the UHBR engine exhibits a slightly larger mean particle radius, which may be attributed to its high bypass ratio. However, after about 0.6 s, the influence of other factors related to the different exhaust conditions as discussed in Segalini and Talamelli (2011), led to the CFM56-5B3/3 surpassing the UHBR, thus exhibiting a greater mean particle radius. Different ambient conditions may affect these differences between engines, as will be discussed in Section 3.3.3.

Figure 3.10(b) presents the evolution of activation/freezing fraction of soot particles over time, for the three engine configurations: UHBR, LEAP-1A/33, and CFM56-5B3/3. The slope of each curve represents how quickly soot particles undergo activation or freezing in different engine models under the same ambient conditions. The UHBR with the highest bypass ratio has the quickest response among the three engines. It rises sharply and reaches a near complete activated/freezing fraction around 0.3 s.

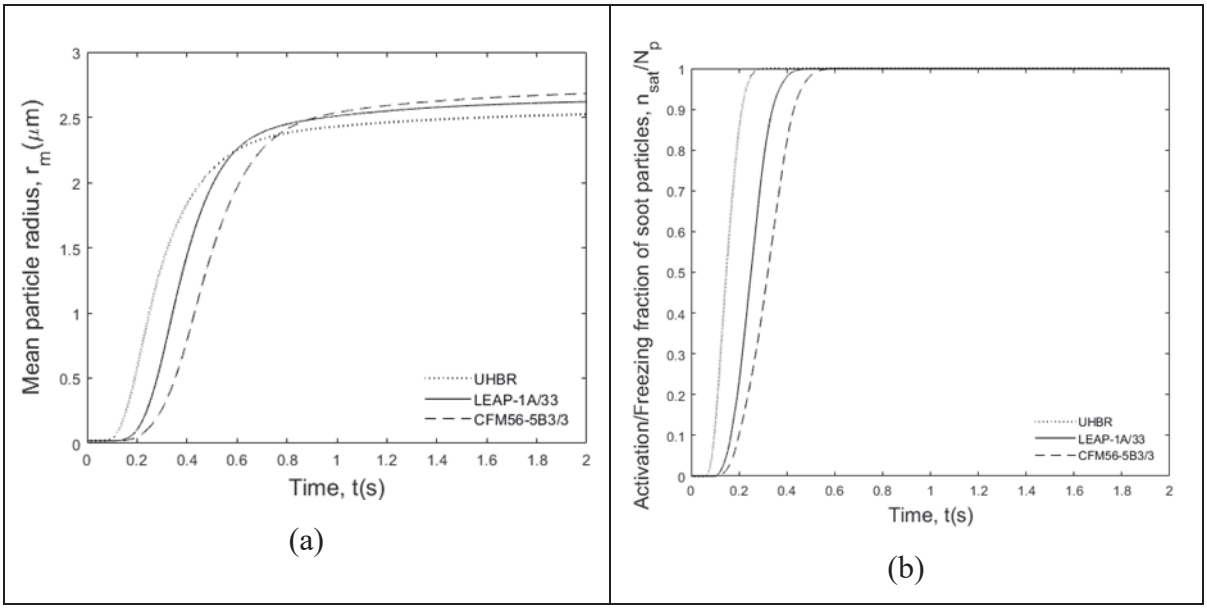

Figure 3.10 Temporal evolution of a) the mean particle radius along the jet plume and b) the fraction of activated soot particles for three engines at T_a=220K

Figure 3.11 displays the Probability Density Functions (PDFs) for particle radii at two subsequent time intervals: 0.5 s and 1 s in plume age from the three studied engines at an ambient temperature of 220 K. As Jeßberger et al. (2013) reported, the total number concentrations and particle size distribution are influenced by the engine type. The comparison of the PDFs in both jet configurations over time confirms the findings in Figure 3.10(a), highlighting that bypass flow promotes the formation of larger ice particles under the same conditions. At 0.5 s, the PDFs for CFM56-5B3/3 and LEAP-1A/33 are broad, with peaks at 1.5 μm and 1.94 μm, respectively, indicating particle size variabilities. In contrast, the UHBR shows a narrower distribution, with a peak at 2 μm, suggesting more consistent particle sizes. By 1 s (Figure 3.11(b)), CFM56-5B3/3 and LEAP-1A/33 continue to exhibit a wider range of particle sizes, while the UHBR still maintains a narrower range, with their peaks moving closer together, likely due to the homogenization effects of plume mixing and dilution over time.

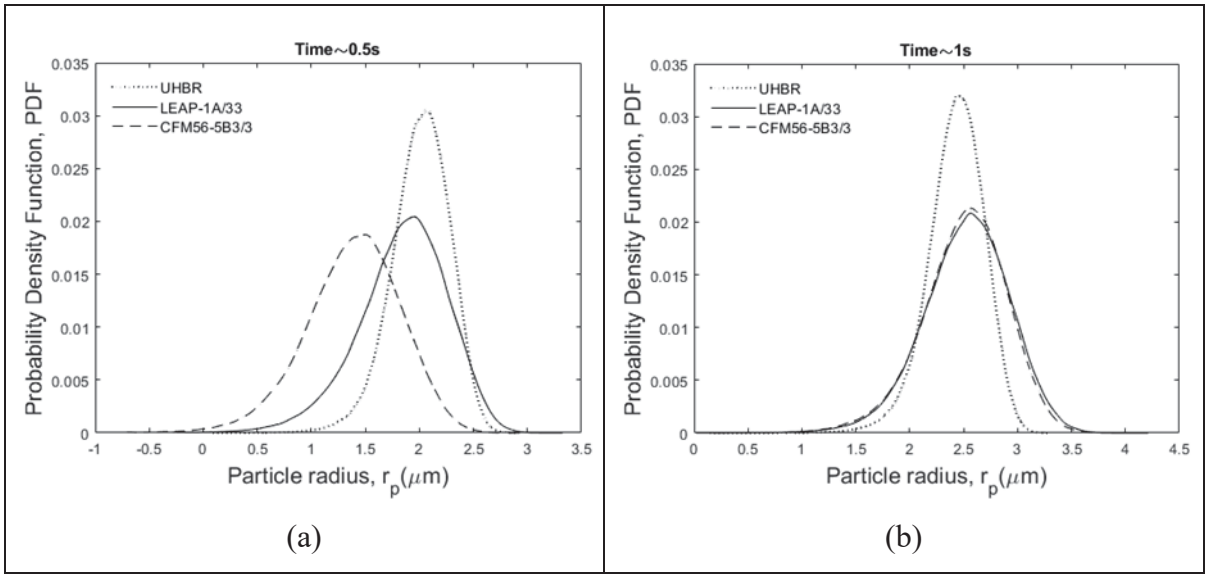

Figure 3.11 PDFs of particle radii at a) 05s, b) 1 s after exhaust emission for three engines: CFM56-5B3/3, LEAP-1A/33, and UHBR at T_a=220 K

3.3.3 Effect of ambient conditions

Figure 3.12 illustrates the temporal evolution of the mean particle radius (r_m) along the jet plume for three different engine types: UHBR (a), LEAP-1A/33 (b), and CFM56-5B3/3 (c), each subjected to three ambient temperatures: 215 K, 220 K, and 225 K. It is apparent from the three panels that lower ambient temperatures generally led to larger particle sizes for all engine types. However, the rate and extent of the particle growth vary between the engines. Notably, the engine with the highest bypass ratio (UHBR) exhibited the least variation across the range of ambient temperatures studied. Conversely, the engine with the lowest bypass ratio (CFM56-5B3/3) exhibited more pronounced differences in particle growth as a function of ambient temperature, suggesting the combined effects of ambient conditions and engine bypass ratio on the ice crystal size.

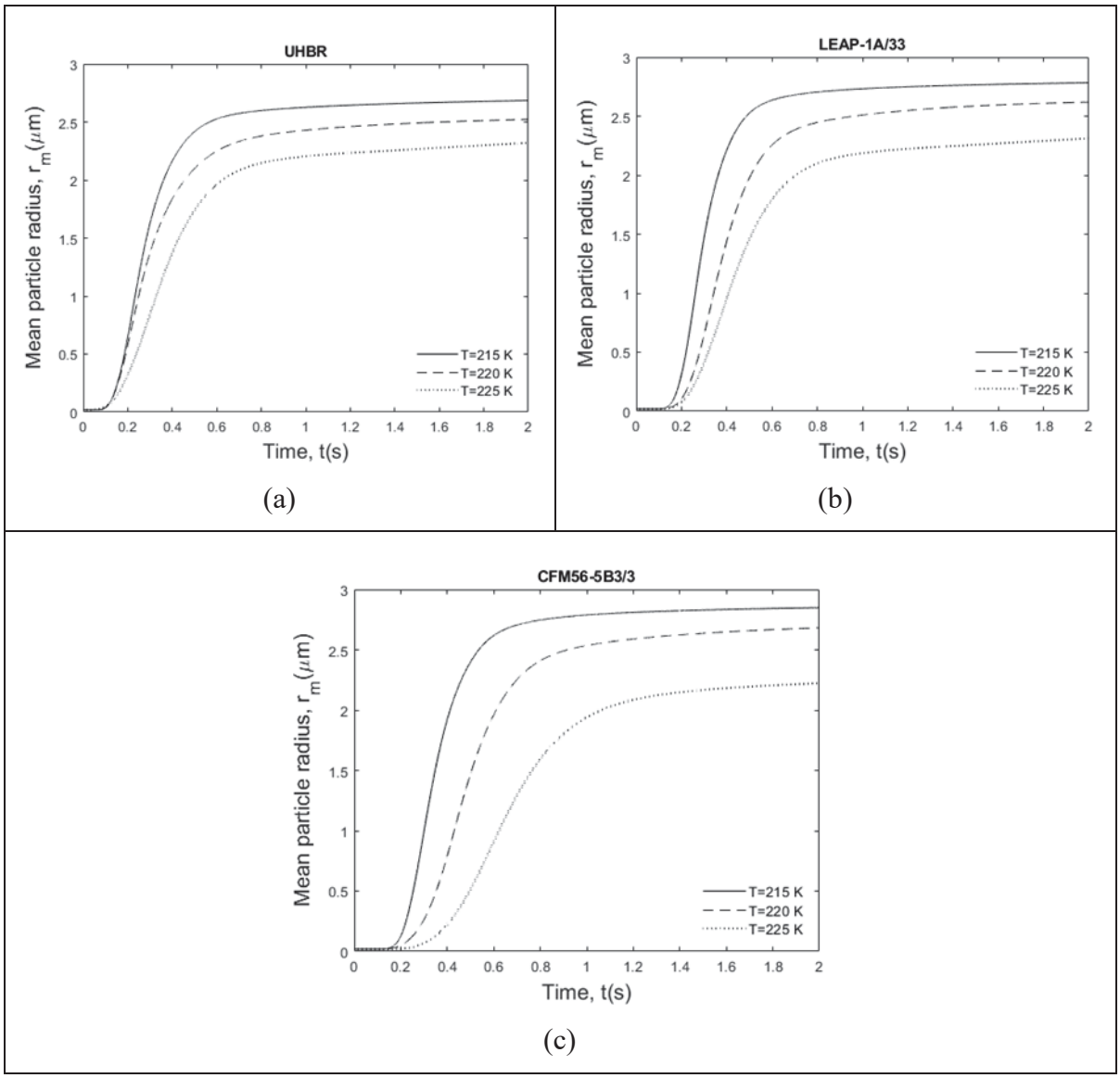

Figure 3.12 Temporal evolution of the mean particle radius for three engine types: a) UHBR, b) LEAP-1A/33, and c) CFM56-5B3/3, under three different ambient conditions

Figure 3.13 illustrates the temporal evolution of the fraction of activated/freezing particles over the total number of exhausted soot particles along the jet plume for three engines: UHBR (a), LEAP-1A/33 (b), and CFM56-5B3/3 (c), evaluated at three ambient temperatures: 215 K, 220 K, and 225 K. The results revealed that a lower ambient temperature significantly enhanced the activation or freezing of soot particles. Similar to the trends observed in particle radius, the activation trends for the UHBR engine exhibited smaller differences across the various

temperatures. This suggests that contrail characteristics formed behind high bypass ratio engines, such as the UHBR, exhibit less sensitivity to variations in ambient temperature in the 215 K-225 K range (i.e., below the contrail formation threshold).

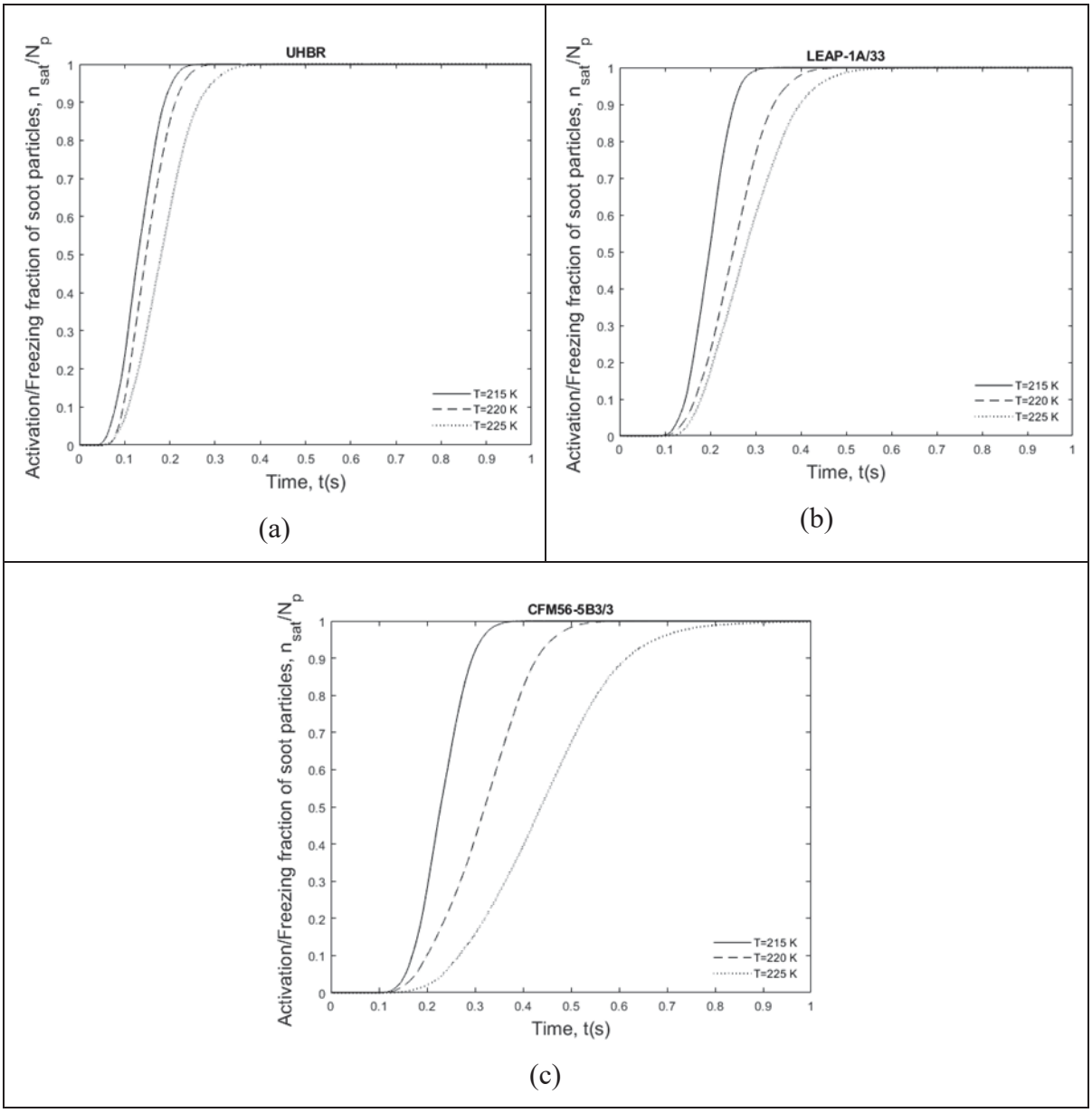

Figure 3.13 Temporal evolution of the activation/freezing fraction of soot particles for three engine types: a) UHBR, b) LEAP-1A/33, and c) CFM56-5B3/3, under three different ambient conditions

To assess the sensitivity to variations in soot particle number emissions for the CFM56-5B3/3 engine at an ambient temperature of T_a=220 K, simulations were conducted using two soot number emission indices (EI_{soot}): 10^{13}(#/kg-fuel), corresponding to the LEAP-1A/33 engine, and 10^{14} (#/kg-fuel), representative of the CFM56-5B3/3 engine. Figure 3.14 presents the associated evolutions of activated/freezing soot particles in plume age. The results were consistent with the findings of Ferreira et al. (2024), showing that soot particles compete for water vapor condensation, and as a result, higher soot number emissions lead to a lower fraction of activated particles under similar ambient conditions, ultimately forming smaller ice particles, as highlighted by H-W Wong et al. (2013).

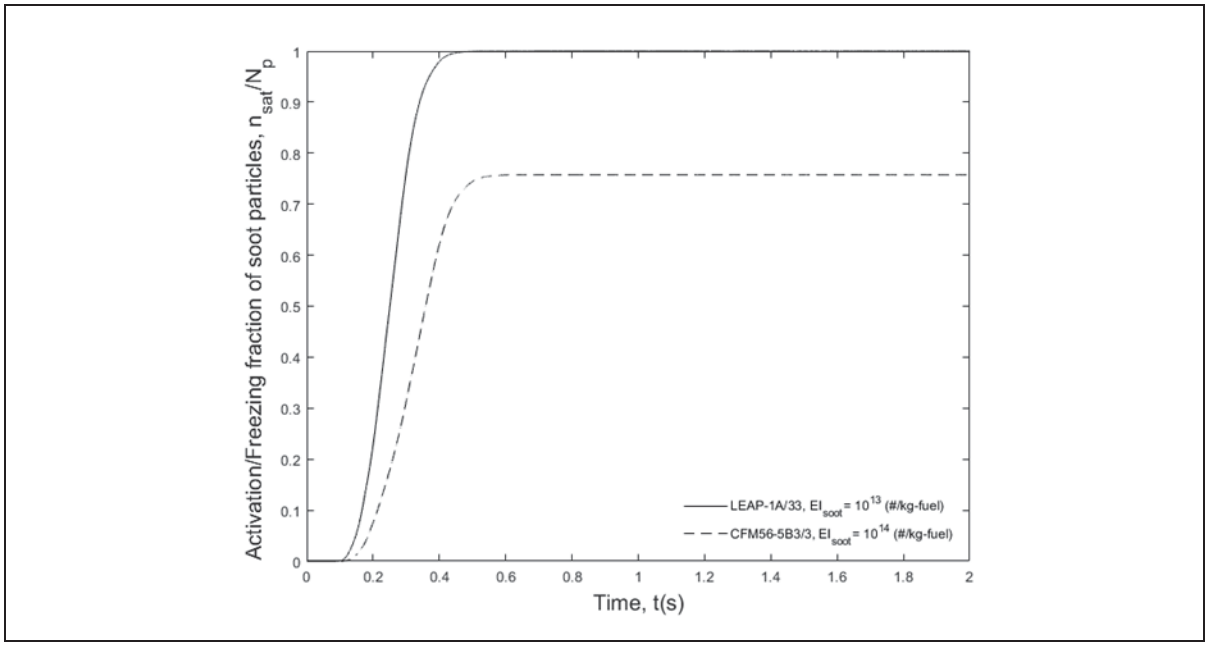

Figure 3.14 Temporal evolution of the fraction of activated soot particles for two emission indices representing LEAP-1A/33 and CFM56-5B3/3 engines at cruise temperature T_a=220 K

The contrail characteristics from the CFM56-5B3/3 engine exhibited greater variations across the different ambient temperatures, as shown in Figure 3.12 and Figure 3.13. The contour plots in Figure 3.15 illustrate the instantaneous temperature fields within the exhaust plume of a CFM56-5B3/3 engine at different ambient temperatures (215 K, 220 K, and 225 K) at 0.3 s in

plume age, highlighting the behavior of dry soot (black spheres) and activating/freezing particles (white spheres). The contours are taken in the spanwise direction, perpendicular to the jet axis. At the lowest ambient temperature of 215 K, the white particles exhibited complete activation/freezing. Increasing the ambient temperature to 220 K and then to 225 K resulted in a lower fraction of soot particles being activated or freezing, especially in the jet core. Notably, Figure 3.15(c) (T_a=225 K) shows predominantly non-activated/freezing black soot particles at 0.3 s, although some particles near the cooler edges of the jet begin to activate/freeze. These observations qualitatively demonstrated how the ambient condition locally affects contrail formation for the same engine operating at the same thrust level.

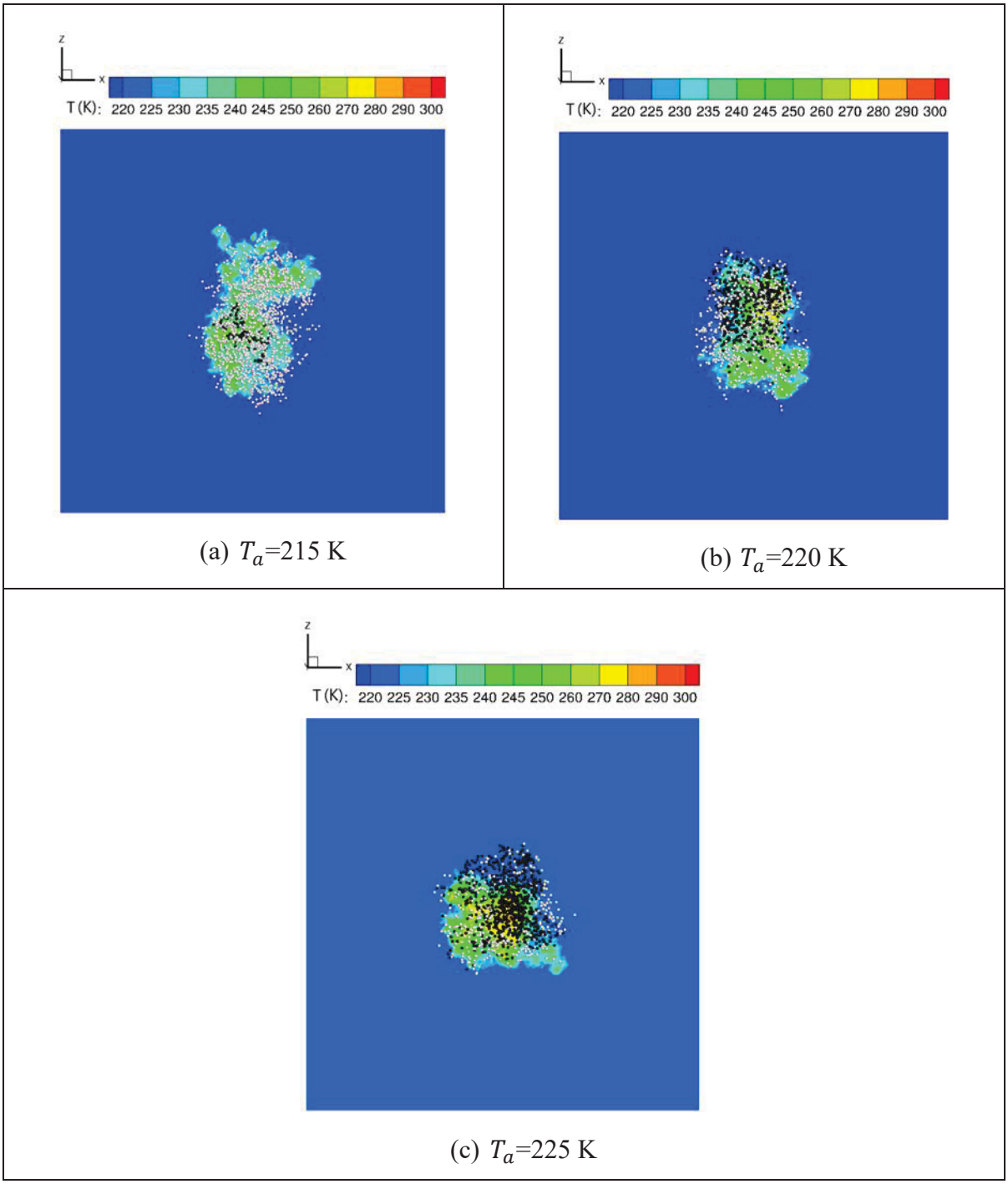

(a) T_a=215 K

(b) T_a=220 K

(c) T_a=225 K

Figure 3.15 Temperature field with soot (black) and activating/freezing particles (white) at 0.3 s for CFM56-5B3/3 at a) T_a=215 K, b) 220 K, and c) 225 K

3.4 Conclusion

Large eddy simulations were performed with a Eulerian-Lagrangian approach to investigate the engine bypass effect on the characteristics of turbofan near field contrails at cruise conditions. The 3D CFD research code, FludiLES, developed and validated for jet contrail applications, was used. Ice crystal formation was modeled as a sequential process: starting with the activation of soot particles using a solubility model, followed by droplet growth, and then, homogeneous freezing with subsequent ice crystal growth.

A comprehensive analysis of the bypass effect was carried out via two comparative studies. In the first, the jet plume from the LEAP-1A/33 turbofan engine was compared to its equivalent turbojet configuration having the same specific thrust to isolate the bypass flow effect on early plume characteristics. The bypass flow enhanced the mixing of the core jet, leading to an increase of up to 30% in the mean ice particle radius as compared to the equivalent single jet (turbofan) configuration. In the second study, the bypass rate effect was investigated by comparing near field contrails formed behind three realistic turbofan engines: CFM56-5B3/3 (bpr= 5.4), LEAP-1A/33 (bpr= 10.5) and UHBR (bpr= 15), characterizing low, medium, and high bypass ratio engines, respectively. The results demonstrated that each engine exhibited distinct contrail characteristics, namely, the fraction of activated soot and the size of formed ice crystals, across varying ambient temperatures (215 K, 220 K, and 225 K). Notably, lowering the ambient temperature generally led to larger particle sizes for all engine types. However, the rate and extent of the particle growth varied between the different bypass ratio engines. Notably, the characteristics of the contrails formed behind the UHBR engine exhibited the least variation across the range of ambient temperatures studied. Conversely, the engine with the lowest bypass ratio (CFM56-5B3/3) exhibited more pronounced differences in ice crystal growth and in the fraction of activated/freezing particles as a function of the ambient temperature. Quantitatively, the UHBR engine led to a fraction of activated/freezing particles (over the exhaust soot particle number) of approximately 1 at 0.3 s in plume age, as compared to only 0.75 and 0.4 for both medium and low bypass ratio engines, respectively. This indicated that the modern high-efficiency engine (with a high bypass ratio) increased the rate of

activation and freezing processes in the near field. These observations are only relevant to the jet regime without wing vortex interactions; after 0.6 s in plume age, the microphysical properties of contrails formed behind the three engines showed minor differences in terms of mean particle radius and fraction of activated/freezing particles. It is important to note that different engines indirectly affect the intensity of generated wake vortices through various factors, including the flight mission, thrust level, and engine/aircraft configuration. These jet-vortex interactions and mixing, which were not considered in this study, could greatly influence the subsequent evolution of the microphysical characteristics of contrails, warranting the need for further investigations.

In this regard, the proposed model can serve as the foundation for more advanced simulations, including jet-vortex interactions with microphysical transformations of aerosols, thereby enabling a comprehensive assessment of the water vapor emission impact from hydrogen-fueled aircraft engines as a promising alternative to conventional-fueled engines.

3.5 Acknowledgements

This research was enabled in part by support provided by the Calcul Québec (calculquebec.ca) and the Digital Research Alliance of Canada (alliancecan.ca).

CHAPTER 4

ROLE OF SOOT PARTICLE PROPERTIES AND ACTIVATION IN CONTRAIL FORMATION USING LES WITH ONLINE-COUPLED MICROPHYSICS

Parisa Afkari [a], Mohamed Chouak [a], Sébastien Cantin [a], François Garnier [a]

[a] Département de Génie Mécanique, École de Technologie Supérieure,
1100 Notre-Dame West, Montreal, Quebec, Canada H3C 1K3

Paper submitted in *Journal of Aerosol Science*, September 2025

Abstract

Aircraft contrails form through ice crystal nucleation initiated primarily by engine-emitted particles. These ice crystals can lead to persistent contrails, contributing to climate warming, thus making understanding their activation a key target for mitigation strategies. This study presents large eddy simulations (LES) coupled with a refined soot activation model. The microphysical scheme incorporates solute effects through the hygroscopicity parameter (κ), enabling a more realistic representation of water activity during soot particle activation. These numerical simulations utilized a LEAP-1A engine under realistic cruise conditions, examining three scenarios: (i) varying κ (0.0005, 0.005, 0.0142), corresponding to an equivalent fuel sulfur content (FSC) of 50, 410, and 1270 ppm, respectively; (ii) varying initial soot emission indices (10^{13}–10^{15}– #/kg-fuel), and (iii) varying initial soot core radii (10–30 nm). The results indicated that reducing κ from 0.0142 to 0.0005 slightly reduced particle radii, yet increased the activation fraction by ~20% due to enhanced water vapor availability. Reducing the initial soot number in two successive steps, from 10^{15} to 10^{13} #/kg-fuel, increased the mean particle radius from ~0.3 μm to 2.4 μm in 1 s and elevated the activated fraction by ~66%. Larger initial soot core radii enhanced activation by ~20%, with mean particle radius differences reaching ~80% in around 0.4 s and narrowing to ~10% by 1s. Additionally, the results highlighted the importance of 3D LES with online-coupled microphysics, whereas the 0D offline box model overpredicted activation and misrepresented the κ sensitivity.

Keywords: Contrails, activation, soot particle, microphysics, water activity, hygroscopicity parameter

4.1 Introduction

An initial contrail forms when moist exhaust mixes with cold ambient air. Depending on surrounding atmospheric conditions, it can be short or long lived, spreading and increasing cloudiness and affecting Earth's radiation balance ((IATA), Report, 2024; Bernd Kärcher, 2018). Mitigating contrail impacts requires both comprehensive data and improved models, which allow to evaluate possible trade-offs between alternative strategies. Recent advances in measurements and modeling now allow contrail formation to be investigated at smaller scales, bridging detailed process-level studies and large-scale models (Bernd Kärcher, 2018).

The dynamics of the exhaust plume, together with ambient atmospheric conditions, are among the key factors influencing near-field contrail formation (Roberto Paoli, Nybelen, Picot, & Cariolle, 2013). However, uncertainties remain about how the mixing of the aircraft engine exhaust plume with ambient air affects microphysical processes during contrail development. Addressing this gap is crucial, as mixing can control initial ice crystal properties, influencing contrail evolution under given ambient conditions (Singh, Sanyal, & Wuebbles, 2024). Early evaluations of plume mixing lines began with the Schmidt-Appleman criterion, which established the fundamental conditions for contrail formation and threshold temperatures (Appleman, 1953; Schmidt, 1941). Ulrich Schumann (1996) later refined this framework by defining the slope of the mixing line based on engine parameters. However, jet plume mixing and cooling are more complex processes, influencing the evolution of individual exhaust particles while preserving their unique physical properties throughout plume development. A detailed examination of mixing processes under diverse conditions poses challenges in experimental campaigns, underscoring the role of numerical studies in providing comprehensive insights. To incorporate additional physical processes, three-dimensional (3D) simulations resolve plume dynamics using turbulence modeling (D. C. Lewellen, 2020),

capturing the inhomogeneity of plume mixing in the radial directions. In contrast, zero-dimensional (0D) mixing models simplify plume dynamics through parameterized or plume-averaged mixing (Kärcher et al., 2015). In recent decades, numerous numerical studies have contributed to understanding the dynamics and mixing processes in the jet and vortex phases of contrail formation. For example, J.-C. Khou et al. (2015) conducted 3D simulations to investigate early contrail development in the near-field of a realistic commercial aircraft, focusing on mixing processes in the bulk plume and achieving alignment with experimental data.

Accurately predicting contrail properties requires coupling exhaust plume mixing dynamics with microphysical processes. Such coupling occurs either through online integration within each time step, enabling real-time interactions, or through offline sequential processing once plume dynamics have been computed. To add complexity while managing computational costs, some studies, such as Roberto Paoli et al. (2008), opted for offline microphysical modeling. However, for improved accuracy, studies like J. Khou et al. (2017) utilized 3D online Reynolds Averaged Navier Stokes (RANS) coupling with an Eulerian approach for ice particle growth, capturing detailed interactions in contrail formation. Furthermore, D. C. Lewellen (2020) ran large eddy simulations (LES) of the exhaust plume and bin-resolved Eulerian microphysics, and then initialized the offline wake/vortex stage from a precomputed 2D RANS wake field. Subsequently, Bier et al. (2022) conducted a Lagrangian particle microphysics box model (LCM) offline along trajectory ensembles extracted from a FludiLES 3D LES and compared it against Lewellen's 3D LES (D. C. Lewellen, 2020) with online microphysics. The offline ensemble yielded a higher ice emission index (EI_{ice}) because inter-parcel mixing in the full 3D LES suppresses subsequent activation—an interaction absent from the offline ensemble. X. Vancassel et al. (2014) also noted that the online approach provided immediate feedback and improved the accuracy of dynamic growth and ice formation predictions as compared to the offline approach.

Aircraft engine exhaust releases a complex mixture of emissions that contribute to contrail formation, either directly, as condensation nuclei, or indirectly, through chemical reactions that

enhance the process. Soot particles can play a major role in the exhaust plume, particularly under soot-rich conditions, by competing with liquid plume particles and ambient aerosols for the formation of contrail ice particles (Kärcher & Yu, 2009). However, soot particles are inherently hydrophobic (Popovicheva et al., 2008). A portion of the fuel sulfur in the exhaust plume is converted into sulfuric acid, which condenses onto the soot surfaces, enhancing their hygroscopicity and promoting water uptake through heterogeneous nucleation (U Schumann et al., 1996). Thus, the presence of sulfuric acid influences aircraft exhaust composition and contrail formation. Ulrich Schumann et al. (2002), as part of SULFUR experiments (SULFUR 1–7), demonstrated that at a fuel sulfur content (FSC) greater than 100 ppm, sulfuric acid becomes the dominant precursor for volatile aerosols, with conversion fractions of 0.34–4.5% for older engines and approximately 3.3 ± 1.8% for modern engines. The number of contrail ice particles correlated strongly with the soot particle number at lower sulfur contents, but became increasingly dependent on the fuel sulfur content as the FSC increased. Additionally, as (Fangqun Yu, Karcher, et al., 2024) indicated, the activation of non-volatile soot particles during contrail formation is primarily influenced by the primary soot particle size, rather than the soot aggregate size, which accounts for the lower-than-expected fraction of soot particles forming ice. The authors also acknowledged large uncertainties regarding the contribution of volatile particles, particularly due to the unaccounted role of organic species in nucleation and growth. However, they noted that under soot-poor and low-FSC conditions, as well as in soot-rich regimes, the influence of volatile particles on ice formation is limited. On the other hand, reducing soot number emissions, the primary factor controlling ice particle formation in contrails, remains a key area of interest, with numerous campaigns evaluating different strategies. Mitigation approaches, such as using alternative fuel blends with lower aromatic content, are particularly relevant for this purpose (Bräuer et al., 2021; Voigt et al., 2021).

Beyond particle type, incorporating particle activation in theoretical and numerical studies provides the basis for activation theory in contrail microphysics. Petzold et al. (2005) experimentally investigated how the fuel sulfur content affects the Cloud Condensation Nuclei (CCN) activation of soot, interpreting measurements with classical Köhler theory. They concluded that a higher FSC (via increased sulfuric acid (H_2SO_4) and sulfate coating) increases

the soluble fraction and decreases the activation diameter (i.e., lowers the critical supersaturation). Subsequently, Petters and Kreidenweis (2007) introduced a method to describe the relationship between the particle dry diameter and CCN activity using a single hygroscopicity parameter (κ). They provided hygroscopicity values ranging from highly soluble to non-hygroscopic components. The model effectively predicts CCN activity for mixed particles, including those containing surface-active materials, with results agreeing within uncertainties of measured values. The κ-Köhler activation method has thus been used in several numerical studies and modeling efforts, such as those by D. C. Lewellen (2020), Bier et al. (2022) and Fangqun Yu, Karcher, et al. (2024). However, in each of these cases, including challenges remained in modeling, particularly with respect to the coupling strategy and the representation of fully 3D mixing.

As such, this study aims to integrate the κ-Köhler theoretical model into an online-coupled microphysical model within the FludiLES high-order LES code. It focuses on the activation of soot particles within 1s of plume age under different κ, simulating different levels of FSC, as well as varying initial soot number emission indices (EI_{soot}) and initial dry soot core radii. To the authors' knowledge, no prior study has numerically evaluated these scenarios while simultaneously coupling soot particle activation online with the 3D plume dynamics.

The paper is structured as follows: Section 4.2 details the numerical methodology adopted, covering both the dynamic and microphysical models. Section 4.3 presents the parametric microphysical analysis in four subsections. The first examines the effect of fuel sulfur content. The second investigates initial soot number emission indices, and the third explores variations in the initial dry soot core radius. Lastly, the fourth subsection compares a 0D offline box model with 3D LES with online-coupled microphysics to evaluate how explicitly resolving plume dynamics influences microphysics.

4.2 Numerical Methodology

The modeling approach simulates an exhaust jet, with a gas phase (air and water vapor) containing soot particles from the core flow. The exhausted particles compete for activation, leading to ice particle formation within the plume. This section presents the mathematical framework for the flow dynamics of the jet gas phase, followed by solid phase modeling for soot particles and their microphysical pathways in contrail formation.

4.2.1 Dynamic Flow Model

Jet flow is simulated using an Eulerian-based temporal LES approach with a high-order compressible computational fluid dynamic (CFD) code, FludiLES. The 3D Navier-Stokes equations for the gas-flow mixture and the numerical setup in FludiLES were detailed in Afkari, Chouak, Cantin, and Garnier (2025). The LES method filters large-scale turbulence while modeling smaller scales using a subgrid-scale hybrid Smagorinsky model. Given the low mass ratio between the solid phase (soot, ambient, and ice particles) and the gas phase (air and water vapor mixture), no coupling terms are included in the continuity and momentum equations. Thermal exchanges from particles to the gas phase are included in the energy equation, as latent heat release from ice particle growth modifies the local temperature field and contributes to thermal coupling. Furthermore, mass exchange is included via the mass transfer term, where the source term in the water vapor mass fraction conservation equation represents the condensation rate, calculated using an ice particle growth model detailed in the microphysical section (4.2.2). This research code, based on the finite-difference scheme with spectral-like resolution, has been extensively used and validated for engine jet and aircraft wake applications (S Brunet et al., 1999; C Ferreira Gago et al., 2002; C Ferreira Gago et al., 2003; F Garnier, Brunet, et al., 1997; F Garnier et al., 2003; François Garnier et al., 2014; Labbe et al., 2007; X. Vancassel et al., 2014).

The velocity field (U(r)) is initialized as the sum of two hyperbolic tangent profiles, based on the core and bypass jet flow parameters described in Afkari et al. (2025). The initial

temperature profile is obtained using the Crocco-Busemann relation, whose validity has been numerically verified for jet flow (Panda, Zaman, & Seasholtz, 2004). To initiate the development of turbulent phenomena, low-amplitude pseudo-random perturbations, weighted by a Gaussian profile and centered at the jet half-width radius, are added to the velocity components, such that:

$$u'_{x,z} = A \times f \times (exp\left\{-\left[\frac{1}{4}\frac{R}{\theta}\left(\frac{r}{R}-\frac{R}{r}\right)\right]^2\right\})^{1/2} \tag{4.1}$$

$$u'_{y} = A \times f \times (0.95\ exp\left\{-\left[\frac{1}{4}\frac{R}{\theta}\left(\frac{r}{R}-\frac{R}{r}\right)\right]^2\right\} + 0.05(1-U(r)))^{1/2} \tag{4.2}$$

The terms $u'_{x,z}$ represent the transverse velocity components, and u'_y represents the velocity component in the flow direction. In the Cartesian coordinate system, the radial distance r is given by $r = \sqrt{x^2 + z^2}$. Here, θ denotes the boundary layer thickness of the jet shear layer, R defines the center of the jet shear layer, A represents the amplitude of the perturbations (set to around 5%), and f is a pseudo-random function generated by the random_number subroutine:

$$f = 2 \times random\_number - 1 \tag{4.3}$$

f depends on each point in space and spans the [−1;1] interval. It should be noted that the values taken by f for each velocity component are, a priori, different and uncorrelated.

A realistic LEAP-1A engine at cruise conditions is considered under a supersaturation ambient condition, followed by a detailed microphysical study, which is presented in the next section. The engine parameters considered for the dynamic simulation are summarized in Table 4.1.

Table 4.1 Input parameters for dynamic simulations of LEAP-1A engine

Parameters	**Values**
Core velocity, U_c (m.s^{-1})	400
Bypass velocity, U_b (m.s^{-1})	306
Bypass static temperature, T_b (K)	233
Core static temperature, T_c (K)	580
Molar fraction of jet core water vapor, $X_{(H_2O)_{v-jet}}$	0.0394
Cruise altitude (ft)	35000
Ambient temperature (K)	218.8
Ice relative humidity	110%
Molar fraction of ambient water vapor, $X_{(H_2O)_{v-\infty}}$	10.5 10^{-5}

In order to discretize the convective terms in the equations of continuity, momentum, and energy, a compact scheme of order 6 is used (Lele, 1992). Aside from being accurate in terms of truncation error, this scheme is also highly precise in terms of pseudo-spectral accuracy (dispersive error) over a wide range of scales. This resolution is quantified from a Fourier analysis described by Vichnevetsky and Bowles (1982). Also, the dissipation terms are discretized by second-order centered schemes. Time discretization is performed using a compact three-step Runge-Kutta scheme. This scheme is third-order accurate, and requires only two storage arrays per variable (DeVries, DeVries, & Hasbun, 2011).

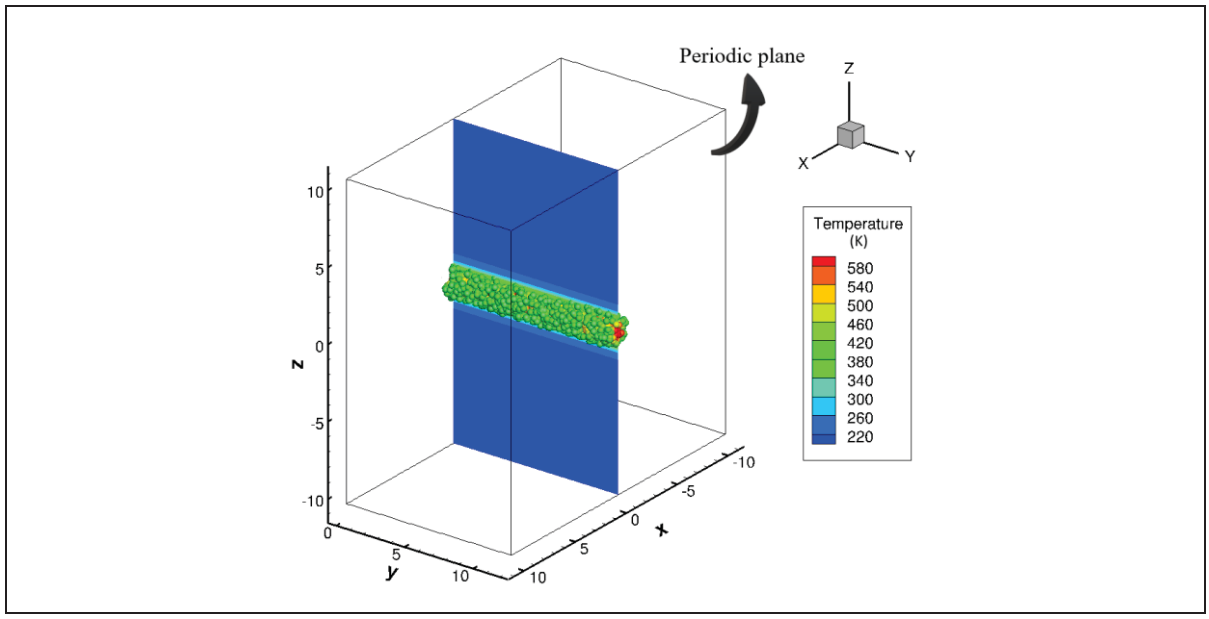

Figure 4.1 Initial state of the computational domain at time zero, showing the temperature distribution on an x-slice plane and the initialized soot particles. The inlet and periodic boundary planes are indicated, defining the domain's flow conditions

The temporal domain comprises approximately 3 million cells with a structured grid of size $\Delta x = \Delta y = \Delta z = 0.15R$ and a maximum Courant number of 0.6. Grid errors are evaluated using the Grid Convergence Index (GCI) method proposed by Celik, Ghia, Roache, and Freitas (2008), comparing this case with finer and coarser meshes. The analysis, based on axial velocity within the mixing layer, resulted in $GCI_{fine}^{23} \approx 0.21\%$ and $GCI_{coarse}^{12} \approx 0.45\%$, confirming mesh convergence.

The initial configuration of the computational domain is depicted in Figure 4.1, showing the temperature initialization on an x-slice plane along with the soot particles distributions. At time zero, the inlet condition is applied, while the outlet follows a periodic condition. For subsequent times, periodic boundary conditions are enforced at both the inflow and outflow faces, ensuring flow continuity by reintroducing outgoing structures at the inflow boundary. Non-reflective boundary conditions are imposed on the remaining surfaces, and a sponge zone is introduced to dampen turbulent fluctuations.

4.2.2 Microphysical Model

The microphysical model in this study builds upon the framework established in Afkari et al. (2025), incorporating an improved activation method for each particle and accounting for the solute effects of the fuel sulfur content by modeling water activity through the hygroscopicity parameter (κ). In the modeling framework, numerical particles each represent a packet of physical particles.

Based on the κ-Köhler theory introduced by Petters and Kreidenweis (2007), the equilibrium saturation ratio over a droplet or ice crystal surface can be expressed using Equation (4.4). This equilibrium depends on the Kelvin effect (Equation (4.5)), the water activity in the droplet solution, α_w and the droplet radius:

$$Ke = \frac{2\sigma_w M_{H_2O}}{RT_p\rho_P} \tag{4.4}$$

$$S_k = \alpha_w . \exp\left(\frac{Ke}{r_p}\right) = \frac{{r_p}^3 - {r_d}^3}{{r_p}^3 - {r_d}^3(1-\kappa)} \exp\left(\frac{Ke}{r_p}\right) \tag{4.5}$$

where r_p represents the droplet radius and r_p denotes the initial dry core radius of particles. On the other hand, the actual saturation ratio of water vapor, S_w, is determined based on the local available water vapor content in the environment, which varies due to the mixing between the jet plume and the ambient atmosphere. It is defined as:

$$S_w = \frac{P_{H_2O,actual}}{P_{sat}(T_P)} \tag{4.6}$$

where P_{sat} is the saturation vapor pressure at particle temperature, T_P, computed based on the equations provided by Murphy and Koop (2005), and $P_{H_2O,actual}$ is the partial pressure of available water vapor determined by the mole fraction of water vapor, X_v, in the environment and the local atmospheric pressure, P:

$$P_{H_2O,actual} = X_v \times P \tag{4.7}$$

The mole fraction X_v depends on the water vapor mass fraction, X_v, and the ratio of molar masses of water vapor (M_{H_2O}) and dry air (M_{Air}). Since mass fractions are typically more accessible in atmospheric modeling, the molar fraction is obtained by:

$$X_v = \frac{Y_v}{Y_v + (1 - Y_{mix}).\frac{M_{H_2O}}{M_{Air}}} \tag{4.8}$$

The mass fraction Y_v reflects the mixing between the ambient air and the jet plume, and varies spatially based on the degree of dilution between these two sources. The governing equation can therefore be written as:

$$Y_v = \mathcal{D}\left(Y_{v,j} - Y_{v,a}\right) + Y_{v,a} \tag{4.9}$$

where D is the plume dilution factor, which equals 1 at the jet exhaust and decreases toward 0 as the ambient entrainment dominates. $Y_{v,j}$ is the water vapor mass fraction of the jet exhaust, and $Y_{v,a}$ is the water vapor mass fraction of the ambient atmosphere.

The initial water vapor content of the ambient air and the jet plume are prescribed based on their respective mole fractions and the molar mass ratio of water vapor to dry air. So, each particle in the microphysical model has its own equilibrium saturation ratio, S_k, which depends on its local properties. By applying the Fukuta-Walter model (Fukuta & Walter, 1970) for particle growth and modifying its equilibrium saturation, which was previously based solely on the Kelvin effect, the equation can be expressed as follows:

$$r_P \frac{dr_P}{dt} = \frac{S_w - S_k}{C_t S_k + C_P} \tag{4.10}$$

$$C_t = \frac{L^2 M_{H_2O} \rho_P}{k_g R\, T_P^2 f_{3\alpha}} \tag{4.11}$$

$$C_P = \frac{R\,T_P \rho_P}{P_{sat} D_v\, M_{H_2O} f_{3\beta}} \tag{4.12}$$

$$f_{3\alpha} = \frac{r_p}{r_p + \frac{k_g \sqrt{2\pi M_{Air} R T_P}}{\alpha P_\infty (C_{P,a} - R/2)}} \tag{4.13}$$

$$f_{3\beta} = \frac{r_p}{r_p + \frac{D_v}{\beta}\sqrt{\frac{2\pi M_v}{R T_P}}} \tag{4.14}$$

where C_t and C_P are factors related to particle growth and evaporation, and ρ_P represents the particle density, calculated using the correlation for water and ice phases as presented by Pruppacher and Klett (1979). The term $f_{3\alpha}$ is a correction factor that accounts for the temperature difference between the particle and the surrounding air. P_∞ represents the fluid pressure in the region far from the particle, beyond the boundary layer, where the influence of the particle on the fluid flow is negligible. D_v denotes the diffusivity of vapor in air, while L is the reference length scale, also used in the calculation of the Reynolds number. $C_{P,a}$ refers to the specific heat capacity of air at constant pressure, R is the universal gas constant, and k_g represents the thermal conductivity of the gas.

The coefficient α (thermal accommodation coefficient) characterizes heat transfer at the interface between the gas and the condensed phase, describing how effectively molecules exchange energy upon collision, with a value of 1 being used in this study (Y. Li, Davidovits, Kolb, & Worsnop, 2001). The parameter β represents the fraction of molecules that condense (or deposit) upon impacting the surface, commonly referred to as the condensation coefficient (or deposition coefficient, depending on the phase change). Observations indicate that β can range from 0.01 to 1, with a value of 1 being used in this case (Mozurkewich, 1986).

Furthermore, freezing is determined by the calculated freezing temperature for each particle, as given by Equation (4.15) (Kärcher et al., 2015):

$$T_* \cong \frac{1}{a_1}\left[\ln\left(\frac{a_1 \dot{T}}{V_w}\right) - a_2\right] \tag{4.15}$$

where $a_1 = -3.5714\ (K^{-1})$ and $a_2 = 858.719$ are empirical constants (Riechers et al., 2013), $\dot{T}$ is the plume cooling rate, and V_w is the droplet volume.

Overall, the microphysical activation and growth strategy for aerosol particles begins with particles in their initial state as dry aerosols possessing a fixed core radius (r_d). Each particle experiences local environmental conditions, notably the saturation ratio (S_w). Since the equilibrium saturation ratio (S_k) depends on particle growth and starts off undefined, it is initialized considering only Kelvin effects. Activation occurs once the environmental saturation exceeds this threshold ($S_w > S_k$), triggering water condensation and marking the transition from a dry to a wet state. As the particle grows, even a slight increase in radius causes the water activity effects described by κ-Köhler theory to become more pronounced, decreasing the equilibrium saturation ratio below that predicted by the Kelvin effect alone; this reduction indeed indicates particle activation. Particle growth continues as long as the environmental saturation, linked to dynamic mixing, remains above the recalculated equilibrium saturation ratio ($S_w > S_k$), with the growth rate governed by diffusion-driven processes. If S_w falls below S_k, evaporation or sublimation may occur. However, particles are constrained from evaporating or sublimating to sizes smaller than their original dry core, thereby conserving the aerosol nucleus. Additionally, the strategy accounts for both liquid and ice phases by incorporating phase-specific properties such as surface tension, density, saturation vapor pressure, and the heat of vaporization or sublimation. Here, the particle's phase is determined by local temperature conditions, ensuring a comprehensive and physically realistic representation of aerosol particle evolution from activation through subsequent growth while maintaining numerical stability.

Initially, a scenario is investigated in which three different FSCs are analyzed at a soot emission index of $EI_{soot} \approx 10^{14}$ (#/kg-fuel). This emission index was adopted to reflect the lean-burn design of the LEAP-1A (ICAO, 2024). Also, the initial dry soot core radius is fixed at 20 nm. Building on the experimentally established correlations between FSC and the soluble volume

fraction (ε_{sol}) of sulfuric acid (Petzold et al., 2005), three distinct FSC levels are considered, as follows:

- Low FSC (50 ppm): $\varepsilon_{sol} < 0.1\%$
- Medium FSC (410 ppm): $0.8\% < \varepsilon_{sol} < 1.2\%$
- High FSC (1270 ppm): $2.7\% < \varepsilon_{sol} < 3\%$

For the effective κ, based on the work of Petters and Kreidenweis (2007) on the hygroscopicity for mixed particles, where $\kappa = \sum_i \varepsilon_i \kappa_i$, it can be expressed as:

$$\kappa = \varepsilon_{sol} \times \kappa_{sol} + (1 - \varepsilon_{sol})\kappa_{insol} \tag{4.16}$$

where κ_{sol} and κ_{insol} denote the hygroscopicity parameter of the soluble and insoluble fractions, respectively. It is assumed that the contribution of each component to the overall hygroscopicity is proportional to its volume fraction. For soot particles coated with diluted sulfuric acid, κ_{sol} is taken as 0.5 (Kärcher et al., 2015), while κ_{insol} is considered 0, reflecting both the absence of the modeled insoluble material associated with the soot particle surface and its inherently insoluble, hydrophobic nature. When κ approaches 0, the particle becomes effectively hydrophobic, meaning it does not induce solute-driven water uptake or activate as a CCN. The water activity tends toward unity ($\alpha_w \approx 1$), corresponding to the wetting of the dry particle by a pure water film. It behaves as an insoluble but wettable particle, forming a thin water layer without significant uptake, following the Kelvin equation for vapor pressure over a curved surface (Petters & Kreidenweis, 2007). Consequently, the κ for soot particles under varying FSC conditions, calculated using Equation (4.16), is presented in Table 4.2.

Table 4.2 Hygroscopicity parameters (κ) for soot particles at varying FSC levels

Fuel Sulfur Content Level	Soluble Volume Fraction of Sulfuric Acid	κ of Coated Soot Particles
50 ppm	$\varepsilon_{sol} \approx 0.1\%$	0.0005
410 ppm	$\varepsilon_{sol} \approx 1\%$	0.005
1270 ppm	$\varepsilon_{sol} \approx 2.85\%$	0.0142

To further assess the parametric study of the microphysical model, the effects of varying soot particle numbers are analyzed for a low FSC content (50 ppm), which has the smallest κ for coated soot particles, with an initial dry soot core radius set at 20 nm. A low FSC level of 50 ppm is selected in a bid to minimize the contribution of volatile particle activation, which is not considered in this study, particularly in soot-poor regimes, as emphasized by Fangqun Yu, Karcher, et al. (2024). An analysis was conducted for the following soot number emission indices:

- Low soot number: $EI_{soot} \approx 10^{13}$ (#/kg-fuel)
- Moderate soot number: $EI_{soot} \approx 10^{14}$ (#/kg-fuel)
- High soot number: $EI_{soot} \approx 10^{15}$ (#/kg-fuel)

Finally, in the last parametric study, the effects of the initial dry soot core radius are evaluated at a soot number emission index of $EI_{soot} \approx 10^{14}$ (#/kg-fuel) under a low FSC (50 ppm). The three selected dry core radii of soot particles are as follows:

- Small initial soot particles radius: $r_d = 10\ nm$
- Medium initial soot particles radius: $r_d = 20\ nm$
- Large initial soot particles radius: $r_d = 30\ nm$

Therefore, this integrated methodology ensures a comprehensive analysis by examining all three critical aspects of the behavior of the particles that may influence their activation and alter the microphysical pathway in contrail formation.

To compare 3D LES with online-coupled microphysics to a 0D offline box model for contrail formation, a temporal 3D LES without microphysics was conducted to isolate jet-phase mixing. A passive exhaust tracer defines the plume, and at each time step, the plume mean temperature $\bar{T}(t)$ and the plume mean dilution/entrainment rate $\bar{\omega}(t)$ are diagnosed from mass-weighted averages of the tracer and thermodynamic fields and saved on the LES time grid. These stored temperature and entrainment histories then drive the time-dependent 0D offline box model, which computes microphysical source terms for phase change mass transfer and latent heat. The box model employs the same κ-Köhler activation, condensational growth, sublimation, and freezing scheme as in the online-coupled microphysics configuration described in Afkari et al. (2025), and is solved offline. The gas-phase water vapor mass fraction and temperature evolve according to below equations (Kärcher, 2016), driven by the $\bar{T}(t)$ and $\bar{\omega}(t)$ exported from the LES:

$$\dot{\bar{Y}}_v(t) = -\bar{\omega}(t)\left[\bar{Y}_v(t) - Y_{v,a}\right] + \xi_{PC}^{micro}(t) \tag{4.17}$$

$$\dot{\bar{T}}(t) = -\bar{\omega}(t)\left[\bar{T}(t) - T_a\right] + \xi_{LH}^{micro}(t) \tag{4.18}$$

where T_a is the ambient temperature and $\bar{Y}_v(t)$ is calculated from Equation (4.9), and the mean plume dilution factor $\bar{\mathcal{D}}$(t) is obtained by integrating the LES-derived dilution rate $\bar{\omega}(t)$ over time. The microphysical source term ξ_{PC}^{micro} represents the phase-change mass transfer (negative for condensation, positive for sublimation) obtained from the κ-Köhler activation criterion using the soot dry core radius and κ, followed by diffusional growth; the thermal term ξ_{LH}^{micro} accounts for latent heat release or uptake. The total ice number and mass moments evolve under the same activation, growth, and freezing parameterizations as in the online model. The offline box carries no spatial coordinates and applies no feedback to the flow; rather, it integrates these equations in time on the LES time grid using the stored drivers.

4.3 Results Analysis

4.3.1 Effect of Particle Hygroscopicity

The LEAP-1A engine with a fixed soot emission index of $EI_{soot} \approx 10^{14}$ (#/kg-fuel) and an initial dry soot core radius of 20 nm has been considered for three FSC levels – low (50 ppm), medium (410 ppm), and high (1270 ppm) – to analyze the effects of the FSC on the activation of soot particles.

Firstly, to visualize the 3D effects of jet microphysical properties, Figure 4.2 presents the evolution of actual water saturation (S_w) over plume particles and along the central plane of the domain at various time steps, for a case with an initial $EI_{soot} \approx 10^{14}$ (#/kg-fuel), an FSC of 410 ppm, and an initial dry soot core radius of 20 nm. As the jet mixes with ambient air, particles attain varying saturation levels, allowing uptake of ambient moisture. When the local saturation exceeds the particle equilibrium saturation, which occurs earlier for particles within the mixing region, droplet formation takes place. Over time, further cooling and supersaturation, particularly in regions of enhanced mixing, drive the transition from liquid droplets to ice crystals, shown as white particles.

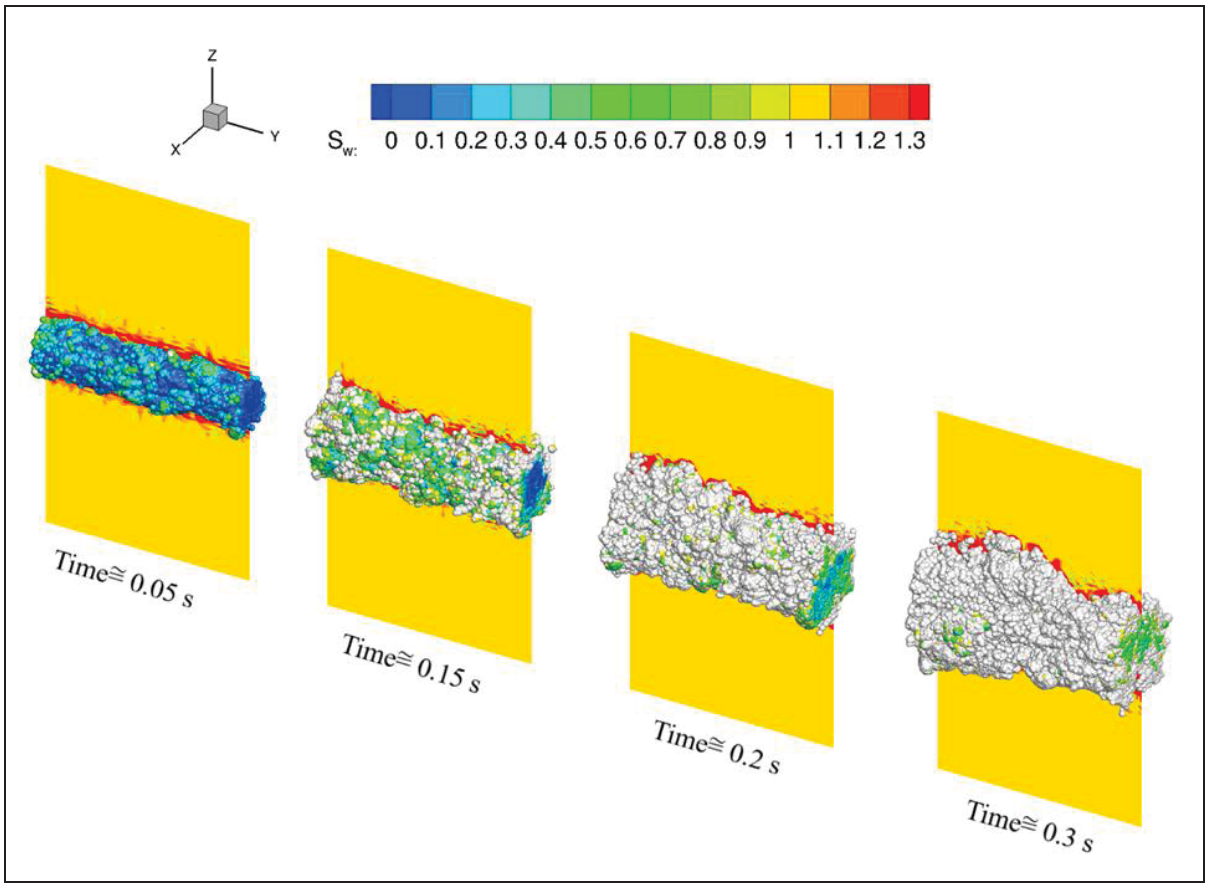

Figure 4.2 Evolution of actual water saturation (S_w) over particles and on the central plane at different plume ages. Colored particles indicate the particles before activation, while white particles represent ice crystals

Figure 4.3 presents the temporal evolution of the mean actual saturation ratio ($\bar{S}_w$) and the mean equilibrium saturation ratio ($\bar{S}_k$), both calculated by averaging over all particles for three levels of fuel sulfur content: low, medium, and high, while maintaining a constant EI_{soot} of 10^{14} (#/kg-fuel) and an initial dry soot core radius of 20 nm. At the initial stage, the actual saturation ratio increases as the jet cools and mixes with ambient air, reaching a peak corresponding to the maximum supersaturation, as shown in Figure 4.3(a). A higher FSC (larger κ) facilitates soot activation at lower supersaturation levels, leading to earlier droplet growth. These early-formed droplets reduce vapor pressure, causing the supersaturation peak to occur sooner and at a lower magnitude. In contrast, a lower FSC delays activation, resulting

in fewer activated particles in the early stages. This delay allows supersaturation to build to a higher peak and to remain elevated.

It should be noted that the equilibrium saturation ratio depends on the particle radius (as defined in Equation (4.5)), and assigning the initial radius equal to the dry core radius yields an unrealistic value of zero. To address this, the Kelvin effect was incorporated at the start of the simulation, explaining the initial peak observed in Figure 4.3(b). The curves show that different κ lead to variations in the equilibrium saturation. A higher FSC results in a lower equilibrium saturation, indicating a lower critical saturation required for activation. This is due to increased particle solubility, which enhances the water uptake and keeps the equilibrium saturation consistently lower than for medium and low fuel sulfur cases. The equilibrium supersaturations observed across different FSC levels in this study are consistent with the findings of Petzold et al. (2005), who reported that lower fuel sulfur reduces the soluble sulfuric acid coating on soot, thereby increasing the equilibrium or critical saturations required for activation, whereas a higher FSC increases the soluble fraction and decreases the equilibrium saturation.

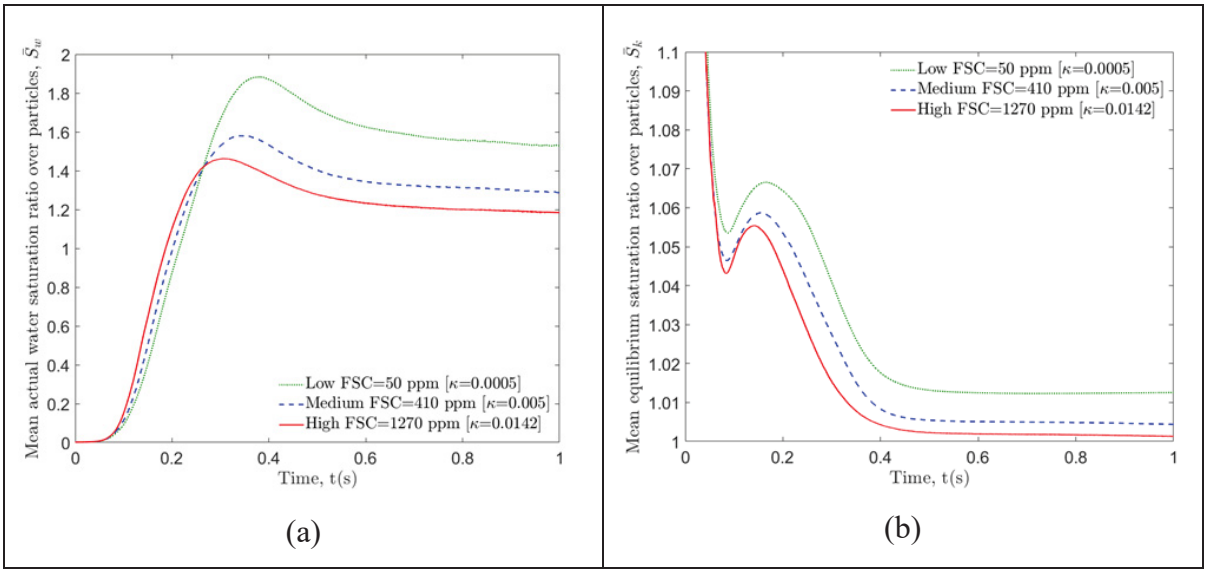

Figure 4.3 Temporal evolution of (a) mean actual saturation ratio and (b) mean equilibrium saturation ratio for three FSC levels: low FSC = 50 ppm, medium FSC = 410 ppm, and high FSC = 1270 ppm, with a fixed EI_{soot} (#/kg-fuel) and an initial dry soot core radius of 20 nm

To examine the influence of the FSC on microphysical properties, Figure 4.4 illustrates its impact on soot particle growth and on the overall activation/freezing fraction, under a constant EI_{soot} of 10^{14} (#/kg-fuel) and an initial dry soot core radius of 20 nm. Once activation begins ($S_w > S_k$) for each particle, the mean radius increases rapidly as particles absorb water and grow into droplets (see Figure 4.4(a)). In Figure 4.4(b), a higher FSC facilitates earlier activation due to increased particle solubility, leading to faster initial growth of up to around 0.3 s and ultimately larger particle sizes, as shown in Figure 4.4(a). In contrast, a lower FSC delays activation, resulting in a slower growth rate. In the high FSC case, early activation and rapid growth quickly deplete the available water vapor, which limits further activation and leads to a lower final activated fraction. Conversely, in the low FSC case, delayed activation allows supersaturation to reach a higher peak and persist longer, resulting in a final activation fraction approximately 20 % higher than that in the high FSC case. These trends are consistent with the saturation behavior presented in Figure 4.3, highlighting the competition for activation driven by multiple interacting parameters.

The findings align with two cases presented by Fangqun Yu, Karcher, et al. (2024), who included both soot and volatile particle activation in their microphysical model. Their results indicate that under nearly identical soot number emissions, the scenario with a lower fuel-sulfur content (FSC≈70 ppm) exhibited a slightly higher soot-to-ice activation fraction as compared to the higher FSC scenario (FSC≈570 ppm). However, this trend was not consistently observed across all their cases. The authors acknowledged large uncertainties arising from multiple controlling variables (e.g., RH_{ice}, temperature, particle size, and plume age), as well as additional complexities introduced by volatile particles and organic species.

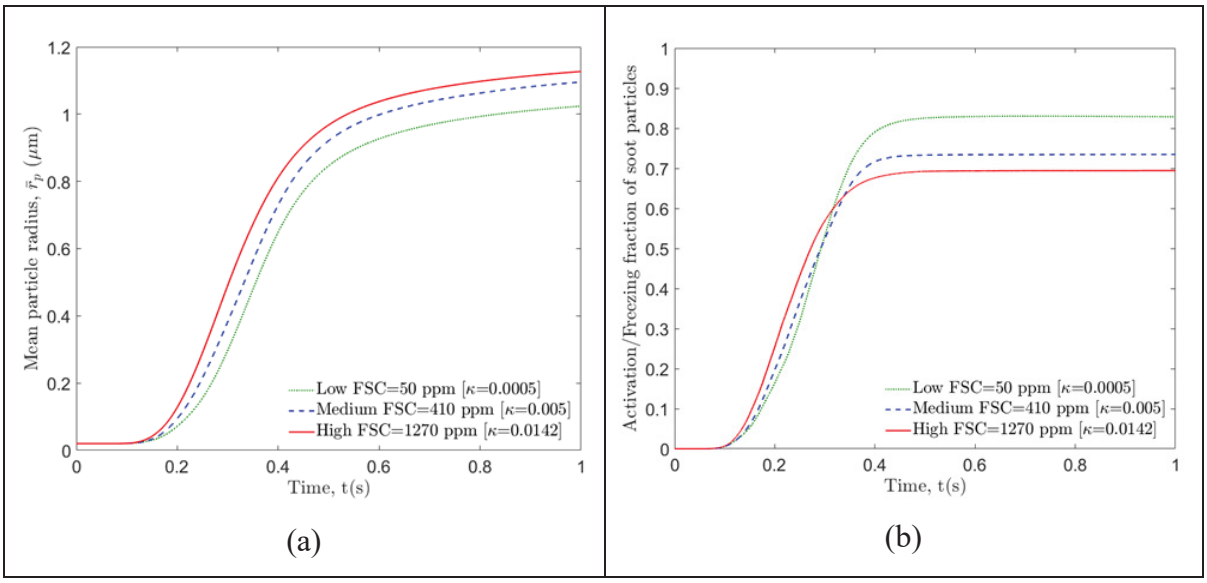

Figure 4.4 Temporal evolution of (a) mean soot particle radius and (b) activation/freezing fraction of soot particles for three FSC levels: low FSC = 50 ppm, medium FSC = 410 ppm, and high FSC = 1270 ppm, with a fixed EI_{soot} of 10^{14} (#/kg-fuel) and an initial dry soot core radius of 20 nm

4.3.2 Effect of Initial Soot Emission Number

This section analyzes three cases relating to the LEAP-1A engine, maintaining a fixed FSC level of 50 ppm (low) and an initial dry soot core radius of 20 nm. The study investigated three soot emission indices ($EI_{soot}\approx 10^{13}$, 10^{14}, and 10^{15}#/kg-fuel) to assess the influence of the initial soot number on particle activation. Figure 4.5 presents the temporal evolution of actual and equilibrium saturation ratios. At high EI_{soot} (10^{15}#/kg-fuel), the large number of particles competing for available water vapor leads to rapid condensation, resulting in a lower peak supersaturation, followed by an almost immediate plateau, as shown in Figure 4.5(a). This strong "condensational sink" prevents supersaturation from building up significantly. In contrast, at low EI_{soot} (10^{13}#/kg-fuel), fewer droplets form, causing less immediate vapor depletion. This allows the actual saturation ratio to reach a higher peak and remain elevated for a longer period. The intermediate soot number case (10^{14}#/kg-fuel) falls between these two trends. Conversely, as shown in Figure 4.5(b), a higher EI_{soot} results in higher sustained equilibrium saturation ratios over time, thereby making soot activation more difficult. While

several factors influence this behavior, at the same sulfur content, a greater number of soot particles increased the total surface area available for condensation. As a result, the system required a higher actual saturation ratio to exceed the equilibrium threshold for activation, thereby reducing the activation efficiency.

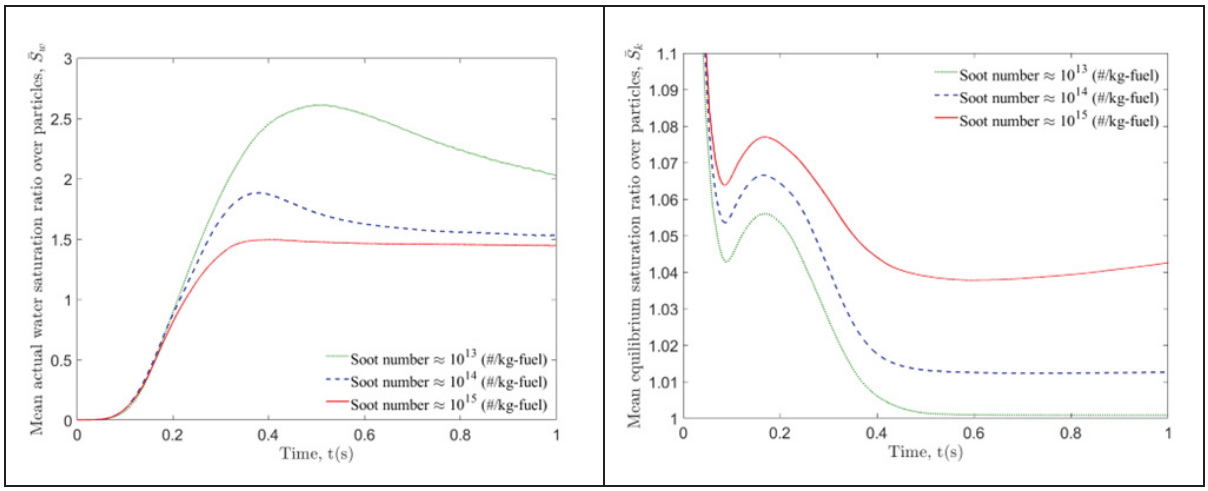

Figure 4.5 Temporal evolution of (a) mean actual saturation ratio and (b) mean equilibrium saturation ratio for three EI_{soot} of 10^{13}, 10^{14}, and 10^{15} (#/kg-fuel) at a fixed low FSC of 50 ppm and an initial dry soot core radius of 20 nm

The temporal evolution of the mean particle radius (averaged over all particles, including soot and condensed ice) and the activation/freezing fraction for different EI_{soot} is presented in Figure 4.6. As shown in Figure 4.6(a), higher EI_{soot} lead to increased competition for water vapor, limiting individual particle growth and resulting in smaller mean radii. Conversely, lower EI_{soot} allow more water vapor per particle, promoting larger droplet growth. This trend is further reflected in Figure 4.6(b), where stronger competition for water vapor at higher soot levels inhibits activation, yielding a lower final activation fraction of approximately 60 %. In contrast, lower soot cases support higher and more sustained supersaturation, leading to nearly full activation (up to 100 %) for 10^{13} (#/kg-fuel) and an activation fraction of about 80 % for 10^{14} (#/kg-fuel). These findings follow the trend reported by Roberto Paoli et al. (2013), where higher EI_{soot} lowered the activated fraction from nearly complete activation at the lowest soot levels to roughly half at the highest levels. The absolute values are also consistent with those

reported by Kärcher (2016), particularly at EI_{soot} of 10^{14} and 10^{15} (#/kg-fuel) for a plume age of 1 s.

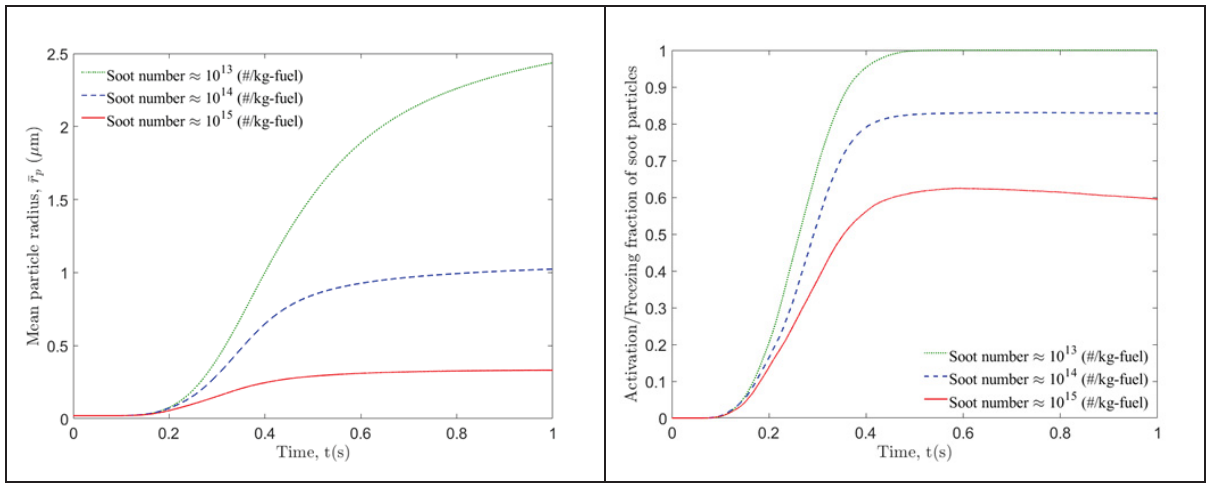

Figure 4.6 Temporal evolution of (a) mean soot particle radius and (b) activation/freezing fraction of soot particles for three EI_{soot} of 10^{13}, 10^{14}, and 10^{15} (#/kg-fuel) at a fixed low FSC of 50 ppm and an initial dry soot core radius of 20 nm

Figure 4.7 presents the particle number emission index distribution ($dEI_N/dlog(D_p)$(#/kg-fuel)) as a function of particle diameter for different soot emission indices and FSC levels, with an initial dry soot core radius of 20 nm, at 1 s plume age. All cases clearly demonstrate distinct peaks separated by FSC levels, with higher FSCs shifting the peak toward larger particle diameters, but at lower EI_{soot}, consistent with the results in Figure 4.4. However, increasing the EI_{soot} from Figure 4.7(a) to Figure 4.7(c) resulted in decreases differences between the FSC levels. Additionally, as the soot number increases, the particle distribution broadens and covers a wider range of diameters—a trend also reported by H-W Wong and Miake-Lye (2010). At EI_{soot}≈10^{15}(#/kg-fuel), the size spectrum thus becomes bimodal: a sub-100 nm mode of soot particles that never activate and a~1 μm mode of fully activated ice crystals. The very large soot surface area reduces the available vapor, leaving a fraction unactivated and producing the twin peaks noted.

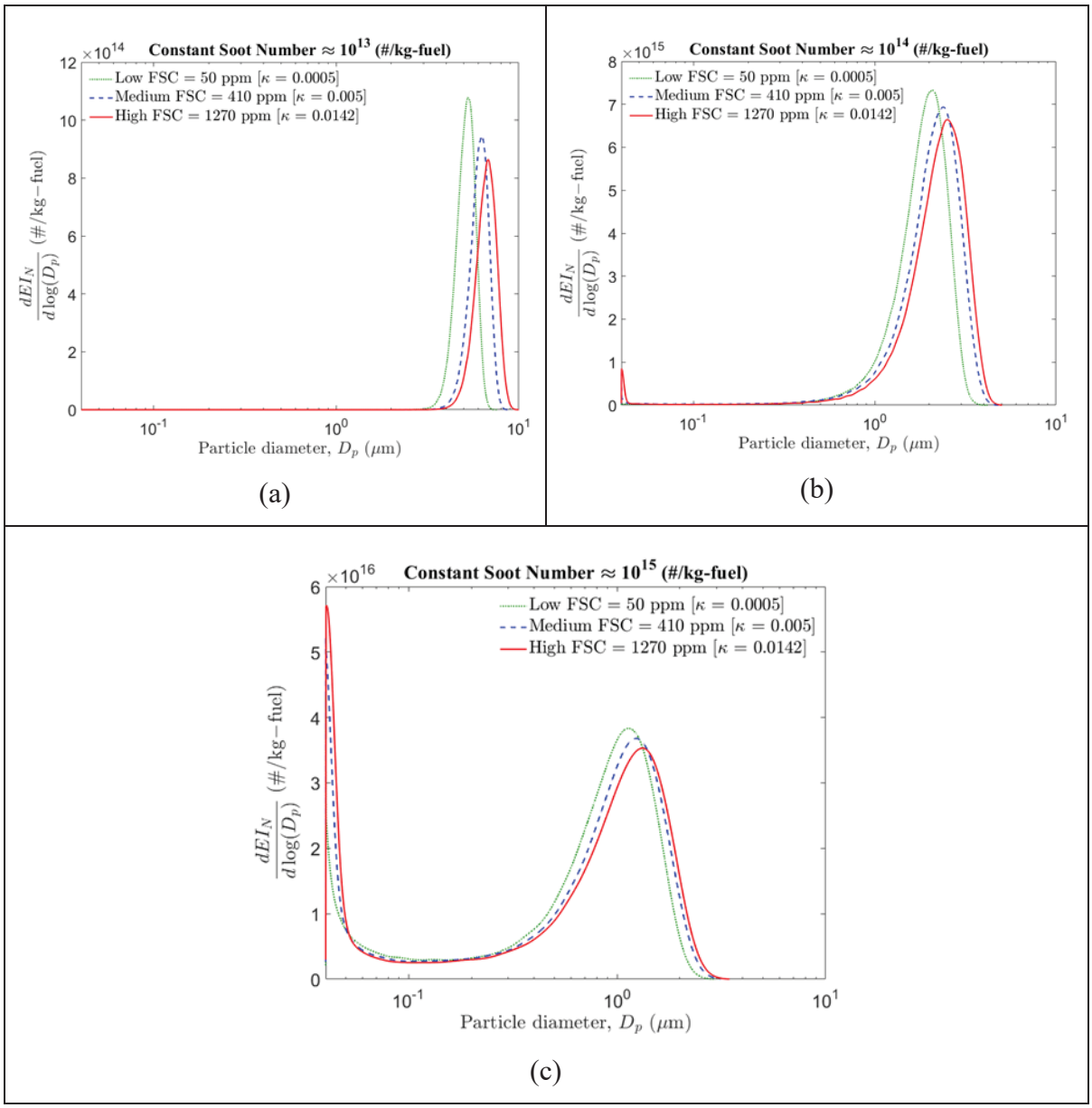

Figure 4.7 Particle number emission index distribution $dEI_N/dlog(D_p)$ (#/kg-fuel) as a function of particle diameter for different FSC levels at 1s plume age, with an initial dry soot core radius of 20 nm for all cases, shown for four cases with varying initial soot number emission indices: (a) EI_{soot}≈10^{13} (#/kg-fuel), (b) EI_{soot}≈10^{14} (#/kg-fuel), and (c) EI_{soot}≈10^{15} (#/kg-fuel)

4.3.3 Effect of Initial Dry Soot Core Radius

The influence of the initial dry soot core radius on particle saturation is shown in Figure 4.8(a), where the peak in $\bar{S}_w$ occurs at different times, ranging from approximately 0.3 to 0.45 s, starting with the largest initial dry radius of 30 nm. This is followed by a decline as water condenses onto particles and the plume dilution progresses. The results demonstrate that smaller dry soot particles (e.g., 10 nm) lead to a higher peak in $\bar{S}_w$, whereas larger particles (e.g., 30 nm) exhibit a lower peak. This behavior stems from the fact that larger particles experience a reduced Kelvin effect (i.e., lower equilibrium/critical supersaturation), and therefore activate earlier, thereby depleting the available supersaturation. In other words, the presence of larger soot cores enhances early vapor uptake and reduces the degree of supersaturation available for further growth. In contrast, smaller particles, with a lower individual condensation capacity, allow the plume to maintain a higher saturation ratio for a longer duration, thereby increasing the potential for additional particle activation and growth. Smaller soot particles at 10 nm exhibit higher equilibrium saturation ratios $\bar{S}_k$, particularly in the early stages of plume evolution, as shown in Figure 4.8(b). These particles require a higher ambient supersaturation to activate. In contrast, larger dry particles at 30 nm have lower equilibrium saturation ratios and can activate at lower supersaturation levels. Over time, $\bar{S}_k$ decreases as the plume cools, water condenses, and particles grow in size, which reduces the Kelvin effect and lowers the required equilibrium saturation. This behavior is consistent with what is observed by Petzold et al. (2005), who demonstrated that increasing the particle size and soluble sulfuric acid coatings reduce the critical supersaturation needed for soot activation.

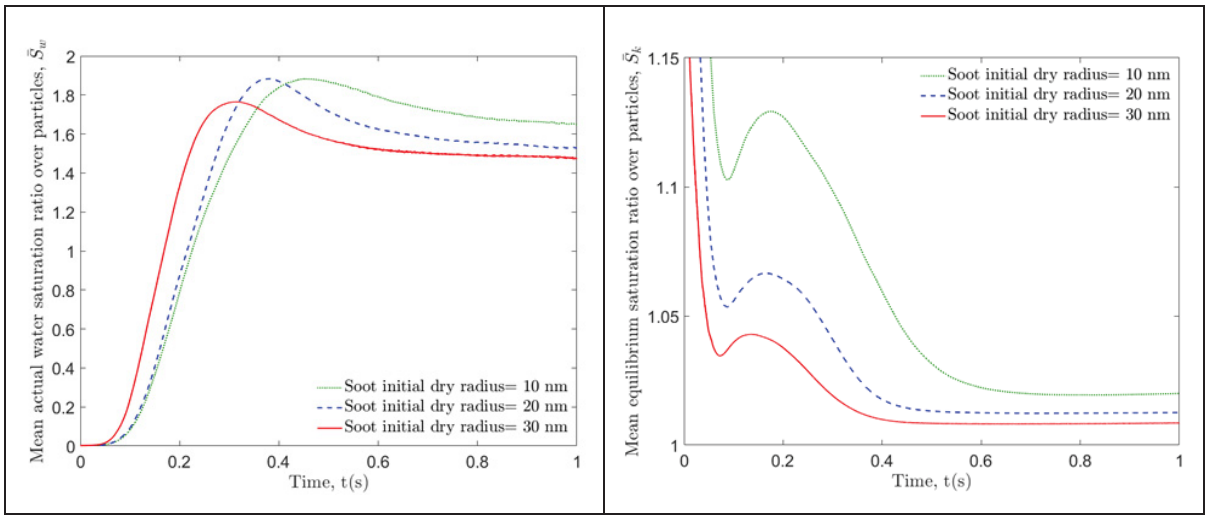

Figure 4.8 Temporal evolution of (a) mean actual saturation ratio and (b) mean equilibrium saturation ratio for three initial dry soot core radii of 10 nm, 20 nm, and 30 nm, with a fixed EI_{soot} of 10^{14} (#/kg-fuel) and a low FSC of 50 ppm

The impact of the initial soot core radius on particle growth and activation is further illustrated in Figure 4.9, using a soot emission index of $EI_{soot} \approx 10^{14}$ (#/kg-fuel) and a low FSC level of 50 ppm. As presented in Figure 4.9(a), all cases exhibit rapid growth between approximately 0.2 and 0.6 s, driven by water vapor condensation in the supersaturated cooling plume. Larger initial soot particles (30 nm) grow more rapidly and reach a greater final size as compared to smaller ones (10 nm) within 1 s. This is because larger particles can activate and condense water more easily, requiring lower ambient supersaturation, as previously shown in the equilibrium saturation results (Figure 4.8(b)). Smaller particles experience delayed activation and slower growth due to their higher critical supersaturation requirements (Kelvin effect), which limits their ability to uptake water during the early stages. Furthermore, Figure 4.9(b) shows the temporal evolution of the activation/freezing fraction of soot particles for different initial dry soot core radii (10, 20 and 30 nm). The results show that activation begins shortly and increases rapidly between 0.2 and 0.45 s, coinciding with the peak in supersaturation (see Figure 4.8(a)). Larger initial soot particles at 30 nm activate earlier and more completely, reaching a higher final activation fraction of about 90%, as compared to smaller particles. Although smaller particles experienced higher actual saturation, their activation/freezing fraction was lower due to their higher equilibrium saturation requirement. The strong size

dependence of $\bar{S}_k$ meant that smaller particles needed a higher supersaturation to activate, resulting in fewer of them freezing, as compared to larger particles.

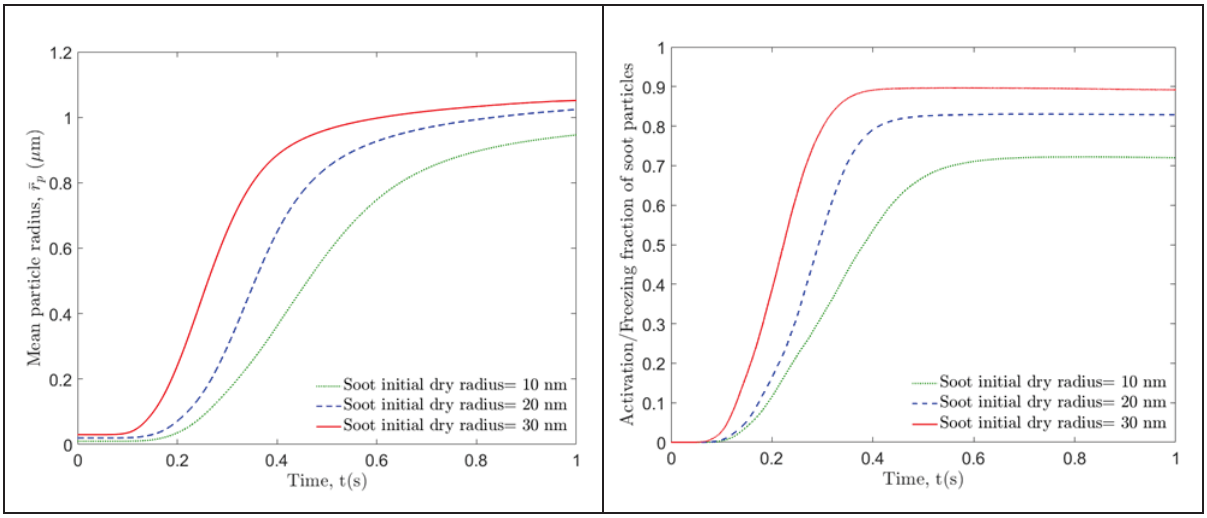

Figure 4.9 Temporal evolution of (a) mean soot particle radius and (b) activation/freezing fraction of soot particles for three initial dry soot core radii of 10 nm, 20 nm, and 30 nm, with a fixed EI_{soot} of 10^{14} (#/kg-fuel) and a low FSC of 50 ppm

The instantaneous particle radius fields (shown as scatter) and actual saturation ratio (shown as contours) in a lateral view of the jet at a plume age of 0.5 s are presented in Figure 4.10 for three different initial dry soot core radii: (a) 10 nm, (b) 20 nm, and (c) 30 nm, under a soot emission index of $EI_{soot} \approx 10^{14}$ (#/kg-fuel) and a constant low FSC of 50 ppm. The case with the largest initial dry soot core radius at 30 nm shows lower saturation levels (as previously shown in Figure 4.8(a)), as faster particle growth depletes water vapor more efficiently, reducing local supersaturation and accelerating the plume's thermodynamic equilibration.

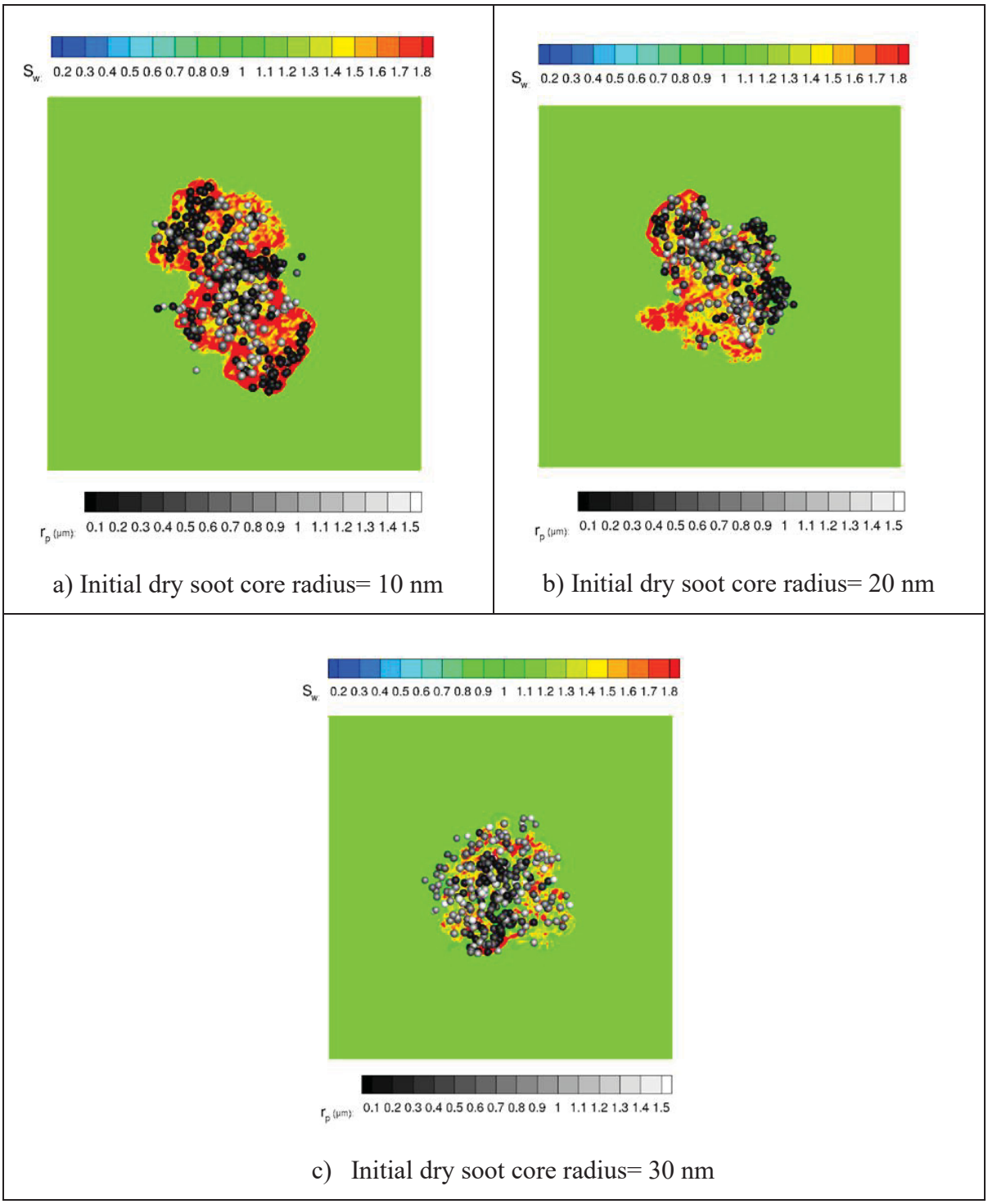

a) Initial dry soot core radius= 10 nm

b) Initial dry soot core radius= 20 nm

c) Initial dry soot core radius= 30 nm

Figure 4.10 Distribution of particle radius (scatter) and actual saturation field (contours) in the lateral view of the exhaust plume at a plume age of 0.5s for three different initial dry soot core radii: (a) 10 nm, (b) 20 nm, and (c) 30 nm, with a fixed EI_{soot} of 10^{14} (#/kg-fuel) and a low FSC of 50 ppm

4.3.4 Comparison of 3D Online-Coupled Microphysics and 0D Offline Box Model

In the literature, 0D box models are widely used to investigate contrail formation and evolution, as they allow extensive parametric studies at relatively low computational cost as compared to LES. However, these models neglect strong fluctuations in temperature and saturation profiles, which can lead to significant prediction errors. To complement the 3D LES with κ-Köhler theory, a 0D offline box model is then analyzed to highlight how the resulting microphysics differs from that predicted by the LES.

The conditions were adapted from the Lewellen's baseline case study (D. C. Lewellen, 2020), as detailed in Table 4.3 below:

Table 4.3 Baseline Simulation Parameters from D. C. Lewellen (2020) study

Parameters	Values
Specific Combustion Heat ($J.kg^{-1}$)	$4.29\ 10^{7}$
Overall Propulsion Efficiency	0.325
Exhaust Jet Temperature (K)	480
Initial plume dilution	92
Initial Plume Cross-Sectional Area (m^2)	0.31
Water Vapor Mass Emission Index (kg-w/kg-fuel)	1.25
Soot Number Emission Index (#/kg-fuel)	10^{16}
Dry Core Radius of Soot Particles (nm)	20
Soot Particle Hygroscopicity (κ)	0.005
Ambient Temperature (K)	218.8
Ice Relative Humidity	110%
Ambient Pressure (Pa)	23840

The simulation was conducted using a monodisperse size distribution for soot particles at initialization, with results presented in Figure 4.11(a). The turbulence realization closely matched Lewellen's third turbulence realization, demonstrating excellent agreement between the results. Lewellen's study employed a κ value of 0.005, corresponding to a medium FSC case; thus, three κ, representative of previously defined FSC levels, were examined here. As

illustrated in Figure 4.11(a), the lower κ value exhibits slightly higher activation fractions as compared to higher κ values, aligning with expectations and trends previously presented in Figure 4.4(b). Subsequently, the plume-averaged mixing fraction and cooling rate extracted from the 3D simulations were utilized to derive 0D offline results. All equations governing the microphysics of the 0D offline box model were identical to those implemented in the FludiLES code, as outlined in Section 4.2.2.

Figure 4.11(b) illustrates a contrasting trend between offline and online simulations, wherein the higher κ value exhibits marginally greater activation fractions than the lower κ value. Moreover, the offline model overpredicts the total ice number because it cannot account for vapor-sink feedback and inter-parcel mixing, which in the online simulation, suppress later activation and cause deactivation of droplets. This comparison underscores the significance of 3D online coupling, especially concerning sensitive parameters like κ, which critically influence the activation behavior.

These findings align with those of Bier et al. (2022), who showed that neither ensemble trajectories offline from an LES nor a single averaged trajectory from a box model can capture online microphysical feedback, leading to overpredictions of ice number relative to a fully coupled 3D LES. Their κ-Köhler analysis also indicated that lower κ slightly reduces activation fractions—consistent with our 0D offline box-model trend (Figure 4.11(b)), while the particle-resolving approach captures fluctuation-driven mixing and vapor-sink feedbacks.

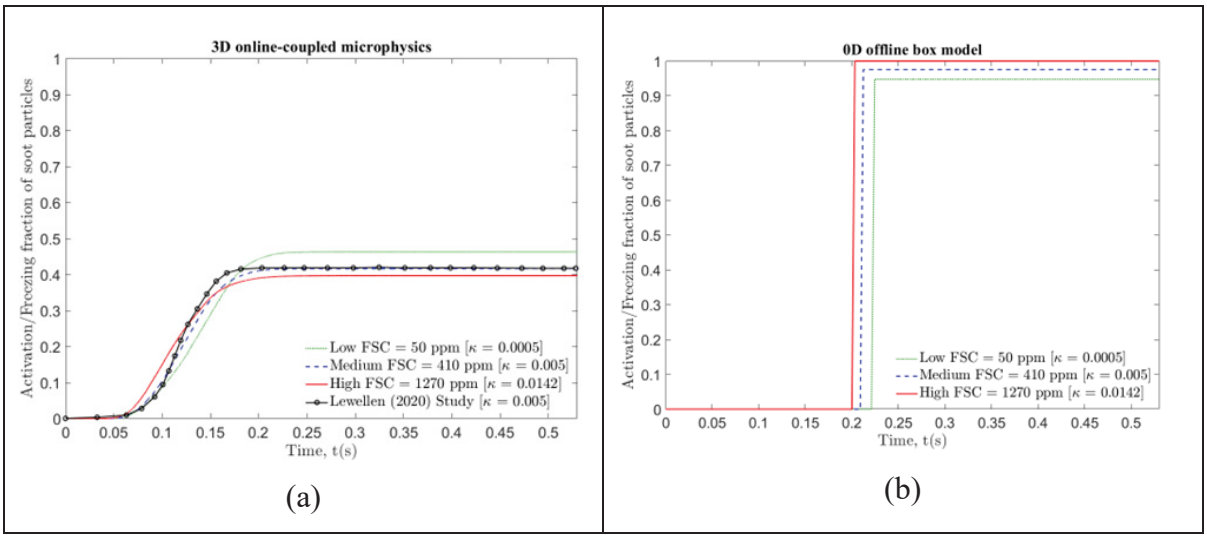

Figure 4.11 Comparison of a) 3D online-coupled microphysics and b) 0D Offline box model for the D. C. Lewellen (2020) Baseline case at three FSC Levels: low FSC = 50 ppm, medium FSC = 410 ppm, and high FSC = 1270 ppm

4.4 Conclusion

This study investigates the effects of the particle hygroscopicity, soot emission indices (EI_{soot}), and initial soot core radius on the formation and growth of ice crystals in aircraft contrails. A refined microphysical model for soot activation, coupled online with LES, was developed to simulate the near-field evolution of exhaust plumes from a LEAP-1A engine under realistic cruise conditions. The model explicitly accounted for solute effects by representing water activity through the hygroscopicity parameter, capturing the influence of sulfuric acid coatings on soot particle activation and growth. Numerical simulations were performed up to 1 s plume age, corresponding to the jet regime, where particle activation predominantly occurs.

The following is a summary of the key findings from the study:

1. Variations in the hygroscopicity parameter (κ), linked to FSC levels (low, medium and high), influenced both the particle size and activation behavior. Increasing κ (or FSC) produced larger mean particle radii but reduced activation fractions. Such trends occurred under conditions where soot particles alone contributed to microphysical

processes: a higher FSC enhanced the growth of already activated particles, depleting available water vapor, thereby hindering further activation. The results highlighted the complex interplay between sulfur-driven water vapor dynamics and particle activation.

2. Variations in EI_{soot} significantly influenced the microphysical properties of soot-derived ice particles. A lower EI_{soot} substantially increased both the mean particle radius and activation fraction, resulting in more uniform particle size distributions. These results underscored the importance of accurately representing EI_{soot}, as variations affect particle activation, growth, and size distribution—key factors governing subsequent contrail development.
3. Variations in the initial soot core radius along with increasing size produced larger mean particle sizes and higher activation fractions. In contrast, smaller soot core radii, being more resistant to activation due to the Kelvin effect, resulted in both lower particle sizes and reduced activation fractions. These results indicate that the initial soot core radius, as a key determinant of particle size at activation, should be explicitly parameterized in contrail microphysics.
4. Comparisons of the 0D offline box model with 3D online-coupled microphysics revealed differences in the sensitivity of activation fractions to κ. These fractions were notably higher in the 0D offline box model, primarily as a result of using a single mean value per time step, which alters the κ sensitivity. The 0D offline box model exhibited an opposing trend, with slightly higher activation fractions at elevated κ values than at lower ones. By contrast, the 3D online-coupled microphysics, which resolves vapor uptake for each individual soot particle, consistently produced lower activation fractions for higher κ values during the initial stages of the plume. This comparison underscored the need for 3D online-coupled microphysics when parameterizing sensitive variables such as κ, owing to the nonlinear behavior inherent in the κ-Köhler theory.

The study underscores the importance of detailed and accurate modeling of activation processes, as they strongly influence the soot-derived ice particle number and size distributions starting from the earliest stages of exhaust plume development, with implications for

subsequent plume evolution. Future work could extend this research by incorporating additional particle types, such as volatile and organic particles, to assess their contributions, particularly in scenarios involving SAFs with very low soot emission indices, which were not considered herein. Moreover, future investigations should examine downstream plume evolution into the vortex phase to provide a more comprehensive understanding of contrail dynamics.

4.5 Acknowledgment

This research was enabled in part by support provided by the Calcul Québec (calculquebec.ca) and the Digital Research Alliance of Canada (alliancecan.ca).

CHAPTER 5

LARGE EDDY SIMULATIONS OF AIRCRAFT CONTRAIL FORMATION: COMPARISON OF SPATIAL AND TEMPORAL MODELING APPROACHES IN JET AND VORTEX PHASES

Parisa Afkari [a], Mohamed Chouak [a], François Garnier [a]

[a] Département de Génie Mécanique, École de Technologie Supérieure,
1100 Notre-Dame West, Montreal, Quebec, Canada H3C 1K3

Paper submitted in *Aerospace Science and Technology*, November 2025

Abstract

Studying the near-field jet/wake is essential for contrail formation because it sets the ice crystal number and persistence. In contrail simulations, two large eddy simulation (LES) formulations are common: a spatial approach, which explicitly resolves spatial development but computationally intensive, and a temporal approach, which assumes frozen-turbulence hypothesis and is computationally efficient. Both approaches have been utilized in prior contrail studies; however, comparisons between them are limited. In this paper, temporal and spatial formulations of LES were compared to analyze near-field jet contrails under cruise conditions representative of an Airbus A320neo with a LEAP-1A engine. The wake-vortex was then initialized from both spatial and temporals jets at two plume ages (t_j=0.12 s and t_j=0.5 s) corresponding to the pre-development and developed microphysical stages, respectively. Microphysics were treated with an online-coupled Lagrangian scheme to evaluate ice activation and growth for (i) soot-only and (ii) soot+ambient nuclei. In the jet phase, temporal jet produced overall equivalent ice microphysical properties as spatial jet under rich-soot plume and supersaturated conditions, with differences within the same order of magnitude for both mean ice radius and ice number-based emission index. In the vortex phase, ice number concentration was inherited from the jet phase, and differences between the temporal and spatial jet initializations diminished with plume age. Delaying the vortex onset led to relatively

smaller particle radii and a slightly higher ice number concentration. Overall, ambient aerosols increased ice number but slowed crystal growth via water vapor competition, thereby reducing sensitivity to vortex initialization.

Keywords: contrails, jet/vortex interaction, wake vortex, ice microphysics, Large Eddy Simulations (LES)

5.1 Introduction

Contrails, commonly formed by aircraft at cruise, contribute to global warming that is comparable to that from aviation CO_2 emissions, making them a critical non-CO_2 driver of aviation's climate impact. Mitigating contrail effects, alongside reducing greenhouse gas emissions, is therefore essential to limiting aviation induced climate change (Lee et al., 2021). However, uncertainties remain in the understanding of near-field contrails and subsequent evolution (Singh et al., 2024). While both experimental and numerical studies have examined contrail formation, the high cost of in-flight measurements and advances in computing have increasingly shifted attention toward numerical modeling to elucidate the contrail formation processes (Cantin et al., 2022; Saulgeot et al., 2023).

According to the Schmidt–Appleman criterion, turbulent mixing of hot, moist exhaust with colder ambient air cools the mixture past saturation, triggering contrail onset in the near field of the exhaust (Appleman, 1953; Schmidt, 1941). The jet regime, dominated by turbulent dynamics, begins immediately after exhaust ejection, in which combustion products mix with ambient air and initiate microphysical processes such as particle activation and ice crystal formation (H. Hoshizaki & J. W. Meyer, 1972; Kärcher, 1994). Radial and axial jet expansion, influenced by Kelvin-Helmholtz instabilities, shapes the initial contrail structure (Hanasz & Sol, 1996). Ulrich Schumann and Heymsfield (2017) mentioned that the number of ice crystals is determined near the jet exhaust and remains relatively constant throughout the contrail's lifetime. Following the jet regime, contrail evolution enters the vortex phase governed by the counter-rotating wingtip vortices (Bier & Burkhardt, 2022; Unterstrasser, Gierens, &

Spichtinger, 2008). Shear-driven mixing at the wake periphery detrains surviving crystals and broadens the plume (Kärcher, Burkhardt, Unterstrasser, & Minnis, 2009; Unterstrasser & Sölch, 2010).

Since jet/wake dynamics govern entrainment and dilution, ice formation proceeds through a sequence of coupled microphysical processes and depends primarily on the number concentration and physicochemical properties of available aerosol nuclei. Aircraft-emitted soot, initially insoluble, can become effective ice-nucleating particles after acquiring a sulfuric-acid coating formed by fuel-sulfur oxidation, which increases hygroscopicity and water uptake (Kärcher, 1999). Ambient aerosols entrained during mixing supply additional heterogeneous nuclei (Kärcher et al., 2015). Kärcher et al. (2022) showed that even low concentrations of ambient ice-nucleating particles can draw down supersaturation, suppress homogeneous freezing, and thereby reduce ice crystal number. The magnitude of this ambient-aerosol effect depends on soot loading: Kärcher and Yu (2009) demonstrated that in soot-rich regimes ice formation is soot-controlled and entrained ambient aerosol plays a minor role, whereas in soot-poor regimes ambient particles exert a stronger influence. Variability in ambient aerosol number and composition thus introduces significant uncertainty in contrail formation (Seinfeld & Pandis, 2016), because these particles compete for available water vapor and modulate ice-nucleation pathways. Consequently, isolating the respective roles of soot and ambient aerosols requires simulations that explicitly resolve plume-scale turbulence and entrainment, which set the supersaturation history of the exhaust and, in turn, control the timing and efficiency of ice nucleation (Kärcher et al., 2015; Kärcher & Yu, 2009).

In contrail modeling, two wake–vortex strategies are commonly employed. RANS/URANS full-aircraft simulations capture the complex aerodynamics around the lifting surfaces and allow the vortex wake to form self-consistently (J. Khou et al., 2017; Kolomenskiy & Paoli, 2018; Ramsay et al., 2024). Complementarily, large eddy simulation (LES) of the wake resolves unsteady plume-scale turbulence and is often initialized with a prescribed Lamb–Oseen vortex pair (e.g., Roberto Paoli et al. (2008); Unterstrasser (2014)). Contrail-relevant dynamics occur in the immediate near wake (≈1–2 wingspans), where vortex roll-up produces

strong jet–vortex interaction that weakens beyond a few spans as the pair separates and entrainment dilutes the plume (Kolomenskiy & Paoli, 2018). Consequently, early wake evolution largely reflects the jet-initialized plume, whereas farther downstream the spreading is governed by ambient turbulence and thermodynamic conditions (Paugam et al., 2010). Recent work (e.g., Pauen, Unterstrasser, and Stephan (2024)) has shown that early-contrail predictions are sensitive to how the wake-vortex system is initialized in LES, whether from RANS-derived slices of a full-aircraft solution or from an analytical Lamb-Oseen pair. Modeling practice varied in the timing of wake-vortex introduction relative to jet age: Roberto Paoli et al. (2013) initialized their temporal LES with a Lamb–Oseen wake field (t = 0 s) at an axial station where the jet half-width was ≈1 m; D. C. Lewellen (2020) advanced a jet-only temporal LES to ≈0.53 s (≈5 spans) before adding prescribed wake fields; and C Ferreira Gago et al. (2002) coupled the Lamb–Oseen pair earlier, at the first downstream station (≈0.11-0.12 s), following a short jet-only temporal DNS. However, despite these differing practices, literature has not isolated the effect of wake-vortex initialization timing in a controlled, side-by-side comparison. Because early-contrail predictions are sensitive to wake initialization, high-fidelity jet/vortex evolution is required for credible microphysical outcomes (Unterstrasser & Sölch, 2010).

In this context, compressible jet flows and wake vortices demand robust numerical schemes to control instabilities and resolve steep gradients (Kaushik, Kumar, & Humrutha, 2015; Misaka, Holzäpfel, & Gerz, 2015). While LES is well suited, contrail studies with coupled microphysics remain computationally intensive, prompting simplifying assumptions that can degrade fidelity (Fritz, Eastham, Speth, & Barrett, 2020; Unterstrasser et al., 2008). A cost-saving alternative is temporal LES, which shortens the streamwise domain and advances the flow in time under Taylor's frozen-turbulence hypothesis (FTH), linking time signals at a point to spatial structure under a steady mean flow, supplemented by specific boundary conditions to preserve continuity (C Ferreira Gago et al., 2002; Roberto Paoli et al., 2008; Taylor, 1938). Temporal LES has been used to investigate jet/vortex coupling and contrail microphysics: Roberto Paoli and Garnier (2005) superimposed a Lamb–Oseen wake to study mixing/chemistry; Roberto Paoli and Moet (2018) showed jets accelerate shear-layer roll-up

and enlarge the merged core; Bier et al. (2022) coupled a Lagrangian cloud module to track microphysical evolution; and Roberto Paoli et al. (2008) generated parcel trajectories for contrail calculations, capturing dynamics even without temperature fluctuations. In contrast, spatial LES resolves streamwise development at higher cost, but can capture jet-regime structures (Kelvin–Helmholtz waves, vortex rings) with good experimental agreement (Zhang, Rong, Wang, & Wang, 2011). Notably, D. C. Lewellen (2020) compared temporal variants for the jet and early-contrail stages against a spatial LES (without microphysics) and found the spatial solution fell between the temporal cases with consistent age-dilution relations, supporting the temporal approximation. Overall, temporal LES offers scalable contrail modeling, with spatial LES providing a higher fidelity, albeit costlier, benchmark.

This work compares temporal and spatial LES for the engine-exhaust round jet during the contrail jet phase, then quantifies how each jet-phase field initializes the wake-vortex phase under cruise conditions. The vortex phase is initialized from the jet phase at two ages to quantify sensitivity to jet history. The dynamical and microphysical properties of near-field contrails across the jet and early vortex phases were compared. To the authors' knowledge, no prior work has assessed how temporal versus spatial LES formulations affect near-field contrail properties and the initialization of vortex-phase simulations. To address this gap, we use the high-order compressible CFD code FludiLES, employing LES to capture jet and wake-vortex dynamics and coupling to an online Lagrangian microphysics model that represents both soot and ambient particles; soot-only and soot+ambient scenarios are run to isolate their respective roles.

The paper is structured as follows: Section 5.2 details the methodology and simulation setup for dynamics and microphysics, including dynamics and microphysics modeling. Section 5.3 presents results in two parts: (i) jet dynamics and microphysics, contrasting temporal vs. spatial LES and soot-only vs. soot+ambient cases; and (ii) jet/vortex interaction initialized from temporal and spatial jet fields, evaluating start-time sensitivity in both dynamics and microphysics as well as ambient particle effects.

5.2 Methodology

5.2.1 Dynamic Modeling

The contrail LES model described in previous work (Afkari et al., 2025) was employed as the baseline, utilizing an Eulerian-based method to simulate flow dynamics. The FludiLES code solves the unsteady Navier–Stokes equations within an LES framework to capture turbulent flow dynamics in jet exhaust and wake-vortex relevant to contrail formation. The equations are formulated in conservative form and non-dimensionalized using appropriate reference scales. LES implementation is based on the filtered equations, with sub-grid scale (SGS) stresses modeled using a hybrid Smagorinsky approach (François Garnier et al., 2014). Thermodynamic closure is provided by the ideal gas law, with specific enthalpy, internal energy, and heat capacity expressions accounting for both dry air and water vapor contributions. The exhaust jets from aircraft engines were characterized by a gaseous mixture of fuel combustion products (gas phase) laden with solid particles, specifically soot and ambient particles. The FludiLES code has been extensively applied to investigate contrail dynamics (jet/vortex) behind aircraft (C Ferreira Gago et al., 2002; C Ferreira Gago et al., 2003; François Garnier et al., 2014; Labbe et al., 2007; X. Vancassel et al., 2014).

Two LES modeling approaches were implemented in FludiLES: spatial and temporal. In spatial modeling, the objective was to encompass the entire computational domain, extending from the exhaust jet immediately downstream of the nozzle to the far outlet boundary, ensuring comprehensive domain coverage. The spatial approach required significantly higher mesh resolution and more computational time compared to temporal modeling.

In contrast, temporal simulation involved computing the flow within a reference frame moving at the mean flow velocity, under the assumption of periodicity in the flow. This approach was based on the FTH (Taylor, 1938), assuming locally parallel flow and neglecting mean flow gradients over the short axial distances within the simulation domain. Convective instabilities

were naturally captured, but absolute instabilities could not be resolved (Roberto Paoli & Moet, 2018).

With both formulations established, differences in conservation and age mapping were accounted for. In the temporal representation, the integrated concentration of a conserved tracer per unit jet length is constant in time. In the spatial representation, that per-length content increases downstream because the plume decelerates relative to the airframe, producing an effective streamwise compression. In contrast, the conserved quantity downstream is the mean tracer flux through planes normal to the jet axis. At a fixed station, parcel ages can vary across the plume in the spatial case, whereas a uniform age characterizes the temporal case (D. C. Lewellen, 2020).

The boundary conditions were formulated to minimize reflections and to emulate an unconfined free jet using artificial boundaries (C. Bogey, Bailly, & Juv′, 2003; Givoli, 1991). In the temporal jet, the flow is initialized with a top-hat (hyperbolic-tangent) axial-velocity profile representing the potential core, superposed with low-amplitude random perturbations, and evolved in a frame moving with the mean jet speed under periodic streamwise boundary conditions. In the spatial jet, the same profile is imposed as an inflow at the nozzle with synthetic turbulence, while a Thompson non-reflecting (characteristic) outlet is applied downstream (Thompson, 1987). A sponge layer was added on boundaries that use non-reflecting conditions, namely the lateral faces in both approaches and the outlet plane of the spatial domain, to damp outgoing turbulent fluctuations. Figure 5.1 illustrates the schematic configuration of the computational jet domain used for both spatial and temporal jet modeling.

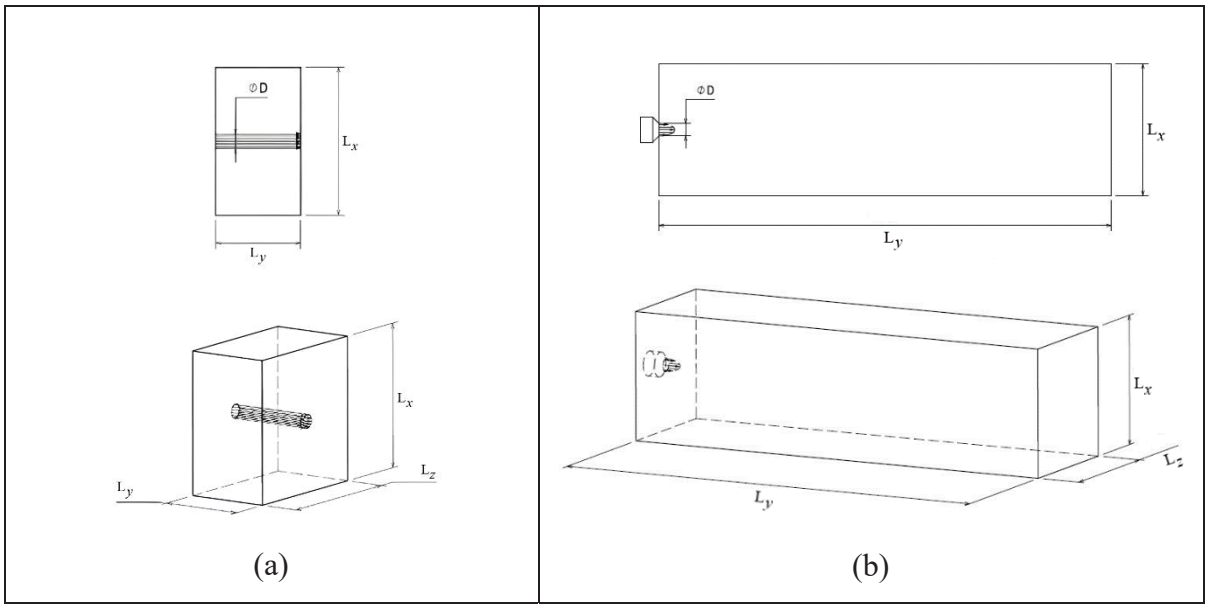

Figure 5.1 Schematic of the computational jet domain in a) temporal and b) spatial modeling

The radius R is used to define the midpoint of the jet shear layer, where $V(R) = (V_0 + V_\infty)/2$, with V_0 representing the jet centerline velocity. Reynolds and Mach numbers are based on these reference quantities. The study focused on a single value of the shape factor, $R/\theta = 10$, which characterizes the ratio of jet radius to momentum thickness. This value was chosen based on the findings of Michalke and Hermann (1982), who identified it as corresponding to the most unstable velocity profile, exhibiting the highest amplification rate of disturbances. The computational domain features a square base tile with dimensions $L_x = L_z = 21\,R$ in both cases. Nevertheless, the streamwise length varies: for the spatial case, it is $L_y = 72\,R$, whereas for the temporal case, it is $L_y = 12\,R$. The latter setup was implemented in the in-house CFD code FludiLES (Afkari et al., 2025).

In this study, the mesh is uniform in all three directions of space for both approaches corresponding to $\Delta_x = \Delta_y = \Delta_z = 0.15\,R$ (C Ferreira Gago et al., 2003). Because the temporal domain is shorter, its total cell count is ≈2 million, whereas the spatial model uses ≈10 million cells. This mesh configuration provides a good resolution in the viscous core of the jet as well as a Courant number (CFL)=0.6. The OpenMP parallelization is implemented in the FludiLES

code to optimize computational costs of LES simulations (Hoeflinger, Alavilli, Jackson, & Kuhn, 2001).

For the jet phase, the LEAP-1A engine was simulated using both temporal and spatial LES formulations. The ambient pressure and temperature were set to the standard atmospheric values at 10.5 km altitude, P = 23840 Pa and T = 218.8 K, respectively. The relative humidity, based on ice, was specified as 110%. The calculation parameters are summarized in Table 5.1. The velocity field was initialized using the typical mathematical jet profile, represented by a top-hat (hyperbolic-tangent) function, as expressed in the equation below for both cases:

$$V(r) = \frac{V_\infty}{2}(a+b)\big(1+T_2(r)\big) + \frac{1}{2}(aV_c + bV_b)(1-T_2(r)) \tag{5.1}$$

$$T_2(r) = \tanh\left(\frac{1}{4}\frac{R}{\theta}\left(c\frac{r}{R} - \frac{1}{c}\frac{R}{r}\right)\right) \tag{5.2}$$

Also, here the V_s can be defined as:

$$V_s = \frac{V_c + bprV_b}{1+bpr} \tag{5.3}$$

The constants a, b, c, and d are determined based on the engine exhaust parameters and are associated with the core and bypass radii. For example, for the LEAP-1A engine, the values of these constants were set as follows: a=0.63, b=0.37, c=1.2, and d=0.5. The velocities of the core jet and bypass jet are denoted by V_c and V_b, respectively. The initial temperature profile was derived using the Crocco-Busemann relation, whose applicability to jet flows has been numerically validated in previous studies (Panda et al., 2004).

Table 5.1 Input parameters used in the simulations for the LEAP-1A engine under cruise condition

Parameters	**LEAP-1A/33**
Mach number (cruise)	0.8
Reference radius, R (m)	0.5
Average mass of the aircraft in cruising flight M_0, (kg)	65,700
Aircraft wingspan, B (m)	35.8
Aircraft speed, $V_{aircraft}$ (m/s)	237
Bypass ratio, bpr (-)	10.5
Core temperature, T_c (K)	580
Bypass temperature, T_b (K)	233
Molar fraction of core water vapor	0.039

To initiate shear-layer transition without spurious transients, low-amplitude pseudo-random perturbations were superimposed on the initialized mean field. Independent pseudo-random variates were generated at every grid point for each velocity component as follows:

$$f_i(x) = 2 \times random\_number - 1 \in [-1,1], \qquad i \in \{x, y, z\} \tag{5.4}$$

This yields turbulence realization of the fluctuation field. Two Gaussian-type envelopes weight the perturbations and confine them to the shear layer:

$$G_{\perp}(r) = \left[\exp\left(-\left[\frac{1}{4}\frac{R}{\theta}\left(\frac{r}{R} - \frac{R}{r}\right)\right]^2\right)\right]^{1/2} \tag{5.5}$$

$$G_{\parallel}(r) = \left[0.95\exp\left(-\left[\frac{1}{4}\frac{R}{\theta}\left(\frac{r}{R} - \frac{R}{r}\right)\right]^2\right) + 0.05\left(1 - \frac{V(r)}{V_j}\right)\right]^{1/2} \tag{5.6}$$

where $V(r)$ is the non-dimensional mean axial profile and θ momentum thickness parameter. With a chosen amplitude A (perturbation) (fraction of a reference speed V_{ref}), The component-wise velocity perturbations are:

$$u'_x = AV_{ref} f_x G_\perp(r), \qquad u'_z = AV_{ref} f_z G_\perp(r), \qquad u'_y = AV_{ref} f_y G_\parallel(r) \tag{5.7}$$

and the initialized field is updated as $u_i + u'_i \rightarrow u_i$. The envelopes peak near $r \approx R$ and decay toward both the jet axis and the far field, ensuring negligible perturbations outside the shear layer. Independent f_x, f_y, f_z yield zero-mean, uncorrelated disturbances, so that no net momentum bias is introduced at t=0 s (Christophe Bogey & Marsden, 2014).

Because the imposed perturbation field is a zero-mean turbulence realization multiplied by a scalar amplitude A, changing A simply rescales the fluctuation magnitudes while leaving the mean profile $V(r)$ and the envelope shapes $G_n(r)$ ($n = \parallel$ or $\perp$) unchanged. Accordingly, the local rms fluctuation varies linearly with A ($u'_{\mathrm{rms}} \propto A$), and the exit turbulence intensity adjusts in direct proportion to A with the same spatial weighting, consistent with turbulence intensity correlation $TI(r) \approx A\, u'_{rms}\, G_n(r)$ (Klein et al., 2003; Xie & Castro, 2008). Different random seeds produce different realizations but with identical statistics for a given A; it is therefore the perturbation amplitude that deterministically sets the prescribed exit turbulence intensity (TI) at t=0 s.

The wake-vortex is initialized at the domain center and coupled to the precomputed jet field from both the temporal and spatial cases. The subsequent vortex simulation is performed in temporal mode owing to the high computational cost of a fully spatial approach. The realistic flow parameters were utilized by incorporating data from an Airbus A320neo aircraft at cruising altitude, powered by the LEAP-1A engine. The jet entrainment into the swirling wake-vortex is characterized by a two-stage progression (C Ferreira Gago et al., 2002). First, jet-only simulations are advanced to a quasi-steady state in the spatial case and to the target jet age in the temporal case, thereby obtaining dynamically consistent fields. Second, a vortex field is initialized at two jet ages (t_j =0.12 s and t_j =0.5 s), corresponding to streamwise distances of approximately 0.5–5 wingspans downstream (Stéphane Brunet, 1999; Labbe et al., 2007; D. C. Lewellen, 2020). These ages bracket regimes reported in the literature, with t_j =0.12 s representing a pre-microphysical development (C Ferreira Gago et al., 2002; Roberto Paoli & Garnier, 2005) and t_j =0.5 s corresponding to a microphysical development

(D. C. Lewellen, 2020). The resulting coupled jet/vortex system is then advanced in time, allowing entrainment to evolve dynamically until 6 s.

Figure 5.2 illustrates the geometric reference adopted for the jet/vortex interaction study. According to Betz's roll-up model (Betz, 1933), the two counter-rotating wing-tip vortices drift apart until their lateral separation approaches $d_v = \frac{\pi}{4}B \approx 28.10$ m; each vortex axis therefore lies at $\pm\frac{d_v}{2} \approx \pm 14.05$ m from the aircraft centerline. Based on the A320neo characteristics document (Airbus, 2024) and the specified vortex positions, the engine core jet is positioned approximately 1.06 m below and 4.45 m inboard (to the right) from the wing-tip vortex axis (Figure 5.2). Therefore, the jet is positioned at a normalized offset from the domain center, defined as (x_{jet}, z_{jet}) = (8.9 *R*, 2.12 *R*).

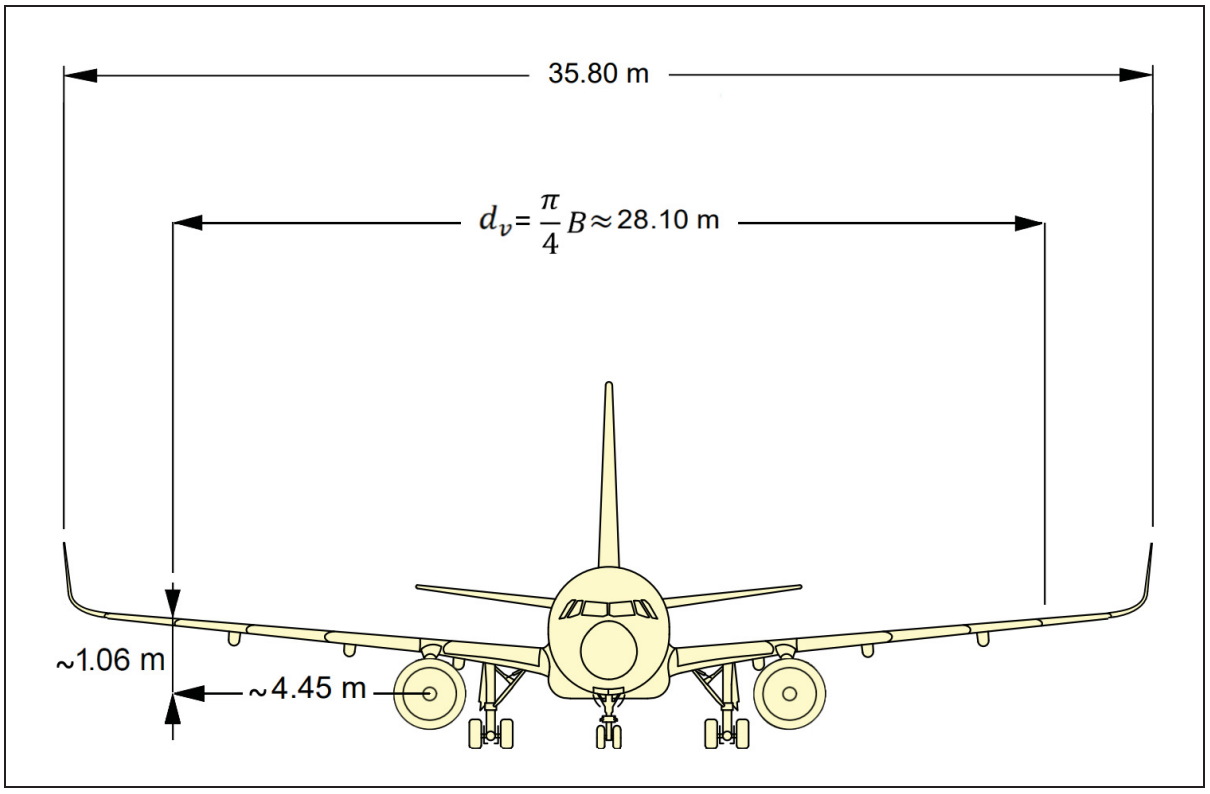

Figure 5.2 Geometric configuration of the A320neo showing the vortex separation and engine jet location, each vortex axis lies at $\pm\frac{d_v}{2}$ from the aircraft centerline (based upon the Airbus documentation (Airbus, 2024))

The chosen jet location ensures it is situated just outside the viscous core of the vortex but within a region exhibiting significant tangential velocities (V_θ), thereby guaranteeing strong yet physically realistic entrainment dynamics. Following the initial jet phase, segments of the computational domain containing the jet flow at two jet ages ($t_j = 0.12\ s$ and $t_j = 0.5\ s$) are transferred to the next computational domain. For comparability, the same reference length and the same extended computational domain were used for both the jet-only and the combined jet and vortex simulations. The domain extents were $L_x = 42\ R, L_y = 6\ R$, and $L_z = 42\ R$.

It is noted that numerous numerical and experimental studies have demonstrated that the vortex becomes two-dimensional at a sufficient distance from the wing trailing edges and undergoes minimal evolution after its formation (S Brunet et al., 1999). For this reason, the Lamb-Oseen model, which is widely recognized as the most commonly used in wake-vortex simulations, was selected (Ahmad & Proctor, 2014; Misaka & Obayashi, 2017; Unterstrasser & Stephan, 2020). The Lamb-Oseen vortex corresponds to an exact solution of the Navier-Stokes equations, the calculations of which are detailed in the study of Ahmad and Proctor (2014). The tangential velocity is written as:

$$V_\theta(r) = aV_{\theta max}\frac{r_c}{r}\left[1 - exp(-b(\frac{r}{r_c})^2)\right] \tag{5.8}$$

with $u_{\theta max}$, the maximum tangential velocity of the turbulent flow and r_c, the associated viscous core radius. *a* and *b* are two constant solutions of Equation (5.9) and (5.10) as below:

$$\exp(b) = 2b + 1 \tag{5.9}$$

$$a = \frac{1}{1 - \exp(-b)} \tag{5.10}$$

To determine the maximum tangential velocity, the circulation formula was used. This is given by:

$$\Gamma(r) = 2\pi u_\theta r = 2\pi a V_{\theta max} r_c \left[1 - \exp\left(-b(\frac{r}{r_c})^2\right)\right] \quad (5.11)$$

The circulation at infinity of a wake-vortex is determined either by the weight and wingspan of the airplane (Thomas Gerz, Holzäpfel, & Darracq, 2002) or based on the maximum tangential velocity (C Ferreira Gago et al., 2002), as shown below:

$$\Gamma_0 = \frac{M_0 g}{\rho_{atmos} \frac{\pi}{4} B V_{avion}} = 2\pi a V_{\theta max} r_c \quad (5.12)$$

The parameter M_0 represents the mass of the airplane, which, in this context, is the average mass of the aircraft at cruise level. This value is calculated relative to the maximum take-off weight of the aircraft. The gravitational acceleration, g, is taken as 9.78 m/s^2, and the air density, ρ_{atmos}, is approximately 0.38 m/s^2 for the altitude under consideration. The airplane wingspan is denoted by B, and its speed is represented by V_{avion}. Based on Table 5.1, the circulation at infinity is determined to be Γ_0=253 m^2/s for the A320neo. Furthermore, among the theories available for estimating the viscous radius of a Lamb-Oseen vortex, the approach presented by S Brunet et al. (1999) has been adopted, which is expressed as follows:

$$r_c \approx \frac{1}{16}\frac{\pi}{4} B \quad (5.13)$$

In this study, the Lamb-Oseen vortex is characterized by a viscous core radius of $r_c = 1.75\ m$ for the A320neo.

5.2.2 Microphysics Modeling

An online Lagrangian microphysics module was coupled to FludiLES, following the framework established in prior work (Afkari et al., 2025). Two particle populations were tracked—engine soot and background ambient aerosols—and two scenarios were simulated: soot-only and soot+ambient. Because mixing between parcels of different ages may alter

microphysical histories, both spatial and temporal jet modeling setups were compared. In the modeling framework, numerical particles, each representing a packet of physical particles, are initialized within the jet at time zero for both temporal and spatial configurations. At each time step, particle evaporation or condensation contributes a source term to the water vapor transport equation and a latent-heat source term to the energy equation; these terms are fed back to the flow solver before advancing the solution. Momentum coupling is one-way: particles sample the resolved velocity field, and their back-reaction on the momentum equations is neglected. In the temporal case, coupling acts on the particle field initialized at t=0 s within the cylindrical core. In the spatial case, particles are injected at the nozzle once the dynamic field is developed, and the evolving scalar and thermal source terms update the downstream flow accordingly.

Ambient particles are initialized uniformly throughout the computational domain, excluding the jet region. It is assumed that the initial jet plume contains no ambient particles, as their contribution is negligible due to the high temperature of the plume at t=0 s. As evidence, Kärcher et al. (2015) noted that the entrainment term, which depends on the dilution factor ($\approx (1-\mathcal{D})$), approaches zero when $\mathcal{D} = \frac{T-T_a}{T_0-T_a}$ equals 1 at the engine exhaust. In this study, soot particles were seeded in the hot core (temporal) or injected at the nozzle (spatial), while ambient particles were initially placed outside the jet and were subsequently ingested solely through resolved mixing. Entrainment was quantified diagnostically via the evolution of the dilution factor $\mathcal{D}$ and ambient particle fluxes across control surfaces, rather than imposed, thereby avoiding correlation-dependent bias and keeping the temporal and spatial setups physically consistent.

Activation was determined using κ-Köhler theory, with hygroscopicity (κ) parameterizing solubility. Super-cooled droplets grew by condensation in water-supersaturated exhaust air and froze into contrail ice crystals at the homogeneous freezing temperature. The homogeneous freezing temperature defined by Kärcher et al. (2015) was used as the criterion for droplet–ice conversion. The Fukuta and Walter microphysical model was used for particle growth, utilizing kinetic mechanisms to calculate radius evolution and particle mass (Fukuta & Walter,

1970). The soot emission index (EI_{soot}) was set to 10^{15} #/kg-fuel (forced rich-burn LEAP-1A scenario (Voigt et al., 2025)), and the ambient particle concentration in the domain was set to 100 $\#/cm^3$ (D. C. Lewellen, 2020). The initial dry core radii of soot and ambient particles were set to 20 nm and 30 nm, respectively.

For soot particles coated with diluted sulfuric acid, and following the study of Petzold et al. (2005), a low fuel sulfur content corresponding to a soluble volume fraction of $\varepsilon_{sol} = 0.1\%$ was assumed in order to minimize the influence of volatile particles (Fangqun Yu, Karcher, et al., 2024), which were not considered in this study. The hygroscopicity parameter for the soluble coating, κ_{sol}, is taken as 0.5 (Kärcher et al., 2015), while the hygroscopicity parameter for the insoluble fraction, κ_{insol}, is assumed to be 0 due to the hydrophobic nature of soot. Accordingly, using the equation provided by Petters and Kreidenweis (2007), the effective hygroscopicity parameter, κ, for the soot particles is calculated to be 0.0005.

To represent a worst-case high-solubility scenario, ambient particles were modeled as ammonium nitrate (NH_4NO_3). Ammonium nitrate, formed by the reaction between nitric acid (HNO_3) and ammonia (NH_3), is considered to be the dominant form of nitrate aerosols in fine-mode particles due to the reduction of sulfate and the presence of abundant ammonia in the atmosphere (S. Yang et al., 2022). The mean soluble volume fraction for ammonium nitrate is 0.67 (Petters & Kreidenweis, 2007), and, as a fully soluble aerosol, the hygroscopicity parameter was set equal to this value (Petters & Kreidenweis, 2007). Ambient temperature and relative humidity influence ammonium nitrate concentrations by controlling the partitioning of ammonium and nitrate between the gas and particulate phases (Seinfeld & Pandis, 2016). However, under the low-temperature conditions typical of cruise altitudes, ammonium nitrate is likely to remain in the solid phase, while still being a highly hygroscopic particle capable of facilitating heterogeneous nucleation (Martin, 2000; Tang & Munkelwitz, 1994). The interaction between ammonium nitrate and excess sulfuric acid, which could lead to a mixed solubility, is considered negligible for this analysis.

5.3 Results Analysis

5.3.1 Comparison of Spatial and Temporal Jets

5.3.1.1 Jet Phase Dynamics

Dynamics properties are first examined as they primarily govern the evolution of contrail microphysical properties discussed thereafter. Figure 5.3 presents the centerline decay, defined as the axial velocity normalized by the jet exit velocity (V/V_j), plotted against the streamwise distance from the nozzle exit plane normalized by the jet exit diameter (y/D_j) for spatial and temporal modeling. To assess sensitivity, three perturbation amplitudes (A) were tested; 1%, 5%, and 10%. For the spatial jet, the inlet perturbation amplitude had no observable effect on the mean plume velocity (identical curves) once quasi-steady conditions were established. For the temporal jet, turbulence initialization at t=0 s produced noticeable differences between amplitudes of 1% and 5%, while further increases beyond 5% had negligible impact.

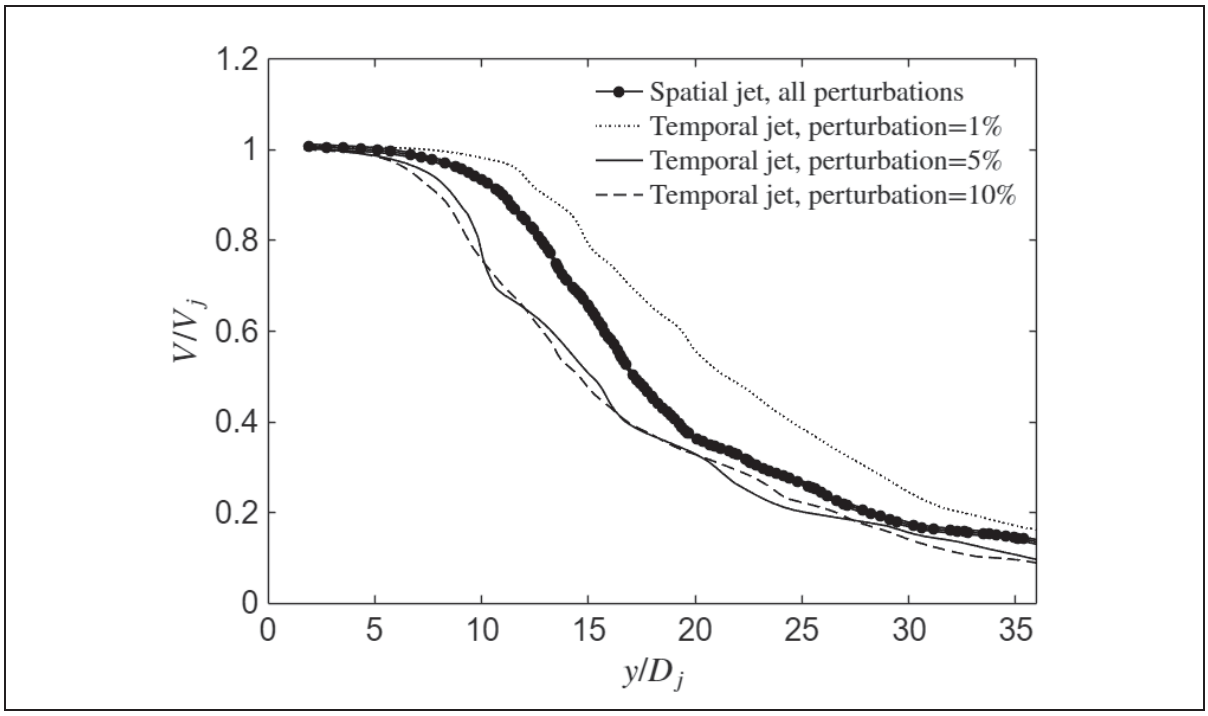

Figure 5.3 Non-dimensional centerline velocity decay (V/V_j) versus normalized axial distance (y/D_j) for spatial and temporal jets at perturbation amplitudes 1%,5%, and 10%

The axial normal (second-order) Reynolds stress $\langle v'v' \rangle / V_0^2$ is plotted versus the self-similar radius $r/r_{1/2}$ in Figure 5.4. All profiles decayed with $r/r_{1/2}$ because the mean shear (and thus production of axial fluctuations) diminished outside the jet core and shear layer, so the variance relaxed toward ambient levels. An analogous behavior was observed for the streamwise and spanwise normal stresses, $\langle u'u' \rangle$ and $\langle w'w' \rangle$ (normalized by V_0^2), whose profiles nearly collapsed across cases and lied slightly below $\langle v'v' \rangle$ over the plotted range. The ordering reflects shear-layer thickness: higher initial perturbation intensities thickened the layer, reduced $|\partial V/\partial r|$, and lowered the stress peak. The spatial jet showed no measurable sensitivity across the tested amplitudes.

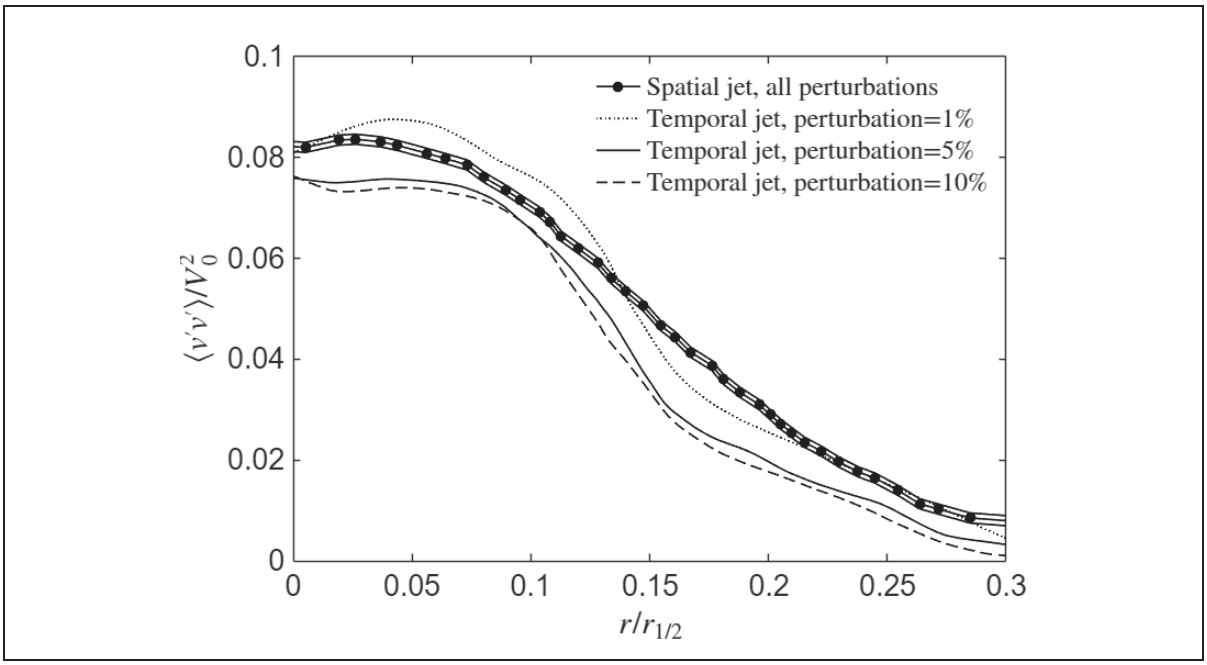

Figure 5.4 Axial normal Reynolds stress $\langle v'v' \rangle / V_0^2$ versus normalized radius $r/r_{1/2}$ in the self-similar region for spatial and temporal jets at perturbation amplitudes 1%,5%, and 10%

In the literature, various criteria have been proposed for identifying vortices in turbulent flows. For this study, the Q criterion was selected, which is based on the second invariant of the velocity gradient tensor (∇u). This means that Q is defined using the symmetric (S_{ij}) and antisymmetric (Ω_{ij}) components of the velocity gradient tensor, which represent the rate of deformation and rate of rotation, respectively (Hunt, Wray, & Moin, 1988). These tensors are expressed as follows:

$$S_{ij} = \left(\frac{\partial u_i}{\partial x_j} + \frac{\partial u_j}{\partial x_i}\right) \tag{5.14}$$

$$\Omega_{ij} = \left(\frac{\partial u_i}{\partial x_j} - \frac{\partial u_j}{\partial x_i}\right) \tag{5.15}$$

The Q criterion can then be defined as:

$$Q = \frac{1}{2}(\Omega_{ij}\Omega_{ij} - S_{ij}S_{ij}) \tag{5.16}$$

Using the Q criterion, vortex rings can be identified as regions where rotation dominates over strain in the shear layer, and these rings form due to Kelvin-Helmholtz instabilities in the interface between the turbulent jet and the stationary external medium (Sbrizzai, Verzicco, Pidria, & Soldati, 2004). In the spatial approach (Figure 5.5), the jet reached the self-similar region by $y/R > 20$ (~0.34 s in convective time based on mean plume velocity). As such, instantaneous turbulent jet structures are illustrated at t=1 s (convective time at quasi-steady state), showing a mature jet where visualized structures are largely dissipated downstream along the y-axis.

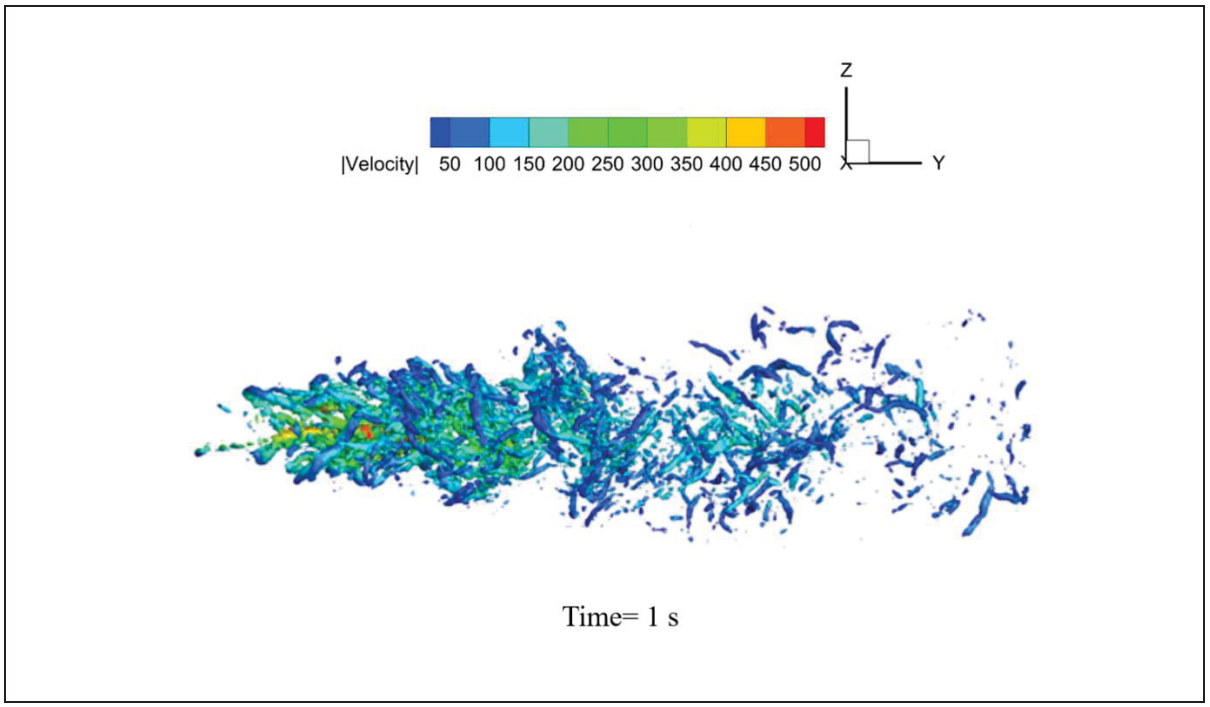

Figure 5.5 Coherent turbulent structures visualized with iso-surfaces of Q criterion and colored by velocity magnitude at physical time of 1 s

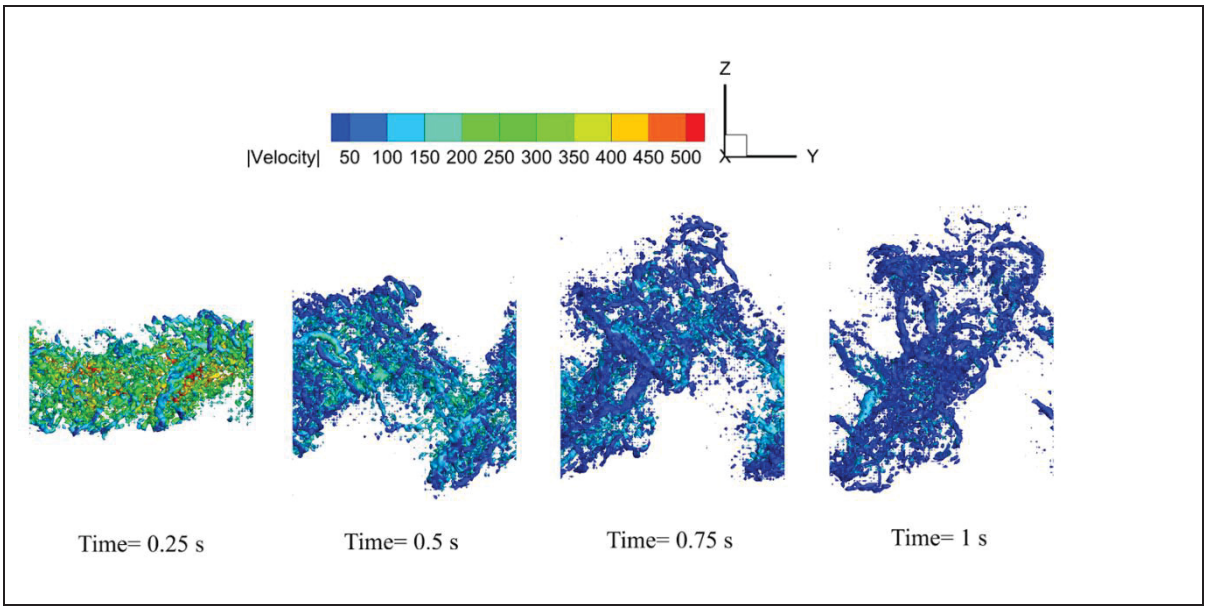

Figure 5.6 Turbulence coherent structures visualized with iso-surfaces of Q criterion and colored by velocity magnitude, at different physical times for the temporal approach

In Figure 5.6 (temporal approach), snapshots illustrate the evolution of the turbulent jet structures between t=0.25s and 1s starting from turbulence initialization at t=0s using 5% of perturbation amplitude. In the temporal approach, turbulent structures evolving from the initial condition appeared smaller and more fragmented than in the spatial case (Figure 5.5), where the turbulent jet attained a quasi-steady state. This difference in dynamics representation, temporal jet developing from an initial condition versus a spatial jet converged at a quasi-steady state, may play a key role in driving contrail microphysics, as particle properties evolve alongside the jet dynamics properties.

5.3.1.2 Jet Phase Microphysics

Figure 5.7 compares the results from temporal and spatial simulations of the mean particle radius $\bar{r}_p$ and the activated/ice number-based emission index $EI_{act,ice}$ (#/kg-fuel) for both soot-only and ambient+soot particles, and shows that by 1 s the plume is past the soot activation phase.

In Figure 5.7(a) both jets show an induction period followed by growth of the $\bar{r}_p$; the temporal jet increased earlier but reached equivalent $\bar{r}_p$ to the spatial jet further downstream for soot-only case. In Figure 5.7(b), adding ambient particles while it lowered $\bar{r}_p$ in both temporal and spatial cases due to water vapor competition, it also increased the difference between temporal and spatial jets as compared to the soot only cases as illustrated in Figure 5.7(a). Consistent with the TI sensitivity presented for the jet dynamics in Figure 5.3-Figure 5.4, the microphysical response in Figure 5.7(c) is evaluated via the $EI_{act,ice}$ for three perturbation amplitudes (1%, 5%, 10%) in both spatial and temporal jets. Effects were most evident in the temporal jet, particularly between 1% and 5%, while differences diminished beyond 5%. The spatial jet was essentially insensitive over the 1–10% perturbation amplitude range. Accordingly, remaining results were provided at 5% of perturbation amplitude. Comparing Figure 5.7(c-d) shows that the temporal jet, whose dynamics evolve from an initial condition, produces a higher ice number by entraining more ambient particles than the spatial jet, whose microphysics develop within a quasi-steady state. Specifically, the temporal jet undergoes an early artificial supersaturation burst that activates soot and incorporates a larger contribution of ambient particles as compared to the spatial jet.

Quantitatively, a closer agreement with the measurements of Voigt et al. (2025), where $EI_{ice} \approx 4.5 \times 10^{14}$ #/kg-fuel at $EI_{soot} \approx 10^{15}$ #/kg-fuel, was obtained with the spatial results, whereas the temporal predictions were slightly higher. Consistency with low fuel sulfur (HEFA-SPK) conditions was also indicated by Märkl et al. (2024): the median EI_{ice} ($\approx 3 \times 10^{14}$ #/kg-fuel) was roughly one-half of the median EI_{soot} ($\approx 6 \times 10^{14}$ #/kg-fuel). Moreover, as shown by Kärcher and Yu (2009), soot-rich plumes are soot-controlled at formation, implying that entrained ambient aerosol contributes little during the first second. Consistent with this, the spatial runs showed a smaller and more physically plausible difference between soot-only and soot+ambient cases than the temporal runs, reinforcing the spatial jet as the more realistic benchmark for near-field comparisons.

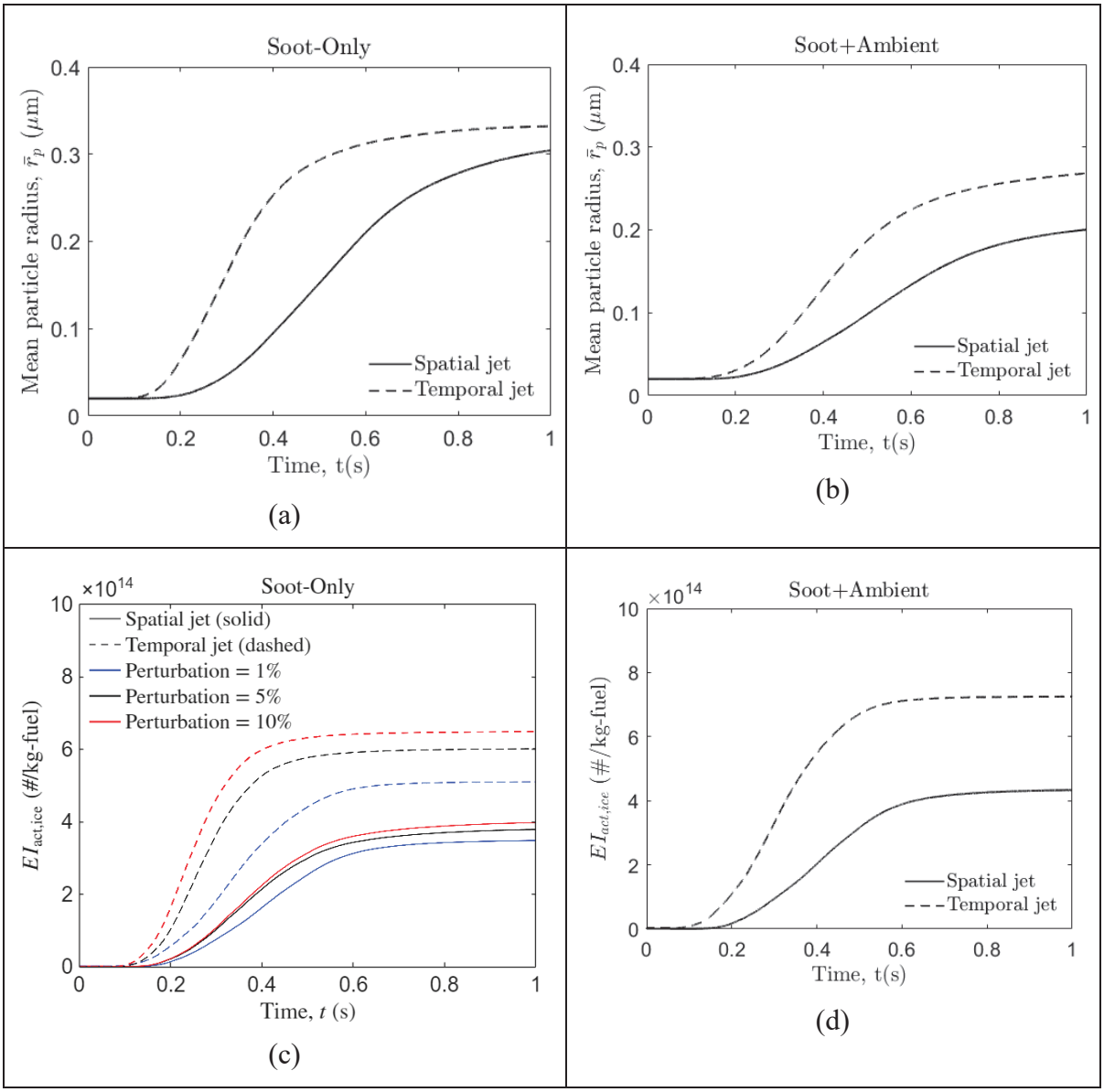

Figure 5.7 Jet phase (up to 1 s) evolution for spatial jet (solid) and temporal jet (dashed) simulations. Top row: plume-mean particle radius for (a) soot-only and (b) soot+ambient. Bottom row: emission index of activated/freezing particles for (c) soot-only and (d) soot+ambient. Panel (c) includes perturbation amplitude sensitivity (1%, 5%, 10%); panels (a), (b), and (d) use 5%

At an early plume age (~1 s), Figure 5.8 shows the particle number–size distributions $dEI_N/dlog(D_P)$ for the temporal and spatial LES cases with soot-only and soot+ambient scenarios. Consistent with the initial dry core radii, 20 nm for soot and 30 nm for ambient

particles, the spectra exhibited a nucleation mode in the sub-0.1 μm range (peak ≈0.06–0.08 μm) and a growth mode near 0.3–0.5 μm. In both frameworks, adding ambient particles increased the number of ice crystals, most prominently in the temporal jet case, where the transient supersaturation burst activated a larger fraction of nuclei as shown in Figure 5.7(c-d). In contrast, the mean particle radius $\bar{r}_p$ was smaller with soot+ambient than with soot-only (Figure 5.7(a-b)): the larger activated population partitions condensable water and latent-heat release over more crystals, reducing per-particle growth. Thus, at t=1 s the soot+ambient case yielded more particles but with a smaller radius, whereas soot-only yielded fewer particles with larger radius. These effects were stronger in the temporal jet owing to its sharper supersaturation history; the spatial jet showed the same tendencies but with a slower rise and lower plateaus as the reference modeling approach.

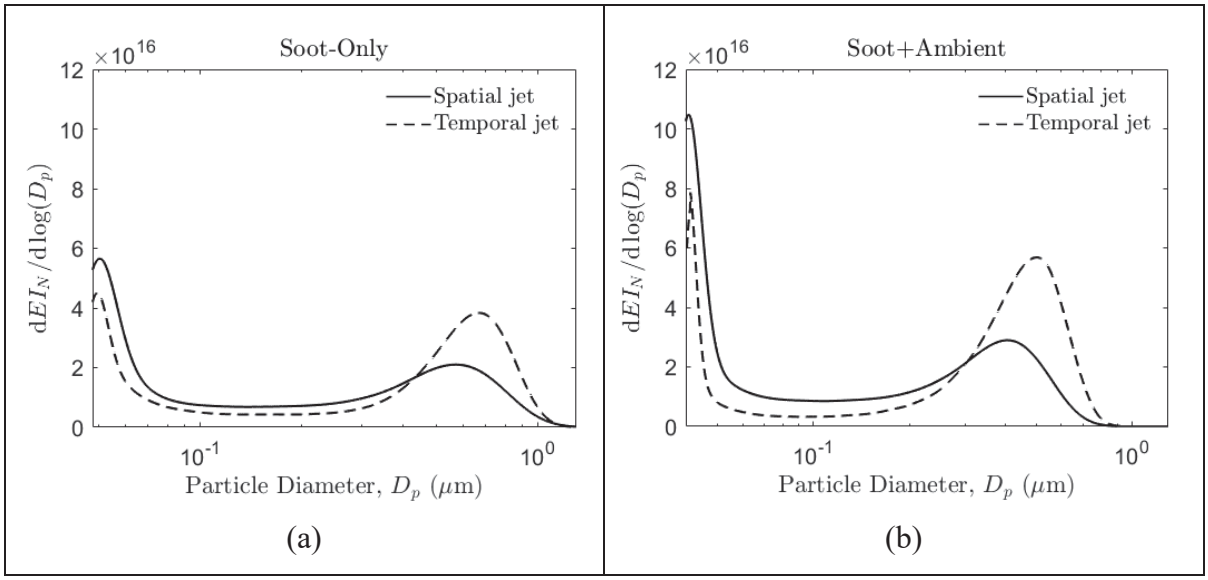

Figure 5.8 Particle number–size distributions $dEI_N/dlog(D_P)$ at t=1 s for spatial jet (solid) and temporal jet (dashed) simulations. (a) soot-only case; (b) soot+ambient case

Figure 5.9 illustrates temporal jet qualitatively for both soot-only (Figure 5.9(a)) and soot+ambient (Figure 5.9(b)) at t=0.5 s. In both cases crystals clustered along the shear layer where $S_i \gtrsim 1$, but the soot+ambient case displayed a denser crystal population and a

thinner/high-S layer. Conversely, the soot-only case showed fewer crystals and more unfrozen particles persisting in regions with lower S_i.

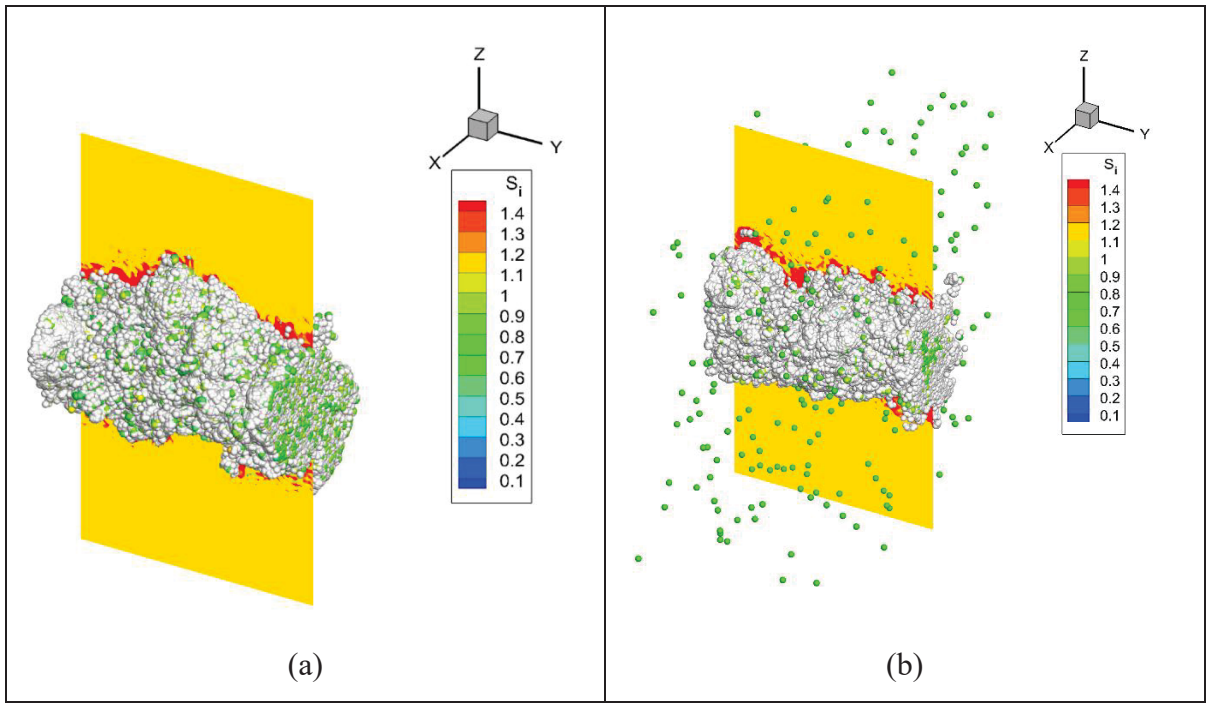

Figure 5.9 Instantaneous field from the temporal jet at t=0.5 s. The center-plane shows the ice saturation ratio S_i (colored slice), with Lagrangian particles overlaid: (a) soot-only and (b) soot+ambient. White spheres denote activated (frozen) ice crystals; colored spheres are unfrozen aerosol particles shaded by their local S_i

Instantaneous fields from the spatial LES at t=0.5s, contrasting soot-only with soot+ambient microphysics are shown in Figure 5.10. In both cases, the near-nozzle centerline was initially sub-saturated with respect to ice (S_i<1); turbulent mixing subsequently raised S_i>1 and triggered soot activation. With ambient aerosols, the number of activated particles was higher and their distribution broader, reflecting the larger pool of nuclei. While in the soot-only case, activation was weaker, and crystals remained concentrated within the plume core.

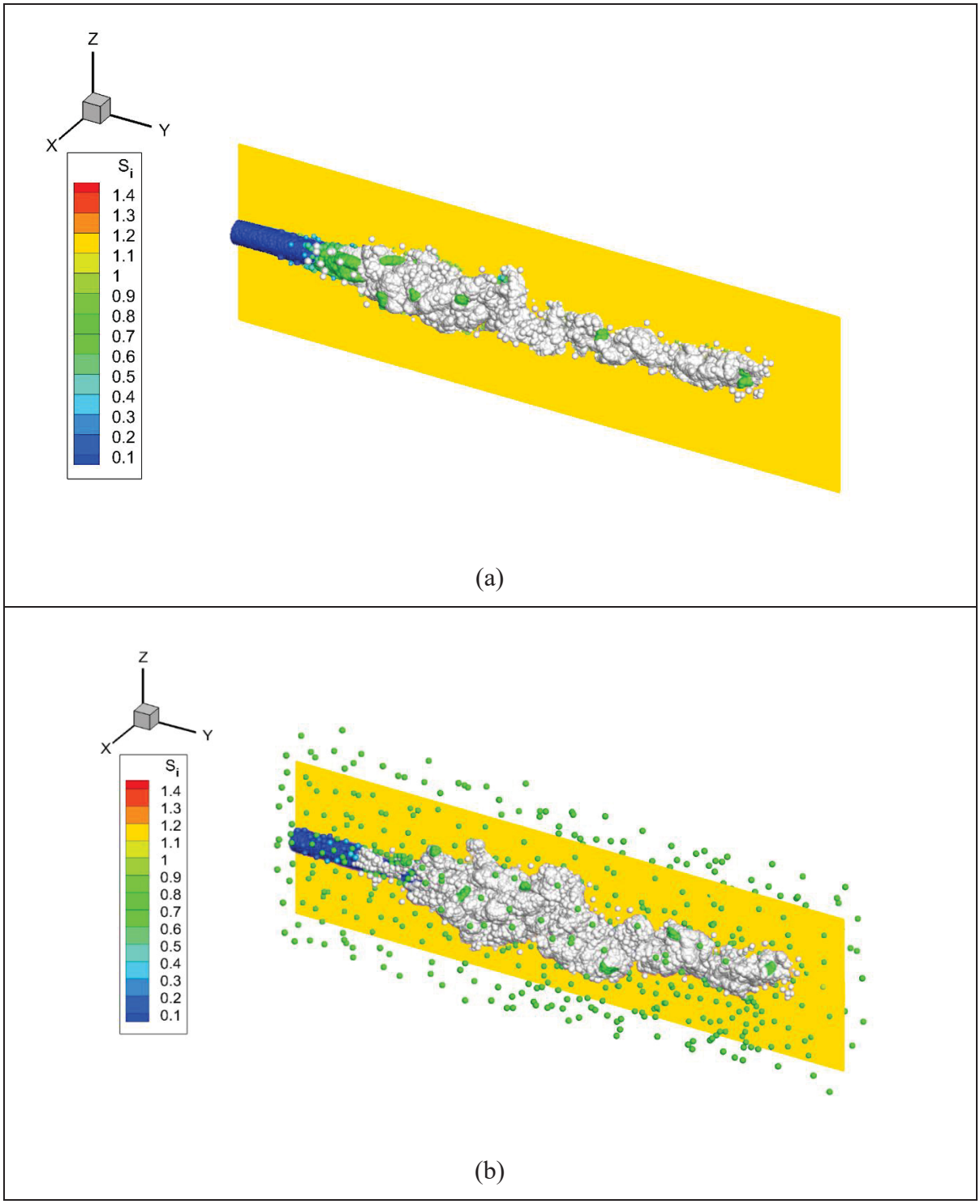

Figure 5.10 Instantaneous field from the spatial jet at t=0.5 s. The center-plane shows the ice saturation ratio S_i (colored slice), with Lagrangian particles overlaid: (a) soot-only and (b) soot+ambient

5.3.2 Vortex Phase: Effect of Initialization from Temporal vs. Spatial Jets

5.3.2.1 Vortex Phase Dynamics

At the onset of the vortex phase, an axisymmetric Lamb–Oseen vortex was superposed at the domain center onto the instantaneous jet fields from the temporal and spatial frameworks. Each jet solution was advanced to t_j =0.12 s and t_j =0.5 s prior to vortex initialization. Figure 5.11 illustrates the imposed Lamb–Oseen field for the spatial jet at both plume ages of vortex initialization. The concentric rings represent the azimuthal-velocity distribution, and the localized high-speed region delineates the jet core. Consistent with the jet phase results, the vortex initialized at 0.5 s exhibited faster dissipation and therefore lower velocity magnitudes than the 0.12 s case. These fields constituted the initial conditions for the subsequent jet/vortex interaction analysis.

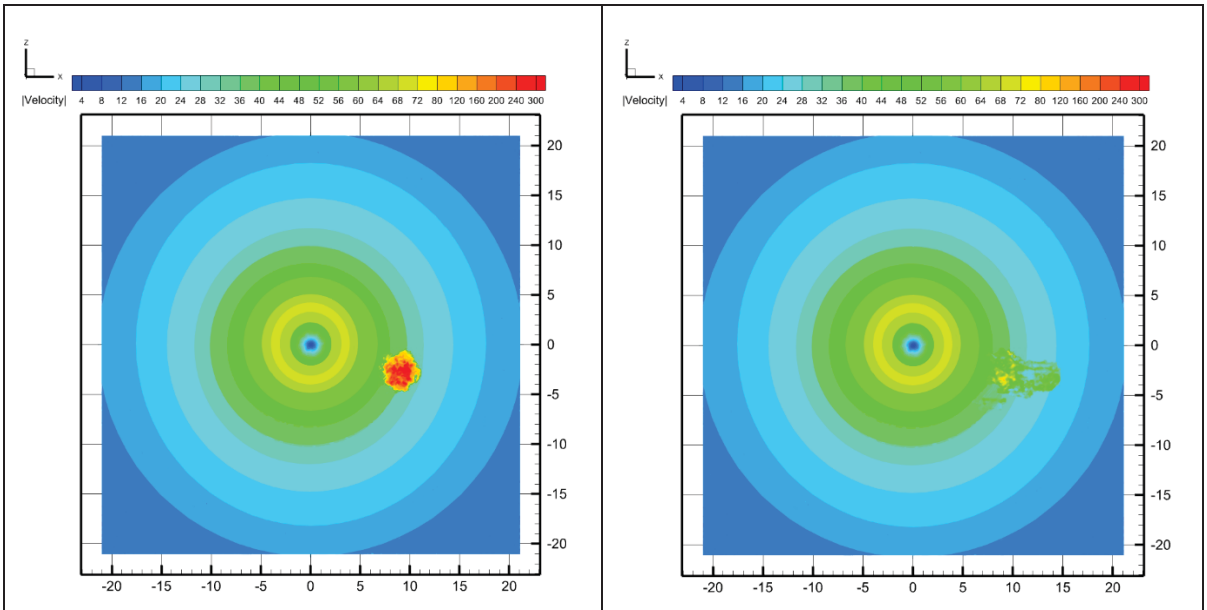

a) Vortex phase initialized at t=0.12 s

b) Vortex phase initialized at t=0.5 s

Figure 5.11 Velocity magnitude contours in the lateral plane at the first time-step after initializing the Lamb–Oseen vortex at the domain center, superimposed on a partially evolved jet flow field up to (a) $t_j = 0.12$ s and, (b) $t_j = 0.5$ s

Figure 5.12 compares the dilution ratio during the jet and vortex phases. In both temporal and spatial cases, the profiles for vortex initialization times (t_j =0.12 s and t_j =0.5 s) coincide up to the vortex switch, as they follow the same jet-only evolution before vortex onset. The rapid increase in dilution observed at t=0.12 s marked the kinematic onset of wake–vortex entrainment, consistent with the canonical spatial criterion x≈0.5–1 B mapped via $t = x/U_\infty$, as discussed by Roberto Paoli and Garnier (2005). Following the initial near-field regime, all cases entered a vortex-dominated phase in which the dilution ratio grew approximately as a power law with a slope in agreement with the Ulrich Schumann et al. (1998) mixing line. The offset relative to the Schumann line was expected because the latter was an empirical fit anchored near t=1 s and derived from heterogeneous near-field data (some inferred rather than directly measured), with acknowledged scatter in the jet phase; consequently, its baseline dilution differed from that in the present study.

The temporal jet initialization produced a larger early-time dilution, reflecting stronger jet phase mixing as compared to the spatial jet initialization. Beyond approximately 0.5–1 s, all curves differed mainly by a vertical offset (a memory of the initial jet mixing) but exhibited similar growth rates up to 6 s. Notably, after 0.5 s, the cases initialized from the spatial jet fields remained closer to each other than those from the temporal framework. Overall, these results indicated that vortex phase entrainment was robust to the choice of jet initialization, although the absolute dilution level at a given time remained sensitive to the near-field jet mixing prior to $t_j = 0.12$ s.

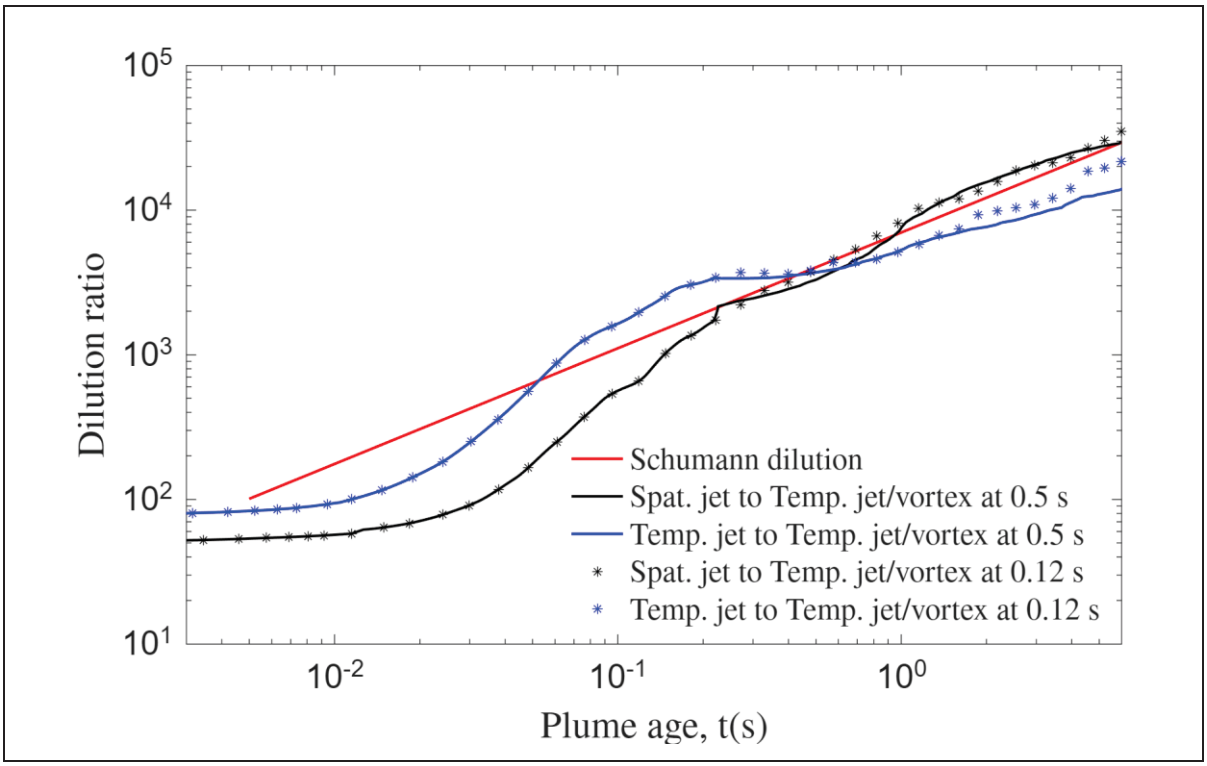

Figure 5.12 Dilution ratio versus plume age t during the vortex phase. A Lamb–Oseen vortex is imposed on temporal (blue) and spatial (black) jet fields at two initialization times: t_j =0.12 s (star markers) and t_j =0.5 s (solid lines). The red line shows the Ulrich Schumann et al. (1998) mixing law for young plumes

Tangential velocity profiles versus radial distance for simulations initialized at t_j= 0.12 s and t_j=0.5 s from both temporal and spatial jets up to 6 s are compared in Figure 5.13. In all cases, the tangential velocity rose from zero, peaked near the core, and then decayed with radius. With increasing *y/R*, the peak shifted outward and its magnitude decreased, indicating core growth with approximately conserved circulation (J.-C. Khou et al., 2015). Differences were confined to the near field. Temporal jet initializations produced a sharper core and higher early peak; most pronounced for the initialization at t_j= 0.12 s case. In contrast, spatial jet initializations yielded a broader core and lower peak. However, both the peak location and the outer-radius decay became increasingly similar downstream at *y/R*=10, showing that vortex phase dynamics rapidly reduced sensitivity to the choice of jet initialization while maintaining the canonical Lamb–Oseen-like evolution of the vortex core.

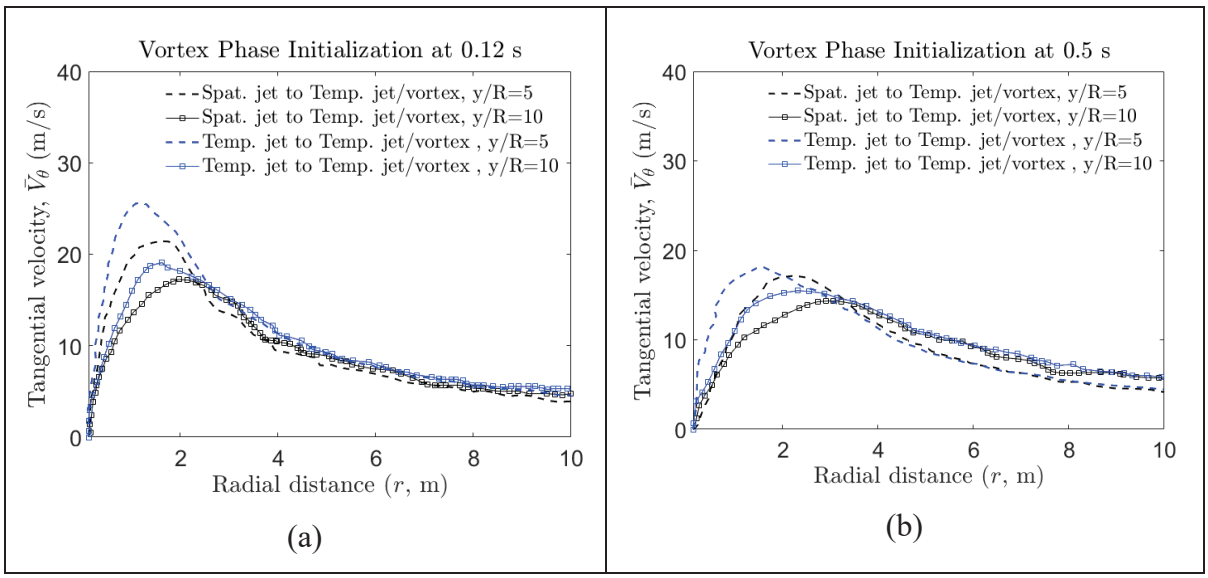

Figure 5.13 Tangential-velocity profiles $V_\theta(r)$ of the imposed Lamb–Oseen vortex in a lateral plane, sampled at *y/R*=5 and *y/R*=10, for spatial- and temporal-jet initializations: (a) initialization at t_j= 0.12 s; (b) initialization at t_j= 0.5 s

Tangential velocity profiles at 2 and 6 s of plume age from temporal and spatial jet simulations with initialization times of t_j= 0.12 s and t_j= 0.5 s were compared with the in-situ measurements of Köpp (1999) behind a Boeing B707 in Figure 5.14. The A320neo simulated in this study has a wingspan approximately 8 m shorter than that of the B707, which contributes to the generally higher tangential velocities observed in the experimental data due to the dependence of vortex strength on wingspan. The temporal jet simulations showed the highest velocity at both initialization time of t_j= 0.12 s and t_j= 0.5 s for the plume age of 2 s, slightly above the experimental range. The spatial-jet initialization results fell mostly within the experimental range, indicating closer alignment in velocity magnitude. As the plume evolved, the discrepancy between the temporal and spatial simulations diminished, with the temporal results progressively converging toward the spatial profiles.

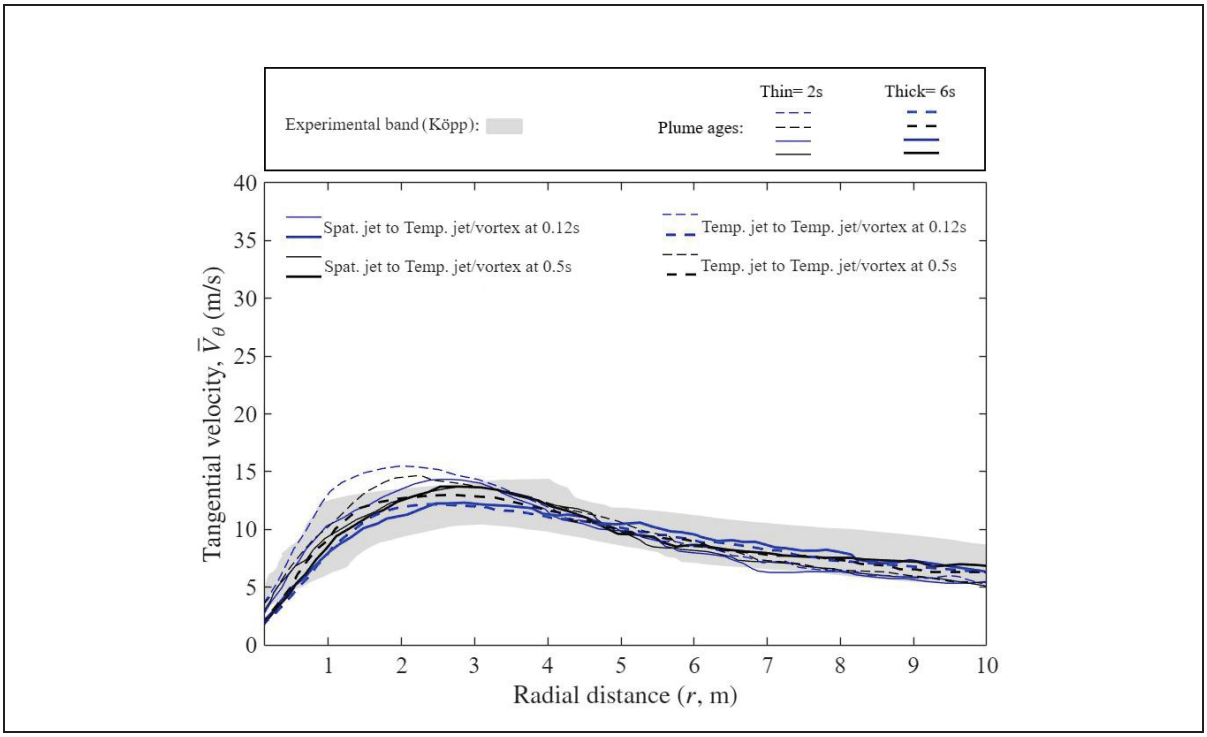

Figure 5.14 Tangential velocity profiles $V_\theta(r)$ radial distance at plume ages of 2 s (thin lines) and 6 s (thick lines) for cases initialized from spatial and temporal jet fields at t_j= 0.12 s and t_j= 0.5 s. The gray shaded band shows in-situ measurements behind a Boeing 707 reported by Köpp (1999)

5.3.2.2 Vortex Phase Microphysics

For the microphysical comparison, simulations were run for both jet initialization approaches (temporal and spatial) at two jet ages (0.12 s and 0.5 s), each with two aerosol compositions (soot-only and soot+ambient). This design isolated the role of ambient particles during the vortex phase and related it to the jet phase differences previously observed. In Figure 5.15, the vortex was initialized from the temporal jet profile at t_j= 0.12 s for both compositions (soot-only and soot+ambient). Colors indicate the ice-particle radius (r_p) in a lateral plane at a plume age of 1 s. Adding ambient aerosol yielded more particles with smaller r_p and a more diffuse envelope; the soot-only case formed larger crystals concentrated along the compressive spiral arms of the wake.

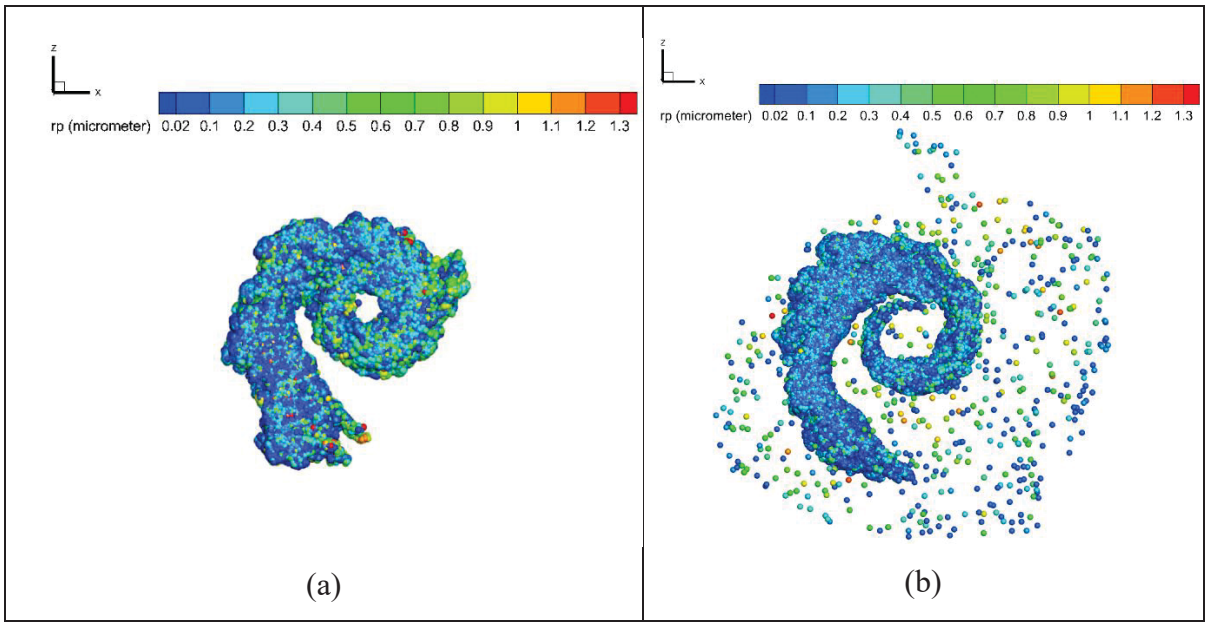

Figure 5.15 Particle radius r_p distribution at a plume age of 1 s in a lateral plane of the Lamb–Oseen vortex, for cases initialized from the temporal jet profile at t_j= 0.12 s: (a) soot-only and (b) soot+ambient

Although wake-vortex entrainment of the jet begins within x≈0.5–1 B, the microphysical response lags the kinematics (Roberto Paoli & Garnier, 2005). Vortex roll-up and strain first amplified adiabatic cooling and entrainment, building plume-mean supersaturation; only thereafter did condensational growth proceed (Naiman et al., 2011; Unterstrasser & Sölch, 2010). Figure 5.16 shows the temporal evolution of the mean ice saturation ratio $\bar{S}_w$ over plume during the first 6 s behind the aircraft for the temporal and spatial profile initializations of the t_j= 0.12 s. The thermodynamic onset manifested as a rapid rise in the plume mean saturation ratio and typically emerged around t≈0.4–0.7 s, with its magnitude sensitive to the jet fields used for initialization. The temporal-initialized plumes attained an earlier and higher maximum supersaturation, about $\bar{S}_w$≈1.9 versus $\bar{S}_w$≈1.6 for spatial initialization in the soot-only case, and $\bar{S}_w$≈1.5 versus $\bar{S}_w$≈1.3 when ambient aerosols were included. These higher early peaks were consistent with the stronger early mixing and scalar gradients inherited from the temporal jet fields. Following the peak, $\bar{S}_w$ declined as mixing and condensational sinks acted; however, the spatial initialization exhibited a slower decay and sustained a slightly higher supersaturation. Comparing compositions, adding ambient particles slightly reduced the peak

supersaturation and accelerated its decay, reflecting enhanced vapor uptake by the larger population of activated particles.

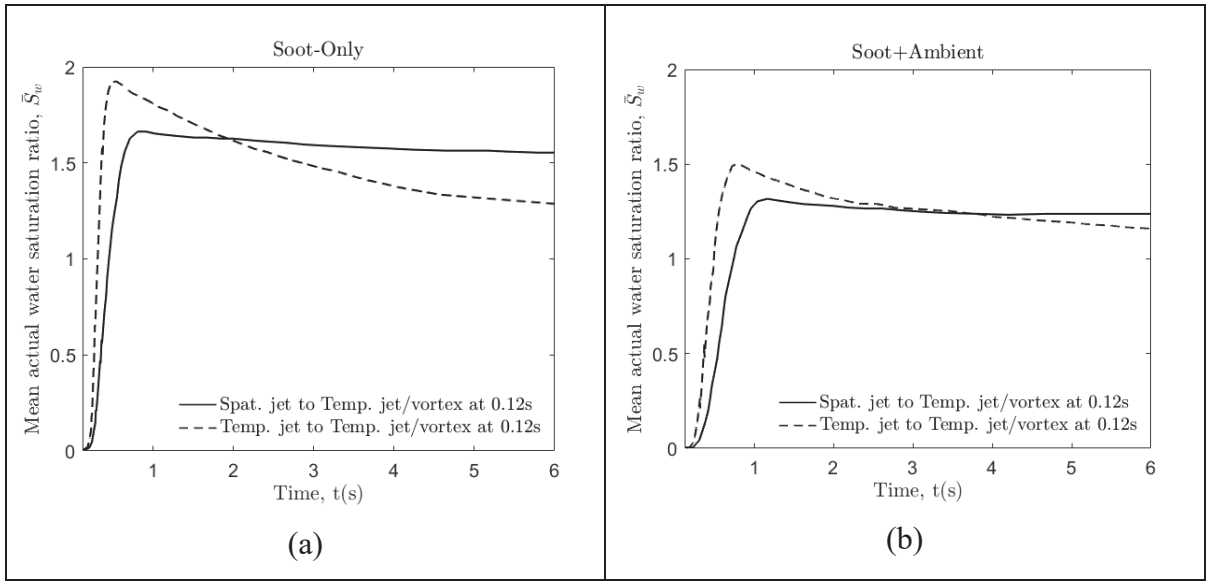

Figure 5.16 Mean actual water saturation ratio, $\bar{S}_w$, versus time t during the vortex phase for cases initialized at from spatial and temporal jet profiles at t_j= 0.12 s: (a) soot-only and (b) soot+ambient

Across the soot-only and soot+ambient cases in vortex phase starting at t_j= 0.12 s, as shown in Figure 5.17(a-b), the plume-mean radius, $\bar{r}_p$, rose rapidly during onset (≈0.4–0.7 s) and then grew more slowly through vortex development. Temporal-jet initialization yielded slightly larger radii during the early supersaturation burst (t<1 s); at t≈1 s the difference is modest for soot-only but more pronounced for soot+ambient. The spatial-initialized cases maintained higher late-time $\bar{S}_w$ (Figure 5.16), overtook the temporal curves (crossovers at ≈1.7 s for soot-only and ≈3.8 s for soot+ambient), and finished larger at 6 s. Overall, at t_j= 0.12 s, temporal–spatial differences were small; later, the spatial case showed a small acceleration in growth and ended slightly larger.

In the soot-only case during the vortex phase (Figure 5.17(c)), the evolution of $EI_{act,ice}$ through t≈1 s mirrored the jet-only trends of Figure 5.7(c) for the temporal jet initialization, with

minimal change induced by the vortex. By contrast, the case initialized from the spatial jet (in Figure 5.17(c)) showed a rise in $EI_{act,ice}$ once the flow was mapped to the temporal jet/vortex framework (in comparison to Figure 5.7(c)). Activation and freezing peaked before 1 s; thereafter the temporal–spatial gap remained nearly constant at ≈12% through 6 s. In the soot+ambient case as shown in Figure 5.17(d), the early evolution up to 1 s was likewise consistent with the jet-only behavior; the larger number of nuclei introduced by ambient particles narrowed the temporal–spatial difference, which settled to ≈2% by 6 s. Thus, wake-vortex dynamics did not significantly change the final $EI_{act,ice}$; the persistent offset primarily reflected the initial jet history and the mapping of the spatial jet to the temporal framework at vortex onset.

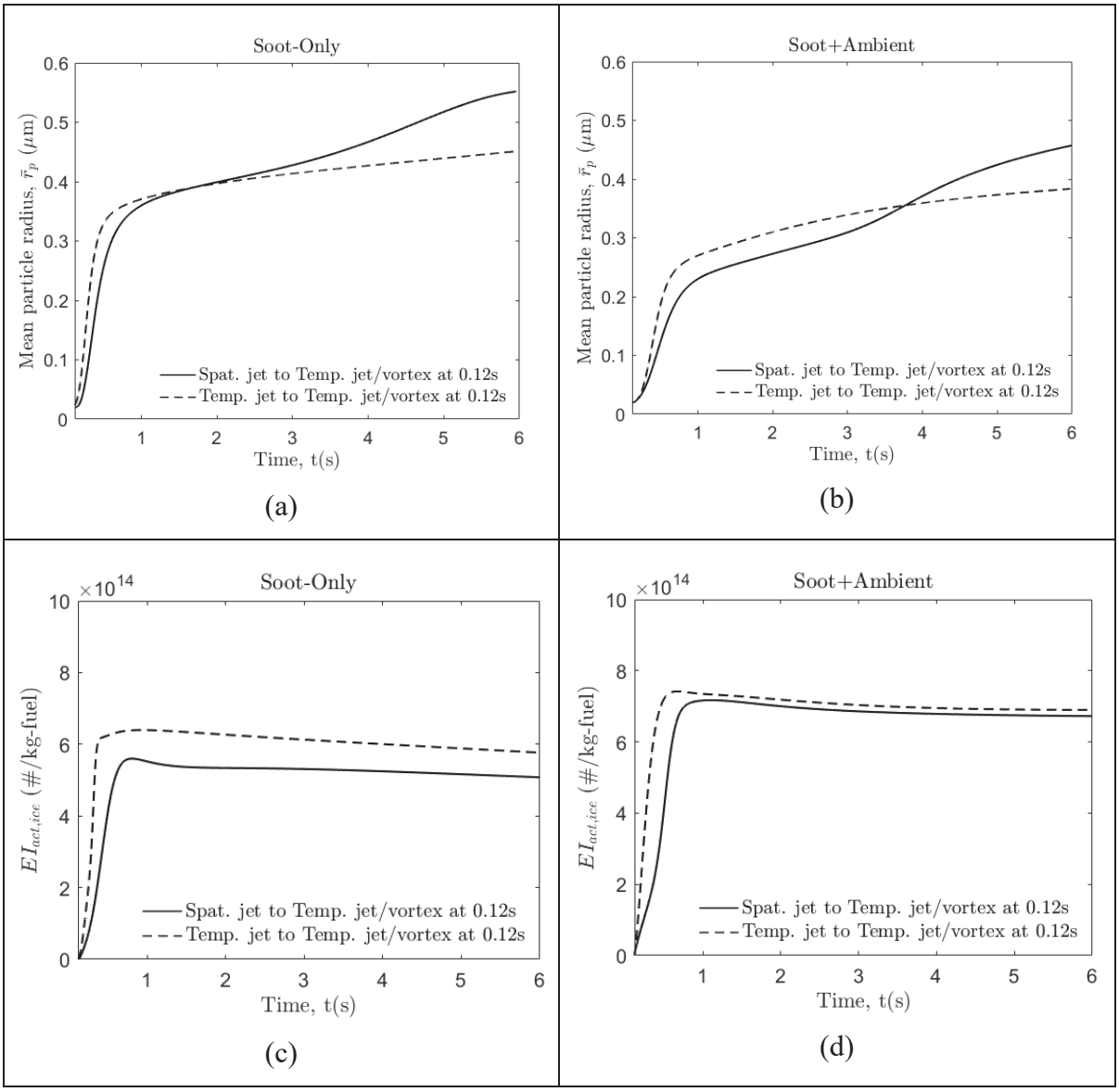

Figure 5.17 Vortex phase (0.12–6 s) evolution for initialization from spatial jet (solid) and temporal jet (dashed) simulations at t_j= 0.12 s. Top row: plume-mean particle radius for (a) soot-only and (b) soot+ambient. Bottom row: emission index of activated/freezing particles for (c) soot-only and (d) soot+ambient

Given the relative sensitivity to jet initialization observed in Figure 5.17, the vortex phase in Figure 5.18 was initialized from a more mature jet state at t_j= 0.5 s. Figure 5.18(a-b) showed that this later initialization produced systematically smaller mean particle radii than the t_j= 0.12 s initialization cases in Figure 5.17. By t_j= 0.5 s, jet phase entrainment had already diluted

the exhaust and smoothed scalar fluctuations, reducing the excess water vapor per unit jet length and the potential for strong ice supersaturation after vortex onset. Thus, even though the supersaturation maximum still occurred before 1 s, its magnitude was lower, leading to slower growth. As in Figure 5.17, the presence of ambient aerosols reduced the temporal, spatial disparity and promoted late-time convergence.

Moving to Figure 5.18(c-d), the $EI_{act,ice}$ increased in all cases relative to Figure 5.17(c-d), reflecting additional activation during the longer jet phase preceding vortex onset. The rise was more pronounced in the soot-only case and more modest in soot+ambient case, which was closer to an activation ceiling due to the larger nuclei pool. Unlike Figure 5.17(c-d), delaying vortex onset reduced per-crystal growth while increasing crystal number, with levels governed primarily by jet history and initialization (temporal vs spatial).

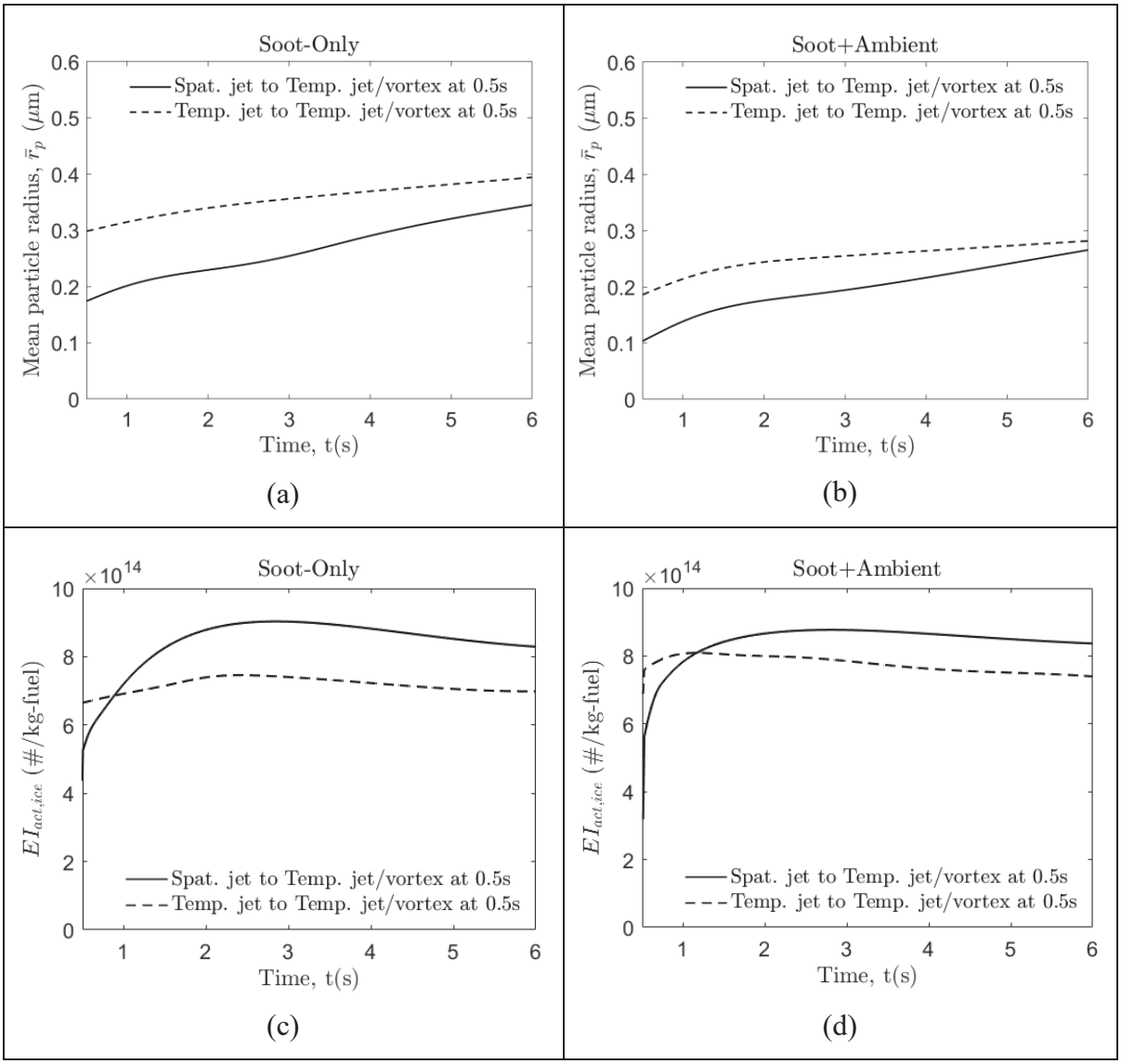

Figure 5.18 Vortex phase (0.5–6 s) evolution for initialization from spatial jet (solid) and temporal jet (dashed) simulations at t_j= 0.5 s. Top row: plume-mean particle radius for (a) soot-only and (b) soot+ambient. Bottom row: emission index of activated/freezing particles for (c) soot-only and (d) soot+ambient

5.4 Conclusion

This study assesses how the near-field dynamics modeling, temporal vs spatial LES of the engine jet, affects contrails microphysical properties. It also examines vortex-phase initialization for both jet approaches at two jet ages (t_j= 0.12 s and t_j= 0.5 s), corresponding

to the pre-development and developed microphysical stages. Ice microphysics in all cases is represented using an online-coupled Lagrangian scheme. Analyses are conducted in a supersaturated environment and under soot-rich plume conditions, considering emissions from a rich-burn LEAP-1A engine. The effect of ambient aerosols on ice formation is also investigated (soot-only and soot+ambient scenarios).

In the jet phase, the temporal jet, evolving from an initial condition, remains more sensitive to initial perturbations than the spatial jet, whose dynamic properties at quasi-steady state are less affected by inlet disturbances. Regarding the microphysical properties, temporal jets trigger earlier artificial activation and a steeper initial growth of mean particle radius $\bar{r}_p$, yielding slightly larger $\bar{r}_p$ in the early plume than the spatial cases. Further downstream after these transients, the temporal jet reaches overall similar ice microphysical properties to the spatial jet; with differences of the same order of magnitude in both the mean ice radius and ice number-based emission index ($EI_{act,ice}$). In all cases, adding ambient particles increase $EI_{act,ice}$; the increase is larger for the temporal case, widening the temporal–spatial gap and indicating stronger sensitivity of the temporal jet to ambient entrained nuclei, especially at early plume where transient effects from turbulence initialization dominates.

In the vortex phase, spatial/temporal jet simulations are used to initialize the jet/vortex interactions at t_j= 0.12 s and t_j= 0.5 s. With early onset of the vortex phase, ice number concentration is primarily inherited from the jet phase, and differences between temporal and spatial jet initializations diminish with plume age, indicating a limited impact of wake-vortex on ice particle number. Delaying the vortex onset yields relatively smaller particle radii and a slightly higher ice concentration number. While ambient aerosols increase ice number overall, they concurrently slow crystal growth via water vapor competition, thereby reducing sensitivity to vortex initialization.

The choice of dynamic-modeling approach for contrail simulations is inherently linked to the soot emission regime and ambient humidity. In soot-rich and strongly supersaturated environments, where engine-emitted nuclei dominate ice formation, both temporal and spatial

approaches yield comparable microphysical outcomes once the plume has matured, making the temporal approach a practical, cost-effective alternative. Conversely, in low-soot or soot-free conditions, such as those expected for future low-emission SAF or hydrogen-fueled engines, ice formation becomes more sensitive to ambient aerosol entrainment and to the detailed representation of mixing and turbulence development. In such regimes, spatial simulations may be more suitable, as they better capture the gradual evolution toward a quasi-steady state and provide a more realistic description of the entrainment-driven activation of ambient particles.

One should note that our analysis highlights the need to assess sensitivity to initial perturbations, particularly in the temporal framework, where early plume development directly depends on the initial turbulence field. Ideally, this should be addressed through ensemble simulations or, at minimum, by considering multiple perturbation amplitudes to ensure a robust statistical characterization of microphysical properties.

5.5 Acknowledgment

This research was enabled in part by support provided by the Calcul Québec (calculquebec.ca) and the Digital Research Alliance of Canada (alliancecan.ca).

CONCLUSION

This thesis developed and validated a high-fidelity numerical framework integrating computational fluid dynamics (CFD) and aerosol microphysics to study the formation of ice crystals in aircraft engine exhaust plumes. The objective was to develop a modeling tool to simulate the exhaust-jet flow downstream of a realistic turbofan and its early entrainment into the wake-vortex. The tool integrates microphysical processes to characterize the initial properties of ice particles. This objective was achieved by structuring the research into three sub-objectives.

To address **Sub-Objective 1**, a microphysics module was developed and online-coupled to the FludiLES CFD solver, enabling high-fidelity 3D large eddy simulations (LES) of soot-dominated aircraft engine exhaust in the near-field jet regime. The gaseous phase was treated in an Eulerian framework, while soot particles were tracked individually in a Lagrangian framework for activation, condensation, sublimation and freezing. This configuration was applied to realistic turbofan engines spanning different bypass ratios (bpr) to isolate how the bypass flow and bpr shape early contrail microphysics. First, results were interpreted relative to an equivalent single-stream (turbojet) configuration at matched specific thrust to separate the bypass effect. Adding a bypass flow was associated with enhanced core–ambient mixing and an increase of up to ~30% in the mean ice particle radius in the jet regime, relative to the matched-thrust single-stream case. Then, across three representative engines—CFM56-5B3/3 (low-bpr), LEAP-1A/33 (high-bpr), and an UHBR (ultra-bpr) case—and ambient temperatures of 215, 220, and 225 K, distinct early-plume behaviors were observed. Higher bypass ratios were associated with reduced sensitivity of initial contrail properties to ambient temperature. The UHBR configuration exhibited the smallest temperature-driven variability, whereas the lowest-bpr engine showed the strongest dependence. The fraction of activated/freezing particles was highest for the UHBR engine, lower for the high-bpr engine, and lowest for the low-bpr engine, indicating that greater bypass ratios expedite activation through enhanced mixing. These conclusions apply to the jet regime; after ≈0.6 s, inter-engine differences in

mean radius and activation fraction diminish, indicating that subsequent evolution is expected to depend on jet/vortex coupling not modeled here.

Within FludiLES, building on the framework established thus far, **Sub-Objective 2** was addressed by extending the microphysical model to incorporate the solubility effect through the κ-Köhler theory for soot particle activation and subsequent microphysical processes. The 3D LES with online-coupled microphysics model was then compared against an 0D offline box model. The study systematically varied (i) the hygroscopicity parameter (κ) to represent solute effects, (ii) the soot number emission index to control the initial particle abundance and vapor competition, and (iii) the initial dry soot-core radius to probe size-dependent activation and condensational growth. Validation was performed by reproducing a published baseline case and by constructing a methodological comparison against a 0D offline box model driven by plume-mean dilution and temperature histories extracted from LES.

Under LEAP-1A cruise conditions and jet regime evolution, the κ-Köhler microphysical model clarified the controls of soot properties on initial contrail microphysics. Decreasing κ from 0.0142 to 0.0005 (lower effective fuel sulfur content) slightly reduced mean particle radii yet increased the activated/freezing fraction, owing to the greater persistence of supersaturation before vapor is depleted by early activations. Reducing the soot number emission index in two steps increased the mean particle radius and raised the activated fraction, reflecting weaker competition for water vapor. Increasing the initial dry soot core radius (10→30 nm) advanced activation and increased the activated fraction, with mean radius differences that narrowed by the end of the jet regime as growth proceeded.

The online–offline coupling test demonstrated that the 0D offline box model (lacking 3D particle positions and vapor-sink feedback) overpredicted ice number and misrepresented κ-sensitivity (showing a slight increase of activation with higher κ), whereas the 3D online-coupled microphysics with LES consistently yielded lower activation at higher κ and captured deactivation due to local vapor competition. Consequently, online coupling is required for reliable prediction and for parameterizations intended for numerical models.

In **Sub-Objective 3**, building upon the previous improvements, ambient particles were added to the microphysical model as a second type along with soot particles. To extend the analysis into the vortex phase, the Lamb–Oseen wake–vortex domain was applied to the two LES jet modeling approaches (spatial and temporal) under cruise conditions representative of an Airbus A320neo with a LEAP-1A engine. Results were obtained by comparing temporal and spatial jet phase LES formulations, quantifying their effects on early contrail microphysics under soot-only and soot+ambient aerosol scenarios, and deriving modeling guidance for vortex phase initialization at two jet ages (0.12 s and 0.5 s). In jet-only simulations, the temporal jet mixed laterally faster, triggered earlier activation, and produced larger and more numerous ice particles, whereas the spatial jets decayed more gradually and retained stronger scalar gradients, favoring a smaller sizes distribution. Ambient aerosol increased ice number but slowed growth via vapor competition, thereby reducing sensitivity to the jet modeling.

Computational limits prevent fully spatial modeling of long jet/vortex runs, motivating alternatives to improve the current options. Using results from the spatial and temporal jets, an early vortex onset was imposed; under this early onset, differences between the formulations faded over time, with the ice number remaining near jet-only levels, particularly for the temporal initialization. The mean ice-crystal radius was initially higher for the temporal initialization—as in the jet phase—but later in the vortex phase the spatial initialization slightly overtook it, owing to greater vapor available per ice crystal. With a later vortex onset, more jet phase properties are preserved and exert greater influence. The mean ice-particle radius remains larger for the temporal initialization, though the gap narrows downstream in the vortex phase. The ice number becomes higher for the spatial initialization, reflecting the longer jet history and greater vapor available per ice crystal, thereby reversing the early-onset ordering. Inclusion of ambient aerosol produced the same qualitative effects as in the jet phase: increasing number, decreasing radius, and damping sensitivity to the modeling choice.

In conclusion, this thesis advances aircraft-engine emissions modeling by integrating realistic turbofan parameters under cruise conditions with an online-coupled LES–microphysics

framework that resolves soot and ambient aerosols through the jet phase and into early vortex entrainment. By systematically comparing temporal and spatial LES formulations and benchmarking online versus offline microphysical coupling, the developed framework provides a robust basis for assessing contrail-related aviation-climate impacts and enables systematic sensitivity and uncertainty analyses in numerical modeling.

RECOMMENDATIONS

Based on the work carried out in this thesis, several improvements and future developments can be considered to refine the modeling of contrail formation.

FludiLES Dynamic Field Export for Offline Use

High-fidelity, time-resolved flow fields for the jet and vortex phases are provided by FludiLES. Because the code is non-dimensional, its outputs can be rescaled and reused in offline analyses. To enable robust offline use, two complementary export paths are recommended for FludiLES:

- Implementing a high-density Lagrangian tracer pathway in FludiLES by advecting massless particles through the resolved 3D velocity field with a high-order Runge–Kutta integrator, using trilinear spatial and linear-in-time interpolation. Seed tracers with a stratified/low-discrepancy pattern across plume cross-sections and periodically reseed to maintain domain coverage as parcels exit. Along each path line, record time-stamped samples of the key fields $(u, v, w, T, P, Y_v, \rho)$ and the passive-scalar mixing field Z. Export two products: (i) raw trajectory records for downstream diagnostics; and (ii) ensemble summaries aggregated by time and space (means, variances, quantiles, PDFs, and coverage metrics) for rapid statistical analysis.
- Partitioning the simulation domain into volumetric zones (axial slabs, radial shells, or azimuthal sectors) to enable offline use of heavy LES outputs. At each output time, compute volume weighted aggregates of the required Eulerian fields (means, variances, minima, maxima). Write a compact matrix for each time step with zones as rows and variables as columns, and include a small zone index table that lists the spatial bounds and volume of every zone.

Offline Implementation of the FludiLES Lagrangian Microphysics

An offline version of the FludiLES Lagrangian microphysics can be implemented that preserves the in-solver parcel state vector, rate equations, and parameterizations. Flow forcing may be supplied by time-resolved Eulerian fields, interpolated in space and time to parcel

positions, or by precomputed Lagrangian path lines carrying the required thermodynamic histories. Additional particle classes beyond soot and ambient can be represented, including volatile aerosols, organics and ions. Chemical reactions can be included along prescribed trajectories. To capture greater soot detail, soot-specific processes such as coagulation or aggregation should be incorporated where relevant. This flexibility enables detailed evaluation of sustainable aviation fuels (SAF), including their emission characteristics and aerosol composition effects.

Incorporate Environmental Heterogeneity and Distributions

The present work was carried out in a homogeneous environment without vertical variation in temperature, humidity, or wind. Under real cruise conditions, however, the distribution and vertical structure of ambient parameters, especially relative humidity, may alter microphysical evolution, and background shear, static stability, and thermal gradients can strongly influence wake development, thereby affecting predictions of contrail persistence. Sensitivity studies across these profiles and distributions should be performed to assess the robustness of the results and to better align simulations with in-situ observations at altitude.

Introducing MPI and Improving OpenMP efficiency

Given the high computational cost of FludiLES, especially for spatial jet and vortex phase simulations, enhanced parallel scalability is recommended. The code currently relies solely on OpenMP and exhibits limited efficiency, while MPI capability is absent. MPI support for spatial runs should be implemented and, where appropriate, a hybrid MPI and OpenMP execution mode enabled. With robust parallelization in place, larger domains and longer integrations can be run within practical wall-clock times, enabling broader parametric studies.

Adopt GPU Solvers for Spatial Jet/Vortex Simulations in FludiLES

To run the vortex phase in FludiLES, including jet/vortex interaction and far-field, at full-domain spatial resolution, it is recommended to adopt graphics processing unit (GPU)–accelerated solvers. These solvers exploit GPU parallelism to deliver faster turnaround and

enable more detailed analyses. Given the availability of GPU resources on modern clusters, updating the code to support GPU execution is advisable.

LIST OF REFERENCES

(IATA), I. A. T. A. (Report, 2024). Aviation Contrails and Their Climate Effect (Tackling Uncertainties and Enabling Solutions). Retrieved from https://www.iata.org/contentassets/726b8a2559ad48fe9decb6f2534549a6/aviation-contrails-climate-impact-report.pdf

Abegglen, M., Brem, B., Ellenrieder, M., Durdina, L., Rindlisbacher, T., Wang, J., . . . Sierau, B. (2016). Chemical Characterization of Freshly Emitted Particulate Matter from Aircraft Exhaust Using Single Particle Mass Spectrometry. *Atmospheric Environment, 134*, 181-197. doi:https://doi.org/10.1016/j.atmosenv.2016.03.051

Afchine, A., Rolf, C., Costa, A., Spelten, N., Riese, M., Buchholz, B., . . . Minikin, A. (2018). Ice Particle Sampling from Aircraft – Influence of the Probing Position on the Ice Water Content. *Atmospheric measurement techniques, 11*(7), 4015-4031. doi:https://doi.org/10.5194/amt-11-4015-2018

Afkari, P., Chouak, M., Cantin, S., & Garnier, F. (2025). Evaluating Bypass Effects of Advanced Turbofan Engines on Contrail Formation Using Large Eddy Simulations. *Journal of Aircraft*, 1-14. doi:https://doi.org/10.2514/1.C038376

Ahmad, N. N., & Proctor, F. (2014). *Review of Idealized Aircraft Wake Vortex Models.* Paper presented at the 52nd Aerospace Sciences Meeting.

Ahrens, D., Méry, Y., Guénard, A., & Miake-Lye, R. C. (2023). A New Approach to Estimate Particulate Matter Emissions From Ground Certification Data: The nvPM Mission Emissions Estimation Methodology. *Journal of Engineering for Gas Turbines and Power, 145*(3), 031019. doi:https://doi.org/10.1115/1.4055477

Airbus. (2024). Aircraft Characteristics Airport and Maintenance Planning. *A320/A320NEO, Revision*(30/85).

Alsante, A. N., & Cheng, M. D. (2024). Aerosol-Cloud Interactions from Aviation Soot Emissions. *Journal of Geophysical Research: Atmospheres, 129*(12), e2023JD040277. doi:https://doi.org/10.1029/2023JD040277

Amielh, M., Djeridane, T., Anselmet, F., & Fulachier, L. (1996). Velocity Near-Field of Variable Density Turbulent Jets. *International Journal of Heat and mass transfer, 39*(10), 2149-2164. doi:https://doi.org/10.1016/0017-9310(95)00294-4

Annunziata, R., Bonne, N., & Garnier, F. (2025). Numerical Investigation of Engine Position Effects on Contrail Formation and Evolution in the Near-Field of a Realistic Aircraft Configuration. *Aerospace Science and Technology*, 110703. doi:https://doi.org/10.1016/j.ast.2025.110703

Appleman, H. (1953). The Formation of Exhaust Condensation Trails by Jet Aircraft. *Bulletin of the American Meteorological Society, 34*(1), 14-20. doi:https://doi.org/10.1175/1520-0477-34.1.14

Ball, C., Fellouah, H., & Pollard, A. (2012). The Flow Field in Turbulent Round Free Jets. *Progress in Aerospace Sciences, 50*, 1-26. doi:https://doi.org/10.1016/j.paerosci.2011.10.002

Barbosa, F. C. (2022). Ultra High Bypass Ratio Engine Technology Review-The Efficiency Frontier for the Turbofan Propulsion. *SAE Technical Paper, 36*(0032). doi:https://doi.org/10.4271/2021-36-0032

Bardina, J., Ferziger, J., & Reynolds, W. (1980). *Improved Subgrid-Scale Models for Large-Eddy Simulation.* Paper presented at the 13th fluid and plasmadynamics conference.

Beer, C. G., Hendricks, J., Righi, M., Heinold, B., Tegen, I., Groß, S., . . . Weinzierl, B. (2020). Modelling Mineral Dust Emissions and Atmospheric Dispersion with MADE3 in EMAC v2.54. *Geoscientific Model Development, 13*(9), 4287-4303. doi:https://doi.org/10.5194/gmd-13-4287-2020

Betz, A. (1933). *Behavior of Vortex Systems*. Retrieved from NACA Technical Memorandum:

Beyersdorf, A. J., Thornhill, K. L., Winstead, E. L., Ziemba, L. D., Blake, D. R., Timko, M. T., & Anderson, B. E. (2012). Power-Dependent Speciation of Volatile Organic Compounds in Aircraft Exhaust. *Atmospheric Environment, 61*, 275-282. doi:https://doi.org/10.1016/j.atmosenv.2012.07.027

Bier, A., & Burkhardt, U. (2022). Impact of Parametrizing Microphysical Processes in the Jet and Vortex Phase on Contrail Cirrus Properties and Radiative Forcing. *Journal of Geophysical Research: Atmospheres, 127*(23), e2022JD036677. doi:https://doi.org/10.1029/2022JD036677

Bier, A., Unterstrasser, S., & Vancassel, X. (2022). Box Model Trajectory Studies of Contrail Formation Using a Particle-Based Cloud Microphysics Scheme. *Atmospheric Chemistry and Physics, 22*(2), 823-845. doi:https://doi.org/10.5194/acp-22-823-2022

Bier, A., Unterstrasser, S., Zink, J., Hillenbrand, D., Jurkat-Witschas, T., & Lottermoser, A. (2024). Contrail Formation on Ambient Aerosol Particles for Aircraft with Hydrogen Combustion: A Box Model Trajectory Study. *Atmospheric Chemistry and Physics, 24*(4), 2319-2344. doi:https://doi.org/10.5194/acp-24-2319-2024

Blaisdell, G., Spyropoulos, E., & Qin, J. (1996). The Effect of the Formulation of Nonlinear Terms on Aliasing Errors in Spectral Methods. *Applied Numerical Mathematics, 21*(3), 207-219. doi:https://doi.org/10.1016/0168-9274(96)00005-0

Bogey, C., & Bailly, C. (2002). Three-Dimensional Non-Reflective Boundary Conditions for Acoustic Simulations: Far Field Formulation and Validation Test Cases. *Acta Acustica united with Acustica, 88*(4), 463-471.

Bogey, C., & Bailly, C. (2010). Influence of Nozzle-Exit Boundary-Layer Conditions on the Flow and Acoustic Fields of Initially Laminar Jets. *Journal of Fluid Mechanics, 663*, 507-538. doi:https://doi.org/10.1017/S0022112010003605

Bogey, C., Bailly, C., & Juv´, D. (2003). Noise Investigation of a High Subsonic,Moderate Reynolds Number Jet Using a Compressible LargeEddy Simulation. *Theoret. Comput. Fluid Dynamics, 16*, 273–297.

Bogey, C., & Marsden, O. (2014). *Influence of Nozzle-Exit Boundary-Layer Profile on High-Subsonic Jets.* Paper presented at the 20th AIAA/CEAS Aeroacoustics Conference.

Boose, Y., Baloh, P., Plötze, M., Ofner, J., Grothe, H., Sierau, B., . . . Kanji, Z. A. (2019). Heterogeneous Ice Nucleation on Dust Particles Sourced from Nine Deserts Worldwide – Part 2: Deposition Nucleation and Condensation Freezing. *Atmospheric Chemistry and Physics, 19*(2), 1059-1076. doi:https://doi.org/10.5194/acp-19-1059-2019

Brancher, P. (1996). Etude Numérique des Instabilités Secondaires de Jets.

Bräuer, T., Voigt, C., Sauer, D., Kaufmann, S., Hahn, V., Scheibe, M., . . . Moore, R. (2021). Reduced Ice Number Concentrations in Contrails from Low Aromatic Biofuel Blends. *Atmospheric Chemistry and Physics Discussions, 2021*, 1-14. doi:https://doi.org/10.5194/acp-21-16817-2021

Brown, R., Miake-Lye, R., Anderson, M., Kolb, C., & Resch, T. (1996). Aerosol Dynamics in Near-Field Aircraft Plumes. *Journal of Geophysical Research: Atmospheres, 101*(D17), 22939-22953. doi:https://doi.org/10.1029/96JD01918

Brunet, S. (1999). *Etude numérique et experimentale du mélange des jets de moteurs dans les tourbillons de sillage d'un avion de ligne.* Aix-Marseille 1,

Brunet, S., Garnier, F., & Sagaut, P. (1999). *Crow Instability Effects on the Exhaust Plume Mixing and Condensation.* Paper presented at the ESAIM: Proceedings.

Burkhardt, U., & Kärcher, B. (2011). Global Radiative Forcing from Contrail Cirrus. *Nature climate change, 1*(1), 54-58. doi:https://doi.org/10.1038/nclimate1068

Burkhardt, U., Kärcher, B., Ponater, M., Gierens, K., & Gettelman, A. (2008). Contrail Cirrus Supporting Areas in Model and Observations. *Geophysical Research Letters, 35*(16). doi:https://doi.org/10.1029/2008GL034056

Busen, R., & Schumann, U. (1995). Visible Contrail Formation from Fuels with Different Sulfur Contents. *Geophysical Research Letters, 22*(11), 1357-1360. doi:https://doi.org/10.1029/95GL01312

Cantin, S., Chouak, M., Morency, F., & Garnier, F. (2022). Eulerian–Lagrangian CFD-Microphysics Modeling of a Near-Field Contrail from a Realistic Turbofan. *International Journal of Engine Research, 23*(4), 661-677. doi:https://doi.org/10.1177/1468087421993961

Celik, I. B., Ghia, U., Roache, P. J., & Freitas, C. J. (2008). Procedure for Estimation and Reporting of Uncertainty Due to Discretization in CFD Applications. *Journal of fluids Engineering-Transactions of the ASME, 130*(7). doi:https://doi.org/10.1115/1.2960953

Coppens, F. (1998). *Simulations Numériques sur le Développement de la Turbulence dans un Tourbillon.* Toulouse, INPT,

Crow, S. C. (1970). Stability Theory for a Pair of Trailing Vortices. *AIAA journal, 8*(12), 2172-2179. doi:https://doi.org/10.2514/3.6083

Curtius, J. (2009). *Nucleation of Atmospheric Particles.* Paper presented at the EPJ Web of Conferences.

Dahm, W. J., Frieler, C. E., & Tryggvason, G. (1992). Vortex Structure and Dynamics in the Near Field of a Coaxial Jet. *Journal of Fluid Mechanics, 241*, 371-402. doi:https://doi.org/10.1017/S0022112092002088

Davidson, M. J., & Wang, H. J. (2002). Strongly Advected Jet in a Coflow. *Journal of Hydraulic Engineering, 128(8)*, 742–752. doi:https://doi.org/10.1061/(ASCE)0733-9429(2002)128:8(742)

Detwiler, A. G., & Jackson, A. (2002). Contrail Formation and Propulsion Efficiency. *Journal of Aircraft, 39*(4), 638-644. doi:https://doi.org/10.2514/2.2976

DeVries, P., DeVries, P. L., & Hasbun, J. (2011). *A First Course in Computational Physics*: Jones & Bartlett Learning.

Enjalbert, N., Galley, D., & Pierrot, L. (2009). An Entrainment Model for the Turbulent Jet in a Coflow. *Comptes Rendus Mecanique, 337*(9-10), 639-644. doi:https://doi.org/10.1016/j.crme.2009.09.005

Ettenreich, R. (1919). Wolkenbildung über einer Feuersbrunst und an Flugzeugabgasen. *Meteorol. Z, 36*, 355-356.

Ferreira, T., Alonso, J., & Gorlé, C. (2025). *Large Eddy Simulation of the Early Jet-Vortex Interaction Phase of Contrails From Hydrogen Aircraft.* Paper presented at the AIAA AVIATION FORUM AND ASCEND 2025.

Ferreira, T., Alonso, J. J., & Gorlé, C. (2024). Developing a Numerical Framework for the High-Fidelity Simulation of Contrails: Sensitivity Analysis for Conventional Contrails. *AIAA Aviation Forum and Ascend 2024, AIAA 2024-3775*, 3775. doi:https://doi.org/10.2514/6.2024-3775

Fritz, T. M., Eastham, S. D., Speth, R. L., & Barrett, S. R. (2020). The Role of Plume-Scale Processes in Long-Term Impacts of Aircraft Emissions. *Atmospheric Chemistry and Physics, 20*(9), 5697-5727. doi:https://doi.org/10.5194/acp-20-5697-2020

Fuchs, N. A. (2013). *Evaporation and Droplet Growth in Gaseous Media*: Elsevier.

Fuglestvedt, J. S., Berntsen, T. K., Godal, O., Sausen, R., Shine, K. P., & Skodvin, T. (2003). Metrics of Climate Change: Assessing Radiative Forcing and Emission Indices. *Climatic Change, 58*(3), 267-331. doi:https://doi.org/10.1023/A:1023905326842

Fukuta, N., & Walter, L. (1970). Kinetics of Hydrometeor Growth from a Vapor-Spherical Model. *Journal of atmospheric sciences, 27*(8), 1160-1172. doi:https://doi.org/10.1175/1520-0469(1970)027%3C1160:KOHGFA%3E2.0.CO;2

Gago, C. F. (2002). *Simulations numériques d'un jet rond turbulent et de son interaction avec un tourbillon de sillage.* PhD thesis, Université de Marne La Vallée,

Gago, C. F., Brunet, S., & Garnier, F. (2002). Numerical Investigation of Turbulent Mixing in a Jet/Wake Vortex Interaction. *AIAA journal, 40*(2), 276-284. doi:https://doi.org/10.2514/2.1643

Gago, C. F., Garnier, F., & Utheza, F. (2003). Direct Testing of Subgrid Scale Models in Large-Eddy Simulation of a Non-Isothermal Turbulent Jet. *International journal for numerical methods in fluids, 42*(9), 999-1026. doi:https://dx.doi.org/10.1002/fld.570

Gamet, L., Ducros, F., Nicoud, F., & Poinsot, T. (1999). Compact Finite Difference Schemes on Non-Uniform Meshes: Application to Direct Numerical Simulations of Compressible Flows. *International journal for numerical methods in fluids, 29*(2), 159-191. doi:https://doi.org/10.1002/(SICI)1097-0363(19990130)29:2%3C159::AID-FLD781%3E3.0.CO;2-9

Garnier, E., Adams, N., & Sagaut, P. (2009). *Large eddy simulation for compressible flows*: Springer Science & Business Media.

Garnier, F., Baudoin, C., Woods, P., & Louisnard, N. (1997). Engine Emission Alteration in the Near Field of an Aircraft. *Atmospheric Environment, 31*(12), 1767-1781. doi:https://doi.org/10.1016/S1352-2310(96)00329-9

Garnier, F., Brunet, S., & Jacquin, L. (1997). *Modelling Exhaust Plume Mixing in the Near Field of an Aircraft.* Paper presented at the Annales Geophysicae.

Garnier, F., Gago, C. F., Brasseur, A., Paoli, R., & Cuenot, B. (2003). *Dispersion and Growing of Ice Particles in a Turbulent Exhaust Plume.* Paper presented at the European Conference on Aviation, Atmosphere and Climate.

Garnier, F., & Laverdant, A. (1999). Exhaust Jet Mixing and Condensation Effects in the Near Field of Aircraft Wakes. *Aerospace Science and Technology, 3*(5), 271-280. doi:https://doi.org/10.1016/S1270-9638(00)86963-1

Garnier, F., Maglaras, E., Morency, F., & Vancassel, X. (2014). Effect of Compressibility on Contrail Ice Particle Growth in an Engine Jet. *International Journal of Turbo & Jet-Engines, 31*(2), 131-140. doi:https://doi.org/10.1515/tjj-2013-0039

Garvey, R., & Fowler, A. (2023). On the Mathematical Theory of Plumes. *Geophysical & Astrophysical Fluid Dynamics, 117*(2), 79-106. doi:https://doi.org/10.1080/03091929.2023.2187054

Georgiadis, N. J., Rizzetta, D. P., & Fureby, C. (2010). Large-Eddy Simulation: Current Capabilities, Recommended Practices, and Future Research. *AIAA journal, 48*(8), 1772-1784. doi:https://doi.org/10.2514/1.J050232

Gerz, T., & Ehret, T. (1997). Wingtip Vortices and Exhaust Jets During the Jet Regime of Aircraft Wakes. *Aerospace Science and Technology, 1*(7), 463-474. doi:https://doi.org/10.1016/S1270-9638(97)90008-0

Gerz, T., & Holzapfel, F. (1999). Wing-Tip Vortices, Turbulence, and the Distribution of Emissions. *AIAA journal, 37*(10), 1270-1276. doi:https://doi.org/10.2514/2.595

Gerz, T., Holzäpfel, F., & Darracq, D. (2002). Commercial Aircraft Wake Vortices. *Progress in Aerospace Sciences, 38*(3), 181-208. doi:https://doi.org/10.1016/S0376-0421(02)00004-0

Gierens, K. (2003). On the Transition Between Heterogeneous and Homogeneous Freezing. *Atmospheric Chemistry and Physics, 3*(2), 437-446. doi:https://doi.org/10.5194/acp-3-437-2003

Gierens, K. M., Monier, M., & Gayet, J. F. (2003). The Deposition Coefficient and Its Role for Cirrus Clouds. *Journal of Geophysical Research: Atmospheres, 108*(D2). doi:https://doi.org/10.1029/2001JD001558

Givoli, D. (1991). Non-Reflecting Boundary Conditions. *Journal of Computational Physics, 94*(1), 1-29. doi:https://doi.org/10.1016/0021-9991(91)90135-8

Grabowski, W. W., Morrison, H., Shima, S.-I., Abade, G. C., Dziekan, P., & Pawlowska, H. (2019). Modeling of Cloud Microphysics: Can We Do Better? *Bulletin of the American Meteorological Society, 100*(4), 655-672. doi:https://doi.org/10.1175/BAMS-D-18-0005.1

Griffin, R. J. (2013). The Sources and Impacts of Tropospheric Particulate Matter. *Nature Education Knowledge, 4*(5), 1.

Guignery, F., Montreuil, E., Thual, O., & Vancassel, X. (2012). Contrail Microphysics in the Near Wake of a Realistic Wing Through RANS Simulations. *Aerospace Science and Technology, 23*(1), 399-408. doi:https://doi.org/10.1016/j.ast.2011.09.011

H. Hoshizaki, R. J. C., L. B. Anderson, K. O. Redler,, & J. W. Meyer, W. J. M., P. E. Cassady. (1972). *Study of high-altitude aircraft wake dynamics*. Palo Alto, California: Lockheed Palo Alto Research Laboratory.

Haglind, F. (2008). Potential of Lowering the Contrail Formation of Aircraft Exhausts by Engine Re-Design. *Aerospace Science and Technology, 12*(6), 490-497. doi:https://doi.org/10.1016/j.ast.2007.12.001

Hanasz, M., & Sol, H. (1996). Kelvin-Helmholtz Instability of Stratified Jets. *arXiv preprint astro-ph/9604156*. doi:https://doi.org/10.48550/arXiv.astro-ph/9604156

Havens, B. S. (1952). *History of Project Cirrus*. Retrieved from Defense Technical Information Center:

Haywood, J. M., Allan, R. P., Bornemann, J., Forster, P. M., Francis, P. N., Milton, S., . . . Thorpe, R. (2009). A Case Study of the Radiative Forcing of Persistent Contrails Evolving into Contrail-Induced Cirrus. *Journal of Geophysical Research: Atmospheres, 114*(D24). doi:https://doi.org/10.1029/2009JD012650

Hennemann, I., & Holzapfel, F. (2007). *Aircraft Wake Vortex Deformation in Turbulent Atmosphere.* Paper presented at the Fifth International Symposium on Turbulence and Shear Flow Phenomena.

Henning, S., Ziese, M., Kiselev, A., Saathoff, H., Möhler, O., Mentel, T., . . . Monier, M. (2012). Hygroscopic Growth and Droplet Activation of Soot Particles: Uncoated, Succinic or Sulfuric Acid Coated. *Atmospheric Chemistry and Physics, 12*(10), 4525-4537. doi:https://doi.org/10.5194/acp-12-4525-2012

Hermann, M., Heintzenberg, J., Wiedensohler, A., Zahn, A., Heinrich, G., & Brenninkmeijer, C. (2003). Meridional Distributions of Aerosol Particle Number Concentrations in the Upper Troposphere and Lower Stratosphere Obtained by Civil Aircraft for Regular Investigation of the Atmosphere Based on an Instrument Container (CARIBIC) Flights. *Journal of Geophysical Research: Atmospheres, 108*(D3). doi:https://doi.org/10.1029/2001JD001077

Heymsfield, A., Baumgardner, D., DeMott, P., Forster, P., Gierens, K., & Kärcher, B. (2010). Contrail microphysics. *Bulletin of the American Meteorological Society, 91*(4), 465-472.

Hirsch, C. (1990). Numerical Computation of Internal and External Flows. *Computational methods for inviscid and viscous flows, 2*.

Hoeflinger, J., Alavilli, P., Jackson, T., & Kuhn, B. (2001). Producing scalable performance with OpenMP: Experiments with two CFD applications. *Parallel Computing, 27(4)*, 391-413. doi:https://doi.org/10.1016/S0167-8191(00)00071-5

Hunt, J. C., Wray, A. A., & Moin, P. (1988). *Eddies, streams, and convergence zones in turbulent flows*. Retrieved from NASA:

Hussein, H. J., Capp, S. P., & George, W. K. (1994). Velocity Measurements in a High-Reynolds-Number, Momentum-Conserving, Axisymmetric, Turbulent Jet. *Journal of Fluid Mechanics, 258*, 31-75. doi:https://doi.org/10.1017/S002211209400323X

ICAO. (2022). Innovation for a Green Transition. *Environmental Report, International Civil Aviation Organization.* Retrieved from https://www.icao.int/environmental-protection/Documents/EnvironmentalReports/2022/ICAO%20ENV%20Report%202022%20F4.pdf

ICAO. (2024). Aircraft Engine Emissions Databank. v30. Retrieved from https://www.easa.europa.eu/en/domains/environment/icao-aircraft-engine-emissions-databank

IPCC. (2023). Climate Change 2023: Synthesis Report. Contribution of Working Groups I, II and III to the Sixth Assessment Report of the Intergovernmental Panel on Climate Change. Retrieved from https://dx.doi.org/10.59327/IPCC/AR6-9789291691647

Iwabuchi, H., Yang, P., Liou, K., & Minnis, P. (2012). Physical and Optical Properties of Persistent Contrails: Climatology and Interpretation. *Journal of Geophysical Research: Atmospheres, 117*(D6). doi:https://doi.org/10.1029/2011JD017020

Jaramillo, P., S. Kahn Ribeiro, P. Newman, S. Dhar, O.E. Diemuodeke, T. Kajino, D.S. Lee, S.B. Nugroho, X. Ou, A. Hammer Strømman, J. Whitehead. (2022). *Climate Change 2022: Mitigation of Climate Change. Contribution of Working Group III to the Sixth Assessment Report of the Intergovernmental Panel on Climate Change*. Retrieved from Cambridge, UK and New York, NY, USA:

Jensen, E. J., Ackerman, A. S., Stevens, D. E., Toon, O. B., & Minnis, P. (1998). Spreading and Growth of Contrails in a Sheared Environment. *Journal of Geophysical Research: Atmospheres, 103*(D24), 31557-31567. doi:https://doi.org/10.1029/98JD02594

Jensen, E. J., Toon, O. B., Kinne, S., Sachse, G. W., Anderson, B. E., Chan, K. R., . . . Miake-Lye, R. C. (1998). Environmental Conditions Required for Contrail Formation and Persistence. *Journal of Geophysical Research: Atmospheres, 103*(D4), 3929-3936. doi:https://doi.org/10.1029/97JD02808

Jeßberger, P., Voigt, C., Schumann, U., Sölch, I., Schlager, H., Kaufmann, S., . . . Gayet, J.-F. (2013). Aircraft Type Influence on Contrail Properties. *Atmospheric Chemistry and Physics, 13*(23), 11965-11984. doi:https://doi.org/10.5194/acp-13-11965-2013

Kanji, Z. A., Ladino, L. A., Wex, H., Boose, Y., Burkert-Kohn, M., Cziczo, D. J., & Krämer, M. (2017). Overview of Ice Nucleating Particles. *Meteorological Monographs, 58*, 1.1-1.33. doi:https://doi.org/10.1175/AMSMONOGRAPHS-D-16-0006.1

Kärcher, B. (1994). Transport of Exhaust Products in the Near Trail of a Jet Engine under Atmospheric Conditions. *Journal of Geophysical Research: Atmospheres, 99*(D7), 14509-14517. doi:https://doi.org/10.1029/94JD00940

Kärcher, B. (1998). Physicochemistry of Aircraft-Generated Liquid Aerosols, Soot, and Ice Particles: 1. Model Description. *Journal of Geophysical Research, 103*(D14), 17111-17128. doi:https://doi.org/10.1029/98JD01044

Kärcher, B. (1999). Aviation-Produced Aerosols and Contrails. *Surveys in geophysics, 20*(2), 113-167. doi:https://doi.org/10.1023/A:1006600107117

Kärcher, B. (2016). The Importance of Contrail Ice Formation for Mitigating the Climate Impact of Aviation. *Journal of Geophysical Research: Atmospheres, 121*(7), 3497-3505. doi:https://doi.org/10.1002/2015JD024696

Kärcher, B. (2018). Formation and Radiative Forcing of Contrail Cirrus. *9*, 1824. doi:https://doi.org/10.1038/s41467-018-04068-0

Kärcher, B. (2018). Formation and Radiative Forcing of Contrail Cirrus. *Nature communications, 9*(1), 1-17. doi:https://doi.org/10.1038/s41467-018-04068-0

Kärcher, B. (2022). A Parameterization of Cirrus Cloud Formation: Revisiting Competing Ice Nucleation. *Journal of Geophysical Research: Atmospheres, 127*(18), e2022JD036907. doi:https://doi.org/10.1029/2022JD036907

Kärcher, B., Burkhardt, U., Bier, A., Bock, L., & Ford, I. (2015). The Microphysical Pathway to Contrail Formation. *Journal of Geophysical Research: Atmospheres, 120*(15), 7893-7927. doi:https://doi.org/10.1002/2015JD023491

Kärcher, B., Burkhardt, U., Unterstrasser, S., & Minnis, P. (2009). Factors Controlling Contrail Cirrus Optical Depth. *Atmospheric Chemistry and Physics, 9*(16), 6229-6254. doi:https://doi.org/10.5194/acp-9-6229-2009

Kärcher, B., Busen, R., Petzold, A., Schröder, F., Schumann, U., & Jensen, E. (1998). Physicochemistry of Aircraft-Generated Liquid Aerosols, Soot, and Ice Particles: 2. Comparison with Observations and Sensitivity Studies. *Journal of Geophysical Research: Atmospheres, 103*(D14), 17129-17147. doi:https://doi.org/10.1029/98JD01045

Kärcher, B., DeMott, P., Jensen, E., & Harrington, J. (2022). Studies on the Competition Between Homogeneous and Heterogeneous Ice Nucleation in Cirrus Formation. *Journal of Geophysical Research: Atmospheres, 127*(3), e2021JD035805. doi:https://doi.org/10.1029/2021JD035805

Kärcher, B., Kleine, J., Sauer, D., & Voigt, C. (2018). Contrail Formation: Analysis of Sublimation Mechanisms. *Geophysical Research Letters, 45*(24), 13,547-513,552. doi:https://doi.org/10.1029/2018GL079391

Kärcher, B., Peter, T., Biermann, U. M., & Schumann, U. (1996). The Initial Composition of Jet Condensation Trails. *Journal of atmospheric sciences, 53*(21), 3066-3083. doi:https://doi.org/10.1175/1520-0469(1996)053%3C3066:TICOJC%3E2.0.CO;2

Kärcher, B., Turco, R., Yu, F., Danilin, M., Weisenstein, D., Miake-Lye, R., & Busen, R. (2000). A Unified Model for Ultrafine Aircraft Particle Emissions. *Journal of Geophysical Research: Atmospheres, 105*(D24), 29379-29386. doi:https://doi.org/10.1029/2000JD900531

Kärcher, B., & Yu, F. (2009). Role of Aircraft Soot Emissions in Contrail Formation. *Geophysical Research Letters, 36*(1). doi:https://doi.org/10.1029/2008GL036649

Kärcher, B., Yu, F., Schröder, F., & Turco, R. (1998). Ultrafine Aerosol Particles in Aircraft Plumes: Analysis of Growth Mechanisms. *Geophysical Research Letters, 25*(15), 2793-2796. doi:https://doi.org/10.1029/98GL02114

Kaushik, M., Kumar, R., & Humrutha, G. (2015). Review of Computational Fluid Dynamics Studies on Jets. *American Journal of Fluid Dynamics, 5*(3A), 1-11. doi:https://doi.org/10.5923/s.ajfd.201501.01

Khou, J.-C., Ghedhaifi, W., Vancassel, X., & Garnier, F. (2015). Spatial Simulation of Contrail Formation in Near-Field of Commercial Aircraft. *Journal of Aircraft, 52*(6), 1927-1938. doi:https://doi.org/10.2514/1.C033101

Khou, J., Ghedhaïfi, W., Vancassel, X., Montreuil, E., & Garnier, F. (2017). CFD Simulation of Contrail Formation in the Near Field of a Commercial Aircraft: Effect of Fuel Sulfur Content. *Meteorologische Zeitschrift, 26*(6), 585-596. doi:http://dx.doi.org/10.1127/metz/2016/0761

Klein, M., Sadiki, A., & Janicka, J. (2003). A Digital Filter Based Generation of Inflow Data for Spatially Developing Direct Numerical or Large Eddy Simulations. *Journal of Computational Physics, 186*(2), 652-665. doi:https://doi.org/10.1016/S0021-9991(03)00090-1

Kleine, J., Voigt, C., Sauer, D., Schlager, H., Scheibe, M., Jurkat-Witschas, T., . . . Anderson, B. E. (2018). In Situ Observations of Ice Particle Losses in a Young Persistent Contrail. *Geophysical Research Letters, 45*(24), 13,553-513,561. doi:https://doi.org/10.1029/2018GL079390

Kolb, C., Jayne, J., Worsnop, D., Molina, M., Meads, R., & Viggiano, A. (1994). Gas Phase Reaction of Sulfur Trioxide with Water Vapor. *Journal of the American Chemical Society, 116*(22), 10314-10315. doi:https://doi.org/10.1021/ja00101a067

Kolomenskiy, D., & Paoli, R. (2018). Numerical Simulation of the Wake of an Airliner. *Journal of Aircraft, 55*(4), 1689-1699. doi:https://doi.org/10.2514/1.C034349

Köpp, F. (1999). Wake-Vortex Characteristics of Military-Type Aircraft Measured at Airport Oberpfaffenhofen Using the DLR Laser Doppler Anemometer. *Aerospace Science and Technology, 3*(4), 191-199. doi:https://doi.org/10.1016/S1270-9638(99)80042-X

Körner, S., & Holzäpfel, F. (2016). Multi-Model Ensemble Wake Vortex Prediction. *Aircraft Engineering and Aerospace Technology: An International Journal, 88*(2), 331-340. doi:https://doi.org/10.1108/AEAT-02-2015-0068

Kreidenweis, S. M., Petters, M. D., & Chuang, P. Y. (2009). Cloud Particle Precursors. *Portion of the eBook, Vol. 2*. doi:https://doi.org/10.7551/mitpress/8300.003.0015

Labbe, O., Maglaras, E., & Garnier, F. (2007). Large-Eddy Simulation of a Turbulent Jet and Wake Vortex Interaction. *Computers & fluids, 36*(4), 772-785. doi:https://doi.org/10.1016/j.compfluid.2006.06.001

Langmuir, I. (1915). The Dissociation of Hydrogen into Atoms. [Part II.] Calculation of the Degree of Dissociation and the Heat of Formation. *Journal of the American Chemical Society, 37*(3), 417-458.

LeBoeuf, R. L., & Mehta, R. D. (1995). On Using Taylor's Hypothesis for Three-Dimensional Mixing Layers. *Physics of Fluids, 7*(6), 1516-1518. doi:https://doi.org/10.1063/1.868539

Leboissetier, A., Okong'o, N., & Bellan, J. (2004). *Large Eddy Simulation of Jets Laden with Evaporating Drops.* Paper presented at the 42nd AIAA Aerospace Sciences Meeting and Exhibit.

Lee, D. S., Fahey, D., Skowron, A., Allen, M., Burkhardt, U., Chen, Q., . . . Fuglestvedt, J. (2021). The Contribution of Global Aviation to Anthropogenic Climate Forcing for 2000 to 2018. *Atmospheric Environment, 244*, 117834. doi:https://doi.org/10.1016/j.atmosenv.2020.117834

Lee, D. S., Fahey, D. W., Forster, P. M., Newton, P. J., Wit, R. C., Lim, L. L., . . . Sausen, R. (2009). Aviation and Global Climate Change in the 21st Century. *Atmospheric Environment, 43*(22-23), 3520-3537. doi:https://doi.org/10.1016/j.atmosenv.2009.04.024

Lee, D. S., Pitari, G., Grewe, V., Gierens, K., Penner, J. E., Petzold, A., . . . Berntsen, T. (2010). Transport Impacts on Atmosphere and Climate: Aviation. *Atmospheric Environment, 44*(37), 4678-4734. doi:https://doi.org/10.1016/j.atmosenv.2009.06.005

Lele, S. K. (1992). Compact Finite Difference Schemes with Spectral-Like Resolution. *Journal of Computational Physics, 103*(1), 16-42. doi:https://doi.org/10.1016/0021-9991(92)90324-R

Lenormand, R. (1999). 2. Visualization of Flow Patterns in 2-D Model Networks. *Experimental Methods in the Physical Sciences, 35*, 43-68. doi:https://doi.org/10.1016/S0076-695X(08)60413-5

Lévêque, E., Toschi, F., Shao, L., & Bertoglio, J.-P. (2007). Shear-Improved Smagorinsky Model for Large-Eddy Simulation of Wall-Bounded Turbulent Flows. *Journal of Fluid Mechanics, 570*, 491-502. doi:https://doi.org/10.1017/S0022112006003429

Lewellen, D. (2014). Persistent Contrails and Contrail Cirrus. Part II: Full Lifetime Behavior. *Journal of the atmospheric sciences, 71*(12), 4420-4438. doi:https://doi.org/10.1175/JAS-D-13-0317.1

Lewellen, D., & Lewellen, W. (2001). The Effects of Aircraft Wake Dynamics on Contrail Development. *Journal of the atmospheric sciences, 58*(4), 390-406. doi:https://doi.org/10.1175/1520-0469(2001)058%3C0390:TEOAWD%3E2.0.CO;2

Lewellen, D., Meza, O., & Huebsch, W. (2014). Persistent Contrails and Contrail Cirrus. Part I: Large-Eddy Simulations from Inception to Demise. *Journal of the atmospheric sciences, 71*(12), 4399-4419. doi:https://doi.org/10.1175/JAS-D-13-0316.1

Lewellen, D. C. (2020). A Large-Eddy Simulation Study of Contrail Ice Number Formation. *Journal of the atmospheric sciences, 77*(7), 2585-2604. doi:https://doi.org/10.1175/JAS-D-19-0322.1

Li, D., Fan, J., Luo, K., & Cen, K. (2011). Direct Numerical Simulation of a Particle-Laden Low Reynolds Number Turbulent Round Jet. *International Journal of Multiphase Flow, 37*(6), 539-554. doi:https://doi.org/10.1016/j.ijmultiphaseflow.2011.03.013

Li, Y., Davidovits, P., Kolb, C., & Worsnop, D. (2001). Mass and Thermal Accommodation Coefficients of H2O (g) on Liquid Water as a Function of Temperature. *The Journal of Physical Chemistry A, 105*(47), 10627-10634. doi:https://doi.org/10.1021/jp012758q

Liu, S., Meneveau, C., & Katz, J. (1994). On the Properties of Similarity Subgrid-Scale Models as Deduced from Measurements in a Turbulent Jet. *Journal of Fluid Mechanics, 275*, 83-119. doi:https://doi.org/10.1017/S0022112094002296

Lobo, P., Durdina, L., Brem, B. T., Crayford, A. P., Johnson, M. P., Smallwood, G. J., . . . Llamedo, A. (2020). Comparison of Standardized Sampling and Measurement Reference Systems for Aircraft Engine Non-Volatile Particulate Matter Emissions. *Journal of Aerosol Science, 145*, 105557. doi:https://doi.org/10.1016/j.jaerosci.2020.105557

Lodato, G., Vervisch, L., & Domingo, P. (2009). A Compressible Wall-Adapting Similarity Mixed Model for Large-Eddy Simulation of the Impinging Round Jet. *Physics of Fluids, 21*(3). doi:https://doi.org/10.1063/1.3068761

Longfellow, C., Ravishankara, A., & Hanson, D. (2000). Reactive and Nonreactive Uptake on Hydrocarbon Soot: HNO_3, O_3, and N_2O_5. *Journal of Geophysical Research: Atmospheres, 105*(D19), 24345-24350. doi:https://doi.org/10.1029/2000JD900297

Lottermoser, A., & Unterstraßer, S. (2025). High-Resolution Modelling of Early Contrail Evolution from Hydrogen-Powered Aircraft. *EGUsphere, 2025*, 1-33. doi:https://doi.org/10.5194/egusphere-2024-3859

Maglaras, E. (2007). *Application de la Simulation Numérique des Grandes Échelles à la Formation des Traînées de Condensation dans le Sillage d'un Avionn.* Bordeaux 1,

Marcolli, C., Mahrt, F., & Kärcher, B. (2021). Soot PCF: Pore Condensation and Freezing Framework for Soot Aggregates. *Atmospheric Chemistry and Physics, 21*(10), 7791-7843. doi:https://doi.org/10.5194/acp-21-7791-2021

Märkl, R. S., Voigt, C., Sauer, D., Dischl, R. K., Kaufmann, S., Harlaß, T., . . . Burkhardt, U. (2024). Powering Aircraft with 100% Sustainable Aviation Fuel Reduces Ice Crystals in Contrails. *Atmospheric Chemistry and Physics, 24*(6), 3813-3837. doi:https://doi.org/10.5194/acp-24-3813-2024

Martin, S. T. (2000). Phase transitions of aqueous atmospheric particles. *Chemical Reviews, 100*(9), 3403-3454.

Matulka, A., López, P., Redondo, J., & Tarquis, A. (2014). On the Entrainment Coefficient in a Forced Plume: Quantitative Effects of Source Parameters. *Nonlinear processes in geophysics, 21*(1), 269-278. doi:https://doi.org/10.5194/npg-21-269-2014

Michalke, A., & Hermann, G. (1982). On the Inviscid Instability of a Circular Jet with External Flow. *Journal of Fluid Mechanics, 114*, 343-359. doi:https://doi.org/10.1017/S0022112082000196

Misaka, T., Holzäpfel, F., & Gerz, T. (2015). Large-Eddy Simulation of Aircraft Wake Evolution from Roll-Up Until Vortex Decay. *AIAA journal, 53*(9), 2646-2670. doi:https://doi.org/10.2514/1.J053671

Misaka, T., Holzäpfel, F., Hennemann, I., Gerz, T., Manhart, M., & Schwertfirm, F. (2012). Vortex Bursting and Tracer Transport of a Counter-Rotating Vortex Pair. *Physics of Fluids, 24*(2), 025104. doi:https://doi.org/10.1063/1.3684990

Misaka, T., & Obayashi, S. (2017). Numerical Study on Jet–Wake Vortex Interaction of Aircraft Configuration. *Aerospace Science and Technology, 70*, 615-625. doi:https://doi.org/10.1016/j.ast.2017.08.038

Montreuil, E., Ghedhaifi, W., Chmielaski, V., Vuillot, F., Gand, F., & Loseille, A. (2018). *Numerical Simulation of Contrail Formation on the Common Research Model Wing/Body/Engine Configuration.* Paper presented at the 2018 Atmospheric and Space Environments Conference.

Moore, R. H., Shook, M., Beyersdorf, A., Corr, C., Herndon, S., Knighton, W. B., . . . Yu, Z. (2015). Influence of Jet Fuel Composition on Aircraft Engine Emissions: A Synthesis of Aerosol Emissions Data from the NASA APEX, AAFEX, and ACCESS Missions. *Energy & Fuels, 29*(4), 2591-2600. doi:https://doi.org/10.1021/ef502618w

Morrison, H., van Lier-Walqui, M., Fridlind, A. M., Grabowski, W. W., Harrington, J. Y., Hoose, C., . . . Pawlowska, H. (2020). Confronting the Challenge of Modeling Cloud and Precipitation Microphysics. *Journal of advances in modeling earth systems, 12*(8), e2019MS001689. doi:https://doi.org/10.1029/2019MS001689

Morton, B. R., Taylor, G. I., & Turner, J. S. (1956). Turbulent Gravitational Convection from Maintained and Instantaneous Sources. *Proceedings of the Royal Society of London. Series A. Mathematical and Physical Sciences, 234*(1196), 1-23. doi:https://doi.org/10.1098/rspa.1956.0011

Mozurkewich, M. (1986). Aerosol Growth and the Condensation Coefficient for Water: A Review. *Aerosol Science and Technology, 5*(2), 223-236. doi:https://doi.org/10.1080/02786828608959089

Murphy, D. M., & Koop, T. (2005). Review of the Vapour Pressures of Ice and Supercooled Water for Atmospheric Applications. *Quarterly Journal of the Royal Meteorological Society: A journal of the atmospheric sciences, applied meteorology and physical oceanography, 131*(608), 1539-1565. doi:https://doi.org/10.1256/qj.04.94

Naiman, A., Lele, S., & Jacobson, M. (2011). Large Eddy Simulations of Contrail Development: Sensitivity to Initial and Ambient Conditions over the First Twenty Minutes. *Journal of Geophysical Research: Atmospheres, 116*(D21). doi:https://doi.org/10.1029/2011JD015806

National Academies of Sciences, E., and Medicine. (2025). Developing a Research Agenda on Contrails and Their Climate Impacts. *Washington, DC: The National Academies Press.* doi:https://doi.org/10.17226/29073

Panda, J., Zaman, K., & Seasholtz, R. (2004). *Measurements of Initial Conditions at Nozzle Exit of High-Speed Jets.* Paper presented at the 7th AIAA/CEAS Aeroacoustics Conference and Exhibit.

Paoli, R., & Garnier, F. (2005). Interaction of Exhaust Jets and Aircraft Wake Vortices: Small-Scale Dynamics and Potential Microphysical-Chemical Transformations. *Comptes Rendus Physique, 6*(4-5), 525-547. doi:https://doi.org/10.1016/j.crhy.2005.05.003

Paoli, R., Helie, J., & Poinsot, T. (2004). Contrail Formation in Aircraft Wakes. *Journal of Fluid Mechanics, 502*, 361-373. doi:https://doi.org/10.1017/S0022112003007808

Paoli, R., Hélie, J., Poinsot, T., & Ghosal, S. (2002). Contrail Formation in Aircraft Wakes Using Large-Eddy Simulations. *Studying Turbulence Using Numerical Simulation Databases-IX: Proceedings of the 2002 Summer Program*.

Paoli, R., & Moet, H. (2018). Temporal Large-Eddy Simulations of the Near-Field of an Aircraft Wake. *Open Journal of Fluid Dynamics, 8*(02), 161. doi:https://doi.org/10.4236/ojfd.2018.82012

Paoli, R., Nybelen, L., Picot, J., & Cariolle, D. (2013). Effects of Jet/Vortex Interaction on Contrail Formation in Supersaturated Conditions. *Physics of Fluids, 25*(5). doi:https://doi.org/10.1063/1.4807063

Paoli, R., & Shariff, K. (2016). Contrail Modeling and Simulation. *Annual Review of Fluid Mechanics, 48*. doi:https://doi.org/10.1146/annurev-fluid-010814-013619

Paoli, R., Vancassel, X., Garnier, F., & Mirabel, P. (2008). Large-Eddy Simulation of a Turbulent Jet and a Vortex Sheet Interaction: Particle Formation and Evolution in the Near Field of an Aircraft Wake. *Meteorologische Zeitschrift, 17*(2), 131-144. doi:https://doi.org/10.1127/0941-2948/2008/0278

Paramonov, M., Drossaart van Dusseldorp, S., Gute, E., Abbatt, J. P., Heikkilä, P., Keskinen, J., . . . Hao, L. (2020). Condensation/Immersion Mode Ice-Nucleating Particles in a Boreal Environment. *Atmospheric Chemistry and Physics, 20*(11), 6687-6706. doi:https://doi.org/10.5194/acp-20-6687-2020

Pauen, J., Unterstrasser, S., & Stephan, A. (2024). *Towards Refined Contrail Simulations of Formation Flight Scenarios.* Paper presented at the 34th Congress of the International Council of the Aeronautical Sciences, ICAS 2024.

Paugam, R., Paoli, R., & Cariolle, D. (2010). Influence of Vortex Dynamics and Atmospheric Turbulence on the Early Evolution of a Contrail. *Atmospheric Chemistry and Physics, 10*(8), 3933-3952. doi:https://doi.org/10.5194/acp-10-3933-2010

Penner, J. E., Lister, D., Griggs, D. J., Dokken, D. J., & McFarland, M. (1999). *Aviation and the global atmosphere: a special report of the Intergovernmental Panel on Climate Change*: Cambridge University Press.

Petters, M., & Kreidenweis, S. (2007). A Single Parameter Representation of Hygroscopic Growth and Cloud Condensation Nucleus Activity. *Atmospheric Chemistry and Physics, 7*(8), 1961-1971. doi:https://doi.org/10.5194/acp-7-1961-2007

Petzold, A., Gysel, M., Vancassel, X., Hitzenberger, R., Puxbaum, H., Vrochticky, S., . . . Mirabel, P. (2005). On the Effects of Organic Matter and Sulphur-Containing Compounds on the CCN Activation of Combustion Particles. *Atmospheric Chemistry and Physics, 5*(12), 3187-3203. doi:https://doi.org/10.5194/acp-5-3187-2005

Petzold, A., Khan, N. F., Li, Y., Spichtinger, P., Rohs, S., Crewell, S., . . . Krämer, M. (2025). Most Long-Lived Contrails Form Within Cirrus Clouds With Uncertain Climate Impact. *Nature communications, 16*(1), 9695. doi:https://doi.org/10.1038/s41467-025-65532-2

Phillips, W., Alley, N., & Goodrich, W. (2004). Lifting-Line Analysis of Roll Control and Variable Twist. *Journal of Aircraft, 41*(5), 1169-1176. doi:http://dx.doi.org/10.2514/1.3846

Picot, J., Paoli, R., Thouron, O., & Cariolle, D. (2015). Large-Eddy Simulation of Contrail Evolution in the Vortex Phase and Its Interaction with Atmospheric Turbulence. *Atmospheric Chemistry and Physics, 15*(13), 7369-7389. doi:https://doi.org/10.5194/acp-15-7369-2015

Poinsot, T. J., amp, & Lelef, S. (1992). Boundary Conditions for Direct Simulations of Compressible Viscous Flows. *Journal of Computational Physics, 101*(1), 104-129. doi:https://doi.org/10.1016/0021-9991(92)90046-2

Ponater, M., Marquart, S., & Sausen, R. (2002). Contrails in a Comprehensive Global Climate Model: Parameterization and Radiative Forcing Results. *Journal of Geophysical Research: Atmospheres, 107*(D13), ACL 2-1-ACL 2-15. doi:https://doi.org/10.1029/2001JD000429

Ponsonby, J., Teoh, R., Kärcher, B., & Stettler, M. (2025). An Updated Microphysical Model for Particle Activation in Contrails: The Role of Volatile Plume Particles. *EGUsphere, 2025*, 1-37. doi:https://doi.org/10.5194/egusphere-2025-1717

Pope, S. B. (2000). *Turbulent Flows*: Cambridge University Press.

Popovicheva, O., Persiantseva, N. M., Shonija, N. K., DeMott, P., Koehler, K., Petters, M., . . . Suzanne, J. (2008). Water Interaction with Hydrophobic and Hydrophilic Soot Particles. *Physical Chemistry Chemical Physics, 10*(17), 2332-2344. doi:https://doi.org/10.1039/B718944N

Poroseva, S. V., Colmenares F, J. D., & Murman, S. M. (2016). On the Accuracy of RANS Simulations with DNS Data. *Physics of Fluids, 28*(11). doi:https://doi.org/10.1063/1.4966639

Proctor, F., Ahmad, N. a., Switzer, G., & Limon Duparcmeur, F. (2010). *Three-Phased Wake Vortex Decay.* Paper presented at the AIAA Atmospheric and Space Environments Conference.

Pruppacher, H. R., & Klett, J. D. (1979). *Microphysics of Clouds and Precipitation*: Reidel, Dordrecht.

Ramsay, J., Tristanto, I., Shahpar, S., & John, A. (2024). Assessing the Environmental Impact of Aircraft/Engine Integration With Respect to Contrails. *Journal of Engineering for Gas Turbines and Power, 146*(11). doi:https://doi.org/10.1115/GT2024-124447

Ricou, F. P., & Spalding, D. (1961). Measurements of Entrainment by Axisymmetrical Turbulent Jets. *Journal of Fluid Mechanics, 11*(1), 21-32. doi:https://doi.org/10.1017/S0022112061000834

Riechers, B., Wittbracht, F., Hütten, A., & Koop, T. (2013). The Homogeneous Ice Nucleation Rate of Water Droplets Produced in a Microfluidic Device and the Role of Temperature Uncertainty. *Physical Chemistry Chemical Physics, 15*(16), 5873-5887. doi:https://doi.org/10.1039/C3CP42437E

Riese, M., Ploeger, F., Rap, A., Vogel, B., Konopka, P., Dameris, M., & Forster, P. (2012). Impact of Uncertainties in Atmospheric Mixing on Simulated UTLS Composition and Related Radiative Effects. *Journal of Geophysical Research: Atmospheres, 117*(D16). doi:https://doi.org/10.1029/2012JD017751

Rojo, C., Vancassel, X., Mirabel, P., Ponche, J.-L., & Garnier, F. (2015). Impact of Alternative Jet Fuels on Aircraft-Induced Aerosols. *Fuel, 144*, 335-341. doi:https://doi.org/10.1016/j.fuel.2014.12.021

Rosenow, J., Hospodka, J., Lán, S., & Fricke, H. (2023). Validation of a Contrail Life-Cycle Model in Central Europe. *Sustainability, 15*(11), 8669. doi:https://doi.org/10.3390/su15118669

Sagaut, P., & Grohens, R. (1999). Discrete Filters for Large Eddy Simulation. *International journal for numerical methods in fluids, 31*(8), 1195-1220. doi:https://doi.org/10.1002/(SICI)1097-0363(19991230)31:8%3C1195::AID-FLD914%3E3.0.CO;2-H

Saulgeot, P. (2023). *Contributions à la compréhension de la formation et de l'atténuation possible des traînées de condensation de l'aviation.* Institut Polytechnique de Paris,

Saulgeot, P., Brion, V., Bonne, N., Dormy, E., & Jacquin, L. (2023). Effects of Atmospheric Stratification and Jet Position on the Properties of Early Aircraft Contrails. *Physical Review Fluids*. doi:https://doi.org/10.1103/PhysRevFluids.8.114702

Sbrizzai, F., Verzicco, R., Pidria, M. F., & Soldati, A. (2004). Mechanisms for Selective Radial Dispersion of Microparticles in the Transitional Region of a Confined Turbulent Round Jet. *International Journal of Multiphase Flow, 30*(11), 1389-1417. doi:https://doi.org/10.1016/j.ijmultiphaseflow.2004.07.004

Schäfer, K. (1932). Verdampfungserscheinungen an Quecksilbertröpfchen: Gekürzte Bearbeitung der Stuttgarter Dissertation 1930. *Zeitschrift für Physik, 77*(3), 198-215. doi:https://doi.org/10.1007/BF01338915

Schlichting, H., & Gersten, K. (2017). *Boundary-Layer Theory* (9 ed.). Berlin: Springer.

Schmidt, E. (1941). Die Entstehung von Eisnebel aus den Auspuffgasen von Flugmotoren. *Schriften der Deutschen Akademie der Luftfahrtforschung, Verlag R. Oldenbourg, München, Heft 44, 5*(44), 1-15. doi:https://elib.dlr.de/107948/

Schooley, A. (1969). Airplane Contrails Related to Vertical Wake Collapse. *Science, 157*, 421-123. doi:https://doi.org/10.1175/1520-0477-50.9.719

Schumann, U. (1996). On Conditions for Contrail Formation from Aircraft Exhausts. *Meteorologische Zeitschrift, 5*, 4-23. doi:https://doi.org/10.1127/metz/5/1996/4

Schumann, U. (2000). Influence of Propulsion Efficiency on Contrail Formation. *Aerospace Science and Technology, 4*(6), 391-401. doi:https://doi.org/10.1016/S1270-9638(00)01062-2

Schumann, U. (2005). Formation, Properties and Climatic Effects of Contrails. *Comptes Rendus Physique, 6*(4-5), 549-565. doi:https://doi.org/10.1016/j.crhy.2005.05.002

Schumann, U. (2012). A Contrail Cirrus Prediction Model. *Geoscientific Model Development, 5*(3), 543-580. doi:https://doi.org/10.5194/gmd-5-543-2012

Schumann, U., Arnold, F., Busen, R., Curtius, J., Kärcher, B., Kiendler, A., . . . Wohlfrom, K. H. (2002). Influence of Fuel Sulfur on the Composition of Aircraft Exhaust Plumes: The Experiments SULFUR 1–7. *Journal of Geophysical Research: Atmospheres, 107*(D15), AAC 2-1-AAC 2-27. doi:https://doi.org/10.1029/2001JD000813

Schumann, U., Baumann, R., Baumgardner, D., Bedka, S. T., Duda, D. P., Freudenthaler, V., . . . Quante, M. (2017). Properties of Individual Contrails: a Compilation of Observations and Some Comparisons. *Atmospheric Chemistry and Physics, 17*(1), 403-438. doi:https://doi.org/10.5194/acp-17-403-2017

Schumann, U., Busen, R., & Plohr, M. (2000). Experimental test of the influence of propulsion efficiency on contrail formation. *Journal of Aircraft, 37*(6), 1083-1087.

Schumann, U., & Heymsfield, A. J. (2017). On the Life Cycle of Individual Contrails and Contrail Cirrus. *Meteorological Monographs, 58*, 3.1-3.24. doi:https://doi.org/10.1175/AMSMONOGRAPHS-D-16-0005.1

Schumann, U., Schlager, H., Arnold, F., Baumann, R., Haschberger, P., & Klemm, O. (1998). Dilution of Aircraft Exhaust Plumes at Cruise Altitudes. *Atmospheric Environment, 32*(18), 3097-3103. doi:https://doi.org/10.1016/S1352-2310(97)00455-X

Schumann, U., Ström, J., Busen, R., Baumann, R., Gierens, K., Krautstrunk, M., . . . Stingl, J. (1996). In Situ Observations of Particles in Jet Aircraft Exhausts and Contrails for Different Sulfur-Containing Fuels. *Journal of Geophysical Research: Atmospheres, 101*(D3), 6853-6869. doi:https://doi.org/10.1029/95JD03405

Segalini, A., & Talamelli, A. (2011). Experimental Analysis of Dominant Instabilities in Coaxial Jets. *Physics of Fluids, 23*(2). doi:https://doi.org/10.1063/1.3553280

Seinfeld, J. H., & Pandis, S. N. (2016). *Atmospheric Chemistry and Physics: From Air Pollution to Climate Change*. New York: John Wiley & Sons.

Singh, D. K., Sanyal, S., & Wuebbles, D. J. (2024). Understanding the Role of Contrails and Contrail Cirrus in Climate Change: a Global Perspective. *Atmospheric Chemistry and Physics, 24*(16), 9219-9262. doi:https://doi.org/10.5194/acp-24-9219-2024

Smagorinsky, J. (1963). General Circulation Experiments with the Primitive Equations: I. The Basic Experiment. *Monthly weather review, 91*(3), 99-164. doi:https://doi.org/10.1175/1520-0493(1963)091%3C0099:GCEWTP%3E2.3.CO;2

Sölch, I., & Kärcher, B. (2010). A Large-Eddy Model for Cirrus Clouds with Explicit Aerosol and Ice Microphysics and Lagrangian Ice Particle Tracking. *Quarterly Journal of the Royal Meteorological Society, 136*(653), 2074-2093. doi:https://doi.org/10.1002/qj.689

Sorokin, A., Katragkou, E., Arnold, F., Busen, R., & Schumann, U. (2004). Gaseous SO_3 and H_2SO_4 in the Exhaust of an Aircraft Gas Turbine Engine: Measurements by CIMS and Implications for Fuel Sulfur Conversion to Sulfur (VI) and Conversion of SO_3 to H_2SO_4. *Atmospheric Environment, 38*(3), 449-456. doi:https://doi.org/10.1016/j.atmosenv.2003.09.069

Stocker, T. (2014). *Climate change 2013: the physical science basis: Working Group I contribution to the Fifth assessment report of the Intergovernmental Panel on Climate Change*: Cambridge university press.

Sussmann, R., & Gierens, K. M. (1999). Lidar and Numerical Studies on the Different Evolution of Vortex Pair and Secondary Wake in Young Contrails. *Journal of Geophysical Research: Atmospheres, 104*(D2), 2131-2142. doi:https://doi.org/10.1029/1998JD200034

Sweby, P. K. (1984). High Resolution Schemes Using Flux Limiters for Hyperbolic Conservation Laws. *SIAM journal on numerical analysis, 21*(5), 995-1011. doi:https://doi.org/10.1137/0721062

Tamamidis, P., & Assanis, D. N. (1993). Evaluation of Various High-Order-Accuracy Schemes with and without Flux Limiters. *International journal for numerical methods in fluids, 16*(10), 931-948. doi:https://doi.org/10.1002/fld.1650161006

Tang, I., & Munkelwitz, H. (1994). Water Activities, Densities, and Refractive Indices of Aqueous Sulfates and Sodium Nitrate Droplets of Atmospheric Importance. *Journal of Geophysical Research: Atmospheres, 99*(D9), 18801-18808. doi:https://doi.org/10.1029/94JD01345

Taylor, G. I. (1935). Statistical Theory of Turbulenc. *Proceedings of the Royal Society of London. Series A-Mathematical and Physical Sciences, 151*(873), 421-444. doi:https://doi.org/10.1098/rspa.1935.0158

Taylor, G. I. (1938). The Spectrum of Turbulence. *Proceedings of the Royal Society of London. Series A-Mathematical and Physical Sciences, 164*(919), 476-490. doi:https://doi.org/10.1098/rspa.1938.0032

Testa, B., Durdina, L., Edebeli, J., Spirig, C., & Kanji, Z. A. (2024). Contrail Processed Aviation Soot Aerosol Are Poor Ice-Nucleating Particles at Cirrus Temperatures. *EGUsphere, 2024*, 1-22. doi:https://doi.org/10.5194/egusphere-2024-151

Thompson, K. W. (1987). Time-Dependent Boundary Conditions for Hyperbolic Systems. *Journal of Computational Physics, 68*(1), 1-24. doi:https://doi.org/10.1016/0021-9991(87)90041-6

Turner, J. S. (1979). *Buoyancy Effects in Fluids*: Cambridge university press.

Ungeheuer, F., Caudillo, L., Ditas, F., Simon, M., van Pinxteren, D., Kılıç, D., . . . Curtius, J. (2022). Nucleation of Jet Engine Oil Vapours Is a Large Source of Aviation-Related Ultrafine Particles. *Communications Earth & Environment, 3*(1), 319. doi:https://doi.org/10.1038/s43247-022-00653-w

Unterstrasser, S. (2014). Large-Eddy Simulation Study of Contrail Microphysics and Geometry During the Vortex Phase and Consequences on Contrail-to-Cirrus Transition. *Journal of Geophysical Research: Atmospheres, 119*(12), 7537-7555. doi:https://doi.org/10.1002/2013JD021418

Unterstrasser, S., & Gierens, K. (2010a). Numerical Simulations of Contrail-to-Cirrus Transition – Part 1: An Extensive Parametric Study. *Atmospheric Chemistry and Physics, 10*(4), 2017-2036. doi:https://doi.org/10.5194/acp-10-2017-2010

Unterstrasser, S., & Gierens, K. (2010b). Numerical Simulations of Contrail-to-Cirrus Transition – Part 2: Impact of Initial Ice Crystal Number, Radiation, Stratification, Secondary Nucleation and Layer Depth. *Atmospheric Chemistry and Physics, 10*(4), 2037-2051. doi:https://doi.org/10.5194/acp-10-2037-2010

Unterstrasser, S., Gierens, K., & Spichtinger, P. (2008). The Evolution of Contrail Microphysics in the Vortex Phase. *Meteorologische Zeitschrift, 17*, 145-156. doi:https://doi.org/10.1127/0941-2948/2008/0273

Unterstrasser, S., & Görsch, N. (2014). Aircraft-Type Dependency of Contrail Evolution. *Journal of Geophysical Research: Atmospheres, 119*(24), 14,015-014,027. doi:https://doi.org/10.1002/2014JD022642

Unterstrasser, S., & Sölch, I. (2010). Study of Contrail Microphysics in the Vortex Phase with a Lagrangian Particle Tracking Model. *Atmospheric Chemistry and Physics, 10*(20), 10003-10015. doi:https://doi.org/10.5194/acp-10-10003-2010

Unterstrasser, S., & Stephan, A. (2020). Far-Field Wake Vortex Evolution of Two Aircraft Formation Flight and Implications on Young Contrails. *The Aeronautical Journal, 124*(1275), 667-702. doi:https://doi.org/10.1017/aer.2020.3

Van Hoot, R., Murugan, S., Mitra, A., & Cukurel, B. (2021). Coaxial Circular Jets—A Review. *Fluids, 6*(147). doi:https://doi.org/10.3390/fluids6040147

Vancassel, X. (2003). *Modélisation Microphysique de la Formation et de l'Évolution d'Aérosols et de Leurs Précurseurs dans les Sillages d'Avions.* Université Louis Pasteur Strasbourg I,

Vancassel, X., Mirabel, P., & Garnier, F. (2014). Numerical Simulation of Aerosols in an Aircraft Wake Using a 3D LES Solver and a Detailed Microphysical Model. *International Journal of Sustainable Aviation, 1*(2), 139-159. doi:https://doi.org/10.1504/IJSA.2014.065480

Vancassel, X. P., Garnier, F. A., & Mirabel, P. J. (2010). In plume physics and chemistry.

Vichnevetsky, R., & Bowles, J. B. (1982). *Fourier Analysis of Numerical Approximations of Hyperbolic Equations*: SIAM.

Villermaux, E., & Rehab, H. (2000). Mixing in Coaxial Jets. *Journal of Fluid Mechanics, 425*, 161-185. doi:https://doi.org/10.1017/S002211200000210X

Voigt, C., Kleine, J., Sauer, D., Moore, R. H., Bräuer, T., Le Clercq, P., . . . Aigner, M. (2021). Cleaner Burning Aviation Fuels Can Reduce Contrail Cloudiness. *Communications Earth & Environment, 2*(1), 114. doi:https://doi.org/10.1038/s43247-021-00174-y

Voigt, C., Lelieveld, J., Schlager, H., Schneider, J., Curtius, J., Meerkötter, R., . . . Crowley, J. N. (2022). Cleaner Skies During the COVID-19 Lockdown. *Bulletin of the American Meteorological Society, 103*(8), E1796-E1827. doi:https://doi.org/10.1175/BAMS-D-21-0012.1

Voigt, C., Sauer, D., Märkl, R. S., Dischl, R. K., Kaufmann, S., Bräuer, T., . . . Le Chenadec, G. (2025). Substantial Aircraft Contrail Formation at Low Soot Emission Levels. *Nature*. doi:https://doi.org/10.21203/rs.3.rs-6559440/v1

Voigt, C., Schumann, U., Jurkat, T., Schäuble, D., Schlager, H., Petzold, A., . . . Borrmann, S. (2010). In-Situ Observations of Young Contrails–Overview and Selected Results from the CONCERT Campaign. *Atmospheric Chemistry and Physics, 10*(18), 9039-9056. doi:https://doi.org/10.5194/acp-10-9039-2010

Wang, L., Khalizov, A. F., Zheng, J., Xu, W., Ma, Y., Lal, V., & Zhang, R. (2010). Atmospheric Nanoparticles Formed from Heterogeneous Reactions of Organics. *Nature Geoscience, 3*(4), 238-242. doi:https://doi.org/10.1038/ngeo778

White, F. M., & Majdalani, J. (2006). *Viscous Fluid Flow* (Vol. 3): McGraw-Hill New York.

Whitman, S. H., Xu, C., & Som, S. (2025). *Comparison of LES and RANS Approaches for Jet-Phase Contrail Modeling.* Paper presented at the AIAA SCITECH 2025 Forum.

Widnall, S. E., Bliss, D. B., & Tsai, C.-Y. (1974). The Instability of Short Waves on a Vortex Ring. *Journal of Fluid Mechanics, 66*(1), 35-47. doi:https://doi.org/10.1017/S0022112074000048

Wilkerson, J., Jacobson, M. Z., Malwitz, A., Balasubramanian, S., Wayson, R., Fleming, G., . . . Lele, S. (2010). Analysis of Emission Data from Global Commercial Aviation: 2004 and 2006. *Atmospheric Chemistry and Physics, 10*(13), 6391-6408. doi:https://doi.org/10.5194/acp-10-6391-2010

Winckelmans, G., Wray, A., & Vasilyev, O. (1998). *Testing of a New Mixed Model for LES: The Leonard Model Supplemented by a Dynamic Smagorinsky Term.* Paper presented at the Summer program.

Wong, H.-W., Beyersdorf, A., Heath, C., Ziemba, L., Winstead, E., Thornhill, K., . . . Bulzan, D. (2013). Laboratory and Modeling Studies on the Effects of Water and Soot Emissions and Ambient Conditions on the Properties of Contrail Ice Particles in the Jet Regime. *Atmospheric Chemistry and Physics, 13*(19), 10049-10060. doi:https://doi.org/10.5194/acp-13-10049-2013

Wong, H.-W., Jun, M., Peck, J., Waitz, I. a., & Miake-Lye, R. C. (2014). Detailed Microphysical Modeling of the Formation of Organic and Sulfuric Acid Coatings on Aircraft Emitted Soot Particles in the Near Field. *Aerosol Science and Technology, 48(9)*, 981–995. doi:https://doi.org/10.1080/02786826.2014.953243

Wong, H.-W., Jun, M., Peck, J., Waitz, I. A., & Miake-Lye, R. C. (2015). Roles of Organic Emissions in the Formation of Near Field Aircraft-Emitted Volatile Particulate Matter: A Kinetic Microphysical Modeling Study. *Journal of Engineering for Gas Turbines and Power, 137*(7), 072606. doi:https://doi.org/10.1115/1.4029366

Wong, H.-W., & Miake-Lye, R. (2010). Parametric Studies of Contrail Ice Particle Formation in Jet Regime Using Microphysical Parcel Modeling. *Atmospheric Chemistry and Physics, 10*(7), 3261-3272. doi:https://doi.org/10.5194/acp-10-3261-2010

Xie, Z.-T., & Castro, I. P. (2008). Efficient Generation of Inflow Conditions for Large Eddy Simulation of Street-Scale Flows. *Flow, turbulence and combustion, 81*(3), 449-470. doi:https://doi.org/10.1007/s10494-008-9151-5

Yang, P., Liou, K.-N., Bi, L., Liu, C., Yi, B., & Baum, B. A. (2015). On the Radiative Properties of Ice Clouds: Light Scattering, Remote Sensing, and Radiation Parameterization. *Advances in Atmospheric Sciences, 32*, 32-63. doi:https://doi.org/10.1007/s00376-014-0011-z

Yang, S., Yuan, B., Peng, Y., Huang, S., Chen, W., Hu, W., . . . Wang, W. (2022). The Formation and Mitigation of Nitrate Pollution: Comparison Between Urban and Suburban Environments. *Atmospheric Chemistry and Physics, 22*(7), 4539-4556. doi:https://doi.org/10.5194/acp-22-4539-2022

Yu, F., Anderson, B. E., Pierce, J. R., Wong, A., Nair, A., Luo, G., & Herb, J. (2024). On Nucleation Pathways and Particle Size Distribution Evolutions in Stratospheric Aircraft Exhaust Plumes with H_2SO_4 Enhancement. *Environmental science & technology, 58*(16), 6934-6944. doi:https://doi.org/10.1021/acs.est.3c08408

Yu, F., Karcher, B., & Anderson, B. E. (2024). Revisiting Contrail Ice Formation: Impact of Primary Soot Particle Sizes and Contribution of Volatile Particles. *Environmental science & technology, 58*(40), 17650-17660. doi:https://doi.org/10.1021/acs.est.4c04340

Yu, F., & Turco, R. P. (1997). The Role of Ions in the Formation and Evolution of Particles in Aircraft Plumes. *Geophysical Research Letters, 24*(15), 1927-1930. doi:https://doi.org/10.1029/97GL01822

Yu, F., & Turco, R. P. (1998). The Formation and Evolution of Aerosols in Stratospheric Aircraft Plumes: Numerical Simulations and Comparisons with Observations. *J GeophysResAtmos, 103*(D20), 25915-25934. doi:https://doi.org/10.1029/98JD02453

Yu, F., Turco, R. P., & Kärcher, B. (1999). The Possible Role of Organics in the Formation and Evolution of Ultrafine Aircraft Particles. *Journal of Geophysical Research: Atmospheres, 104*(D4), 4079-4087. doi:https://doi.org/10.1029/1998JD200062

Zhang, H., Rong, Y., Wang, B., & Wang, X. (2011). Large Eddy Simulation of a 3-D Spatially Developing Turbulent Round Jet. *Science China Technological Sciences, 54*(11), 2916-2923. doi:https://doi.org/10.1007/s11431-011-4577-8